ALEXANDER ERHARD

TOWARDS SCALABLE QUANTUM COMPUTATION WITH TRAPPED IONS

TOWARDS SCALABLE QUANTUM COMPUTATION WITH TRAPPED IONS

ALEXANDER ERHARD

universität innsbruck

Doctoral thesis submitted to the faculty for
MATHEMATICS, COMPUTER SCIENCE AND PHYSICS

In partial fulfillment of the requirements for the degree of
DOCTOR OF PHILOSOPHY
(Physics)

Carried out at the Institute for Experimental Physics under supervision of Univ.-Prof. Dr. Rainer Blatt in the group for Quantum Optics and Spectroscopy.

MAY 2021

ABSTRACT

Computers are devices that have revolutionized our daily lives in many different ways. Although processing power has tremendously increased, the underlying principle of storing information in a binary format based on 0's and 1's is the same. In contrast to this classical way of information processing, a more general way of describing computers might be more powerful. One such non-classical option are quantum computers, where information is stored in quantum binary digits (qubits). In fact, algorithms have been found to work exponentially faster on quantum computers than any known algorithm for classical devices. With Shor's algorithm, for example, it would be possible to factorize a large prime number within minutes on a quantum computer, which takes thousands of years on the best classical computer.

The realization of such complex algorithms requires quantum computers with thousands to millions of qubits. Although quantum computers have been proven to work in principle, today's devices are limited to perform quantum operations with tens of qubits. On the way to sufficiently large and thus useful quantum computers there are several difficulties to overcome. In this work, we investigate two important open questions using a quantum information processor based on trapped atomic ions.

The first open milestone is the characterization of quantum operations acting on many qubits. Early techniques require resources that scale exponentially with the qubit number and are therefore unsuitable for practical implementation on large quantum computers. We present a technique that allows us to rigorously characterize quantum processes in a very short time. We demonstrate that our method, called *Cycle Benchmarking*, does not depend on the qubit number and is thus an important tool for the development of large quantum computers in the future.

The second open milestone is the mitigation and correction of errors. In real-world devices, noise that can affect the computation is unavoidable. Fortunately, techniques have been developed to make quantum computers robust against any kind of noise. One way to detect and correct errors is to distribute the information across multiple qubits. Here we present a technique that allows us to split and to stitch blocks of qubits arranged on a two-dimensional lattice. This method, called *Lattice Surgery*, enables us to work with error-corrected qubits while requiring fewer computational steps than before.

ZUSAMMENFASSUNG

Computer haben unser tägliches Leben in verschiedensten Formen revolutioniert. Obwohl sich die Rechenleistung enorm gesteigert hat, ist das zugrundeliegende Prinzip der Speicherung von Information in einem binären Format, das auf den Werten 0 und 1 basiert, das gleiche. Im Gegensatz zu dieser klassischen Art der Informationsverarbeitung könnte eine allgemeinere Art der Beschreibung von Computern leistungsfähiger sein. Eine solche nicht-klassische Möglichkeit sind Quantencomputer, bei denen die Information in Quanten-Bits (Qubits) gespeichert wird. Tatsächlich hat man Algorithmen gefunden, die auf Quantencomputern exponentiell schneller arbeiten als alle bekannten Algorithmen für klassische Rechner. Mit dem Shor'schen Alogrithmus zum Beispiel wäre es möglich, eine große Primzahl innerhalb von Minuten auf einem Quantencomputer zu faktorisieren, was auf dem besten klassischen Computer Tausende von Jahren dauert.

Die Realisierung solch komplexer Algorithmen erfordert Quantencomputer mit Tausenden bis Millionen von Qubits. Obwohl die prinzipielle Funktionsfähigkeit von Quantencomputern bewiesen ist, sind die heutigen Rechner auf die Durchführung von Quantenoperationen mit einigen zehn Qubits beschränkt. Auf dem Weg zu ausreichend großen und damit auch für relevante Probleme nützlichen Quantencomputern gibt es mehrere Schwierigkeiten zu überwinden. In dieser Arbeit untersuchen wir zwei wichtige offene Meilensteine in der Realisierung von funktionsfähigen Quanteninformationsprozessoren. Die Untersuchungen beruhen dabei auf Experimente mit gespeicherten atomaren Ionen.

Der erste offene Meilenstein ist die Charakterisierung von Quantenprozessen, die auf viele Qubits wirken. Gängige Tomographie-Methoden erfordern jedoch Ressourcen, die exponentiell mit der Anzahl der Qubits skalieren und daher ungeeignet für die praktische Umsetzung auf großen Quantencomputern sind. Daher stellen wir eine Technik vor, die es uns erlaubt, Quantenprozesse in sehr kurzer Zeit rigoros zu charakterisieren. Wir demonstrieren, dass unsere Methode, genannt *Cycle Benchmarking*, nicht von der Qubit-Zahl abhängt und somit ein wichtiges Werkzeug für die Entwicklung großer Quantencomputer in der Zukunft ist.

Der zweite offene Meilenstein ist die Korrektur von Fehlern. In realen Geräten ist Rauschen, das die Berechnung beeinflussen kann, unvermeidbar. Glücklicherweise wurden Techniken entwickelt, um Quantencomputer fehlertolerant zu machen. Eine Möglichkeit, Fehler zu erkennen und zu korrigieren, besteht darin, die Information auf mehrere Qubits zu verteilen. Hier stellen wir eine Technik vor, die es uns erlaubt, Blöcke von Qubits, die auf einem zweidimensionalen Gitter angeordnet sind, zu vernähen und wieder aufzutrennen. Diese Methode, *Gitterchirurgie* genannt, ermöglicht es uns, mit fehlerkorrigierten Qubits zu arbeiten und dabei weniger Rechenschritte als bisher zu benötigen.

Leider läßt sich eine wahrhafte Dankbarkeit mit Worten nicht ausdrücken,
und ebensowenig darf sie an eine unmittelbare Wiedervergeltung denken.

— Johann Wolfgang von Goethe

ACKNOWLEDGMENTS

First of all I would like to thank my family, my parents Kurt and Gertrud and my brother Manuel with girlfriend Nicole. The unconditional and endless support of my family gave me the motivation and perseverance that I needed to graduate as a PhD in physics. I would also like to express my greatest appreciation to my dear friends here in Innsbruck as well as at home in Vorarlberg.

During my doctoral studies I was lucky to meet many inspiring people, from whom I could learn, who helped me when I needed it, and with whom I was able to have a good time. These include members of the university, members of the IQOQI and all the others who have accompanied me over the last years. Unfortunately, I cannot list every single person's name here, but I would like to mention that I am grateful to each and every one.

At this point I would like to thank my Professor Rainer Blatt. It was a real pleasure for me to be part of this amazing group. Rainer Blatt has created an extraordinary working environment with highly motivated people who are always ready to give their best and share their wisdom with everyone else. By interacting with all the national and international members within our group and with people from all over the world, I was able to grow both as a scientist and as a citizen of the earth. Most importantly, Rainer Blatt never got tired of trying to motivate us and always stood behind us. Thank you so much!

I spent most of my PhD life with my work colleagues and friends from the "Linear" team. An important part of our sub-group are the seniors Thomas Monz, Philipp Schindler and Martin Ringbauer. Philipp provided the greatest help in realizing the projects presented. Without him and his constant commitment our experimental results and the publications thereof would not have been possible. For this and for all the things he has taught me, I am most grateful to him. A big thank you goes to Thomas, from whom I learned a lot and who saved me all the bureaucracy, which enabled me to concentrate on my work in the laboratory. Thank you Martin for the many fruitful discussions and your engagement at all times. Another essential part of our group are of course the other PhD students. When I joined the team in 2015, it was Daniel Nigg and Esteban Martinez who taught me a lot about the experiment and quantum computation in general. After working alone on the experiment for some time, I was pleased that Roman Stricker, Lukas Postler and Michael Meth joined our team shortly after each other. Together we were able to significantly extend and improve the experimental setup, which led to many great publications and will continue to give us great pleasure in the future. Thank you very much for all the good times, I would sign up to work with you again anytime.

A large part of the success of our results is based on the great cooperation with other groups. In the project "Benchmarking" we had a wonderful collaboration with Joel J. Wallman and Joseph Emmerson from the University of Waterloo in Canada. The project "Lattice Surgery" was a great success thanks to the joint work with Hendrik Poulsen Nautrup, Nicolai Friis and Hans J. Briegel from the University of Innsbruck and the IQOQI Vienna. I really want to point out that this interplay between theory and experiment is and will be a

key component in the development of future quantum devices. Thank you very much, I really enjoyed working with you.

A special thanks goes to a group of people with whom I had a lot of fun playing cards during my lunch breaks. In the so called “Führungskräfte” meeting we played the funniest and most complex card game, Tarock. Thanks to Marian Kreyer, Martin Meraner, Lukas Postler, Arne Schiller and Klemens Schüppert it was possible to take the edge off the otherwise serious and hard work at the university a little (^^).

Our working group as a whole would not be there without the hard work of the people in the secretariat and workshops. Whenever I had any problem or needed help, I found open ears and active support. Thank you very much for your help.

Last but not least, I would like to thank all the other people I have not mentioned before and who have accompanied me on this amazing journey over the last few years.

Thank you all!

CONTENTS

LIST OF FIGURES

LIST OF TABLES

ACRONYMS

AOM	Acousto-Optic Modulator
BS	Beam Splitter
CB	Cycle Benchmarking
CCD	Charge-Coupled Device
CNOT	Controlled-NOT
DC	Doppler Cooling
DFS	Decoherence-Free-Subspace
EOM	Electro-Optic Modulator
FNC	Fiber Noise Cancellation
GTP	Glan-Thompson Polarizer
IGP	Ion Getter Pump
LD	Lamb-Dicke
LP	Low-Pass
LS	Lattice Surgery
HFC	High Finesse Cavity
HP	High-Pass
MFC	Medium Finesse Cavity
MS	Mølmer-Sørensen
NA	Numerical Aperture
NISQ	Noisy Intermediate-Scale Quantum
OI	Optical Isolator
PBS	Polarizing Beam Splitter
PID	Proportional–Integral–Derivative
PD	Photodiode
PDH	Pound-Drever-Hall
PG	Pressure Gauge
PMT	Photo Multiplier Tube

PGC Polarization Gradient Cooling

POVM Positive Operator-Valued Measure

QEC Quantum Error Correction

QECC Quantum Error Correction Code

QND Quantum-Non-Demolition

QPT Quantum Process Tomography

QST Quantum State Tomography

RAM Residual Amplitude Modulation

RB Randomized Benchmarking

RC Randomized Compiling

RF Radio Frequency

RSC Resolved Sideband Cooling

SP Survival Probability

SPAM State Preparation and Measurement

TA Tapered Amplifier

TA-SHG Tapered Amplifier - Second Harmonic Generation

TSP Titanium Sublimation Pump

VCO Voltage-Controlled Oscillator

1 INTRODUCTION

The development of the computer is one of the great success stories of the 20th century. As technology improved, computers evolved from room filling systems, able to run basic algorithms, to processors, which fit in our pockets and can be programmed to perform complex algorithms. Because these processing units got smaller, more powerful and more affordable over time, they found usage in almost any sector of modern live.

The description of currently available information processing devices is based on the classical theory of computation, essentially the universal Turing machine [1]. Such a machine can compute any possible algorithm, as stated by D. Deutsch [2]*"A universal computer is a single machine that can perform any physically possible computation".* Although the development of classical information theory and the growth of computing power have been tremendous in recent decades, some problems have been found that cannot be solved by classical computers in a reasonable time.

Therefore, people have begun to explore more general ways to describe computers that might be more powerful. One approach is to store and manipulate information in quantum systems. Quantum information processing theory describes algorithms as quantum operations acting on *quantum bits* (qubits), in analogy to binary digits (bits) in which information is stored in classical devices. In chapter 2 a introduction into the theory of quantum information processing is given.

In the following, we highlight three arguments why quantum computers can be advantageous compared to classical devices. Note that these arguments are based on fundamental differences between the two theories, but we focus here on possible applications that arise from these differences.

First, quantum algorithms have been found, e.g. Shor's algorithm for factorization [3], which perform exponentially faster than any known classical algorithm. This has far-reaching consequences, since, for example, widely used encryption algorithms today are based on factorization and a quantum computer is able to break this encryption in a short time.

Second, it is believed that quantum mechanical problems cannot be simulated efficiently on classical computers, since the required resources scale exponentially with the system size. The idea of simulating quantum mechanical problems with quantum machines goes back to a lecture by Richard Feynman in 1982 and his famous quote *"Nature isn't classical, dammit, and if you want to make a simulation of nature, you'd better make it quantum mechanical, and by golly it's a wonderful problem, because it doesn't look so easy."* [4].

Third, quantum information processing allows us to perform quantum cryptography [5–7], a task beyond the capabilities of classical devices.

In summary, quantum computers would be of extraordinary interest for many applications. On the way to successfully realize quantum computers there are still some technical challenges to overcome. Although the best suited physical platform and the related concepts are yet to be found, it should be possible to build quantum information processors in principle. In order to process relevant problems, a quantum computer needs a large number of qubits. The ability to add more and more qubits without loosing the capability to process

quantum information is termed scalability. As explained below, this thesis addresses two specific aspects of scalability and is organized as follows.

After discussing the general concepts of quantum computation in chapter 2, the importance of characterizing quantum computers is summarized. Then, the challenges of building and characterizing quantum computers are considered in the context of system size scaling. Finally, techniques to make quantum computers robust against errors are motivated.

The theoretical description of quantum information processors is very general and admits many different physical realizations. In chapter 3, we discuss the requirements that a physical system must meet in order to perform meaningful quantum computations. In this chapter, we then present a suitable and very promising physical platform based on trapped atomic ions. Specifically, we outline how individual $^{40}Ca^{+}$ ions are confined in a trap and how quantum information is stored in the electronic degrees of freedom of the ions. We then present how lasers can be used to prepare, coherently manipulate, and read out the quantum state of the trapped ions.

In chapter 4, the experimental building blocks of our trapped ion quantum computer are presented. In detail, the design of the ultra-high vacuum chamber enclosing the ion trap, the laser systems used, and the constructions for generating a bias magnetic field are discussed.

This thesis is primarily concerned with two major issues affecting the development of future quantum computers.

First, important techniques to characterize quantum computers are introduced in chapter 5. Here, the well-established but not scalable methods Quantum State Tomography and Quantum Process Tomography are discussed. Then a scalable technique called Randomized Benchmarking and a recently developed derivative thereof called *Cycle Benchmarking* is presented. In chapter 6, the first experimental implementation of characterizing large-scale quantum computers using Cycle Benchmarking is demonstrated.

Second, the principles of Quantum Error Correction are explained in chapter 7. As a specific example of Quantum Error Correction codes the so called surface code is discussed. Finally, an experimental implementation of *Lattice Surgery*, a promising technique to efficiently manipulate encoded quantum information is presented in chapter 8.

2 QUANTUM INFORMATION PROCESSING

Information is physical.

— Rolf Landauer, 1991 [8]

Processing information is a task, electronic devices perform routinely in our everyday lives. As mentioned in the introduction, these processors can be described by the classical theory of information processing. In contrast, quantum information processing is formulated in the language of quantum mechanics. In this chapter we give a brief introduction to the theory of quantum computation in section 2.1. Afterwards, the importance of the characterization and scalability of quantum computers are discussed in sections 2.2 and 2.3 Finally in section 2.4, we outline Quantum Error Correction, a procedure that makes quantum computers robust against errors.

2.1 QUANTUM COMPUTATION

In a *classical* computer the central carrier of information is the binary digit (bit), which can take the values of either 0 or 1. Programmed algorithms can be solved by sending strings of bits through circuits of computational gates.

Quantum computation can be formulated in a similar fashion. The smallest carrier of information is the quantum bit (qubit). The quantum mechanical description of a qubit is a two-level system (e.g. a spin 1/2 particle). Hence, the state of a qubit can be described as a superposition of two states $|0\rangle$ and $|1\rangle$ as [9]

$$|\psi\rangle = \alpha\,|0\rangle + \beta\,|1\rangle\,, \tag{2.1}$$

where $\alpha, \beta \in \mathbb{C}$ with $|\alpha|^2 + |\beta|^2 = 1$. The states $|0\rangle$ and $|1\rangle$ are orthonormal and hence form a basis in the two dimensional complex vector space, called the Hilbert space. If we measure the qubit, we find it either in the state $|0\rangle$ and obtain the outcome 0 with probability $|\alpha|^2$ or the qubit is projected into the state $|1\rangle$ and we receive the outcome 1 with probability $|\beta|^2$. Since the total probability of finding the qubit in one of the states has to be 1, a valid qubit state has to fulfill the normalization condition $|\alpha|^2 + |\beta|^2 = 1$. The state of the qubit is a state of the two dimensional complex vector space and thus it can be represented by the Pauli matrices [9]

$$\sigma_x = \begin{pmatrix} 0 & 1 \\ 1 & 0 \end{pmatrix}, \quad \sigma_y = \begin{pmatrix} 0 & -i \\ i & 0 \end{pmatrix}, \quad \sigma_z = \begin{pmatrix} 1 & 0 \\ 0 & -1 \end{pmatrix}. \tag{2.2}$$

The Pauli matrices are Hermitian, where a Hermitian matrix A fulfills the equation $A = A^\dagger$, with $A^\dagger$ being the transposed and complex conjugated matrix of A. Hermitian matrices have real eigenvalues, which ensures that quantum measurements have real outcomes. Furthermore, the Pauli matrices obey the commutation relations $[\sigma_j, \sigma_k] = 2i \sum_{l=1}^{3} \epsilon_{jkl} \sigma_l$ and the anti-commutation relations $\{\sigma_j, \sigma_k\} = 0$.

Together with the identity matrix $\sigma_I = \mathbb{1}$ the Pauli matrices form a basis for the real vector space of 2×2 Hermitian matrices. Therefore, any single qubit state can be parameterized by its *density operator* or *density matrix* as [9]

$$\rho = \frac{1}{2}\left(\mathbb{1} + \vec{r} \cdot \vec{\sigma}\right) \tag{2.3}$$

where $\vec{r} \in \mathbb{R}^3$ with $|\vec{r}| \leq 1$ is the three dimensional *Bloch vector* and $\vec{\sigma} = (\sigma_x, \sigma_y, \sigma_z)^T$ [9]. If the Bloch vector of a state has unity length $|\vec{r}| = 1$ the state is called *pure*. Suppose, a quantum system is in a superposition of an ensemble of pure states $\{p_i, |\psi_i\rangle\}$ with probability amplitudes p_i, where a pure state is exactly known and satisfies $\mathrm{tr}\left((|\psi_i\rangle\langle\psi_i|)^2\right) = 1$. The density matrix of the quantum system is then described by a so called *mixture* of pure states as [9]

$$\rho = \sum_i p_i |\psi_i\rangle\langle\psi_i|. \tag{2.4}$$

Geometrically the state of a single qubit can be described with a Bloch vector inside the Bloch sphere, as depicted in fig. 2.1. Note that throughout this thesis we also use the following notation for the Pauli matrices $\sigma_I = I, \sigma_x = X, \sigma_y = Y, \sigma_z = Z$.

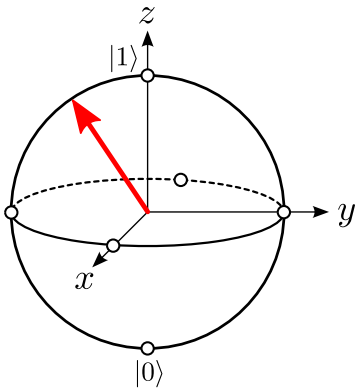

Figure 2.1: **Bloch sphere.** The state of the qubit can be represented by the Bloch vector (red arrow), where the vector can point towards any point inside the Bloch sphere.

An important measure of the distance between two quantum states is the so called *state fidelity*. We often use the state fidelity to describe how close an experimentally prepared state is to an ideal state. In theory, the fidelity between the states $\rho = |\psi\rangle\langle\psi|$ and $\sigma = |\phi\rangle\langle\phi|$ is defined as [9]

$$F = \sqrt{\sqrt{\sigma}\rho\sqrt{\sigma}} \geq \sqrt{\langle\psi|\sigma\rangle}. \tag{2.5}$$

We now consider two arbitrary quantum systems A and B with respective Hilbert spaces H_A and H_B. Then the Hilbert space of the composite system is described by the tensor product of the individual Hilbert spaces $H_A \otimes H_B$. If the states $\{|i\rangle_A\}$ form a basis for system A and $\{|j\rangle_B\}$ form a basis for system B, the spectral decomposition of the composite system is defined as [9]

$$|\psi\rangle_{AB} = \sum_{i,j} c_{ij} |i\rangle_A \otimes |j\rangle_B . \tag{2.6}$$

If the states of the systems A and B are pure states $|\psi\rangle_A = \sum_i c_i^A |i\rangle_A$ and $|\phi\rangle_B = \sum_j c_j^B |j\rangle_B$, also the state of the composite system is a pure state $|\psi\rangle_{AB} = |\psi\rangle_A \otimes |\phi\rangle_B$ and is called

separable [9]. In this case the equation $c_{ij} = c_i^A c_j^B$ applies to the state coefficients. If there exists any pair of coefficients such that $c_{ij} \neq c_i^A c_j^B$ the composite state cannot be written as a product of pure states of the individual systems and the composite state is called *inseparable* or *entangled* [9]. The Bell state $|\psi\rangle_{AB} = 1/\sqrt{2}\,(|0\rangle_A \otimes |0\rangle_B + |1\rangle_A \otimes |1\rangle_B)$ for example is an entangled state.

In general, an N-qubit state $|\psi\rangle_N$ can be described by a linear combination of 2^N basis states $\{|i\rangle\}$ as [9]

$$|\psi\rangle_N = \sum_{i=1}^{2^N} a_i \,|i\rangle\,, \tag{2.7}$$

where the probability amplitudes a_i fulfill the normalization condition $\sum_i |a_i|^2 = 1$. Note that the dimension $d = 2^N$ of the complex Hilbert space grows exponentially with qubit number N. This implies that in general there exists an exponential number of complex probability amplitudes, which makes it hard to simulate large quantum systems on a classical computer.

At the beginning of the computation the qubits are prepared in some state, e.g. $|\psi\rangle = |0_1\rangle \otimes |0_2\rangle \otimes \cdots \otimes |0_N\rangle = |0\rangle^{\otimes N}$. An algorithm is realized by the implementation of *quantum gates* (short for quantum gate operations), which are operations that act on the state of the qubits. A quantum gate can be expressed as a matrix U acting on the state $|\psi\rangle$ by $|\psi'\rangle = U\,|\psi\rangle$ [9]. Since the state $|\psi'\rangle$ as well as the state $|\psi\rangle$ have to fulfill the normalization condition, U has to be unitary, requiring $U^\dagger U = \mathbb{1}$ [9]. A quantum algorithm typically contains a sequence of unitary operations, which can be described by the circuit model, as depicted in fig. 2.2.

It can be shown, that any N-qubit unitary operation $U^N \in \mathrm{SU}(2^N)$ can be decomposed into a sequence of gates from a set, that includes all 1-qubit gates $U^1 \in \mathrm{SU}(2)$ and one entangling 2-qubit gate $U^2 \in \mathrm{SU}(4)$ [9, 10]. Such a set of gates is called a *universal gate set*. Furthermore the Solovay-Kitaev theorem states, that even with a *finite* set of gates an arbitrary 1-qubit unitary ($SU(2)$) can be efficiently approximated to an accuracy ϵ with only $\mathcal{O} = \log^c(1/\epsilon)$ gates [9], where c is a constant factor. Hence the Solovay-Kitaev theorem implies that a circuit containing m 2-qubit gates and 1-qubit operations can be approximated to an accuracy ϵ by $\mathcal{O} = m\log^c(m/\epsilon)$ gates from a finite gate set [9]. However, in general not all unitary transformations can be approximated by a quantum circuit efficiently. A commonly used finite and universal gate set $\{H, P, T, \mathrm{CNOT}\}$ contains the Hadamard-, the Phase-, the T- and the CNOT-gate, where these gates are described in detail in section 3.4.

At the end of the computation the qubits are measured individually. Quantum measurements are described by a set of measurement operators $\{M_m\}$ with eigenvalues or outcomes m. If a state $|\psi\rangle$ is measured, the probability $p(m)$ to get the outcome m can be calculated by $p(m) = \langle\psi|M_m^\dagger M_m|\psi\rangle$. The state of the qubit after the measurement is $|\psi'\rangle = M_m\,|\psi\rangle\,/\sqrt{p(m)}$. Since all measurement probabilities have to sum up to 1, the measurement operators have to fulfill the completeness equation $\sum_m M_m^\dagger M_m = 1$. In the computational basis $\{|0\rangle\,, |1\rangle\}$ the projectors are $M_0 = |0\rangle\langle 0|$ and $M_1 = |1\rangle\langle 1|$.

2.2 CHARACTERIZATION OF QUANTUM COMPUTERS

Like any physical device, quantum computers suffer from imperfect control and noisy environments that limit their computational power. The characterization of operations in a quantum computer offers the ability to find limitations and to possibly eliminate them in the future. Hence, a lot of effort in the field of quantum information science is put into the inves-

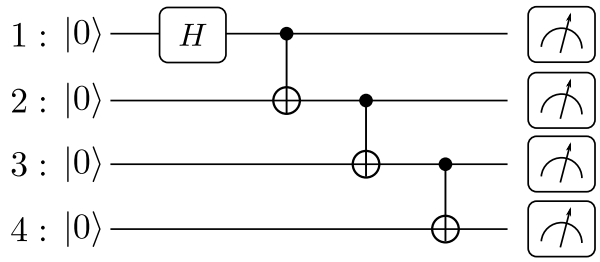

Figure 2.2: **Quantum gate sequence in the circuit representation.** In the circuit representation an algorithm starts with a register of quits, all prepared in an individual initial state. Then a sequence of discrete gates is applied to the qubits (e.g. a 1-qubit Hadamard gate and 2-qubit CNOT gates, as described in section 3.4), where the time of application is from left to right. In the end the qubits are measured and a classical outcome for each qubit is obtained.

tigation on how to rigorously characterize quantum processes. There exist various methods to fully describe quantum processes, for example, quantum process tomography [11] or gate set tomography [12–14]. However, any protocol for fully characterizing a quantum process requires a number of experiments that grows exponentially with the number of qubits, even with improvements such as compressed sensing [15, 16]. For example, it would take ~ 4000 years to perform the measurements for process tomography of one specific 10-qubit quantum operation in our ion trap quantum computer. As a result, the largest quantum processes that have been fully characterized to date acted only on three qubits [17, 18].

The exponential resources required for a full characterization can be circumvented by extracting partial information about quantum processes. A partial characterization typically yields some figure of merit comparing the noisy implementation of a quantum process to the desired operation. We will consider the *process fidelity* (also known as the entanglement fidelity), which is equivalent to the average gate fidelity up to a dimensional factor that is approximately 1 [19, 20]. The process fidelity can be efficiently estimated by e.g. Randomized Benchmarking (RB) [21–23].

However, implementing an operation in RB requires $\mathcal{O}(N^2/\log N)$ primitive two-qubit operations [24], so that RB provides very coarse information about the primitive operations. Furthermore, for error rates as low as 0.1% per two-qubit operation, a single 10-qubit Clifford operation will have a cumulative error rate on the order of 10%, which substantially increases the number of measurements required to accurately estimate the process fidelity.

One method to overcome this practical limitation is to only perform gates in fixed modes of parallel operation. We refer to a parallel set of gates as a *cycle*, in analogy with a digital clock cycle and introduce a technique called Cycle Benchmarking (CB) [25].

In chapters 5 and 6 we present an overview about the characterization of quantum computers, as well as the detailed methods and the experimental results of the Cycle Benchmarking project.

2.3 SCALABILITY ISSUES

As discussed in the introduction, it is believed that quantum computers can outperform classical computers. A natural question that arises is, under which circumstances this will happen. The company Quantum Benchmark Inc. presented an estimate of a classical "Horizon", above which quantum computers will be better than their classical counterparts,

see fig. 2.3. The illustration compares two figures of merit. The first one is the circuit depth, which describes how many quantum gates a successful circuit implementation contains. For a single qubit the circuit depth corresponds to number of gates that can be implemented before the result gets meaningless. Typically results are a called meaningless if the success probability is below 1/2 or 2/3. The second figure of merit is the number of qubits, which expresses how many qubits can interact in the system in a controllable manner.

Although the classical "Horizon" is a blurry threshold, we can see in fig. 2.3 that a quantum computer with an error rate of 10^{-3} per operation and a register size of 72 will probably have an advantage over any classical device. In general, the performance of a quantum computer increases with increasing circuit depth and greater qubit number.

In practice, the achievable circuit depth is limited by the fidelity of the implemented quantum operations. Since the fidelity of current devices is limited to values of $\mathcal{F} = 1 - 10^{-3}$, it is not possible to outperform classical computers even with a 49 qubit system. One way to improve the fidelity of quantum operations significantly is to use a technique called Quantum Error Correction, which shall be outlined in the next section.

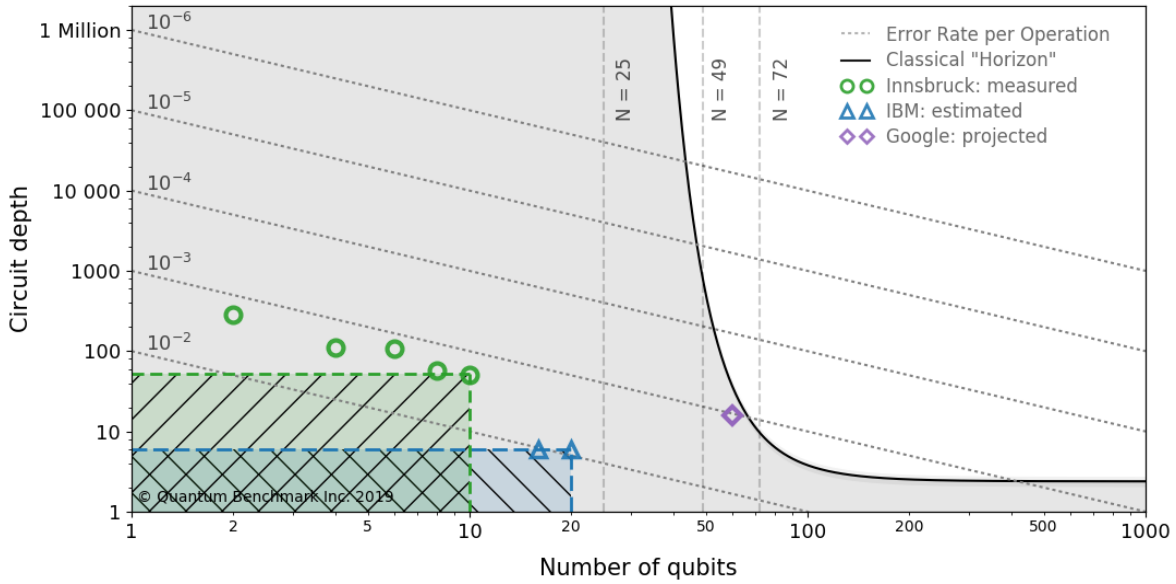

Figure 2.3: **Quantum computing performance.** Plotted is the circuit depth (number of implemented gates) against the number of qubits for three different experimental platforms. Initially the circuit depth corresponds to the inverse of the error rate per operation. The classical "Horizon" is a blurry line which indicates when quantum computation can outperform classical computers. By courtesy of Quantum Benchmark Inc. 2019.

2.4 QUANTUM ERROR CORRECTION

Real-world quantum devices are prone to errors, due to imperfect calibration, instabilities in the experimental apparatus or unwanted coupling to the noisy environment. Quantum Error Correction (QEC) was developed to protect quantum computers against arbitrary errors. The basic idea of QEC is the same as for classical error correction, namely to encode information redundantly on many qubits [9, 26]. The general scheme is to use blocks of

physical qubits to encode e.g. a single logical qubit. These logical qubits are constructed such that they can be treated in the same way as physical qubits.

Remarkably, it can be shown that quantum information can be protected against noise while being stored in an encoded qubit, and also during the action of noisy quantum operations [26–28]. Even the operations implemented to do QEC themselves are allowed to be imperfect. QEC techniques that are able to protect quantum information in the presence of noisy quantum operations (including state preparation, quantum gates, readout, etc.) are called *fault-tolerant* [9, 26–28]. The basic design principle in fault-tolerant QEC schemes is that local errors do not propagate to other physical qubits from the same block.

An important technique to facilitate fault-tolerance is the local and bit-wise application of logical gates, called *transversality* [29]. If a logical gate can be implemented transversally, it is sufficient to implement only gates acting on a single qubit per block at a time.

One of the most important findings related to fault-tolerant quantum computation is the *threshold theorem* [9, 30, 31]. The theorem states that if the error rate of every quantum operation is below a certain error threshold, arbitrary accurate computation can be achieved. Hence, if enough physical qubits are available and reasonable assumptions about the noise in the underlying hardware hold [9, 30] this finding paves to way for practical quantum computation.

Most quantum computing platforms, such as quantum dots [32, 33], superconducting qubits [34, 35], trapped atoms [36], nitrogen–vacancy diamond arrays [37], and some ion trap architectures [38], are limited to next-neighbour (NN) interactions. Although ion trap setups offer all-to-all coupling on small scales (up to 100 qubits), scalable ion trap architectures also have limited connectivity [39, 40]. The limited connectivity between qubits typically introduces an overhead in the require resources, such as the number of gates and qubits needed for one round of QEC [41].

In conclusion, the performance of error correction depends on the error threshold, on the transversely implementable gates and on the required connectivity of the underlying hardware. The search for the best possible protection against errors in realistic devices has led to the development of a number of different Quantum Error Correction Codes (QECCs).

The first QECCs were the 9-qubit code proposed by Peter Shor [42] and the 7-qubit code proposed by Andrew Steane [43]. Although these codes already support a number of transversal gates, the error thresholds are very low around 10^{-5} [44]. The smallest possible code to protect against arbitrary errors is the 5-qubit code [45]. This code is very efficient in the number of required qubits, but suffers from the fact that complex entangling operations are required to implement logical gates.

An important step to support the limited NN connectivity in today's architectures was the development of lattice codes. In the first version, the Kitaev *toric code* [46], qubits are arranged in a regular lattice pattern on the surface of a torus. This code was also the first *topological* QECC. The basic idea of topological codes is to encode quantum information in global degrees of freedom protected against local errors. Moreover, is the number of encoded qubits dictated by the topology of the code [47]. Shortly afterwards, the toric code was further developed into the *surface code* [48, 49]. In contrast to the toric code, the surface code is defined on a planar 2D lattice with open boundaries, which relates perfectly to realistic architectures. The surface code is one of the most promising QECCs, because it offers the highest known thresholds of up to $0.7 - 1.4\,\%$ [44, 50–52]. Note that the exact error threshold depends on a number of parameters such as e.g. the underlying noise model and the implemented error syndrome decoder. One drawback of the surface code is, that it does only support very few transversal gates.

Another promising QECC is the *color code* [53, 54]. The color code also offers a high error threshold of up to 0.2 % [52] and in addition allows the transversal implementation of a large class of operations.

Unfortunately, it was shown, that no 2D QECC can support a universal gate set by using unitary operations only [55]. Hence dissipative techniques such as the distillation of magic states [56] were proposed to enable universal fault-tolerant quantum computation in 2D.

Another challenge when using lattice codes is, that even if multi-qubit operations can be implemented transversally, they require long-range interactions. If we are restricted to NN interactions, resource intensive techniques [57, 58] have to be implemented. In the surface code for example, these techniques require more than three times the number of qubits compared to the transversal implementation using long-range interactions [41].

Therefore, one of the most resource efficient ways to implement logical multi-qubit operations is to only utilize operations along the boundary of encoded qubits [41, 59, 60]. With this technique, called lattice surgery, it is possible to generate entanglement and to teleport logical information between encoded qubits.

In chapter 7 an introduction into QEC in general is given. As a specific example, that is also implemented experimentally as described in the following chapter, the surface code is discussed. In chapter 8 we report on the experimental realization of lattice surgery between two topologically encoded qubits in our ion trap quantum information processor. In particular, we demonstrate the creation of entanglement between two logical qubits and we implement logical state teleportation.

3

THE TRAPPED ION QUANTUM COMPUTER

In the first place it is fair to state
that we are not experimenting with single particles
any more than we can raise Ichtyosauria in the zoo.

— Erwin Schrödinger, 1952 [61]

In contrast to the nineteen fifties it is now possible to experiment with single particles. One way to perform experiments with single atoms is to use electro-magnetic potentials to trap single atomic ions. In addition, it is possible to use radio-frequency fields or lasers to manipulate the state of the atoms. Such a system is an ideal candidate for quantum computation, because trapped ions offer long coherence times [62, 63].

Around 2000, DiVincenzo published a collection of requirements for the physical implementation of quantum computation [64]. The following list is a summary of the upcoming sections, which illustrates how our ion trap architecture meets these criteria.

1. A scalable system with well defined qubits: The linear Paul trap in section 3.1 and the $^{40}Ca^{+}$ ion in section 3.2. Note that scalability requires more advanced trap architectures [39, 40] than a linear Paul trap.
2. The ability to initialize the state of the qubits in a simple fiducial state: Laser cooling in section 3.6 and state preparation in section 3.7
3. Long relevant coherence time: The $^{40}Ca^{+}$ ion in section 3.2 and in chapter 4
4. A universal set of quantum gates: Coherent laser-ion interaction in section 3.3
5. A qubit specific measurement capability: Readout in section 3.7

3.1 LINEAR PAUL TRAP

A central building block of our apparatus is the ion trap. Specifically, we utilize a Paul trap, named after its inventor Wolfgang Paul [65]. The Paul trap employs a combination of time varying and static electric fields to confine charged particles in 3D. Typically, the dynamic electric field frequencies are in the Radio Frequency (RF) domain, in the range of $1 \ldots 100\,\mathrm{MHz}$. In our experiment we use a so-called linear Paul trap [66], as illustrated in fig. 3.1. In this design the ions are strongly bound in the x, y direction, but weakly bound in an harmonic potential along the z direction. In such a potential the equilibrium positions of the ions form a *linear* string along the z axis, thus the design is called the *linear* Paul trap.

In practice an RF signal is connected to four parallel electrodes, which are extruded in the z (axial) direction. These RF-electrodes generate an electric quadrupole field in the x/y (radial) plane and nearly a zero-field in the center of the electrodes along the z direction. In addition, two electrodes are placed symmetrically around the center along the axial direction. These end-caps provide an axial parabolic field, which ensures the confinement in the z direction. By applying the RF voltage $V_{\mathrm{RF}} \cos \Omega_{\mathrm{RF}} t$ and the DC voltage U_{R} (usually

zero) to the RF electrodes and the constant DC voltage U_{DC} to the end-caps the following approximate potentials Φ_{RF} and Φ_{DC} for charged particles is generated [67]

$$\Phi_{\mathrm{RF}}(\boldsymbol{r},t) = (V_{\mathrm{RF}}\cos\Omega_{\mathrm{RF}}t + U_{\mathrm{R}})\left(\frac{1}{r_0^2}(\alpha_x x^2 - \alpha_y y^2) + \frac{1}{z_0^2}\alpha_z z^2\right), \tag{3.1}$$

$$\Phi_{\mathrm{DC}}(\boldsymbol{r}) = \frac{\beta_z U_{\mathrm{DC}}}{2z_0^2}(2z^2 - x^2 - y^2), \tag{3.2}$$

where $r_0 = \sqrt{x_0^2 + y_0^2}$ is the radial distance to the RF electrodes, z_0 the distance from the trap center to the end-caps, $(\alpha_x, \alpha_y, \alpha_z, \beta_z)$ are geometric factors [67] given by the trap design and $\boldsymbol{r} = (x, y, z)$ describes the position of the particle. For infinitely long hyperbolic RF electrodes the geometric factors are $\alpha_{x,y} = 1, \alpha_z = 0, \beta_z = 0$. The equations of motion for a single charged particle with mass M and charge Q obey $\boldsymbol{F} = -Q\boldsymbol{\nabla}\Phi = M\ddot{\boldsymbol{r}}$ and we can derive the Mathieu equations [67]

$$\frac{\mathrm{d}^2 u}{\mathrm{d}\tau^2} + (a_u + 2q_u\cos(2\tau))\,u = 0, \tag{3.3}$$

where $u \in \{x, y, z\}$ and we have made the following substitutions

$$a_z = -2a_{x,y} = \frac{8QU_{\mathrm{DC}}\beta_z}{Mz_0^2\Omega_{\mathrm{RF}}^2}, \tag{3.4}$$

$$q_x = -q_y = \frac{4QV_{\mathrm{RF}}\alpha_{x,y}}{Mr_0^2\Omega_{\mathrm{RF}}^2}, \quad q_z = \frac{4QV_{\mathrm{RF}}\alpha_z}{Mz_0^2\Omega_{\mathrm{RF}}^2}, \tag{3.5}$$

$$\tau = \frac{\Omega_{\mathrm{RF}}t}{2}. \tag{3.6}$$

Stable solutions can be found for $0 < a_u < q_u \lesssim 1$ and the ion's trajectories can be approximated as [67]

$$r_u(t) \approx r_{u,0}\cos(\omega_u t + \phi_u)\left(1 + \frac{q_u}{2}\cos\Omega_{\mathrm{RF}}t\right), \tag{3.7}$$

where $r_{u,0}$ and ϕ_u are determined by the initial position of the particle and the motional frequencies ω_u are described as

$$\begin{aligned}\omega_z &= \frac{\Omega_{\mathrm{RF}}}{2}\sqrt{a_z + \frac{q_z^2}{2}} = \sqrt{\omega_{z,0}^2 + \omega_{z,\mathrm{RF}}^2} \\ &= \sqrt{\frac{2QU_{\mathrm{DC}}\beta_z}{Mz_0^2} + \frac{2Q^2V_{\mathrm{RF}}^2\alpha_z^2}{M^2z_0^4\Omega_{\mathrm{RF}}^2}},\end{aligned} \tag{3.8}$$

$$\begin{aligned}\omega_{x,y} &= \frac{\Omega_{\mathrm{RF}}}{2}\sqrt{\frac{q_{x,y}^2}{2} + a_{x,y}} = \sqrt{\omega_{x,y,0}^2 - \frac{\omega_{z,0}^2}{2}} \\ &= \sqrt{\frac{2Q^2V_{\mathrm{RF}}^2\alpha_{x,y}^2}{M^2r_0^4\Omega_{\mathrm{RF}}^2} - \frac{QU_{\mathrm{DC}}\beta_z}{Mz_0^2}},\end{aligned} \tag{3.9}$$

where $\omega_{z,0}$ is the axial frequency without the RF contribution $\omega_{z,\mathrm{RF}}$ and $\omega_{x,0}$, $\omega_{y,0}$ are the radial frequencies without end-cap voltages. As can be seen from eqs. (3.8) and (3.9), the RF potential supports a small additional confinement in z direction, whereas the DC potential acts anti-confining in the x, y direction.

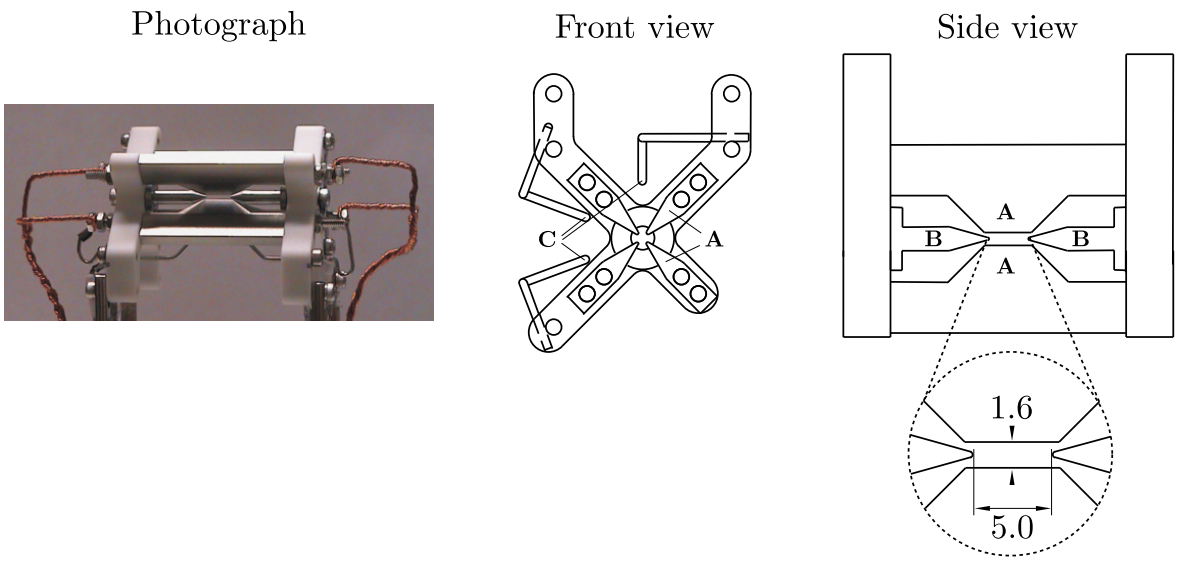

Figure 3.1: **Linear Paul trap setup.** The trap holder (made from Macor©) supports the RF electrodes **A**, the compensation electrodes **C** (manufactured from stainless steel) and the end-caps **B** (fabricated from Molybdenum) [68]. The distance between the end-caps is $2z_0 = 5.0\,\mathrm{mm}$ and the distance of the RF electrodes is 1.6 mm which corresponds to a distance $r_0 = 1.131\,\mathrm{mm}$ from one RF electrode to the trap axis [68].

As can be seen in eq. (3.7), the oscillation of the particle can be approximately described by two separate motions, one with amplitude $r_{u,0}$ and frequency ω_u called the *secular motion* and one with an amplitude modulated motion with frequency Ω called *micro-motion*. If the particle position is close to the trapping axis, where the RF-field is nearly zero, the micro-motion can be neglected and the trap acts as a harmonic pseudo-potential $V(\vec{r})$ for a charged particle

$$V(\vec{r}) = \sum_{u\in\{x,y,z\}} \frac{1}{2} M\omega_u^2 r_u^2. \tag{3.10}$$

The experiments presented in this thesis were carried out in the trap depicted in fig. 3.1. The trap features an ion to RF-electrode distance of $r_0 = 1.131\,\mathrm{mm}$ and an ion to end-cap distance of $z_0 = 2.5\,\mathrm{mm}$, where details of the trap design considerations are given in Ref. [68].

In the harmonic potential approximation we can write the equation of motion as [67]

$$M\frac{\mathrm{d}^2x}{\mathrm{d}t^2} = -M\omega_x^2 x = -Q\frac{\mathrm{d}D_x}{\mathrm{d}x}, \tag{3.11}$$

$$\overline{D}_x = \int_0^{r_0} \frac{\mathrm{d}D_x}{\mathrm{d}x}\mathrm{d}x = \frac{M}{2Q}\omega_x^2 r_0^2 \approx \frac{QV_{\mathrm{RF}}^2\alpha_x^2}{2Mr_0^2\Omega_{\mathrm{RF}}^2}, \tag{3.12}$$

with $\overline{D}_x$ being the parabolic pseudo-potential in radial direction. For a single $^{40}Ca^+$ ion with a typical motional frequency of $\omega_x = (2\pi)\,4\,\mathrm{MHz}$ this corresponds to a trap depth of $Q\overline{D}_x = M\omega_x^2 r_0^2/2 \approx 168\,\mathrm{eV} \approx 2\cdot 10^6\,\mathrm{K}/k_{\mathrm{B}}$.

We now consider multiple ions in a linear Paul trap, which experience the global potential generated by the trap electrodes as well as a repelling force between each other due to the

Coulomb interaction. For N ions in the linear Paul trap the potential energy is described as [69]

$$V = \sum_{i=1}^{N} \frac{1}{2} M\omega_z^2 z_i(t)^2 + \sum_{\substack{i,j=1 \\ i\neq j}}^{N} \frac{Q^2}{8\pi\epsilon_0} \frac{1}{|z_i(t) - z_j(t)|}, \tag{3.13}$$

where $z_i(t)$ is the position of the ith ion and ϵ_0 is the permittivity of free space. Assuming that the ions are sufficiently cold, the ions experience only a small displacement $q_i(t)$ around their equilibrium position z_i^0 and their position can be approximated as $z_i(t) \approx z_i^0 + q_i(t)$.

Importantly, the motion of the ions can be quantized into normal motional modes [69]. Since the equations of motion in the principle directions x, y, z are separable, there exist $3N$ independent modes with N modes in each direction. The displacement from the equilibrium position of ion i and mode j in direction $q \in \{x, y, z\}$ can be described as [69]

$$\hat{q}_i(t) = i\sqrt{\frac{\hbar}{2M\omega_q}} \sum_{j=1}^{N} \frac{\vec{b}_{i,j}}{\sqrt[4]{\mu_j}} \left(\hat{a}_j e^{-i\omega_j t} - \hat{a}_j^\dagger e^{-i\omega_j t}\right), \tag{3.14}$$

where $\hat{a}^\dagger, \hat{a}$ are the quantum mechanical creation and annihilation operators of motion, μ_j is the eigenvalue that defines the eigenfrequency $\omega_{q,j} = \sqrt{\mu_j}\omega_q$ and $\vec{b}_{i,j}$ the eigenvector that defines the amplitude of the motion of ion i.

The calculation of the respective eigenfrequencies and eigenvectors of the ion's motion is explained in detail in Ref. [69]. In the first motional mode, for example, the ions move all together as if they would be rigidly connected, hence this mode is often called the Centre Of Mass (COM) mode. In a two ion crystal for example, the two modes in the axial direction z are the COM mode characterized by the eigenfrequency $\omega_{z,1} = \omega_z$ and motional eigenvector $\vec{b}_{(1,2),1} = 1/\sqrt{2}(1,1)^{\mathrm{T}}$ and the breathing mode described by the eigenfrequency $\omega_{z,2} = \sqrt{3}\omega_z$ and motional eigenvector $\vec{b}_{(1,2),2} = 1/\sqrt{2}(1,-1)^{\mathrm{T}}$. The first 10 axial eigenfrequencies relative to the COM frequency are $\omega_{z,j} \in \{1, 1.73, 2.42, 3.07, 3.69, 4.30, 4.88, 5.46, 6.02, 6.58\} \cdot \omega_z$ [69].

In this picture of a quantum mechanical harmonic oscillator, the motional state $|\psi\rangle$ of the ion can be expressed in terms of number or Fock states $|n\rangle$ as [70]

$$|\psi\rangle = \sum_{n=0}^{\infty} c_n |n\rangle, \tag{3.15}$$

where $\hat{a}^\dagger\hat{a}|n\rangle = n|n\rangle$ and the motional ground state of the ion is described as $|\psi\rangle = |0\rangle$. Assuming a thermal phonon distribution, the parameters c_n can be completely described by the mean phonon number $\bar{n}$ as [70]

$$c_n = \frac{\bar{n}^n}{(\bar{n}+1)^{n+1}}. \tag{3.16}$$

3.2 THE CALCIUM ION

The choice of the atomic species is important for several reasons. For example are the trapping frequencies determined by the mass of the particles, see section 3.1. In practice it is also important to have lasers available to drive the atomic transitions. In addition, it is necessary that the species has transitions to cool the ions, to encode quantum information and to read out the stored quantum information, as discussed in detail in the following.

Singly ionized Calcium has a hydrogen-like energy diagram, where the $4^2S_{1/2}$ ground state, the short lived $4^2P_{1/2}$, $4^2P_{3/2}$ and the meta-stable $3^2D_{3/2}$, $3^2D_{5/2}$ states are depicted in fig. 3.2. Note that in the presence of a bias magnetic field, the degeneracy of the fine structure levels is lifted due the Zeeman effect, as discussed in appendix A.

The $4^2S_{1/2} \leftrightarrow 4^2P_{1/2}$ transition with a wavelength around 397 nm in combination with the $3^2D_{3/2} \leftrightarrow 4^2P_{1/2}$ transition with a wavelength of 866 nm offers a closed loop cycling transition, which can be utilized for various laser cooling schemes. For trapped ion experiments the available laser cooling techniques are Doppler cooling (see section 3.6.1), polarization gradient cooling (see section 3.6.2), electromagnetically induced transparency cooling [71–73] or sideband cooling [74]. In addition, this transition can be employed for state preparation and state detection (see section 3.7).

The $4^2S_{1/2} \leftrightarrow 3^2D_{5/2}$ transition with a wavelength around 729 nm in combination with the $3^2D_{5/2} \leftrightarrow 4^2P_{3/2}$ transition at 854 nm can also be used to for state preparation (see section 3.7) and for resolved sideband cooling (see section 3.6.3). Importantly, the long lived meta-stable $3^2D_{5/2}$ state is well suited to store quantum information. Because the $4^2S_{1/2}(m_j = -1/2) \leftrightarrow 3^2D_{5/2}(m_j = -1/2)$ transition experiences the smallest frequency shift in the presence of an external magnetic field (see appendix B), we typically encode a qubit in the states $|0\rangle = 4^2S_{1/2}(m_j = -1/2)$ and $|1\rangle = 3^2D_{5/2}(m_j = -1/2)$ of a single ion. In order to manipulate the state of the qubit we utilize optical transitions around 729 nm, as outlined in section 3.3.1. Important transition properties in $^{40}Ca^+$, the corresponding g-factors and the frequency shifts due to a bias magnetic field are summarized in appendix B. Further details can be found in other PhD theses [75–77].

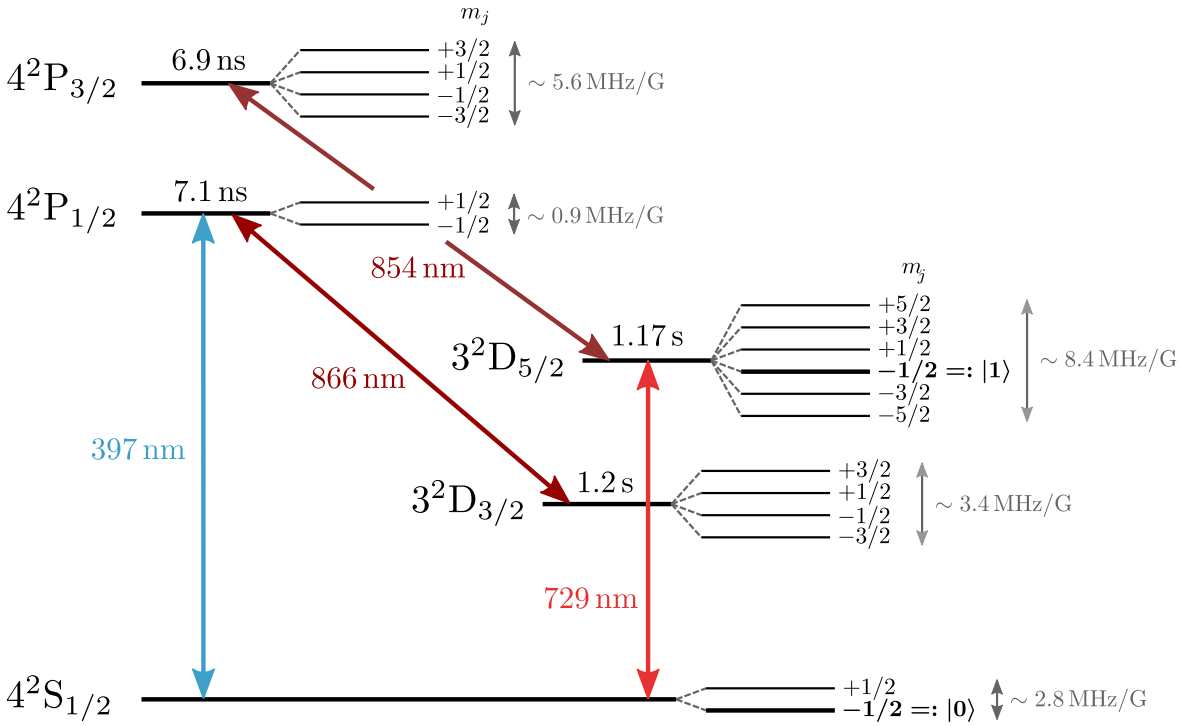

Figure 3.2: **$^{40}Ca^+$ energy level diagram.** The lasers used to drive optical transitions are depicted by blue and red arrows labelled with their approximate wavelengths. For the excited states the approximate lifetimes as well as the Zeeman sublevels are presented. The sublevels are labelled with the respective total angular momentum quantum number m_j and the approximate frequency shift in the presence of a bias magnetic field is given. Detailed state and transition properties are described in appendix B.

3.3 LASER-ION INTERACTION

According to DiVincenzo's criteria, introduced in the beginning of this chapter, it is essential in quantum computation to be able to manipulate the state of the qubit. In our experiment we use interactions between lasers and the trapped ions to manipulate the quantum state. This laser-ion interaction has been discussed in many references [70, 78–80], thus only the basic principles will be reviewed in this section.

A trapped ion has motional degrees of freedom, due to the confining potential of the Paul trap, as well as electronic degrees of freedom, specifically the internal quantum states of $^{40}Ca^{+}$ presented in section 3.2. In the simplest case, the ion can be seen as a two level system, which consists of a ground state e.g. $|0\rangle = |S\rangle$ and an excited state e.g. $|1\rangle = |D\rangle$ separated by the energy $E = \hbar\omega_0$. In the semi-classical description the laser is modeled as monochromatic wave $E(z,t) = E_0 \cos(k_z z - \omega_L t + \phi)$ coupled to the ion, with frequency ω_L, phase ϕ and $k_z = k\cos\theta$ being the projection of the wave vector along the direction of the ion motion. The motion of the ion along the z-direction in the trap can be approximated by a harmonic oscillator with frequency ω_z. For now we assume that the coherence time of the laser and the ion motion is much longer than the typical interaction time.

The Hamiltonian of this system contains a stationary part describing the harmonic potential generated by the trap H_t and the internal electronic potential of the ion H_e. The dynamic part is determined by the interaction the laser and the ion H_i. The total Hamiltonian is then defined as [70]

$$\begin{aligned} H =& H_t + H_e + H_i \\ =& \hbar\omega_z(\hat{a}^\dagger\hat{a} + \frac{1}{2}) \\ &+ \frac{\hbar\omega_0}{2}\sigma_z \\ &+ \frac{\hbar\Omega}{2}(\sigma^+ + \sigma^-)\left(e^{i(k_z\hat{z} - \omega_L t + \phi)} + e^{-i(k_z\hat{z} - \omega_L t + \phi)}\right), \end{aligned} \tag{3.17}$$

where $\hat{a}^\dagger, \hat{a}$ are the motional creation and annihilation operators, $\hat{n} = \hat{a}^\dagger\hat{a}$ is the number operator of motional quanta (phonons), $\sigma^+ = \sigma_x + i\sigma_y$ and $\sigma^- = \sigma_x - i\sigma_y$ are the electronic creation and annihilation operators with $\sigma_x, \sigma_y, \sigma_z$ being the Pauli operators, Ω the Rabi frequency is related to the interaction strength between the electric moment of the transition and the electromagnetic wave of the laser (e.g. $\hbar\Omega = -\mu_d E_0/4$ for an electric dipole transition with dipole moment μ_d and electric field amplitude E_0), and $\hat{z} = z_0(\hat{a}^\dagger + \hat{a})$ describes the motion in the harmonic trapping potential, where $z_0 = \sqrt{\hbar/2M\omega_z}$ is the spread of the ground state wave function with the ground state energy $\hbar\omega_z/2$. At a trap frequency of $\omega_z = (2\pi)\,1\,\text{MHz}$ the ground state wave function of a $^{40}Ca^{+}$ ion has a size $z_0 \approx 11\,\text{nm}$.

The interaction part H_i of the Hamiltonian in eq. (3.17) couples the electronic quantum states with the motional state, as illustrated in fig. 3.3 **a)**. The wavefunction of the coupled system can be described by a superposition of tensor products of the electronic states $|0\rangle$, $|1\rangle$ and the motional state $|n\rangle$ as

$$|\psi(t)\rangle = \sum_{m_z=0,1}\sum_{n=0}^{\infty} C_{m_z,n}(t)\,|m_z, n\rangle\,, \tag{3.18}$$

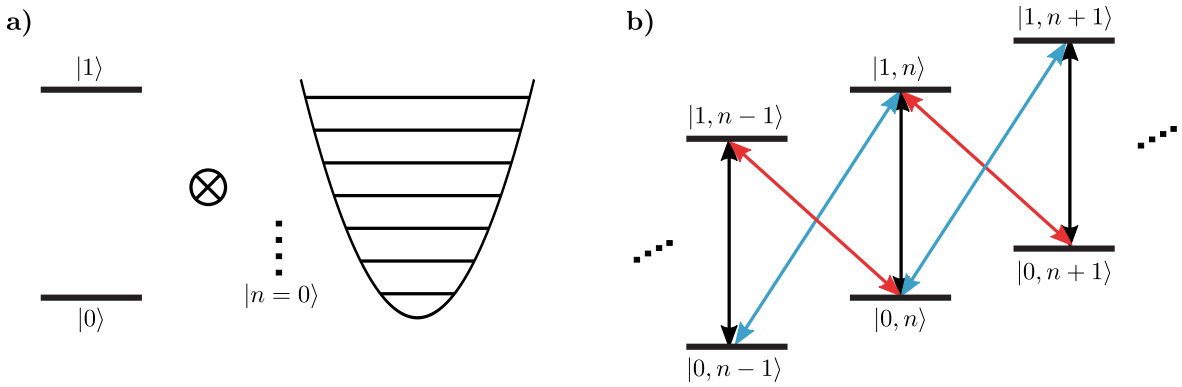

Figure 3.3: **Laser-ion interaction. a)** The quantum state of the ion can be coupled to the motion, which is expressed by the tensor product of the electronic and the motional state, e.g. $|0\rangle \otimes |n\rangle \hat{=} |0,n\rangle$. **b)** The coupled system can be seen as a ladder of many two-level systems, where the red and the blue sideband can be used to increase or decrease the phononic excitation.

where n is the motional quantum number. By changing to the rotating frame of the ion and doing the rotating wave approximation (neglecting the sum-frequency terms $e^{\pm i(\omega_0+\omega_L)t}$) the interaction Hamiltonian H_I can be approximated as [70]

$$H_I = U_0^\dagger H_i U_0 \approx \frac{\hbar\Omega}{2}\left(\sigma^+ e^{i[\eta(\hat{a}e^{-i\omega_z t}+\hat{a}^\dagger e^{i\omega_z t})-\Delta t+\phi]} + h.c.\right), \tag{3.19}$$

where $U_0 = e^{-i(H_t+H_e)t/\hbar}$ is the unitary operator of the time-independent part of the Hamiltonian H, $\eta = k_z z_0$ is the Lamb-Dicke (LD) parameter and $\Delta = \omega_L - \omega_0$ describes the detuning of the laser with respect to the electronic transition. The LD parameter η can be interpreted as the ratio between the wave packet size z_0 of an ion in the motional ground state and the laser wavelength λ as [70]

$$\eta = k_z z_0 = 2\pi \cos\theta \frac{z_0}{\lambda} = \frac{2\pi\cos\theta}{\lambda}\sqrt{\frac{\hbar}{2M\omega_z}}, \tag{3.20}$$

where θ is the angle between the wave vector and the direction of the ion motion. In our experiment we use laser beams with various wavelengths that are coupled to the ions from different directions. Typically the LD parameter for $^{40}Ca^+$ ions is in the range of $\eta = 0.02 \ldots 0.09$, see table 3.1.

Table 3.1: **Lamb-Dicke parameters.** Theoretical LD parameters η for $^{40}Ca^+$ with typical trapping frequencies ω, where θ describes the angle between the wave vector of the laser and the direction of the ion motion. We list laser beams for qubit manipulation at a wavelength of 729 nm and the Doppler Cooling (DC) beam at a wavelength of 397 nm. The laser beam alignment is illustrated in fig. 4.1.

Motional mode	Global 729 nm	Addressed 729 nm	DC 397 nm
Axial	$\theta = 22.5°$	$\theta = 67.5°$	$\theta = 67.5°$
$\omega_z = (2\pi)\,1\,\text{MHz}$	$\eta = 0.090$	$\eta = 0.037$	$\eta = 0.068$
Radial	$\theta = 67.5°$	$\theta = 22.5°$	$\theta = 22.5°$
$\omega_x = (2\pi)\,4\,\text{MHz}$	$\eta = 0.019$	$\eta = 0.045$	$\eta = 0.082$

The dynamics of the state $|\psi(t)\rangle$ are given by the Schrödinger equation $i\hbar\frac{\mathrm{d}}{\mathrm{d}t}|\psi(t)\rangle = H|\psi(t)\rangle$, which yields the unitary time evolution:

$$|\psi(t)\rangle = U(t)|\psi(0)\rangle = e^{-iH_I t/\hbar}|\psi(0)\rangle . \tag{3.21}$$

If we assume that the laser is tuned close to a resonant transition with detuning $\Delta = (n'-n)\omega_z + \delta$, where n and n' are integers and $\delta \ll \omega_z$, the transition $|0,n\rangle \leftrightarrow |1,n'\rangle$ is coherently driven and the coefficients in eq. (3.18) can be calculated as

$$\dot{C}_{1,n'} = -i^{1+|n'-n|}e^{-i(\delta t-\phi)}\Omega_{n,n'}C_{0,n}, \tag{3.22}$$

$$\dot{C}_{0,n} = -i^{1-|n'-n|}e^{i(\delta t-\phi)}\Omega_{n,n'}C_{1,n'}, \tag{3.23}$$

with the Rabi frequencies $\Omega_{n,n'}$ described as [70]

$$\begin{aligned}\Omega_{n,n'} &= \Omega_{n',n} = \Omega|\langle n'|\, e^{i\eta(\hat{a}+\hat{a}^\dagger)}\,|n\rangle\,| \\ &= \Omega e^{-\eta^2/2}\eta^{|n'-n|}\sqrt{\frac{n_<!}{n_>!}}L_{n_<}^{|n'-n|}(\eta^2),\end{aligned} \tag{3.24}$$

where $n_<$ is the lesser, $n_>$ the greater of n' and n, and $L_n^{(\alpha)}(x)$ are the generalized Laguerre polynomials

$$L_n^{(\alpha)}(x) = \sum_{i=0}^{n}(-1)^i\binom{n+\alpha}{n-i}\frac{x^i}{i!}. \tag{3.25}$$

The coupled system of eqs. (3.22) and (3.23) can be solved using Laplace transforms. The solutions are the so called *Rabi oscillations* [9] that transform the state of the ion as

$$|\psi(t)\rangle = T_{n,n'}(t)|\psi(0)\rangle , \tag{3.26}$$

where the unitary matrix $T_{n,n'}(t)$ can be described as [70]

$$T_{n,n'}(t) = \begin{bmatrix} e^{-i\delta t/2}\left[\cos(\widetilde{\Omega}_{n,n'}t/2) + i\frac{\delta}{\widetilde{\Omega}_{n,n'}}\sin(\widetilde{\Omega}_{n,n'}t/2)\right] & -i\frac{\Omega_{n,n'}}{\widetilde{\Omega}_{n,n'}}e^{i(\phi+|n'-n|\pi/2-\delta t/2)}\sin(\widetilde{\Omega}_{n,n'}t/2) \\ -i\frac{\Omega_{n,n'}}{\widetilde{\Omega}_{n,n'}}e^{-i(\phi+|n'-n|\pi/2-\delta t/2)}\sin(\widetilde{\Omega}_{n,n'}t/2) & e^{i\delta t/2}\left[\cos(\widetilde{\Omega}_{n,n'}t/2) - i\frac{\delta}{\widetilde{\Omega}_{n,n'}}\sin(\widetilde{\Omega}_{n,n'}t/2)\right] \end{bmatrix}, \tag{3.27}$$

with the effective Rabi frequency $\widetilde{\Omega}_{n,n'} = \sqrt{\Omega_{n,n'}^2 + \delta^2}$.

An important regime is where the extent of the wave packet of the ion $\Delta z = z_0\sqrt{n+1/2}$ is much smaller than the wavelength $\lambda/(2\pi)$ (up to 2π) of the laser. In this, so called Lamb-Dicke regime, the relationship $\Delta z \ll \lambda/(2\pi) \rightarrow \eta^2(2n+1) \ll 1$ holds for all times and thus we can simplify the interaction Hamiltonian from eq. (3.19) as [70]

$$e^{\pm i\eta(\hat{a}e^{-i\omega_z t}+\hat{a}^\dagger e^{i\omega_z t})} \approx 1 \pm \eta(\hat{a}e^{-i\omega_z t} + \hat{a}^\dagger e^{i\omega_z t}) + \mathcal{O}(\eta^2), \tag{3.28}$$

$$\rightarrow H_I \approx \frac{\hbar\Omega}{2}\left(\sigma^+\{1+\eta(\hat{a}e^{-i\omega_z t} + \hat{a}^\dagger e^{i\omega_z t})\}e^{-i(\Delta t-\phi)} + h.c.\right). \tag{3.29}$$

In eq. (3.29) we can identify three different laser detunings $\Delta = 0, \pm\omega_z$ where we find special transitions. The respective Hamiltonian and the Rabi frequencies of these three transitions are illustrated in fig. 3.3 **b)** and they are described as:

1. *Carrier* (C) transition $|0,n\rangle \leftrightarrow |1,n\rangle$:
   Detuning $\Delta = 0$

$$\begin{aligned} H_{\mathrm{C}} &= \frac{\hbar\Omega}{2}\left(\sigma^{+}e^{i\phi} + \sigma^{-}e^{-i\phi}\right), \\ \Omega_{n,n} &= \Omega(1 - n\eta^2)^{1}. \end{aligned} \tag{3.30}$$

2. *Red-sideband* (RSB) transition $|0,n\rangle \leftrightarrow |1,n-1\rangle$:
   Detuning $\Delta = -\omega_z$

$$\begin{aligned} H_{\mathrm{RSB}} &= \frac{i\hbar\Omega\eta}{2}\left(\hat{a}\sigma^{+}e^{i\phi} + \hat{a}^{\dagger}\sigma^{-}e^{-i\phi}\right), \\ \Omega_{\mathrm{n,n-1}} &= \sqrt{n}\eta\Omega. \end{aligned} \tag{3.31}$$

3. *Blue-sideband* (BSB) transition $|0,n\rangle \leftrightarrow |1,n+1\rangle$:
   Detuning $\Delta = +\omega_z$

$$\begin{aligned} H_{\mathrm{BSB}} &= \frac{i\hbar\Omega\eta}{2}\left(\hat{a}^{\dagger}\sigma^{+}e^{i\phi} + \hat{a}\sigma^{-}e^{-i\phi}\right), \\ \Omega_{n,n+1} &= \sqrt{n+1}\eta\Omega. \end{aligned} \tag{3.32}$$

[1] Note, to determine the reduction of the Rabi frequency with $\propto n\eta^2$ one has to take into account the $\mathcal{O}(\eta^2)$ terms in the Lamb-Dicke approximation in eq. (3.28)

3.3.1 *Coherent laser-ion interaction*

Quantum operations that change the state of a qubit require coherent interactions between the laser and the ion. Typically, such quantum operations are carried out on a carrier transition of an ion in the LD regime, where the interaction Hamiltonian from eq. (3.29) simplifies to

$$H_I = \frac{\hbar\Omega}{2}\left(\sigma^+ e^{-i(\Delta t-\phi)} + \sigma^- e^{+i(\Delta t-\phi)}\right). \tag{3.33}$$

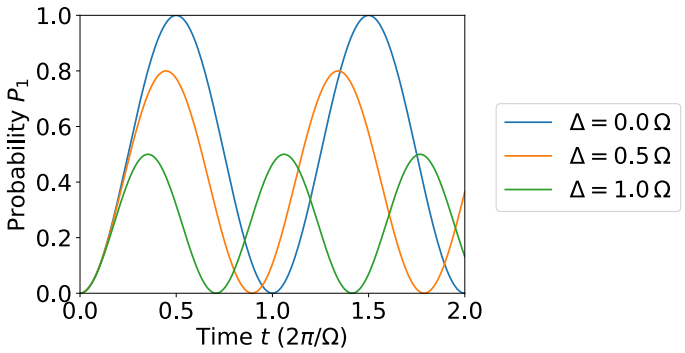

Figure 3.4: **Rabi oscillations.** The plot shows the probability $P_1(t)$ of finding the ion in the excited state after switching on the laser-ion interaction for the time t for three different detunings Δ.

Starting from the initial state $|\psi(0)\rangle = |S\rangle = |0\rangle$ the probability P_0 of finding the ion in the ground state $|0\rangle$ after time t for $\Delta \ll \omega_z$ can be calculated using eqs. (3.26) and (3.27) as

$$P_0(t) = |\langle\psi(t)\,|\psi(0)\rangle|^2 = \frac{\Omega^2}{\widetilde{\Omega}^2}\cos^2(\widetilde{\Omega}t/2), \tag{3.34}$$

with the effective Rabi-frequency $\widetilde{\Omega} = \sqrt{\Omega^2+\Delta^2}$, Rabi-frequency $\Omega = \Omega_{n,n}$ and laser detuning Δ from the carrier transition frequency. The probability P_1 of finding the ion in the excited state $|D\rangle = |1\rangle$ can be calculated by

$$P_1(t) = 1 - P_0(t) = \frac{\Omega^2}{\widetilde{\Omega}^2}\sin^2(\widetilde{\Omega}t/2). \tag{3.35}$$

The effective frequency of the Rabi oscillation increases with larger detunings, whereas the amplitude decreases, as depicted in fig. 3.4.

For a given phonon distribution, the Rabi oscillations on resonance ($\Delta = 0$) are described as

$$P_1(t) = \sum_n c_n \sin^2(\Omega_{n,n'}t/2), \tag{3.36}$$

where c_n describes the probability that the ion is measured in the motional Fock state $|n\rangle$ and $\Omega_{n,n'}$ defines the Rabi frequency of a given transition according to eq. (3.24).

If the ion is not cooled close to the motional ground state, we can assume a thermal distribution of the phononic excitation as described in eq. (3.16). Such a thermal occupation of the phononic state leads to an exponential decay of the Rabi oscillation, as can be seen in fig. 3.11.

3.3.1.1 *Resonant qubit operations*

The time evolution of a resonant laser beam (carrier H_C with $\Delta = 0$) interacting with two levels of an ion can be described by the following unitaries

$$U(t) = e^{-iH_C t/\hbar} \tag{3.37}$$

$$R(\theta, \phi) = e^{-i\theta(S_x \cos\phi + S_y \sin\phi)}, \tag{3.38}$$

where the interaction Hamiltonian H_C is defined in eq. (3.30), $\theta = \Omega t$ is the rotation angle, ϕ is the laser phase which defines the rotation axis in the x,y-plane of the Bloch sphere and $S_{x,y} = \sigma_{x,y}/2$ correspond to the spin operators. If we choose the phase $\phi \in \{0, \pi/2\}$ the Bloch-vector oscillates around the $\{x, y\}$ axis as

$$\begin{aligned} R_x(\theta) = X(\theta) = U(\theta, 0) &= e^{-i\theta S_x} \\ &= \begin{pmatrix} \cos(\theta/2) & -i\sin(\theta/2) \\ -i\sin(\theta/2) & \cos(\theta/2) \end{pmatrix} \end{aligned} \tag{3.39}$$

$$\begin{aligned} R_y(\theta) = Y(\theta) = U(\theta, \pi/2) &= e^{-i\theta S_y} \\ &= \begin{pmatrix} \cos(\theta/2) & -\sin(\theta/2) \\ -\sin(\theta/2) & \cos(\theta/2) \end{pmatrix}. \end{aligned} \tag{3.40}$$

Following eq. (3.39) for example, a resonant $X(\pi)$ rotation requires the implementation of a laser pulse with length t and electric field amplitude E_0 that defines the Rabi frequency as $\Omega \propto E_0$ such that the pulse area fulfills the criterion $\theta = \Omega t = \pi$.

If a set $\mathcal{A}$ of ions with size $|\mathcal{A}| \leq N$ of a string containing N ions is illuminated by the laser, the resonant qubit operations can be readily extended by expanding the spin operator to

$$S_{x,y} = \frac{1}{2} \sum_{i \in \mathcal{A}} ... \otimes \mathbb{1}^{(i-1)} \otimes \sigma_{x,y}^{(i)} \otimes \mathbb{1}^{(i+1)} \otimes ... \tag{3.41}$$

with $\sigma_{x,y}^{(i)}$ acting on qubits i.

3.3.1.2 *Off-resonant qubit operations*

For a large enough laser detuning ($\Delta \gg \Omega$) from a transition, the resonant coupling to the transition can be neglected, as can be seen in eq. (3.35). But a far detuned laser beam changes the energy difference between atomic levels, due to the so called *AC-Stark effect*. The AC-Stark shift can be calculated by using second-order time-independent perturbation theory [81]. For non-degenerated states with interaction Hamiltonian H_I the energy shift of a state i with unperturbed energy $\mathcal{E}_i$ can be estimated by

$$\Delta E_i = \sum_{j \neq i} \frac{|\langle j| H_I |i\rangle|^2}{\mathcal{E}_i - \mathcal{E}_j} \tag{3.42}$$

For a laser with electric field $\vec{E}$ coupling for example to a single dipole transition between a ground state $|g\rangle$ and an excited state $|e\rangle$ with dipole moment $\vec{\mu}$ the dipole matrix element

is $\langle e|\,\vec{\mu}\vec{E}\,|g\rangle = \hbar\Omega/2$. The energy shift of the involved states can be calculated according to eq. (3.42) as

$$\Delta E = \pm\frac{|\,\langle e|\,\vec{\mu}\vec{E}\,|g\rangle\,|^2}{\hbar\Delta} = \pm\frac{\hbar\Omega^2}{4\Delta} \tag{3.43}$$

Compared to the unperturbed rotating frame of the ion, the AC-Stark shift induces an effective rotation around the z-axis during the interaction with Rabi frequency

$$\Omega_{\mathrm{AC}} = \frac{\Omega^2}{2\Delta}. \tag{3.44}$$

Note that in the experiment one needs to take into account all relevant transitions to which the laser couples off-resonantly (all Zeeman transitions in the $4^2S_{1/2} \leftrightarrow 3^2D_{5/2}$ manifold and the dipole transitions $4^2S_{1/2} \leftrightarrow 4^2P_{1/2}$, $4^2S_{1/2} \leftrightarrow 4^2P_{3/2}$, $3^2D_{5/2} \leftrightarrow 4^2P_{3/2}$) [82].

The effective rotation around the z-axis is (up to a global phase) described by the following unitary operation

$$R_z(\theta) = Z(\theta) = e^{-i\theta S_z} = \begin{pmatrix} 1 & 0 \\ 0 & e^{i\theta} \end{pmatrix}, \tag{3.45}$$

where $\theta = \Omega_{\mathrm{AC}}t$ is the rotation angle. Similar to eq. (3.41), a rotation around the z-axis can be extended to a register containing many ions by expanding the spin operator S_z.

3.3.1.3 *Entangling qubit operations*

In our experiment we utilize the so called Mølmer-Sørensen (MS)-gate [83, 84] to entangle the electronic states of the ions. The MS-gate employs a spin-dependent force by using the motional degrees of freedom of the ions. To realize this gate two laser beams with opposite detunings from the carrier $\omega_0 - \omega_{\mathrm{L}} = \pm\Delta$ interact with the ions. The interaction Hamiltonian from eq. (3.19) can then be written as [84]

$$\begin{aligned} H_{\mathrm{I}} = 2\Omega S_y\cos(\Delta t) - \sqrt{2}\eta\Omega S_x[\hat{x}\cos(\omega_z-\Delta)t + \hat{x}\cos(\omega_z+\Delta)t \\ +\hat{p}\sin(\omega_z-\Delta)t + \hat{p}\sin(\omega_z+\Delta)t], \end{aligned} \tag{3.46}$$

where $S_{x,y}$ correspond to the spin operators defined in eq. (3.41), $\hat{x} = 1/\sqrt{2}(\hat{a}+\hat{a}^\dagger)$ is the position operator and $\hat{p} = i/\sqrt{2}(\hat{a}^\dagger - \hat{a})$ is the momentum operator. If we use laser beams with small enough intensities $\Omega \ll \Delta$ and tune the laser close to the motional frequency $\delta = \omega_z - \Delta \ll \Delta$ we can neglect the S_y term and the fast oscillating terms $(\omega_z + \Delta)$ and the interaction Hamiltonian simplifies to

$$H_{\mathrm{I}} = f(t)S_x\hat{x} + g(t)S_x\hat{p}, \tag{3.47}$$

with $f(t) = -\sqrt{2}\eta\Omega\cos\delta t$ and $g(t) = -\sqrt{2}\eta\Omega\sin\delta t$. As can be seen in eq. (3.47), the ions experience a state-dependent force and they follow a circular trajectory in phase-space during the interaction, as shown in fig. 3.5 **a)**. If the ions undergo a complete circle in phase-space we refer to this as one loop. The unitary time evolution can be described by the following propagator

$$U_{\mathrm{MS}}(t) = e^{-iA(t)S_x^2}e^{-iF(t)S_x\hat{x}}e^{-iG(t)S_x\hat{p}}, \tag{3.48}$$

with $A(t) = -\frac{\eta^2\Omega^2}{\delta}\left[t - \frac{1}{2\delta}\sin 2\delta t\right]$, $F(t) = -\frac{\sqrt{2}\eta\Omega}{\delta}\sin\delta t$ and $G(t) = -\frac{\sqrt{2}\eta\Omega}{\delta}\left[1-\cos\delta t\right]$.

Since we encode quantum information only in the electronic states of the ions, the electronic states should not be entangled with the motion after the gate evolution. Therefore we tune the experimental parameters such that after a specific gate time τ the terms in eq. (3.48) vanish, i.e. $F(\tau) = G(\tau) = 0$. The motion is disentangled from the electronic states after times $\tau = 2\pi K/\delta$, where K is an integer and defines the number of loops the ions make in phase-space.

The action of the MS gate on the electric states of two ions is described (up to a global phase) as

$$\begin{aligned} \mathrm{MS}(\theta) &= e^{-i\theta S_x^2} \\ &= \begin{pmatrix} \cos(\theta/2) & 0 & 0 & -i\sin(\theta/2) \\ 0 & \cos(\theta/2) & -i\sin(\theta/2) & 0 \\ 0 & -i\sin(\theta/2) & \cos(\theta/2) & 0 \\ -i\sin(\theta/2) & 0 & 0 & \cos(\theta/2) \end{pmatrix}, \end{aligned} \tag{3.49}$$

with the spin operator $S_x = 1/2(\sigma_x \otimes \mathbb{1} + \mathbb{1} \otimes \sigma_x)$ for two ions, as defined in eq. (3.41). In the experiment it is also possible to set the phase ϕ of the laser beams allowing us to change the rotation axis of the MS-gate as

$$\mathrm{MS}_\phi(\theta) = e^{-i\theta(S_x \cos\phi + S_y \sin\phi)^2}. \tag{3.50}$$

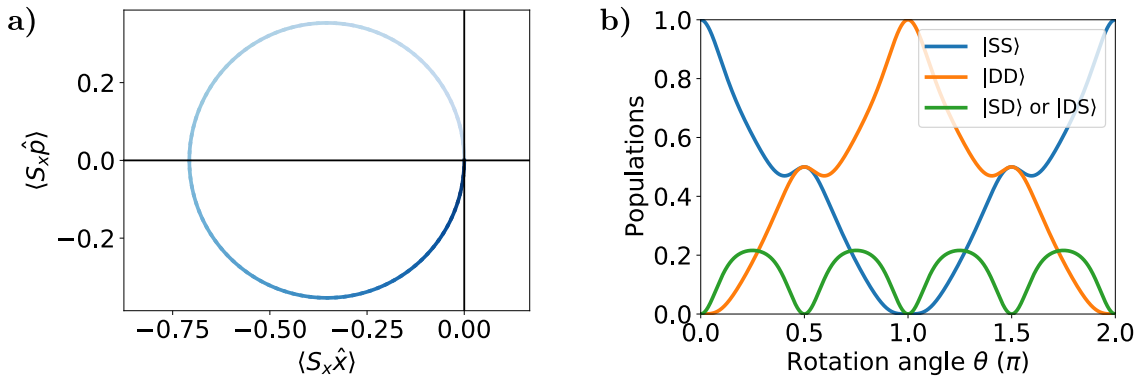

Figure 3.5: **MS-gate evolution. a)** Trajectory describing the state evolution in phase-space from 0 to $\pi/2$ (light blue to dark blue) corresponding to $K = 1$ loop. **b)** Time evolution of the state populations during a 2-qubit MS-gate from 0 to 2π corresponding to $K = 4$ loops in phase-space.

3.4 QUANTUM GATE OPERATIONS

As mentioned in the introduction, algorithms in quantum computation are realized by a series of gate operations acting on register of qubits. These discrete gates can be schematically described by the circuit model.

A commonly used finite and universal gate set $\{H, P, T, \text{CNOT}\}$ contains the Hadamard-, the Phase-, the T- and the CNOT-gate, where the 1-qubit operations are described in fig. 3.6 and the CNOT-gate is depicted in fig. 3.7. Another, slightly smaller set of gates $\{H, P, \text{CNOT}\}$ is also quite important in quantum information theory, since it can be simulated efficiently on a classical computer and thus plays an important role in quantum benchmarking (see chapter 5) and quantum error correction (see chapter 7). The generation and other details of the so-called Clifford group is described in appendix E.

The Pauli operations X, Y, Z can be implemented by laser pulses, which rotate the state of the qubit by an angle of π, as $X = R_x(\pi), Y = R_x(\pi), Z = R_z(\pi)$. The Hadamard gate is realized by a $\pi/2$ rotation around the y-axis followed by a π pulse around the z-axis, as $H = R_z(\pi)R_y(\pi/2)$. A $\pi/4$ rotation about the z-axis corresponds to the $T = R_z(\pi/4)$ gate, which is an important gate since together with the gates from the Clifford group a universal set of gates is formed. The CNOT-gate is implemented by a fully entangling MS($\pi/2$) gate dressed with four local gates, as illustrated in fig. 3.7.

Since the set of gates $\{H, P, T, \text{CNOT}\}$ can be implemented in our ion trap apparatus, our architecture provides a universal set of gates for quantum computation.

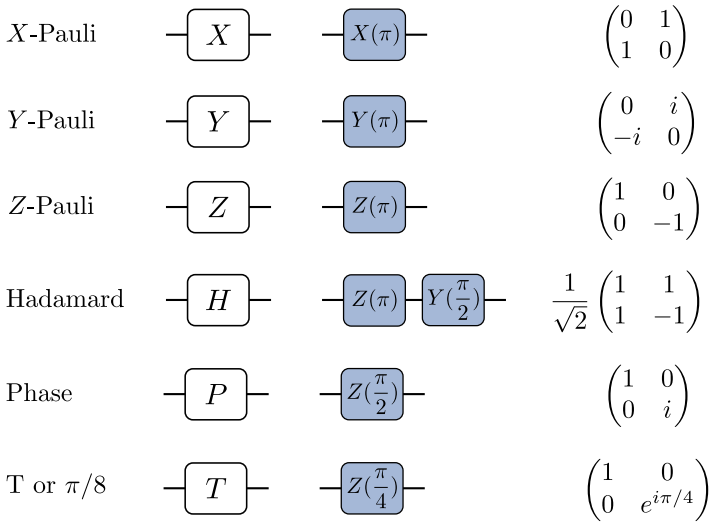

Figure 3.6: **1-qubit quantum gates.** Name, standard circuit model symbols, ion gate implementation and matrix representation of frequently used quantum gates.

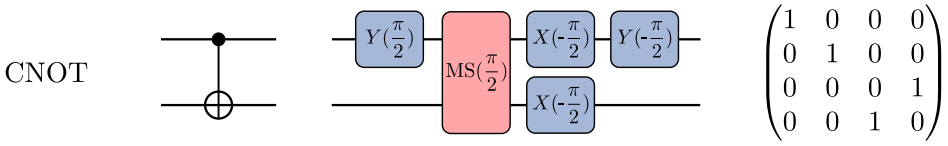

Figure 3.7: **2-qubit Controlled-NOT (CNOT)-gate.** Standard circuit model symbol, ion gate implementation and matrix representation of the CNOT-gate. Depending on the state of qubit 1 (control qubit), qubit 2 (target qubit) is inverted (by an X operation) or not.

3.5 RAMSEY SPECTROSCOPY

Ramsey's technique of separated oscillatory fields [85] is an efficient tool to estimate the phase coherence of atomic transitions and the driving fields. The idea is to generate an equal superposition of two specific states, let this state evolve for a certain time τ and bring the population back into one of the two states to measure the resulting population.

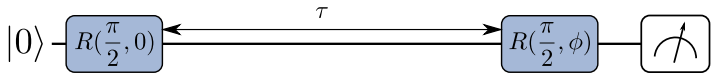

Figure 3.8: **Pulse sequence for Ramsey spectroscopy.** The qubit is prepared in the state $|0\rangle$, then a $\pi/2$ rotation $R(\frac{\pi}{2},0)$ is applied to the qubit. After a waiting time τ a second $\pi/2$ rotation $R(\frac{\pi}{2},\phi)$ with phase ϕ is implemented before the qubit is measured.

Experimentally we implement the sequence $R(\pi/2,0) \rightarrow \text{Wait}(\tau) \rightarrow R(\pi/2,\phi)$, as depicted in fig. 3.8. Using eq. (3.35), we can calculate the probability to excite the ion to the state $|1\rangle$ as [76]

$$P_1(\tau) = \frac{4\Omega^2}{\widetilde{\Omega}^2}\sin^2(\widetilde{\Omega}t'/2)\Big[\cos(\widetilde{\Omega}t'/2)\cos(\Delta\tau/2+\phi) + \frac{\Delta}{\widetilde{\Omega}}\sin(\widetilde{\Omega}t'/2)\sin(\Delta\tau/2+\phi)\Big]^2, \tag{3.51}$$

where $\widetilde{\Omega} = \sqrt{\Omega^2+\Delta^2}$ is the effective Rabi-frequency, Δ the detuning, t' the $\pi/2$ pulse duration, τ the Ramsey waiting time and ϕ describes the phase difference between the two $\pi/2$ pulses. For typical experiments we can assume that the detuning is small compared to the Rabi frequency $\Delta \ll \Omega$ and that the $\pi/2$ pulse duration is much smaller than the Ramsey time $t' \ll \tau$ and eq. (3.51) simplifies to [76]

$$P_1(\tau) = \frac{1}{2}\left[1 + C(\tau)\cos(\Delta\tau + 2\phi)\right]\sin^2(\widetilde{\Omega}t'/2), \tag{3.52}$$

where we have introduced the waiting time dependent contrast $C(\tau)$. If we assume for example, that the detuning Δ of the laser fluctuates slowly from shot to shot, the measured state depends on the realized phase $e^{i\Delta\tau}$ of each single shot. If we average over these individual realizations, the contrast $C(\tau)$ is reduced. If the specific phase is not correlated from shot to shot, the contrast can be estimated as the expectation value of this random phase as [76]

$$C(\tau) = \left|\langle e^{i\Delta\tau}\rangle\right| = \left|\int_{-\infty}^{\infty} p(\Delta)e^{i\Delta\tau}\mathrm{d}\Delta\right|, \tag{3.53}$$

where we average the random phase over a probability density function $p(\Delta)$. The frequency fluctuations of a laser can typically be modeled by a Lorentzian function as [76]

$$p(\Delta) = \frac{1}{\pi}\frac{\gamma}{\gamma^2+\Delta^2}, \tag{3.54}$$

where γ describes the half width at half maximum (HWHM). Note that eq. (3.53) basically describes the Fourier transform of the probability density function $p(\Delta)$, which results in an exponential decay in the case of a Lorentzian laser linewidth as [76]

$$C(\tau) = e^{-\gamma\tau} = e^{-\frac{\tau}{T_2}}, \tag{3.55}$$

where $T_2 = 1/\gamma$ is the coherence time. Since the full width at half maximum (FWHM) from eq. (3.54) can be described as $2\gamma = \Delta\omega_{\mathrm{FWHM}} = 2\pi\Delta\nu_{\mathrm{FWHM}}$, the coherence time is related to the FWHM laser linewidth as

$$T_2 = \frac{1}{\gamma} = \frac{1}{\pi\Delta\nu_{\mathrm{FWHM}}}. \tag{3.56}$$

In a similar fashion the frequency fluctuations can be modeled by a Gaussian distribution as [76]

$$p(\Delta) = \frac{1}{\sigma\sqrt{\pi}} \exp\left(-\frac{\Delta^2}{\sigma^2}\right) \tag{3.57}$$

and for the time dependent contrast follows [76]

$$C(\tau) = \exp\left(-\frac{\sigma^2\tau^2}{4}\right). \tag{3.58}$$

Using the FWHM definition $2\pi\Delta\nu_{\mathrm{FWHM}} = 2\sqrt{\ln 2}\sigma$ and that T_2 is the time for which the contrast reduces to $1/e$ of the initial value, the corresponding coherence time is given by

$$T_2 = \frac{2\sqrt{\ln 2}}{\pi\Delta\nu_{\mathrm{FWHM}}}. \tag{3.59}$$

If we assume that the frequency fluctuations are induce by magnetic field fluctuations, we can exchange the term $\Delta\nu_{\mathrm{FWHM}} = \mu\Delta B/h$, since the frequency shift depends linearly on the magnetic field, as discussed in appendix A.

In reality, fluctuations are rarely perfectly described by a Gaussian noise process as assumed in the cases above. Typically, in the laboratory there are additional components in the frequency spectrum, such as e.g. 50 Hz noise components and harmonics thereof originating from the AC power line or other noise peaks in various frequency domains coming from electronic devices.

For a given power spectral density $A(\omega)$ of the noise, we can compute the Ramsey contrast $C(\tau)$ as [86, 87]

$$C(\tau) = \exp\left\{-\int_0^\infty \frac{A(\omega)^2}{\omega^2} \sin^2(\omega\tau/2)\mathrm{d}\omega\right\}. \tag{3.60}$$

Note, that for constant noise spectrum $A(\omega) = a$ the integral is $\int_0^\infty \frac{A(\omega)^2}{\omega^2} \sin^2(\omega\tau/2)\mathrm{d}\omega = a^2\pi\tau/4$ and the Ramsey contrast decays exponentially in agreement with eq. (3.55).

If we want to cancel noise that is slower varying than half the Ramsey waiting time, we add a π pulse at half the waiting time, that will refocus the slow noise in the second half of the experiment. This Ramsey spectroscopy with *spin-echo* [88] is for example helpful when the transition frequency changes slowly compared to the waiting time. Experimentally we implement the sequence $R(\pi/2, 0) \to \mathrm{Wait}(\tau/2) \to R(\pi, 0) \to \mathrm{Wait}(\tau/2) \to R(\pi/2, \phi)$, as depicted in fig. 3.9.

The Ramsey contrast with spin-echo can be estimated as [89]

$$C(\tau) = \exp\left\{-4\int_0^\infty \frac{A(\omega)^2}{\omega^2} \sin^4(\omega\tau/4)\mathrm{d}\omega\right\}. \tag{3.61}$$

Note, that similar to the case before, a constant noise spectrum $A(\omega) = a$ leads to an exponential decay with decay constant $T_2 = 4/(a^2\pi)$.

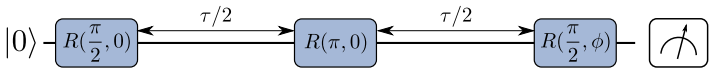

Figure 3.9: **Pulse sequence for Ramsey spectroscopy with spin-echo.** The qubit is prepared in the state $|0\rangle$, then a $R(\frac{\pi}{2},0)$ rotation is applied to the qubit. After half the waiting time $\tau/2$ a $R(\pi,0)$ pulse is applied. Finally, after a second waiting $\tau/2$ a $R(\frac{\pi}{2},\phi)$ rotation with phase ϕ is implemented before the qubit is measured.

In general, we model peaks in the noise spectrum with either a Lorentzian $L(\omega,\omega_0,\Gamma)$ or a Gaussian $G(\omega,\omega_0,\sigma)$ function as

$$L(\omega,\omega_0,\Gamma) = \frac{\Gamma^2}{\Gamma^2+(\omega-\omega_0)^2}, \tag{3.62}$$

$$G(\omega,\omega_0,\sigma) = \exp\left\{-\frac{(\omega-\omega_0)^2}{\sigma^2}\right\}, \tag{3.63}$$

where Γ and σ describe the widths and ω_0 the center of the distributions. As an example the noise spectrum can be modeled as

$$A(\omega) = a + bG(\omega,\omega_0,\sigma) + cL(\omega,\omega_0',\Gamma). \tag{3.64}$$

3.6 LASER COOLING

Coherent laser-ion interaction, as described in section 3.3.1, requires the trapped ions to be inside the Lamb-Dicke regime. As outlined in section 3.3.1 this means that the ions must be cold enough such that the spatial spread of the ion's wave function is small compared to the wavelength of the interacting laser. In order to realize high-fidelity quantum computation it is even necessary that the ions are close to their motional ground state. Experimentally, this can be achieved by laser cooling [78, 90–92],. This section gives a brief overview on how to reduce the temperature of trapped ions from hundreds of Kelvin down to the micro-Kelvin regime.

After atoms are emitted from the oven with a temperature $T \approx 600\,\mathrm{K}$ they are ionized and confined inside the trap. At these temperature the ions follow chaotic trajectories and they form a cloud of ions. Inside the trap the ions repel each other due to the Coulomb force. The Coulomb interactions can be described by the Coulomb correlation parameter $\Gamma_{\mathrm{Coul}} = \frac{Q^2}{4\pi\epsilon_0 a_0}\frac{1}{k_B T}$, which is defined as the ratio between the Coulomb interaction energy of two ions at distance a_0 and their kinetic energy [67]. Without cooling the trapped particles are in the weak coupling regime $\Gamma_{\mathrm{Coul}} \ll 1$ and form a cloud. By means of laser cooling it is possible to reduce the thermal energy of the ions and bring them into the strongly interacting regime $\Gamma_{\mathrm{Coul}} \gg 1$, where the kinetic energy becomes significantly lower than the Coulomb interaction energy $k_B T \ll Q^2/4\pi\epsilon_0 a_0$ and the particles form a periodic structure, a so called Coulomb crystal [67, 93–96]. Since the ions localize at the classical equilibrium position of the effective pseudo-potential, they form a one-dimensional crystal, or a string in a linear Paul trap. In the experiment the exact crystallization temperature depends on many factors, such as the particle number, the trapping frequencies and power/detuning of the cooling laser [67]. In the following we outline three techniques that enable us to decrease the ion temperature over more than 7 orders of magnitude.

Laser cooling in general utilizes absorption and emission of photons from a laser beam by the trapped ions. We can characterize laser cooling by two fundamental frequencies:

the trapping frequency ω_z and the rate of spontaneous emission Γ, which determines the minimum length of a cooling cycle. In our experiment we employ the following three types of laser cooling subsequently.

1. Doppler Cooling (DC) works in the *weak binding* or *unresolved sideband* regime, where the sideband transitions cannot be addressed individually because the linewidth is large compared to the motional frequency $\Gamma > \omega_z$. A detailed discussion follows in section 3.6.1

   Note, that at a temperature $T \approx 600\,\mathrm{K}$ after loading, all optical transitions are affected by the so called Doppler broadening $\Gamma_\mathrm{D} = 1/\lambda\sqrt{8\ln 2 k_\mathrm{B} T/M}$ [97]. The $4^2\mathrm{S}_{1/2} \leftrightarrow 4^2\mathrm{P}_{1/2}$ transition in $^{40}\mathrm{Ca}^+$ with a wavelength around 397 nm for example is broadened to $\Gamma_\mathrm{D} \approx (2\pi)\,330\,\mathrm{MHz}$. Hence DC is typically the first cooling technique of an experimental sequence.

2. Polarization Gradient Cooling (PGC) also works in the *unresolved sideband* regime, where $\Gamma > \omega_z$ holds. For PGC to work the extent of the ion wave packet must be smaller than the wavelength of the cooling laser, as opposed to DC. Hence the ions are typically pre-cooled before employing PGC. Importantly, the achievable cooling limit using PGC is lower compared to DC, as outlined in section 3.6.2.

3. Resolved Sideband Cooling (RSC) is employed in the *strong binding* or *resolved sideband* regime, where the sideband transitions can be addressed spectroscopically due to the narrow linewidth compared to the motional frequency $\Gamma < \omega_z$. With this cooling technique the ions can be cooled close to their motional ground state, which is explained in detail in section 3.6.3.

3.6.1 *Doppler cooling*

Here we utilize the Doppler effect, where the frequency of the laser is shifted in the rest frame of the ion, if the ion moves relative to the laser source. Hence this technique is called Doppler Cooling (DC). In the following we use a description of the cooling process that is derived from free particles, but leads to the same results as more evolved descriptions for confined particles [70, 78, 90–92].

If we describe the velocity $v(t) = v_0 \cos(\omega_z t)$ of the ion classically in the case of a large linewidth $\Gamma \gg \omega_z$, we can assume that the velocity does not change significantly during an absorption-emission cycle $t \propto 1/\Gamma$. The average force F_a acting on the ion can be described by the momentum change per absorption-emission cycle of photons with momentum $\hbar k$ at rate Γ times the probability $\rho_{ee} = \langle e|\,\rho\,|e\rangle$ of the ion to be in the excited state $|e\rangle$ as [70]

$$F_a = \langle \frac{\mathrm{d}p}{\mathrm{d}t} \rangle \approx \hbar k \Gamma \rho_{ee}, \tag{3.65}$$

with the Lorentzian excitation probability

$$\rho_{ee} = \frac{s_0/2}{1 + s_0 + 4\Delta_\mathrm{eff}^2/\Gamma^2}, \tag{3.66}$$

where $s_0 = 2\Omega^2/\Gamma^2$ is the saturation parameter on resonance and $\Delta_\mathrm{eff} = \Delta - kv$ is the difference between the laser detuning and the Doppler shift. As can be seen in eq. (3.66) the force is maximized for $\Delta_\mathrm{eff} = 0$ when the laser detuning matches the Doppler shift. For

small velocities, where the spatial extend of the ion is comparable to the laser wavelength, the Doppler broadening vanishes [98] and the Doppler shift becomes small compared to the natural linewidth $kv \ll \Gamma$ and the force F_a can be linearized in v [70]

$$\begin{aligned} F_a &\approx F_0(1+\kappa v) \\ &= \hbar k\Gamma \frac{s_0/2}{1+s_0+4\Delta^2/\Gamma^2}\left(1+\frac{8k\Delta\Gamma}{1+s_0+4\Delta^2/\Gamma^2}v\right), \end{aligned} \tag{3.67}$$

where F_a becomes a restoring force for red detuning ($\Delta < 0$). Averaging over many oscillations the cooling rate is defined as [70]

$$\dot{E}_{\text{cool}} = \langle F_a v\rangle = F_0\left(\langle v\rangle + \kappa\langle v^2\rangle\right) = F_0\kappa\langle v^2\rangle, \tag{3.68}$$

since $\langle v\rangle = 0$ for a particle in a harmonic potential. Due to the recoil energy $E_{\text{rec}} = \hbar^2k^2/2M$ of absorbed and emitted photons there is a diffusion in the kinetic energy of the ion. For low enough laser intensity, below saturation $s_0 \ll 1$ ($\Omega \ll \Gamma$), the absorption and emission of photons is not correlated and we can calculate the heating rate $\dot{E}_{\text{heat}}$ for small velocities ($v \approx 0$) as [70]

$$\begin{aligned} \dot{E}_{\text{heat}} &= \dot{E}_{\text{abs}} + \dot{E}_{\text{emi}} = \dot{E}_{\text{abs}}(1+\xi) = E_{\text{rec}}\Gamma\rho_{ee}(1+\xi) \\ &\approx \frac{\hbar^2k^2}{2M}\Gamma\rho_{\text{ee}}(v=0)(1+\xi), \end{aligned} \tag{3.69}$$

where ξ takes into account the anisotropy of the spontaneous emission ($\xi = 2/5$ for dipole radiation). In the steady state the heating rate is equal to the cooling rate ($\dot{E}_{\text{cool}} = \dot{E}_{\text{heat}}$) and thus the kinetic energy can be expressed as [70]

$$M\langle v^2\rangle = k_{\text{B}}T = \frac{\hbar\Gamma}{8}(1+\xi)\left(\frac{\Gamma}{2\Delta}(1+s_0)+\frac{2\Delta}{\Gamma}\right). \tag{3.70}$$

From eq. (3.70) the temperature limit for DC can be determined as [70]

$$T_{\text{min}} = \frac{\hbar\Gamma\sqrt{1+s_0}}{4k_{\text{B}}}(1+\xi), \quad \text{for} \quad \Delta = \frac{\Gamma\sqrt{1+s_0}}{2}. \tag{3.71}$$

If the temperature is not too low, such that $\hbar\omega_z \ll k_{\text{B}}T$ holds, we can relate the minimum achievable thermal energy from eq. (3.71) to the energy of a harmonic oscillator $k_{\text{B}}T \approx \hbar\omega_z(\bar{n}+1/2)$ with mean phonon number $\bar{n}$ and thus estimate the minimum mean phonon number as

$$\bar{n}_{\text{min}} \approx \frac{\Gamma\sqrt{1+s_0}}{4\omega_z}(1+\xi) - \frac{1}{2}. \tag{3.72}$$

The estimated mean phonon number after DC in our experiment is $\bar{n}_{\text{min}} \approx 7$, with a linewidth of $\Gamma = (2\pi)\,22.4\,\text{MHz}$, $s_0 \approx 0$, $\omega_z = (2\pi)\,1\,\text{MHz}$ and $\xi = 2/5$. Although, effects of the micro-motion [70, 99] and the existence of a third level ($D_{3/2}$) [100] are neglected, this limit is a good approximation in many experimental realizations. A more detailed analysis of the dynamics during DC of a single trapped atom can be found in Ref. [101].

3.6.2 *Polarization gradient cooling*

Polarization Gradient Cooling (PGC) is a technique routinely used in ultra-cold atom experiments. After the initial proposal [102], recent experiments demonstrated the usefulness of PGC also for trapped ion setups [103, 104].

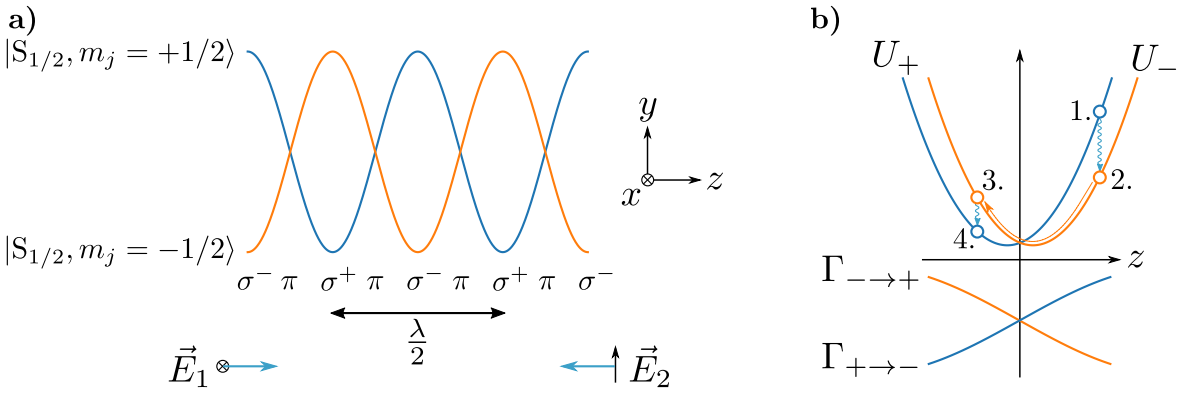

Figure 3.10: **Polarization Gradient Cooling (PGC) scheme. a)** Two counter-propagating beams ($\vec{E}_1$ and $\vec{E}_2$) with perpendicular linear polarization are overlapped along the z direction, forming a standing wave. Due to the off-resonant coupling of the standing wave to an excited state, the energies of the two ground states are shifted with a periodicity of $\lambda/2$. **b)** The state-dependent potentials (U_+ and U_-) are shifted and the transition rates ($\Gamma_{-\to+}$ and $\Gamma_{+\to-}$) vary along the z direction. This configuration favours an evolution like $1. - 4.$ and the ion is cooled.

PGC uses two counter-propagating laser beams in linear-perpendicular-linear polarization configuration interacting with the $4^2S_{1/2} \leftrightarrow 4^2P_{1/2}$ transition in $^{40}Ca^+$, as depicted in fig. 3.10 **a)**. The laser beams form a periodic polarization gradient field along the propagation direction z. If the quantization axis is aligned with the propagation direction of the lasers, the ion cannot interact with π polarized light. The frequency of the laser beams is blue detuned by Δ relative to the $4^2S_{1/2} \leftrightarrow 4^2P_{1/2}$ transition and gives rise to a periodically varying AC-Stark shift on the Zeeman ground states $|4^2S_{1/2}, m_j = \pm 1/2\rangle$, where the energy shifts of the two ground states have a phase difference of π. Combining the axial potential $U = 1/2M\omega_z^2 z^2$ of the trap and the state-dependent dipole potentials formed by the laser beams leads to the total potential [104]

$$U_\pm = 1/2M\omega_z^2 z^2 + \frac{1}{3}\Delta s\,(1 \mp \sin(2kz + 2\phi))\,, \tag{3.73}$$

where k expresses the wave vector, ϕ defines the phase at $z = 0$ and $s = \frac{\Omega^2/2}{\Gamma^2/4+\Delta^2}$ is the saturation parameter. In addition to the trapping potential, also the transition rates $\Gamma_{\pm\to\mp} \hat{=} \Gamma(U_\pm \to U_\mp)$ between the two ground states change periodically along the z axis [104]

$$\Gamma_{\pm\to\mp} = \frac{1}{9}\Gamma s(1 \mp \sin(2kz + 2\phi)), \tag{3.74}$$

as depicted in fig. 3.10 **b)**. If the ion moves in the periodically varying potential, it's energy changes before being transferred from one Zeeman state to the other. On average, the change of the kinetic energy in this process can be described as [104]

$$\dot{E} = p_+\langle\Gamma_{+\to-}(U_- - U_+)\rangle + p_-\langle\Gamma_{-\to+}(U_+ - U_-)\rangle + R_{sc}\hbar\omega_z, \tag{3.75}$$

where $p_\pm = 1/2(1 \pm \sin(2kz + 2\phi))$ are the populations of the Zeeman ground states in the steady state and R_{sc} describes the rate of scattered photons which lead to heating. In the Lamb-Dicke regime the two main heating effects are photon absorption on the carrier transition followed by a spontaneously scattered photon on the sideband R_{SB} and photon

absorption on the sideband followed by a spontaneously emitted photon on the carrier R_C. In the trap center ($z = 0$) the heating rate of these processes can be defined as [104]

$$R_{sc} = R_C + R_{SB} = \frac{1}{3}\eta^2\Gamma s\left[\alpha(1-\sin^2 2\phi) + (1+\sin^2 2\phi)\right], \tag{3.76}$$

where α takes the spatial emission pattern of the scattered photon into account ($\alpha = 1/3$ for a dipole transition). In our example, with blue detuned laser beams, the probability of changing the state is correlated with the potential such that it is likely that the ion climbs the potential hill and loses kinetic energy before it gets transferred back to the lower lying potential at rate R_{cool}. In analogy of the story of King Sisyphus in Greek mythology, who was punished by being forced to roll a rock up the hill over and over again for eternity, this process is called the Sisyphus effect.

The opposite case, where the ion gets transferred from a lower to the higher potential state, together with the spontaneously scattered photons defines the heating rate R_{heat}. After expanding eq. (3.75) to first order in kz we obtain the PGC dynamics [104]

$$\dot{E} = -R_{cool}(E - E_0) = -R_{cool}E + R_{heat}\hbar\omega_z, \tag{3.77}$$

$$R_{cool} = \frac{16}{9}\eta^2\Gamma s\xi\cos^2 2\phi, \tag{3.78}$$

$$R_{heat} = \frac{2}{9}\eta^2\Gamma s(8\xi^2\cos^4 2\phi + 3 - \cos^2 2\phi), \tag{3.79}$$

with $\xi = \frac{\Delta s}{3\omega_z}$. It can be seen that the cooling is most efficient for $\phi = 0$ and vanishes for $\phi = \pm\pi/4$. The mean phonon number $\bar{n}$ in the steady state is defined as [104]

$$\bar{n} = \frac{R_{heat}}{R_{cool}} - \frac{1}{2} = \xi + \frac{1}{4\xi} - \frac{1}{2} = \frac{\Delta s}{3\omega_z} + \frac{3\omega_z}{4\Delta s} - \frac{1}{2}, \tag{3.80}$$

which is minimized for $\xi = 1/2$ when the potential well depth equals the trap frequency $2\Delta s/3 = \omega_z$ and a minimum mean phonon number of $\bar{n}_{min} = 1/2$ is achievable, if the ion position is at $z = 0$ where $\phi = 0$. To make the scheme robust against misalignment of the ion position relative to the standing wave pattern, we detune one of the beams by the frequency δ to get a moving wave instead of a standing wave. If the cooling and heating rates are smaller than this detuning and $R_{heat} \leq R_{cool} < \delta < \omega_z$ holds, we can assume that the ion samples the phase of the moving wave uniformly and for the mean phonon number follows [104]

$$\bar{n} = \frac{3}{4}\xi + \frac{5}{8\xi} - \frac{1}{2}, \tag{3.81}$$

which is minimized for $\xi = \sqrt{5/6}$ resulting in an achievable minimum mean phonon number of $\bar{n}_{min} = \sqrt{15/8} - 1/2 \approx 0.87$ [104].

In our setup we use two counter-propagating beams, blue detuned by $\Delta = 206\,\text{MHz}$, detuned by $\delta = 200\,\text{kHz}$ relative to each other and with an angle of $\theta = 22.5^\circ$ between the cooling beams and the trap axis/magnetic field axis, as illustrated in fig. 4.1. Since the laser beams are not aligned along the magnetic field, the ions can also couple to π polarized light. The π polarized light does not change the potential energy of the ion, as depicted in fig. 3.10, and thus does not support cooling but only heating due to the scattered photons. Hence the ratio between cooling and heating rate changes and the minimum achievable mean phonon number $\bar{n}_{min}$ increases.

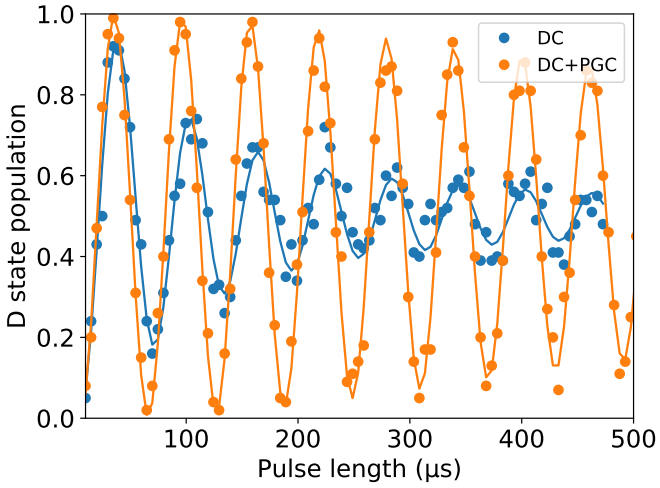

Figure 3.11: **Rabi oscillations after cooling.** Presented are Rabi oscillations after Doppler cooling (DC) in blue and Rabi oscillations after polarization gradient cooling (PGC) in orange. The estimated mean phonon numbers are $\bar{n}_{\mathrm{DC}} = 25(1)$ after DC and $\bar{n}_{\mathrm{PGC}} = 2.3(1)$ after PGC.

Experimentally, we utilize PGC right after DC. To estimate the mean phonon number we measure Rabi oscillations on the $|\mathrm{S}, m_j = -1/2\rangle \leftrightarrow |\mathrm{D}, m_j = -1/2\rangle$ transition and fit the results to an evolution with thermally distributed phonon numbers n, according to eq. (3.36).

We implement PGC for 0.5 ms on a single ion with an axial trapping frequency of $\omega_z \approx (2\pi)\,1215\,\mathrm{kHz}$ and Lamb-Dicke parameter for the 729 nm laser of $\eta = 0.0837(1)$. The measurements are illustrated in fig. 3.11 and we estimate a mean phonon number of $\bar{n}_{\mathrm{DC}} = 25(2)$ with the undisturbed Rabi frequency on the carrier $\Omega = (2\pi)\,16.84(6)\,\mathrm{kHz}$ after DC and $\bar{n}_{\mathrm{PGC}} = 2.3(1)$ with $\Omega = (2\pi)\,16.73(1)\,\mathrm{kHz}$ after PGC.

Another method to estimate the achievable $\bar{n}$ is to implement Rabi oscillations on the red and the blue motional sideband and fit the results again according to eq. (3.36). The measurements are depicted in fig. 3.12 and we estimate a mean phonon number of $\bar{n}_{\mathrm{PGC}} = 2.10(6)$ with a Rabi frequency on the carrier of $\Omega = (2\pi)\,17.0(5)\,\mathrm{kHz}$.

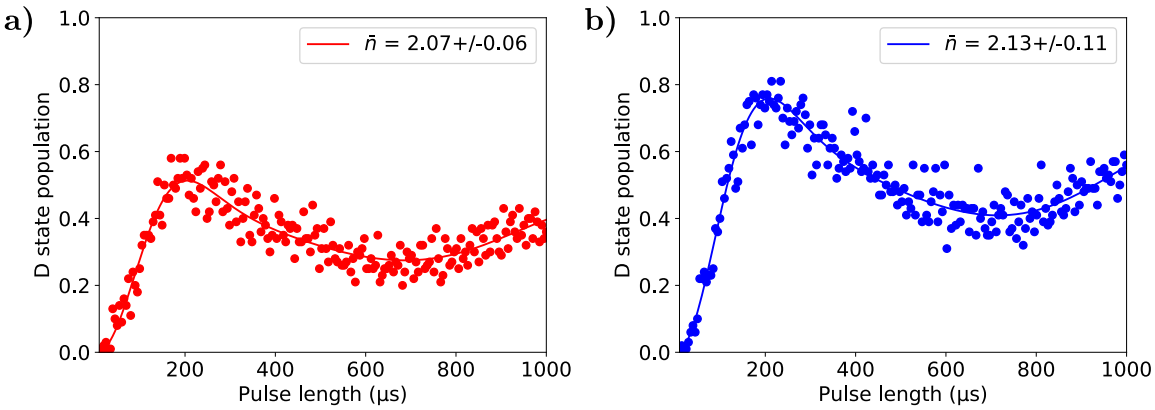

Figure 3.12: **Mean phonon number measurements after PGC.** Rabi oscillations on the **a)** red and **b)** blue sideband after applying PGC for 0.5 ms. We estimate a mean phonon number of $\bar{n}_{\mathrm{PGC}} = 2.10(6)$.

As can be seen in the results, all the estimated Rabi frequencies and mean phonon numbers agree well with each other. The theoretically achievable mean phonon number after DC is $\bar{n}_{\mathrm{DC}} \approx 6$ according to eq. (3.72). Our results of $\bar{n}_{\mathrm{DC}} = 25(1)$ reveal that DC was not optimized, which in turn shows that PGC is a technique to cool the ions below the Doppler limit to $\bar{n}_{\mathrm{PGC}} = 2.10(6)$ in a short time of 0.5 ms even without optimal DC.

3.6.3 *Resolved sideband cooling*

Resolved Sideband Cooling (RSC) works in the regime where the transition linewidth is small compared to the motional frequency $\Gamma < \omega_z$. By tuning the laser to the frequency $\Delta = -\omega_z$, a photon is absorbed on the red sideband transition and the phonon number is reduced by the subsequent emission of a photon on the carrier transition, as depicted in fig. 3.13 [105].

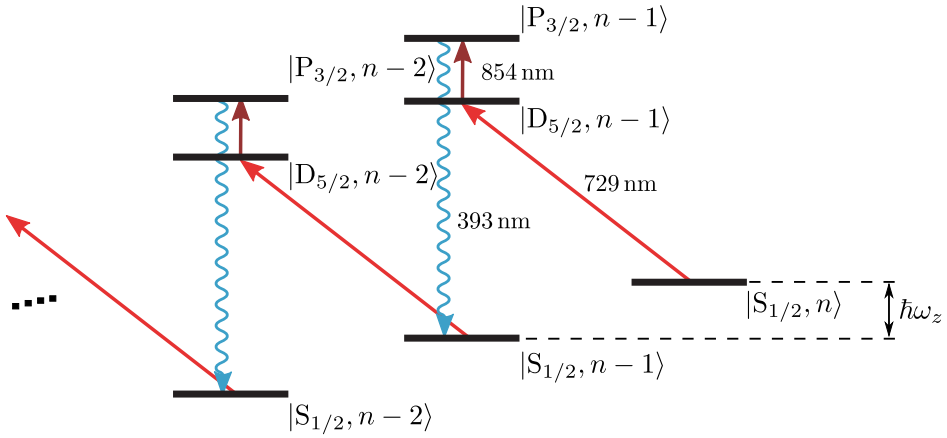

Figure 3.13: **Resolved sideband cooling.** A frequency selective 729 nm beam pumps the population from the $|S_{1/2}, n\rangle$ to the $|D_{5/2}, n-1\rangle$ level. At the same time the ion gets illuminated with a 854 nm laser beam, which effectively increases the transition rate to ground state $|S_{1/2}, n-1\rangle$ according to eq. (3.83) by pumping the ion to the short lived $|P_{3/2}, n-1\rangle$ state.

In the Lamb-Dicke regime ($\eta^2(2n+1) \ll 1$), the excited state predominantly decays on the carrier transition and by assuming a Lorentzian line shape of the excited state as in eq. (3.66) with detuning $\Delta_{\mathrm{eff}} = 0$ and Rabi frequency $\Omega_{\mathrm{RSB}} = \sqrt{n}\eta\Omega$ the cooling rate is given by [70]

$$R_{\mathrm{cool}} = \Gamma\rho_{\mathrm{ee}} = \Gamma\frac{n\eta^2\Omega^2}{\Gamma^2 + 2n\eta^2\Omega^2}. \tag{3.82}$$

Note that the cooling rate now depends on the phonon number n and vanishes for $n = 0$. The employed narrowband $4^2S_{1/2} \leftrightarrow 3^2D_{5/2}$ transition at a wavelength of 729 nm has a very small linewidth on the order of $\Gamma \approx (2\pi)136$ mHz, which severely limits the cooling rate to about 0.5 phonons/s. Therefore, the excited state lifetime is shortened by illuminating the ions with the 854 nm laser driving the $3^2D_{5/2} \leftrightarrow 4^2P_{3/2}$ transition yielding the effective linewidth [70]

$$\Gamma' = \frac{\Omega^2_{\mathrm{quench}}}{(\Gamma_{\mathrm{quench}} + \Gamma)^2 + 4\Delta^2_{\mathrm{quench}}}, \tag{3.83}$$

with a rabi frequency Ω_{quench} and a detuning Δ_{quench} determined by the 854 nm quench laser, and the linewidth Γ_{quench} of the $3^2D_{5/2} \leftrightarrow 4^2P_{3/2}$ transition.

The main heating mechanisms in this process are off-resonant excitation on the carrier transition followed by a spontaneous emission on the red sideband and off-resonant excitation on the blue sideband followed by a spontaneous emission on the carrier transition. The probability of exciting the carrier transition is $\Omega^2/(4\omega_z^2)$ for $\Omega \ll \Delta_{\text{eff}} = \omega_z$ and the excited state decays on the red sideband at rate $\eta'^2\Gamma'$ leading to a heating rate of $\eta'^2\Gamma'\Omega^2/(4\omega_z^2)$. Note that the spontaneous emission has a different Lamb-Dicke parameter η' because the photon can be scattered into any direction and the emitted photon has a different wavelength $\lambda' \sim 393\,\text{nm}$. The excitation probability on the blue sideband is $\eta^2\Omega^2/(4(2\omega_z)^2)$ followed by a decay on the carrier at rate Γ' causes a heating rate of $\Gamma'\eta^2\Omega^2/(4(2\omega_z)^2)$. Therefore the total heating rate can be described as [70]

$$R_{\text{heat}} = \frac{\Gamma'\Omega^2}{4\omega_z^2}\left(\eta'^2 + \frac{\eta^2}{4}\right). \tag{3.84}$$

Note that there exists an additional heating mechanism induced by the ion trap itself due to noise in the electric field. This heating effect can play a role close to the motional ground state and can be taking into account in eq. (3.84) to estimate the achievable ground state population in the experiment.

In equilibrium, the cooling rate equals the heating rate ($R_{\text{cool}} = R_{\text{heat}}$) and for small phonon numbers ($\Gamma'^2 > 2n\eta^2\Omega^2$) the cooling limit can be estimated by [70]

$$\bar{n}_{\text{min}} \approx \left(\frac{\Gamma'}{2\omega_z}\right)^2 \left[\left(\frac{\eta'}{\eta}\right)^2 + \frac{1}{4}\right]. \tag{3.85}$$

Note that the cooling rate in eq. (3.82) as well as the minimum phonon number in eq. (3.85) depend on the quenched linewidth Γ', hence there is a trade-off between cooling speed and cooling limit. In our experiment we can cool a single ion closed to the motional ground state with a mean phonon number $\bar{n}_{\text{SBC}} = 0.006(6)$, as illustrated in fig. 3.14.

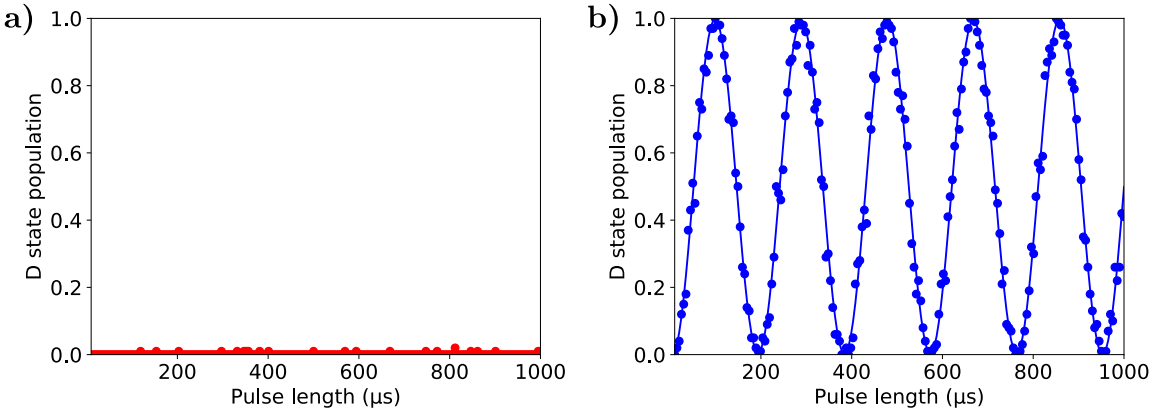

Figure 3.14: **Resolved sideband cooling results.** Rabi oscillations on the **a)** red and **b)** blue sideband after applying SBC. We estimate a mean phonon number of $\bar{n}_{\text{SBC}} = 0.006(6)$.

3.7 STATE PREPARATION AND READOUT

Prior to every quantum algorithm, it is important to prepare the ion in a specific state of the Zeeman manifold. Typically, we prepare the ions in the $|0\rangle = |S_{1/2}, m_j = -1/2\rangle$ state. To do so, we tune the frequency of the 729 nm laser to drive the $|S_{1/2}, m_j = +1/2\rangle \leftrightarrow |D_{5/2}, m_j = -3/2\rangle$ transition. At the same time the 854 nm laser is switched on to effectively shorten the lifetime of the excited state, as depicted in fig. 3.15 **a)**. From the excited $4^2P_{3/2}$ state the ion decays back into one of the ground states. Once the ion decays into the state $|S_{1/2}, m_j = -1/2\rangle$ it is trapped there and the state preparation is finished [86]. In analogy to pumping water from one bucket to another, this procedure is called optical pumping.

At the end of every sequence the state of ion is measured. The read out is done by shining a resonant laser beam with a wavelength of 397 nm onto the ions, as illustrated in fig. 3.15 **b)**. At the same time the 866 nm laser is switched on to prevent population trapping in the long lived $|D_{3/2}\rangle$ state. If the ion is projected into the $|S_{1/2}\rangle$ state, it scatters 397 nm photons which can be detected via the Photo Multiplier Tube (PMT) or the Charge-Coupled Device (CCD) camera. If the ion is projected into the $|D_{5/2}\rangle$ state, it does not interact with the 397 nm laser and therefore remains dark. Hence the $|S_{1/2}\rangle$ state is called the bright state and the $|D_{5/2}\rangle$ state is referred to be the dark state.

We repeat every sequence n times to measure the probability $P_1 = n(P_1)/n$ of finding the ion in the excited $|D_{5/2}\rangle$, where $n(P_1)$ is number of times the ion was measured in the dark state. The statistical uncertainty of this repetition is $\Delta P_1 = \sqrt{P_1(1-P_1)/n}$, which is called the quantum projection noise [106]. Typically, we implement $n = 100$ cycles of each experiment to keep the projection noise below 5 %.

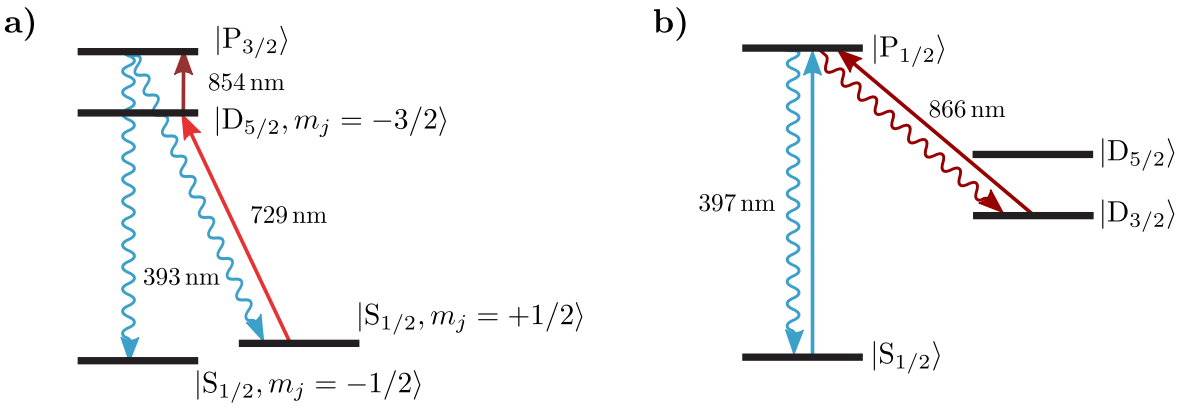

Figure 3.15: **State preparation and readout techniques. a)** Optical pumping using lasers with wavelengths of 729 nm and 854 nm to bring the population from the $|S_{1/2}, m_j = +1/2\rangle$ state to the $|S_{1/2}, m_j = -1/2\rangle$ ground state. **b)** The state of the ion is detected by illumination with the 397 nm laser. If the ion is projected into the $|S_{1/2}\rangle$ state, fluorescence light at 397 nm can be measured. If the ion is projected into the $|D_{5/2}\rangle$ state, it remains dark. The laser at 866 nm is used to prevent population trapping in the $|D_{3/2}\rangle$ state.

3.8 EXPERIMENTAL IMPERFECTIONS

Up to now, the tools used in ion-trap quantum computers were described in an idealized fashion, but real-world devices are prone to errors. In principle, every experimental parameter can be controlled to finite precision, that will lead to imperfect gate operations. In Ref. [80] a detailed overview about issues related to trapped ion experiments is given.

In this section we discuss only a few important errors to provide an insight into the main limiting factors of our experiment. We group them into three different sections, in analogy to Ref. [80]. First, we outline errors that affect the motional state of the ions in section 3.8.1. Second, errors affecting the internal electronic states are discussed in section 3.8.2. Third, we consider operational errors induced by the laser in section 3.8.3.

3.8.1 *Errors affecting the motional state*

High-fidelity quantum operations, as described in section 3.3.1, require that the ions are close to the motional ground state $\bar{n} \approx 0$. Otherwise, the Rabi frequencies fluctuate, which lead to errors in quantum operations, see section 3.8.3. This can be easily observed in fig. 3.11, where the interference of different Rabi frequencies leads to the decay of Rabi flops. In addition, the entangling MS operation utilizes the motion to mediate excitations between ions, as introduced in section 3.3.1.3. Hence, high fidelity entangling operations require low motional errors, as explained in [84].

In ion trap experiments, there exist many sources of noise that can affect the motional state of the ions. Here, we discuss two effects, motional heating and fluctuating trapping frequencies, that limit the coherence of the motional state in our experiment. Many other mechanims that can be detrimental in principle, but typically do not limit the motional coherence in our experiment, are outlined in Ref [80].

First we discuss motional heating, that is a limiting factor in many ion-trap experiments. Motional heating is typically characterize by the heating rate $\dot{\bar{n}}$, that describes the number of phononic excitations per unit of time. A major source inducing motion heating is electric field noise that interacts with the ions. The effects of electric field noise in ion traps are discussed in detail in Refs. [107–109]. In our trap, the heating rate is about $\dot{\bar{n}} \sim 2\,\text{phonon/s}$ at a trapping frequency of $\omega_z = (2\pi)\,1\,\text{MHz}$. This limits the motional coherence time to $T_\text{m} \leq 0.5\,\text{s}$. According to Ref. [84], the measured heating results in an MS gate infidelity of $\epsilon_\text{MS} \sim 2 \cdot 10^{-4}$. Importantly, the heating rate for the COM mode of motion increases linearly with the ion number N [110], which can severely limit the motional coherence time for long ion strings.

The MS gate is implemented by tuning two laser beams close to the red and blue sideband of the ion's motion, as described in section 3.3.1.3. The detuning between the motional frequency and the laser frequency defines the ideal MS gate time. Therefore, if the motional frequency fluctuates, also the ideal MS gate time fluctuates. The motional frequencies ω_x, ω_y and ω_z in our experiment are defined in eqs. (3.8) and (3.9). For small fluctuations of the parameters, we can describe the fractional stability of the motional frequencies as [80]

$$\frac{\delta\omega_{x,y}}{\omega_{x,y}} = \frac{\delta V_\text{RF}}{V_\text{RF}} + \frac{\delta\Omega_\text{RF}}{\Omega_\text{RF}} + \frac{2\delta r_0}{r_0}, \tag{3.86}$$

$$\frac{\delta\omega_z}{\omega_z} = \frac{\delta U_\text{DC}}{2U_\text{DC}} + \frac{\delta z_0}{z_0}, \tag{3.87}$$

where V_{RF} is the RF voltage, Ω_{RF} the RF frequency, r_0 the distance from the ion to the RF electrode, U_{DC} the end-cap voltage and z_0 the distance from the ion to the end-cap. If we require the motional coherence time to be better than the coherence time limited by motional heating of $T_m \geq 0.5\,s$, the fractional stability of the axial frequency must be better than $\frac{\delta\omega_z}{\omega_z} \leq 2 \cdot 10^{-6}$ for $\omega_z = (2\pi)\,1\,MHz$. Assuming that the distance of the ion to the end-cap does not fluctuate $\frac{\delta z_0}{z_0} \approx 0$, the fractional stability of the voltage must be $\frac{\delta U_{DC}}{U_{DC}} \leq 4 \cdot 10^{-6}$. Hence, the voltage noise must be on the mV level for an end-cap voltage of $U_{DC} = 1000\,V$, which is already quite demanding and special care must be taken in the electronic voltage supply[2] selection and the filtering.

3.8.2 *Errors affecting the internal state*

Ideally, quantum information is encoded in a two level system. In such a two level system we typically use two figures of merit, the longitudinal and transversal relaxation time T_1 and T_2, to characterize the coherence properties [9, 111]. Fundamentally both coherence times are limited by the lifetime of the excited state. For $^{40}Ca^+$, the coherence time is limited by the lifetime of the $3^2D_{5/2}$ to $T_1 \sim 1\,s$ and to $T_2 \leq 2T_1 \sim 2\,s$, see section 3.2.

Starting from eq. (3.17) and changing to the interaction picture, noise affecting the internal electronic state of the ion can be described as

$$H' = \frac{1}{2}\sigma_z\beta(t), \tag{3.88}$$

where we introduce a small time-dependent perturbation $\beta(t)$. This perturbation can either come from magnetic field fluctuations $\beta(t) = \mu\Delta B(t)$ that shift the transition frequency due to the Zeeman effect (see appendix A) or from frequency fluctuations $\beta(t) = \hbar\Delta\omega_L(t)$ of the interacting laser.

In sections 4.2 and 4.3 we study the effects of laser frequency and magnetic field noise on the coherence time T_2 using Ramsey spectroscopy (see section 3.5).

3.8.3 *Operational errors*

The imperfect implementation of quantum gates or quantum operations leads to operational errors. Two major sources of noise are fluctuations in the intensity I and phase ϕ of the applied laser pulses. Recalling eq. (3.38), perfect resonant qubit rotations are described as

$$R(\theta,\phi) = \cos(\frac{\theta}{2})\mathbb{I} + i\sin(\frac{\theta}{2})\left(\cos\phi\sigma_x + \sin\phi\sigma_y\right). \tag{3.89}$$

According to eq. (3.27) the time dependent pulse area and the phase can be estimated as

$$\theta_{n,n'}(t) = \int_{t'=0}^{t} \Omega_{n,n'}(t')\mathrm{d}t', \tag{3.90}$$

$$\phi(t) = \int_{t'=0}^{t} \delta(t')\mathrm{d}t' + \phi'(t), \tag{3.91}$$

where the Rabi frequency depends on the laser intensity $\Omega_{n,n'}(t) \propto \sqrt{I(t)}$ and the overall phase depends on the frequency detuning $\delta(t)$ and the laser phase $\phi'(t)$. Hence, if $I(t)$, $\delta(t)$ and $\phi'(t)$ are known, noisy rotations $R(\theta(t),\phi(t))$ can be simulated. Note, that eq. (3.90)

[2] ISEG EBS Co 30 voltage supply specifications: Ripple and noise $< 20\,mV$ peak-to-peak.

similarly holds for AC-Stark pulses $R_z(\theta)$, where the Rabi frequency scales as $\Omega_{\mathrm{AC}}(t) \propto I(t)$. Therefore, AC-Stark pulses are quadratically more sensitive to intensity noise compared to resonant laser pulses.

For small fluctuations in the control parameters, the fractional error in the rotation angle and the rotation phase can be estimated as

$$\frac{\Delta\theta}{\theta} = \frac{\Delta I}{2I} + \frac{\Delta t}{t}, \tag{3.92}$$

$$\frac{\Delta\phi}{\phi} = \frac{\Delta\delta}{\delta} + \frac{\Delta t}{t} + \frac{\Delta\phi'}{\phi'}, \tag{3.93}$$

where $\frac{\Delta I}{I}, \frac{\Delta t}{t}, \frac{\Delta\delta}{\delta}, \frac{\Delta\phi'}{\phi'} \ll 1$ describe relative intensity, timing, frequency and phase fluctuations.

Estimating the fidelity of a quantum state after the implementation of a sequence of noisy gates is not trivial in general. Solutions for this demanding task are discussed in detail in chapters 5 and 6. But we can make a crude estimate for the resulting fidelity after a sequence of M pulses with the following assumptions. If the resulting state fidelity is high and if the rotation errors are small and distributed approximately random, we can estimate the fidelity as [80]

$$F \approx 1 - M\left(F_\theta\left(\frac{\Delta\theta}{\theta}\right)^2 + F_\phi\left(\frac{\Delta\phi}{\phi}\right)^2 + F_{\theta\phi}\frac{\Delta\theta}{\theta}\frac{\Delta\phi}{\phi}\right), \tag{3.94}$$

where $\frac{\Delta\theta}{\theta}, \frac{\Delta\phi}{\phi} \ll \pi$ and the coefficients $F_\theta, F_\phi, F_{\theta\phi} \lesssim 1$.

As an example we assume that intensity fluctuations on the order of $\frac{\Delta\theta}{\theta} \sim \frac{\Delta I}{I} \sim 10^{-4}$ are the limiting factor for the fidelity. According to eq. (3.94), we could then implement $M_{\max} \simeq \frac{\theta}{\Delta\theta} \sim 10^8$ pulses before the fidelity drops significantly. Note, in the worst case the errors add coherently and the fidelity reduces linearly with the pulse errors, which reduces the maximum number of pulses to $M_{\max} \sim 10^4$.

Importantly, the laser power and hence the intensity fluctuations are fundamentally limited by the photon shot noise. Following Ref. [80], the intensity fluctuations of an intensity stabilized laser pulse can be estimated to be $\frac{\Delta I}{I} \geq \sqrt{\hbar\omega_{\mathrm{L}}/P\tau\eta\epsilon(1-\epsilon)}$, where a fraction ϵ of the light is sent onto a detector with an efficiency of η, and the laser pulse has length τ and power P at a frequency of ω_{L}. Using typcial experimental laser puls parameters of $\epsilon = 0.5$, $\eta = 0.5$, $\tau = 1\,\mu$s, $P = 1\,$mW and $\omega_{\mathrm{L}} = 411\,$THz we deduce a fractional intensity error of $\frac{\Delta I}{I} \geq 2 \cdot 10^{-5}$.

For errors in gates other than the aforementioned resonant pulses, the error budget can be more complex, as e.g. for the MS gate discussed in Ref. [84].

Another important kind of error when working with strings of multiple ions is crosstalk. As explained in chapter 4 we use a tightly focused laser beam to address individual ions. Since the laser beam for single ion addressing can be described by a Gaussian laser beam, there is always some amount of intensity on the neighbouring ions. In our experiment the crosstalk is typically around $2-5\,\%$ of the resonant Rabi frequency. A more detailed discussion about the crosstalk in our setup and about strategies to cancel it are presented in Ref. [89].

4

EXPERIMENTAL SETUP

Der Tag hat 24 Stunden,
und wenn das nicht reicht,
nehmen wir die Nacht noch dazu.

— Rainer Blatt

As one could guess from the citation above, the major part of PhD students life consists of working on the experimental setup. The basic principles of trapped ion experiments have been studied extensively in previous works [70, 112]. The better part of the specific experimental setup is already discussed in a publication [86] and various Master and PhD theses [68, 76, 77, 89, 113–115]. Thus the following chapter gives a brief overview about the changes implemented during my PhD studies.

First, the details of the vacuum vessel are presented in section 4.1. Afterwards, the laser systems utilized to manipulate the ions are described in section 4.2. Finally, the setup used to generate the bias magnetic field is outlined in section 4.3.

4.1 VACUUM VESSEL

The heart of our experimental setup consists of a steel chamber, enclosing the ion trap in ultra-high vacuum. The schematic of the vacuum vessel including the viewports supporting optical access is depicted in fig. 4.1. The flanges supporting the viewports are labeled by their orientation (north - N, east - E, south - S, west - W).

An Ion Getter Pump (IGP), connected close to the flange N, retains the ultra-high vacuum with a pressure of $\sim 5 \cdot 10^{-11}$ mbar[1], measured with the Pressure Gauge (PG) placed opposite to the pump. On the same side as the PG a Titanium Sublimation Pump (TSP) is installed.

On flanges SW and NE rings of permanent magnets are mounted, generating the magnetic field $\vec{B}_\sigma$. Another pair of ring magnets is placed on the flanges SE and NW and produces the magnetic field $\vec{B}_\mathrm{D}$. Together these two pairs of ring magnets generate the bias magnetic field $\vec{B} = \vec{B}_\sigma + \vec{B}_\mathrm{D}$ that is rotated 57.5° relative to the trap axis. The design considerations for the permanent magnet setup are discussed in section 4.3.

Through the same viewports SW and NET two counter propagating PGC laser beams are coupled. Both laser beams have a beam diameter of $d_\mathrm{PGC} \sim 120\,\mu$m, where one laser beam is horizontally (H) and the other is vertically (V) polarized. The repumping and DC beams are send through viewports SE and NW with a diameter of $d_\mathrm{DC} \sim 80\,\mu$m in the center.

The flange W embodies an objective[2] with an NA $\sim$ 0.2 and a working distance of 65 mm. This objective images the fluorescence light of the ions onto the Photo Multiplier Tube (PMT) [116]. The flange E contains an objective[3] with an NA = 0.29 and a working distance of 66 mm. This objective maps the ions onto a CCD camera.

[1] Agilent XGS-600 Vacuum Gauge Controller
[2] Nikon MNH-23150 ED Plan 1.5x
[3] Silloptics S6ASS2241

Through this objective also a laser beam with a resulting diameter $d_A \sim 3\,\mu$m [89] and a wavelength of 729 nm is sent, which is used to address only a single ion. Thus we refer to this beam as the *addressed* beam. An elliptically shaped laser beam with dimensions of $d_{G,y} \sim 100\,\mu$m by $d_{G,x} \sim 300\,\mu$m and a wavelength of 729 nm illuminates all the ions through viewport S. Hence, we call this beam the *global* beam.

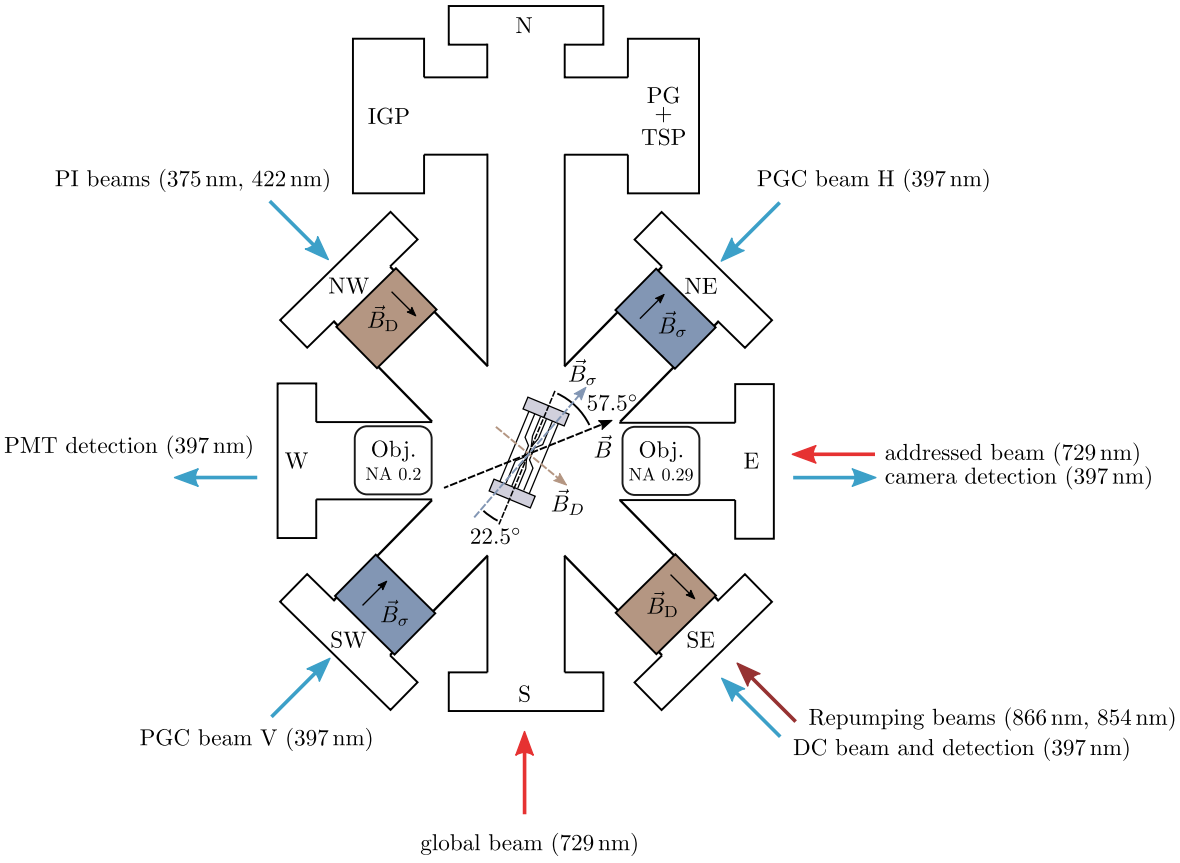

Figure 4.1: **Vacuum vessel setup.** Schematic view of the horizontal plane of the vacuum chamber. Around the center 8 viewports are situated, labelled in accordance of their direction (north - N, east - E, south - S, west - W). Close the flange N an Ion Getter Pump (IGP), a Titanium Sublimation Pump (TSP) and a Pressure Gauge (PG) are connected. In the center of the chamber the ion trap is located at an angle of 22.5° with respect to the N-S axis. Two pairs of ring magnets (B_σ, B_D) generate a magnetic field rotated 57.5° to the trap axis $\vec{B} = \vec{B}_\sigma + \vec{B}_D$. Inside the flanges W and E high NA objectives (Obj.) are mounted.

4.2 LASERS

In this section the laser systems used to manipulate $^{40}Ca^{+}$ ions in our experiment are briefly explained. Details of the optical transitions in $^{40}Ca^{+}$ are presented in section 3.2 and appendix B.

4.2.1 *Dipole lasers with 397 nm, 866 nm and 854 nm*

The lasers driving dipole transitions are commercial systems from Toptica. To generate light at 397 nm we use a frequency doubled laser system[4]. There, a laser diode emits 794 nm light, which is sent through a Tapered Amplifier (TA) and a frequency doubling cavity system. The TA has an output power of $P_{794} \sim 700\,\mathrm{mW}$ at 794 nm resulting in a output power of $P_{397} \sim 300\,\mathrm{mW}$ at 397 nm. To reduce the laser linewidth and to achieve long term stability of the center frequency, the fundamental laser at 794 nm is stabilized to an optical cavity via the Pound-Drever-Hall (PDH) laser locking technique [117, 118]. The cavity has a finesse of $\mathcal{F} \sim 300$ [119] and is hence called the Medium Finesse Cavity (MFC).

The 866 nm laser is generated with a combined system[5] comprising a laser diode and a TA. The light emitted from the laser diode is amplified by the TA and stabilized to the MFC. The output power is $P_{866} \sim 100\,\mathrm{mW}$ at 866 nm.

The 854 nm laser is produced with a laser diode system[6] and a separate TA system[7]. The output power of the system is $P_{854} \sim 50\,\mathrm{mW}$ at 854 nm and the laser is also stabilized to the MFC.

4.2.2 *Quadrupole laser with 729 nm*

As discussed in section 3.2, we encode quantum information in the Zeeman manifold of the $4^2S_{1/2} \leftrightarrow 3^2D_{5/2}$ quadrupole transition with a wavelength around 729 nm. See appendix B for more precise transition wavelengths. In section 3.3 it was outlined how a narrowband laser can be utilized to cool the ions to the motional ground state as well as to implement quantum operations for quantum computation.

In quantum computation, a commonly used figure of merit is the coherence time T_2 of the qubit. A simple argument is, that the longer the coherence time is, the more quantum gates can be implemented before a phase error occurs. If we neglect magnetic field fluctuations, the coherence time is either limited by the linewidth $\Delta\nu_L$ of the laser or by the natural linewidth $\Delta\nu$ of the qubit transition, which can be expressed as $T_2 \leq 1/(\pi\Delta\nu_L) \leq 1/(\pi\Delta\nu)$ (see section 3.8). To ensure that the laser linewidth is not limiting the coherence time of the qubit, the laser linewidth has be smaller than the natural linewidth $\Delta\nu_L \leq 136\,\mathrm{mHz}$ [B] of the 729 nm quadrupole transition in $^{40}Ca^{+}$.

In addition, the frequency spectrum of the laser should be as clean as possible. If for example, the laser is coupled to a certain carrier transition, any spurious frequency component, like e.g. 50 Hz components and harmonics, kHz-noise induced by vibrations or servo bumps in the kHz to MHz regime, can couple to motional sidebands or to other carrier transitions and thereby corrupt the desired quantum operation.

[4] Toptica Tapered Amplifier - Second Harmonic Generation (TA-SHG)
[5] Toptica TAPro
[6] Toptica DL100
[7] Toptica BoosTA

In the following we discuss how our 729 nm laser system is set up and we highlight the elements which are important to meet the aforementioned criteria.

We use a Titanium:Sapphire (Ti:Sa) laser system[8] which has a high output power of $P_{729} \sim 4\,\mathrm{W}$ at 729 nm and a narrow intrinsic linewidth of $\Delta\nu_{\mathrm{L,int}} \sim 120\,\mathrm{kHz}$ [89]. We stabilize the frequency of the laser to a cavity via the PDH locking technique [117, 118]. This cavity has a finesse of $\mathcal{F} = 479500(1600)$ [76] and is hence called the High Finesse Cavity (HFC).

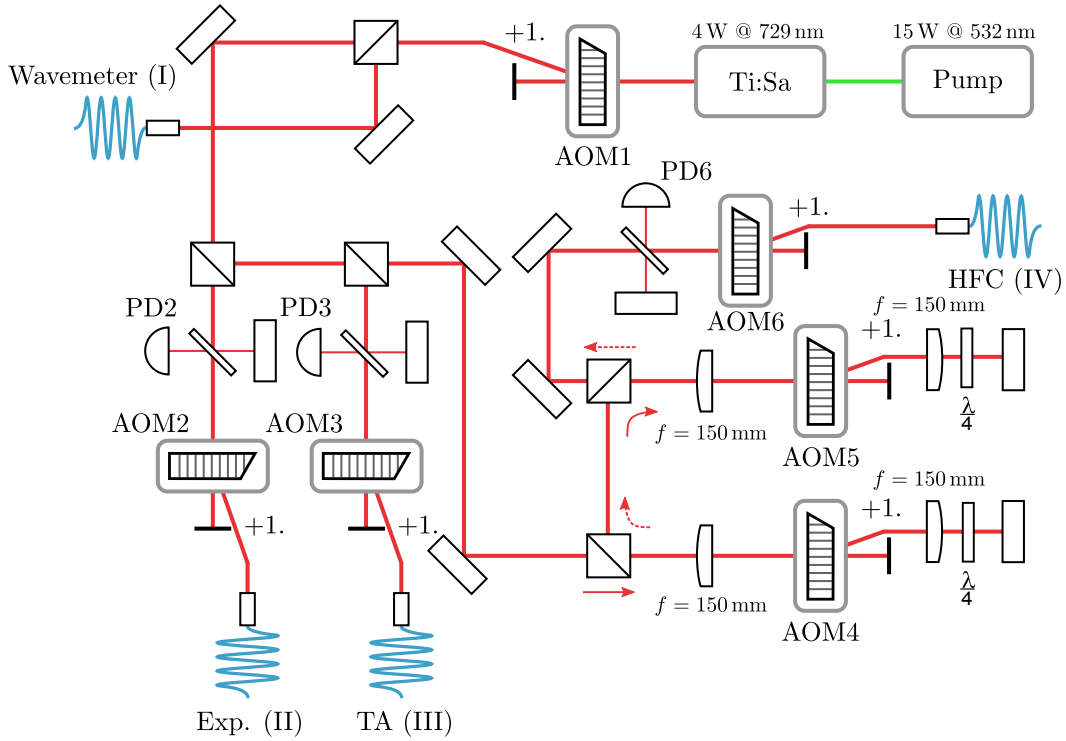

Figure 4.2: **Optical setup of the 729 nm laser system.** The 729 nm light is generated inside the Ti:Sa and stabilized via a noise-eater (AOM1). Then the light is split into four parts, to the wavemeter (I), to the experiment (II), to a distribution TA (III) and to the HFC (IV). Fiber noise cancelling setups are installed in paths (II-IV) containing Photodiodes (PD4-PD6) and Acousto-Optic Modulators (AOM4-AOM6).

Laser setup. A schematic of the 729 nm laser source and the distribution optics is presented in fig. 4.2. The Ti:Sa laser[8] is pumped by a laser[9] with a wavelength at 532 nm. Unfortunately both pump lasers we used broke after a roughly a year of operation and had to be repaired. If the pump laser brakes, it has to be replaced. Due to the compact design of the Ti:Sa laser[8] the exchange of the pump laser is rather simple and can be done within half a day. With a pump power of $P_{532} \sim 15\,\mathrm{W}$ at 532 nm an output power of the Ti:Sa laser of $P_{729} \sim 4\,\mathrm{W}$ at 729 nm can be achieved. Due to contamination of the surface of the laser optics the output power decreases over time. Hence the laser power at the moment is $P_{729} \sim 1.5\,\mathrm{W}$ at 729 nm. The first element in the beam path is an Acousto-Optic Modulator (AOM1, +1. order at $\sim 80\,\mathrm{MHz}$) used as an frequency actuator for the PDH lock, providing a closed-loop bandwidth of $\omega_{\mathrm{AOM}} \sim 300\,\mathrm{kHz}$. After this AOM the light is distributed to four locations (I-IV), which are described in the following.

[8] M² SolsTiS
[9] Lighthouse Sprout or a Coherent Verdi V18

First, a small part ($P_{WM} \sim 1\,mW$) of the light is send to the wavemeter[10] (I). The rest of the light is distributed to our experiment (II) ($P_{EXP} \sim 1\,W$), a TA (III) ($P_{TA} \sim 300\,mW$) and the HFC (IV) ($P_{HFC} \sim 100\,mW$). As depicted in fig. 4.2 we use fibers to send the light to the respective locations.

Since the optical path length of a fiber changes over time, the linewidth of the laser after the fiber is broadened [120]. The induced frequency noise can be removed by a technique called Fiber Noise Cancellation (FNC) [76, 120]. The first element of a FNC setup is a beam sampler, that picks off 4 % of the incident light which is then retro-reflected by a mirror and detected by a Photodiode (PD2, PD3 and PD6). Next, the beam passes an AOM (AOM2, AOM3 and AOM6, +1. order at 80 MHz) and a fiber. At the end of the fiber again 4 % of the light is reflected and passes the fiber and the AOM a second time. The back propagating light is reflected by the beam sampler and overlapped with the incident laser and a beat at 160 MHz is measured by a Photodiode (PD2, PD3 and PD6). The beat signal is used to generate the error signal for the FNC.

In the path to the HFC (IV) there are two additional double pass AOMs (AOM2 and AOM2, +1. order at $\sim 318.264\,MHz$) before the FNC setup, to compensate the difference frequency between the ion's transitions frequency and the closest cavity mode. The double pass AOMs are placed inside a 1:1 telescope containing two lenses with a focal length of $f = 150\,mm$, to prevent beam direction changes due to frequency changes.

Inside the Ti:Sa laser a Ti:Sa crystal is placed in an optical cavity. The frequency of the emitted laser thereby depends on the cavity length. Mechanical vibrations can change the cavity length, which broadens the laser linewidth. To minimize acoustic noise that can excite mechanical vibrations, we enclose the complete laser setup inside a wooden box. On the outside of the wooden box we mount heavy acoustic walls to lower the eigenfrequency of the box and thus improve the acoustic attenuation. To decouple the setup from vibrations originating from the floor we fill the box with $\sim 500\,kg$ of sand. The breadboard holding the laser system is placed on an active vibration isolation system[11] on the sand.

The temperature of the crystal inside the Ti:Sa laser and the base plate of the pump laser is stabilized by water cooling systems. As we found out, also the cooling systems induce vibrations. To reduce acoustic noise that is transported from the water pump to the laser, we install new water coolers[12] with a better pump. Since acoustic waves in water decay with the distance, we extended the cooling pipes that connect the chillers to the lasers by about 10 m. Turbulent water flow in the cooling circuit can also induce vibrations. Therefore we install flow controllers to reduce the water flow to a minimum ($1.5\,l/min \rightarrow 0.4\,l/min$). Together these upgrades reduce the acoustic noise on the laser significantly, where the measurements showing the improvements on the laser characteristics are presented in appendix C.

High finesse cavity setup. The optical setup is depicted in fig. 4.3. The first element is an Optical Isolator (OI) that prevents back reflections to the laser source and minimizes etalon effects along the optical pathway, which can introduce residual amplitude modulation [121]. Next, a Polarizing Beam Splitter (PBS) is used to send a part of the light onto a Photodiode (PD)[13], where the signal is utilized to stabilize the laser intensity. Then the beam passes a Glan-Thompson Polarizer (GTP)[14] for polarization cleanup. Then an EOM[15] is used to

[10] HighFinesse WS-7
[11] Accurion Halcyonics Vario 60-360
[12] SMC HECR002-A5
[13] Thorlabs PDA36A
[14] Polarization extinction ratio $\sim 10^5 : 1$
[15] Linos PM 25

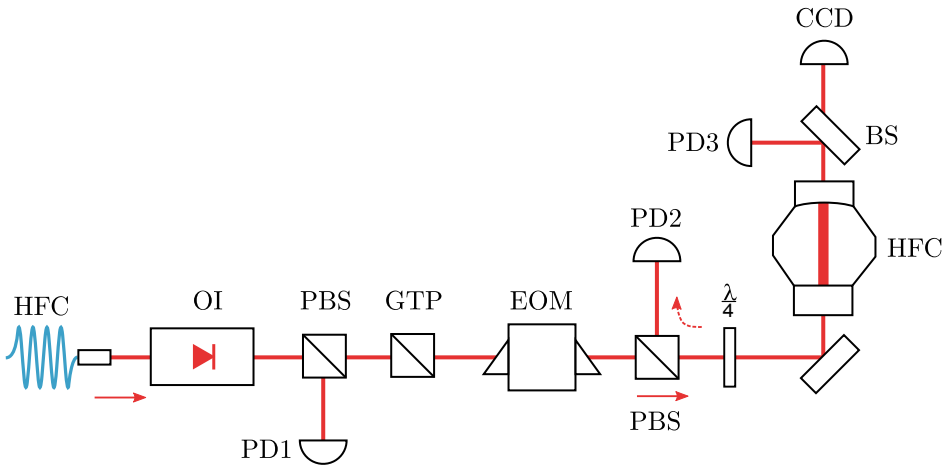

Figure 4.3: **Optical setup of the high finesse cavity.** The light comes from the laser via an optical fiber and is send through an Optical Isolator (OI), a Polarizing Beam Splitter (PBS), a Glan-Thompson Polarizer (GTP), an EOM, a PBS and a $\lambda/4$ waveplate onto the HFC. The transmitted light after the cavity is divided by a 50:50 Beam Splitter (BS) and detected by a photodiode (PD3) and a camera (CCD). The first photodiode (PD1) is used to detect the reflection of the first PBS. The second photodiode (PD2) measures the reflected light from the cavity.

generate sidebands in the frequency spectrum of the laser, which are needed for the PDH lock. After the EOM the laser is send through a PBS and a $\lambda/4$ wave plate in order to guide the reflected light of the cavity onto a PD[16].

A problem that might occur in this setup is, that if the polarization of the laser beam is not perfectly aligned with the crystal axis inside the EOM, the polarization of the laser beam is modulated by the EOM. The polarization modulation is converted into amplitude modulation by the subsequent PBS, so called Residual Amplitude Modulation (RAM) [121]. The GTP in front of the EOM ensures a linear polarization and thus minimizes the modulation of the laser polarization.

Finally the laser is coupled to the HFC. The transmitted light of the cavity is divided with a 50:50 Beam Splitter (BS) and detected by a photodiode (PD3)[17] and a CCD camera. The CCD and the PD are there for adjustment and monitoring purposes.

The HFC is used as a reference to stabilize the frequency of the 729 nm laser, where the laser frequency is locked to the frequency of a cavity mode. The fractional frequency stability of a cavity mode depends on the fractional stability of the optical cavity length as $\Delta\nu/\nu = \Delta L/L$ [97]. The optical length L of the cavity depends on the distance d of the mirrors and on the refractive index n of the material in between the mirrors as $L = d \cdot n$.

Pressure fluctuations induce refractive index fluctuations Δn, which in turn result in cavity length fluctuations ΔL. To minimize refractive index fluctuations the cavity is mounted inside a vacuum chamber[18]. Since vacuum is the best thermal insulator, also temperature drifts can be made smaller in a vacuum setup, compared to a setup at ambient pressure.

Mechanical vibrations can induce noise in the mirror distance Δd, which result in noise optical path length ΔL. To reduce acoustic noise affecting the cavity mirrors, the HFC setup is enclosed in a wooden box filled with sand. The optical breadboard is placed on a active

[16] Home-built PD with $\sim$ 250 MHz bandwidth
[17] Thorlabs PDA36A
[18] Pressure $\sim 5 \cdot 10^{-9}$ mBar.

vibration isolation system[19]. Special care was taken in the design of the HFC holder inside the vacuum chamber to suppress the acoustic noise that is transferred onto the mirrors. The details of the hole HFC apparatus can be found in previous theses [76, 122].

The cavity has a design length of $L = 77.5\,\mathrm{mm}$ and a measured free spectral range FSR= $1.934(2)\,\mathrm{GHz}$ [76]. The finesse is $\mathcal{F} = 479500(1600)$ which results in cavity linewidth of $\Delta\nu = 4.03(2)\,\mathrm{kHz}$ [76]. As explained in appendix D, the cavity length changes quadratically with the temperature, which means that there is a zero expansion temperature $T_0 = 8.38(3)\,^\circ\mathrm{C}$, where the cavity length does not change with temperature to first order. Due to material aging [123], which changes the distance between the mirrors, the cavity resonance changes linearly over time with a rate of $19.426\,\mathrm{mHz/s}$.

We estimate a coherence time of magnetic field insensitive $|m_S = -1/2\rangle \leftrightarrow |m_D = -1/2\rangle$ transition (1) of $T_2^{(1)} = 0.21(4)\,\mathrm{s}$ via Ramsey spectroscopy, as depicted in fig. 4.4. Assuming that magnetic field fluctuations are not limiting the performance, the measured coherence time results according to eq. (3.56) in an estimated FWHM linewidth of the laser of $\Delta\nu_L = 1/(\pi T_2) = 1.5(3)\,\mathrm{Hz}$, which is roughly a factor of 10 larger than the natural linewidth of the transition $\Delta\nu \sim 136\,\mathrm{mHz}$ [B]. The estimated linewidth corresponds to a fractional frequency stability of $\Delta\nu/\nu \approx 3.4 \cdot 10^{-15}$. With next generation cavities, a laser linewidth on the order of tens of mHz ($\sim 10^{-16}$ fractional stability) can be realized [124–127].

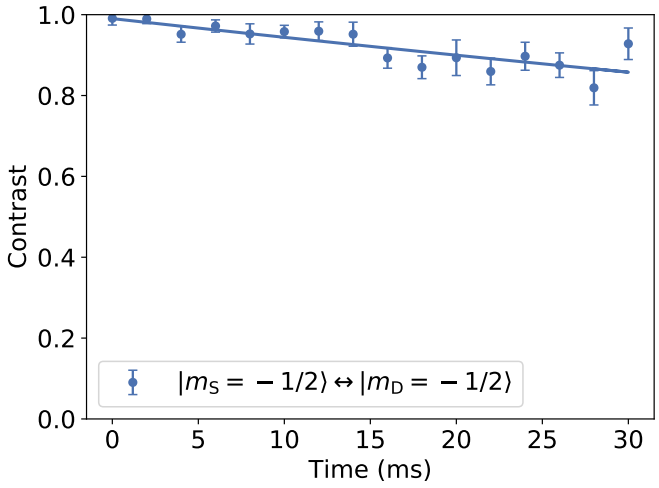

Figure 4.4: **Stability of the laser frequency.** Short-term characterization via Ramsey spectroscopy with an estimated coherence time $T_2^{(1)} = 209(38)\,\mathrm{ms}$.

Locking setup. The electronic setup used for PDH-locking is depicted in fig. 4.5. A typical electronic control loop consists of three parts (I-III). (I) a setup that measures and generates the error signal. (II) a Proportional–Integral–Derivative (PID) controller that calculates the feedback signal from the error signal. (III) an actuator that feeds back corrections into the system. The generation of the error signal is discussed in the next paragraph. As PID controller we use commercial devices[20]. In total we have three actuators available. The Ti:Sa laser offers two actuators, a slow piezo (SP) and fast piezo (FP), with a closed-loop bandwidth of $\omega_{SP} \sim 50\,\mathrm{Hz}$ and $\omega_{FP} \sim 30\,\mathrm{kHz}$ respectively. These piezos are mounted on mirrors inside the laser, which can be used to change the cavity length and hence the laser

[19] Accurion Halcyonics
[20] Toptica FALC110

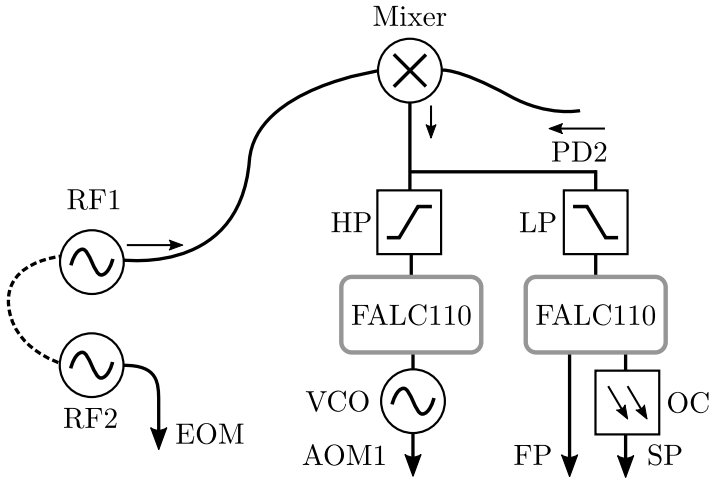

Figure 4.5: **Electronic setup of the 729 nm laser system.** The PDH error signal is generated by mixing the signals from the radio-frequency generator (RF1) and the photodiode (PD2) detecting the cavity reflection. The error signal is split and send into a high-bandwidth and a low bandwidth feedback branch. The high-bandwidth branch contains a High-Pass (HP) filter with cutoff frequency $f_C = 1\,\text{kHz}$, a Toptica FALC110 servo and a Voltage-Controlled Oscillator (VCO), which drives the noise-eater (AOM1). The low-bandwidth branch consists of a Low-Pass (LP) filter with cutoff frequency $f_C = 3\,\text{kHz}$ and a Toptica FALC110 servo, where the main output is connected to the fast piezo (FP) and the output of the unlimited integrator is connected to the slow piezo (SP) via optocoupler (OC).

frequency. Since we were not able to lock the laser to the HFC with the piezos only, we had to install an additional actuator, the first AOM1 in the beam path. As mentioned before, the AOM provides a closed-loop bandwidth of $\omega_{\text{AOM}} \sim 300\,\text{kHz}$.

The RF modulation signal for the PDH stabilization is produced by an RF generator[21] (RF2). We use a second, phase-locked, RF generator[21] (RF1) to tune the phase of the PDH error signal. The reflection signal from the HFC (measured with PD2) is mixed with the signal from RF1 by an RF mixer[22]. The output of the mixer is the PDH error signal. The error signal is split up by a Low-Pass (LP) filter ($f_C = 7\,\text{kHz}$) and a High-Pass (HP) filter ($f_C = 1\,\text{kHz}$) into a slow and a high bandwidth feedback branch.

The low bandwidth (DC…7 kHz) branch comprises a PID controller[23], which is set up to generate high gain at low frequencies (XSLI=1, FLI=8+9). The unlimited integrator output is connected to the slow piezo of the laser, whereas the main output is connected to fast piezo of the laser. Note that we use a home-build optocoupler for the connection to the slow piezo, because otherwise we observed large 50 Hz noise components on the laser frequency.

The high bandwidth (1…300 kHz) branch consists of a PID controller[24] and a Voltage-Controlled Oscillator (VCO)[25], where the VCO converts the DC output signal of the PID controller into an RF signal, which is connected to the actuator (the first AOM1 in the laser setup). In the fast branch only the proportional (P) part of the regulator is used.

[21] SRS DS345 at 12.562 MHz
[22] Mini-Circuits ZAD-3+ Mixer
[23] Toptica FALC110
[24] Toptica FALC110
[25] Micronetics MW500-1531 VCO

4.3 MAGNETIC FIELD

Due the *anomalous Zeeman* effect, discussed in appendix A, the degeneracy of the fine-structure levels in the ion is lifted. The frequency shift of an electronic level depends on the projection of the magnetic moment of the electron onto the direction of the bias magnetic field. Therefore the direction of the magnetic field is called the quantization axis. Since the frequency shift of a state depends on its total angular quantum number m_j, also the transition frequencies shift depending on the quantum numbers of the involved states. The magnetic field sensitivity of various states and transitions in $^{40}Ca^+$ are summarized in appendix B.

Typically we measure the frequency of the $|m_S = -1/2\rangle \leftrightarrow |m_D = -1/2\rangle$ transition (1) with a shift of about $\mu^{(1)}/h \approx +0.56\,\mathrm{MHz/G}$ and the frequency of the $|m_S = -1/2\rangle \leftrightarrow |m_D = -5/2\rangle$ transition (2), which shifts about $\mu^{(2)}/h \approx -2.80\,\mathrm{MHz/G}$. Using eq. (A.3) we can estimate the magnitude of the magnetic field as

$$B = \frac{h\Delta\nu^{(1-2)}}{\Delta\mu^{(1-2)}} \approx \frac{\Delta\nu^{(1-2)}}{3.36\,\mathrm{MHz/G}}, \tag{4.1}$$

where $\Delta\nu^{(1-2)} = \nu^{(1)} - \nu^{(2)}$ is the difference frequency and $\Delta\mu^{(1-2)} = \mu^{(1)} - \mu^{(2)}$ is the difference in magnetic field sensitivity of the two transitions.

Since we changed from an electric coil system to a permanent magnet setup, both systems are described in the upcoming two sections. In fig. 4.6 photographs of the two individual setups are presented.

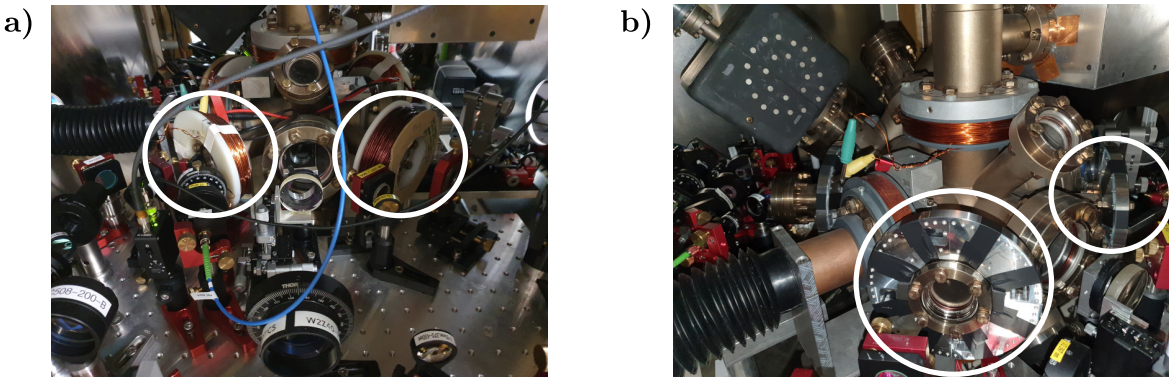

Figure 4.6: **Photographs of the setup.** In white circles there are electric coils in **a)** and permanent magnets in **b)**.

4.3.1 *Current stabilized coils*

In this setup a set of coils is driven by electric currents. The current for each pair of coils is generated by a highly stable current driver, where Details can be found in Ref. [89]. The current stabilized coils have the advantage, that the current and thus the magnitude of the magnetic field can easily be adjusted. The disadvantage is, that current fluctuations lead to magnetic field fluctuations which induce decoherence.

We perform Ramsey spectroscopy to characterize the short-term stability of the magnetic field, as discussed in section 3.5. These Ramsey contrast measurements of the $|m_S = -1/2\rangle \leftrightarrow |m_D = -1/2\rangle$ transition (1) and of the $|m_S = -1/2\rangle \leftrightarrow |m_D = -5/2\rangle$

transition (2) are depicted in fig. 4.7 **a)**. In the case of transition (2) the Rabi frequencies were not calibrated perfectly, which is unfortunate but does not corrupt the coherence time estimate. If we assume a white noise model for the magnetic field fluctuations, the decay of the Ramsey contrast is described by an exponential function and the coherence time is linearly dependent on the magnetic field sensitivity of the transition. We thus fit the data with an exponential function according to eq. (3.55) and we estimate coherence times of $T_2^{(1)} = 171(45)\,\mathrm{ms}$ and $T_2^{(2)} = 39(6)\,\mathrm{ms}$.

The Zeeman shift of these two transitions differs by the ratio of the magnetic field sensitivities of $\delta\mu = \mu^{(2)}/\mu^{(1)} \sim 5$. Depending on the correlation time of the noise, the coherence time depends from linearly $T_2 \propto \delta\mu$ to quadratically $T_2 \propto \delta\mu^2$ on the induced frequency fluctuations, as discussed in Ref. [113]. If the coherence times are limited by magnetic field fluctuations, the coherence time ratio of the two transitions differs by $T_2^{(1)}/T_2^{(2)} = \delta\mu \ldots \delta\mu^2 \sim 5 \ldots 25$. If the coherence is predominantly restricted by laser phase fluctuations, the ratio would be $T_2^{(1)}/T_2^{(2)} \sim 1$. The measured coherence times differ by a factor ~ 4.4. Hence, we conclude that the coherence is mainly limited by magnetic field fluctuations and some laser frequency fluctuations in addition. According to eq. (3.59) we can estimate the coherence time as $T_2^{(2)} = 2\ln(2)h/(2\pi\mu_\mathrm{B}\Delta B) = 39(6)\,\mathrm{ms}$ which results in a short-term magnetic field noise of $\Delta B \sim 4\,\mu\mathrm{G}$ and in fractional magnetic field fluctuations of $\Delta B/B \sim 1 \cdot 10^{-6}$.

The long-term stability of the magnetic field is shown in fig. 4.7 **b)**. We can observe that the magnetic field strength is strongly correlated with the temperature. Note that the temperature sensor[26] is placed inside the μ-metal shield where also the coils are mounted, but the current drivers are outside the shield. Since the resolution of the digital temperature sensor is 0.03125 K we filter the temperature data with a first-order Savitzky–Golay filter [128]. Over a time span of about 3.5 days the magnetic field changes by $\Delta B = 0.37\,\mathrm{mG}$ around $B = 4.21386(37)\,\mathrm{G}$, where ΔB is the standard deviation of the data set. The temperature changes by $\Delta T = 0.1\,\mathrm{K}$ around $T = 24.4(1)\,^\circ\mathrm{C}$. Correspondingly, the relative magnetic field changes depending on temperature can be estimated as $\Delta B/B(T) = \Delta B/(B\Delta T) \sim 9 \cdot 10^{-4}\,\mathrm{K}^{-1}$.

[26] Microchip MCP9808

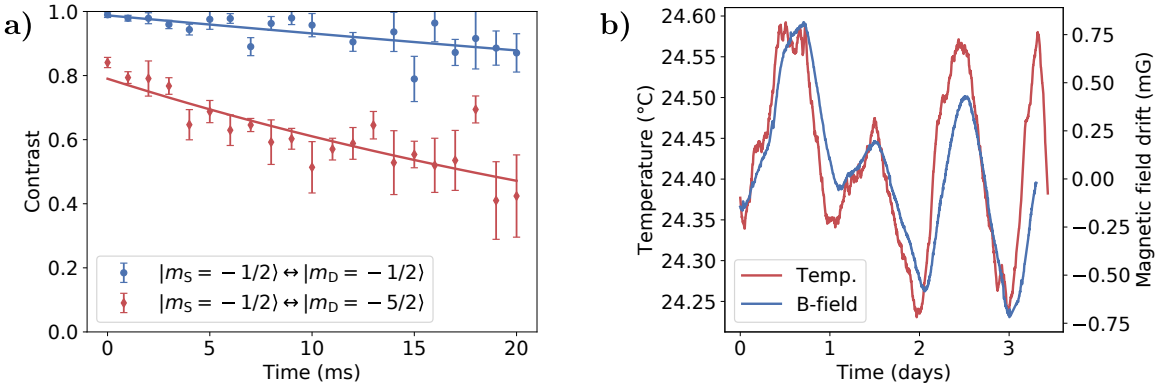

Figure 4.7: **Stability of the magnetic field generated by electric coils. a)** Short-term characterization via Ramsey spectroscopy with estimated coherence times $T_2^{(1)} = 171(45)\,\mathrm{ms}$ and $T_2^{(2)} = 39(6)\,\mathrm{ms}$ (measured with the old Coherent laser). **b)** Long-term drift of the temperature and the magnetic field, where the B-field drifts for $\Delta B = 0.37\,\mathrm{mG}$ around $B = 4.21386(37)\,\mathrm{G}$ over a temperature range of $\Delta T = 0.1\,\mathrm{K}$ around $T = 24.4(1)\,^\circ\mathrm{C}$.

4.3.2 *Permanent Magnets*

The bias magnetic field can also be generated using permanent magnets. We adopted the idea from another $^{40}Ca^{+}$ experiment [62], where long coherence times were demonstrated. In our setup the most feasible option is to replace the electric coils with rings of permanent magnets, as illustrated in fig. 4.6. The disadvantage with permanent magnets is that the magnetic field strength cannot be varied easily, as opposed to electric coils. The advantage is, that the short-term fluctuations in the magnetic field are ought to be orders of magnitudes smaller compared to the noise of current driven coils, as outlined in the following.

The relative magnetic field fluctuation of permanent magnets[27] with a volume of $V = 1\,\mathrm{cm}^3$ at room temperature is $\Delta B/B = 2 \cdot 10^{-12}$ [129]. In the experiment we use cylindrical magnets[28] with a diameter of 6 mm, a height of 10 mm and a remanence of $B_r = 1.00(4)$ T. Since the fluctuations scale with the volume as $\Delta B/B \propto \sqrt{1/V}$ [129], the noise of the magnets we use with a volume of $V \sim 0.28\,\mathrm{cm}^3$ is $\Delta B/B \sim 3.8 \cdot 10^{-12}$. In a setup containing 240 magnets, which is discussed in the following, we estimate the relative magnetic field fluctuation to be $\Delta B/B \sim \sqrt{240} \cdot 3.8 \cdot 10^{-12} \sim 6 \cdot 10^{-11}$. Hence the noise induced by the permanent magnets is expected to be about four orders of magnitude lower than the noise estimated for the current driver setup of $\Delta B/B \sim 1 \cdot 10^{-6}$ (see section 4.3.1).

Consequently, using the fact that the frequency shift is linearly dependent on the magnetic field $\Delta\nu = 2\mu_B/h\Delta B$ (see appendix A) and eq. (3.59), we can estimate an achievable coherence time of $T_2^{(2)} = 2\sqrt{\ln 2}\hbar/(\mu_\mathrm{B} \cdot \Delta B) \sim 600\,\mathrm{s}$, if magnetic field fluctuations of $\Delta B \sim 3 \cdot 10^{-10}\,\mathrm{G}$ in a magnetic field of $B \sim 4.61\,\mathrm{G}$ are the only source of noise. In the laboratory there might be additional magnetic field noise present, originating from electronic devices, power lines or neighboring experiments, which reduces the achievable coherence time.

In the following we discuss the simulation of the magnetic field generated by permanent magnets in order to design the arrangement of the permanent magnets. The magnetic flux density at location $\vec{r}$ for a single permanent magnet at location $\vec{r_0}$ with magnetic moment $\vec{m}$ is described as [130]

$$\vec{B}(\vec{r}, \vec{r_0}, \vec{m}) = \frac{\mu_0}{4\pi}\left(\frac{3(\vec{r}-\vec{r_0})(\vec{m}\cdot(\vec{r}-\vec{r_0}))}{|\vec{r}-\vec{r_0}|^5} - \frac{\vec{m}}{|\vec{r}-\vec{r_0}|^3}\right), \tag{4.2}$$

where μ_0 is the vacuum permeability and the magnetic moment $\vec{m} = \vec{B_r}V/\mu_0$ of a permanent magnet can be described by its volume V and residual flux density $\vec{B_r}$. The magnetic field strength can be increased by arranging N magnets with magnetic moment $\vec{m} = (0, 0, m_z)$ in a circular pattern around the z-axis such that the total magnetic field is determined as

$$\vec{B}(\vec{r}, N) = \sum_{i=0}^{N-1} \vec{B}(\vec{r}, \vec{r_0}^{\,i}, \vec{m}) \quad \text{with} \quad \vec{r_0}^{\,i} = \begin{pmatrix} r_0\cos(2\pi i/N) \\ r_0\sin(2\pi i/N) \\ 0 \end{pmatrix}. \tag{4.3}$$

For simplicity we only investigate the magnetic field along the z-axis with $\vec{r} = (0, 0, z)$. Thus it follows from eq. (4.3) that $\vec{m}\cdot(\vec{r}-\vec{r_0}^{\,i}) = (0, 0, m_z(z-z_0))$ and $|\vec{r}-\vec{r_0}^{\,i}| = \sqrt{r_0^2 + (z-z_0)^2}$ is the same for all individual magnets i and the magnetic field of a ring comprising N magnets is $B(z, N) = N \cdot B(z)$.

[27] Estimated for Samarium-Cobalt SmCo5 magnets, where the noise estimation is approximately the same for the Sm2Co17.

[28] Samarium-Cobalt XGS24LT from BVI-Magnete

Importantly, since the transition frequency of the ions depends on the magnetic field $\Delta\nu \propto |\vec{B}(\vec{r})|$ [B], all the ions in the trap should experience the same magnetic field. Therefore the magnetic field gradient $\vec{\nabla}\vec{B}(\vec{0})$ in the center of the trap should be as small as possible. In general the gradient is minimized when the magnetic field curvature is zero $\vec{\Delta}\vec{B}(\vec{0}) = \vec{0}$.

In our setup we mount one ring of magnets on a flange at $z_0 = -d/2$ and a second ring on a flange at $z_0 = +d/2$ symmetrically around the trap center $z = 0$, where the rings have a distance of $d = 310\,\text{mm}$ as depicted in fig. 4.1. Because there are eight neighboring flanges, the radius of the rings is limited to $r_0 = 70\,\text{mm}$. The simulated magnetic field and magnetic field gradient of this configuration comprising 32 magnets in each ring are depicted in fig. 4.8 (Standard).

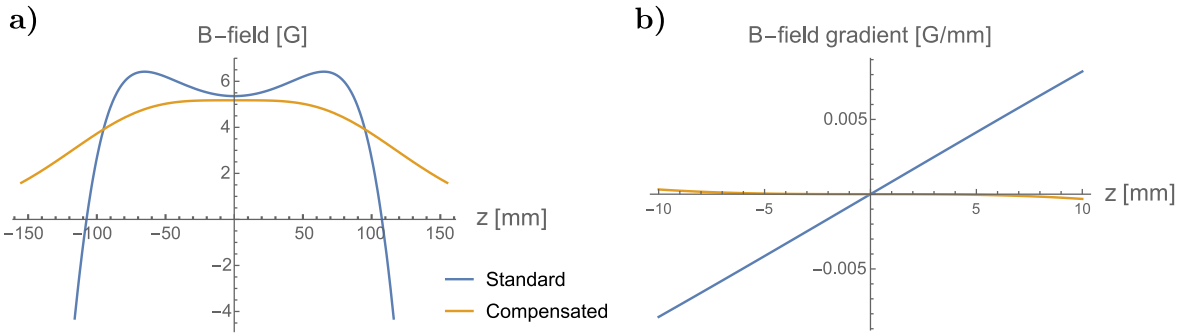

Figure 4.8: **Magnetic field simulations for permanent magnets.** Two configurations are simulated, the first (**Standard**) with one ring ($d = 310\,\text{mm}$, 32 magnets at $r = 70\,\text{mm}$) and the second (**Compensated**) with an additional compensation ring ($d = 310\,\text{mm}$, 60 magnets at $r_1 = 70\,\text{mm}$, 20 magnets at , $r_2 = 44.7\,\text{mm}$) **a)** The absolute value of the magnetic field along the z-axis. **b)** The gradient of the magnetic field along the z-axis.

Since we do not know the exact position of the ion trap inside the vacuum chamber and because the distance of the rings to the trap cannot be measured precisely, we assume in a worst case scenario that the ions are trapped at a position $z = 5\,\text{mm}$. For an absolute magnetic flux density of $|\vec{B}| = 4.12\,\text{G}$ we estimate a magnetic field gradient of $\mathrm{d}B(z)/\mathrm{d}z = 34\,\mu\text{G}/\mu\text{m}$, which corresponds to a frequency shift for the $|m_S = -1/2\rangle \leftrightarrow |m_D = -5/2\rangle$ transition (2) of $\Delta\nu^{(2)}/\Delta z \sim 100\,\text{Hz}/\mu\text{m}$. With a typical ion separation of $\Delta z \sim 4\,\mu\text{m}$ this results in a frequency shift of $\Delta\nu^{(2)} \sim 400\,\text{Hz}$ between neighboring ion pairs. Such a frequency difference is problematic for various reasons, for example if we want to entangle ions using the MS gate with high fidelity, see section 3.3.1.3.

For the configuration with two rings of permanent magnets at distance d we use a software program[29] to minimize the magnetic field gradient by solving the equation $\mathrm{d}^2B(z)/\mathrm{d}z^2|_{z=0} = 0$ for r_0, where $B(z) = B(z_0 = +d/2) + B(z_0 = -d/2)$. We find that there exist two analytic solutions $r_0 = \sqrt{1 - \sqrt{5/6}}d \approx 0.295\,d$ and $r_0' = \sqrt{1 + \sqrt{5/6}}d \approx 1.383\,d$ for which the curvature of the field vanishes. In practice it makes sense to use the smaller radius r_0, since the generated magnetic field is two orders of magnitudes stronger than the one produced from rings with radius r_0'. Unfortunately, due to space constraints, we cannot install rings in our apparatus with a radius of $r_0 \sim 0.295\,d \sim 91\,\text{mm}$.

[29] Wolfram Mathematica

Another option to minimize the gradient is to place a smaller ring with N_2 magnets and radius r_2 inside the main ring with N_1 magnets and radius r_1. If the magnetic field of the inner ring points into the opposite direction compared to the outer ring, the total magnetic field and the magnetic field gradient is reduced. To find an optimal inner ring radius r_2 we numerically solve the equation $\mathrm{d}^2B(z)/\mathrm{d}z^2|_{z=0} = 0$ with rings placed at a distance $d = 310\,\mathrm{mm}$ and for an outer ring radius of $r_1 = 70\,\mathrm{mm}$. Here, the result for r_2 depends on the ratio N_1/N_2 of the number of magnets used for each ring. Since we mount the magnetic rings on CF40 flanges, the radius of the inner ring has to be larger than the radius 35 mm of the flange. We find a feasible result of $r_2 = 44.7\,\mathrm{mm}$ using a ratio of $N_1/N_2 = 3$. The simulation of the magnetic field and the magnetic field gradient for a configuration with $N_2 = 60$ and $N_1 = 20$ is shown in fig. 4.8 (Compensated).

For an absolute magnetic flux density of $|\vec{B}| = 4.12\,\mathrm{G}$ we estimate a magnetic field gradient of $\mathrm{d}B(z)/\mathrm{d}z = 0.034\,\mu\mathrm{G}/\mu\mathrm{m}$, which corresponds to a frequency shift of $\Delta\nu^{(2)}/\Delta z = 0.1\,\mathrm{Hz}/\mu\mathrm{m}$ for the $|m_\mathrm{S} = -1/2\rangle \leftrightarrow |m_\mathrm{D} = -5/2\rangle$ transition (2) at $z = 5\,\mathrm{mm}$. Compared to the configuration without the inner compensation ring, we achieve the the same magnetic field strength using 2.5 times more magnets with a gradient that is ~ 1000 times smaller.

The CAD drawing of the holder we designed to mount the permanent magnets on the vacuum chamber is depicted in fig. 4.9.

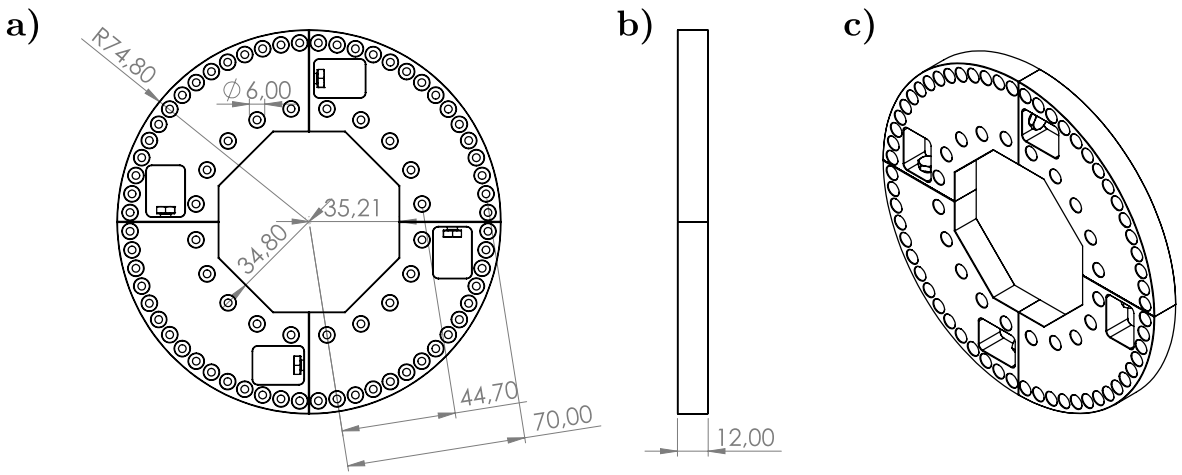

Figure 4.9: **CAD drawing of the holder for the permanent magnets.** The holder consists of four equal parts fabricated from aluminium. There are cylindrical depressions with diameters of 6 mm in two circular patterns with radius $r_1 = 70.00\,\mathrm{mm}$ and $r_2 = 44.70\,\mathrm{mm}$. **a)** Front view. **b)** Side view. **c)** Isometric projection.

In addition to the analytical calculations we simulate the magnetic field with a finite element software[30] to recheck the resulting magnetic field strength. For a configuration with 60 magnets in the outer ring and 20 magnets in reverse direction in the inner ring we simulate an absolute magnetic field of $|\vec{B}|_{\text{Sim},1} \approx 4.12\,\text{G}$, as depicted in fig. 4.10 **a)** and **b)**.

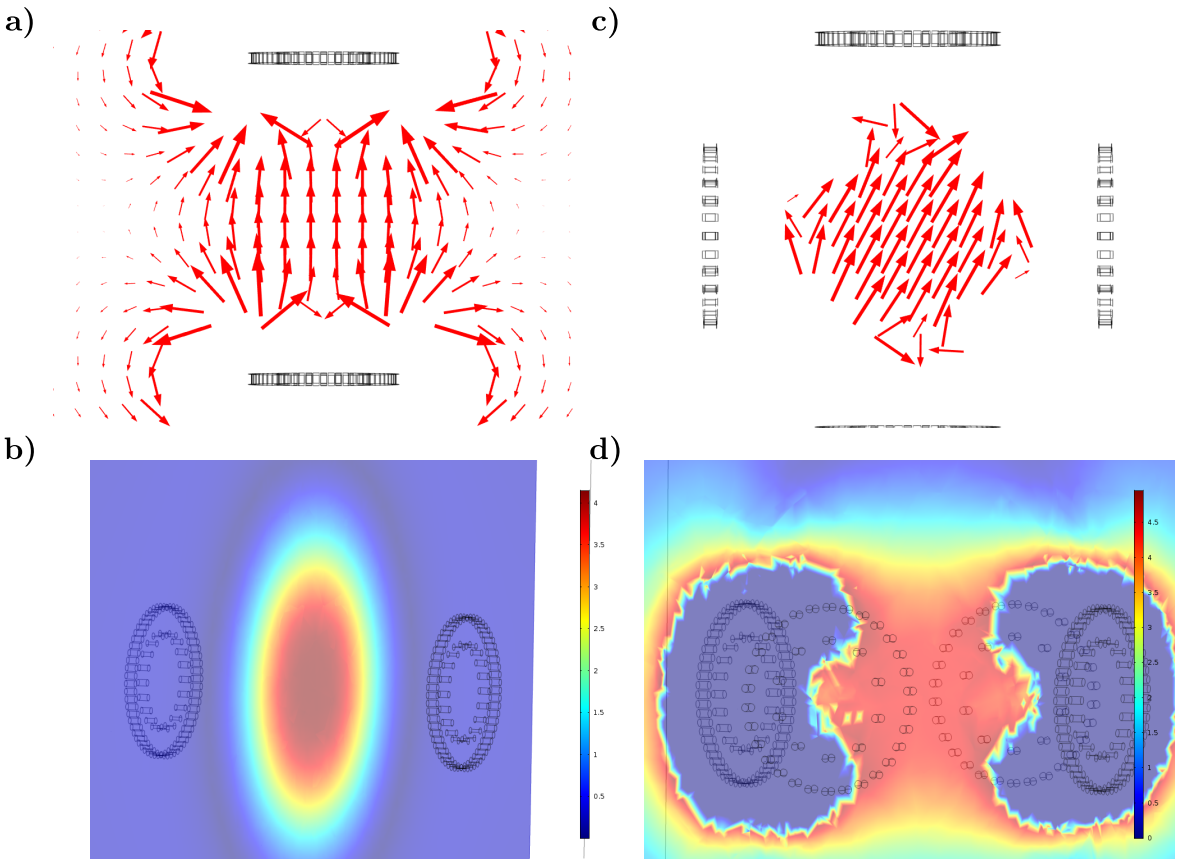

Figure 4.10: **Magnetic field generated by permanent magnets.** Vector components of the magnetic field for **a)** the two ring setup and **c)** the four ring setup. In **a)** the quantization axis is aligned with the symmetry axis of the rings where in **c)** the quantization axis is rotated by 26.6 ° using a second pair of rings containing half the magnets. **b)** and **d)** show the magnetic field strength on a slice in the center normal to the quantization axis. In **b)** we simulate a magnetic field of $|\vec{B}|_{\text{Sim},1} \approx 4.12\,\text{G}$ whereas in **d)** the simulation yields a magnetic field strength of $|\vec{B}|_{\text{Sim},2} \approx 4.61\,\text{G}$.

If we want to align the magnetic field with the trap axis, that is rotated by 22.5 ° relative to the viewports, as depicted in fig. 4.1, we have to tilt the magnetic field. We achieve a rotation of $\sim 26.6\,^\circ$ of the magnetic field by adding a pair of rings containing half the magnets (30 in the outer ring and 10 per inner ring) perpendicular to the first pair of rings. As illustrated in fig. 4.10 **c)** and **d)** the simulation shows a magnetic field that is tilted by $\sim 26.6\,^\circ$ with a magnetic flux density of $|\vec{B}|_{\text{Sim},2} \approx 4.61\,\text{G}$ in the center.

Experimentally, we measure magnetic flux densities of $|\vec{B}|_{\text{Exp},1} \approx 4.24\,\text{G}$ for the two ring and $|\vec{B}|_{\text{Exp},2} \approx 4.78\,\text{G}$ for the four ring setup. The measured magnetic field strengths are in good agreement with the simulated values. For the magnetic field gradient we measure a value of $\mathrm{d}B(z)/\mathrm{d}z \sim 3\,\mu\text{G}/\mu\text{m}$, which is at least a factor of 100 too high compared to the simulation. This discrepancy comes from the fact, that in the experiment the magnetic

[30] COMSOL Multiphysics

rings are not the only components that generate or influence magnetic fields. Components that can alter the magnetic field are e.g. the steel chamber, steel screws, the μ-metal shield and the ion-getter pump, which has U-shaped permanent magnet built-in. Once we remove the permanent magnet of the ion-getter pump, we are not able to measure a magnetic field gradient over a distance of $55\,\mu$m and we thus estimate the gradient to be $\mathrm{d}B(z)/\mathrm{d}z < 0.1\,\mu\mathrm{G}/\mu\mathrm{m}$. Hence, we think that the main source for the magnetic field gradient is the ion-getter pump. Since the magnet is necessary for the pump to work, we decided to mount additional permanent magnets on the outside of the ion-getter pump until we cannot measure a magnetic field gradient anymore, see fig. 4.6.

If we work with ion strings that contain many ions, the electric field gradient of the neighboring ions induce a quadrupole shift [131, 132], which is the largest in the center and get smaller towards the edges of the string. We can minimize this quadrupole shift by minimizing the term $\{3\cos^2(\theta) - 1\}$ with $\theta \sim 54.74^\circ$, where θ describes the angle between the trap axis and the magnetic field. Therefore we recently changed the direction of the magnetic field, away from the trap axis to an angle of $\sim 57.5^\circ$ as depicted in fig. 4.1.

As in the previous section 4.3.1 about current coils, we estimate the short-term stability of the magnetic field via Ramsey experiments. Because a neighboring experiment is switching magnetic fields, which shift our transitions on the order of tens to hundreds of Hz, standard Ramsey experiments on the times scales of milliseconds are not possible at the moment. Therefore we do Ramsey experiments with spin-echo (see section 3.5, where a π pulse is added after half the waiting time τ in the sequence $R(\pi/2, 0) \rightarrow \mathrm{Wait}(\tau/2) \rightarrow R(\pi, 0) \rightarrow \mathrm{Wait}(\tau/2) \rightarrow R(\pi/2, \phi)$. Due to the spin-echo, changes in the magnetic field that are slower than $\tau/2$ get refocused in the second half of the sequence. Hence also DC magnetic field changes from shot to shot, or from one minute to the next minute do not disturb the Ramsey contrast measurement.

We perform the experiment on the ground state ($|m_S = -1/2\rangle \leftrightarrow |m_S = +1/2\rangle$) transition (3), for which the laser phase and hence laser frequency fluctuations do not play a role during the waiting time. The results are depicted in fig. 4.11 **a)**. As can be seen in the data, the main limitation is a noise component at 50 Hz, most likely originating from power lines or devices outside the μ-metal shield.

First, we fit the data with a constant power spectral density $A(\omega) = a$ according to eq. (3.61), depicted in blue in fig. 4.11 **a)**. Although a simple exponential decay does not fit the observed data perfectly, we get a rough estimate of the noise level $a = 2.8(6)$ and of the coherence time $T_2^{(3)} = 4/(a^2\pi) = 162(37)$ ms. Since the magnetic field sensitivity of the transition (3) is the same as for the $|m_S = -1/2\rangle \leftrightarrow |m_D = -5/2\rangle$ transition (2) probed in section 4.3.1, we can compare the two coherence times. Recalling that the coherence time with current coils was $T_2^{(3)} = 39(6)$ ms, we can conclude that the coherence got a factor of ~ 4 better with the permanent magnet setup.

Second, we fit the data with a constant power spectral density plus a Gaussian peak at 50 Hz that is described as $A(\omega) = a + bG(\omega, (2\pi)50\,\mathrm{Hz}, \sigma)$. The fit is depicted in red in fig. 4.11 **a)**. The fit result is a constant noise level of $a = 2.1\,\sqrt{\mathrm{Hz}}$ and a Gaussian 50 Hz noise peak with an amplitude of $b = 70.1\,\sqrt{\mathrm{Hz}}$ and a width of $\sigma = (2\pi)\,0.2\,\mathrm{Hz}$. The constant noise level a corresponds to a decay time of $T_2^{(3)} = 4/(a^2\pi) = 287\,\mathrm{ms}$.

We should be able to improve the coherence time further by installing an active magnetic field stabilization system in the future.

Measurements of the long-term stability of the magnetic field are presented in fig. 4.11 **b)**. The data is acquired in the same fashion as described in section 4.3.1.

Over the course of about 2.5 days the magnetic field changes by $\Delta B = 0.58\,\mathrm{mG}$ around $B = 4.77372(58)\,\mathrm{G}$, where ΔB is the standard deviation of the data set. The temperature changes by $\Delta T = 0.16\,\mathrm{K}$ around $T = 24.16(16)\,^{\circ}\mathrm{C}$. Correspondingly, the relative magnetic field changes depending on temperature can be estimated as $\Delta B/B(T) = \Delta B/(B\Delta T) \sim 7 \cdot 10^{-4}\,\mathrm{K}^{-1}$. This is in the same order of magnitude than the reversible temperature coefficient (RTC) of (3-5)$\cdot 10^{-4}\,\mathrm{K}^{-1}$ stated by the manufacturer.

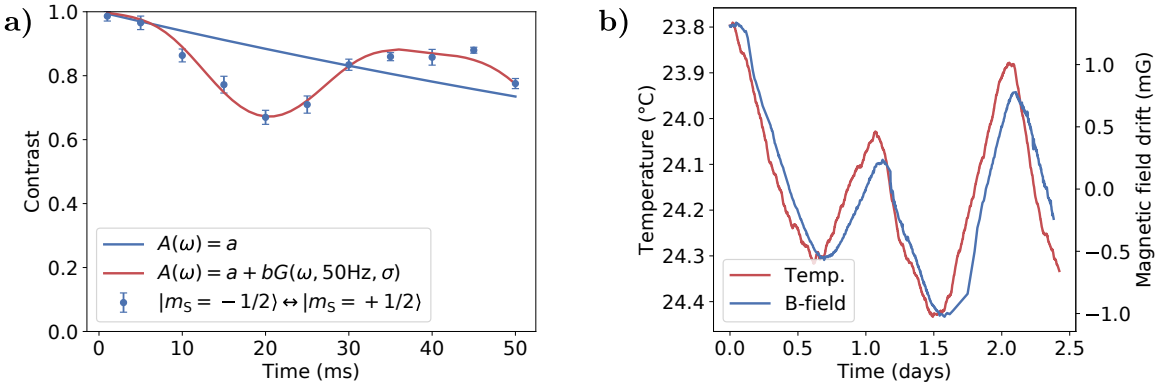

Figure 4.11: **Stability of the magnetic field generated by permanent magnets. a)** Short-term spin-echo Ramsey measurements, where the data is fitted with two different power spectral densities $A(\omega)$ of the noise, see eq. (3.61). In the first fit in blue we assume a constant noise level a that results in an exponential decay and we estimate a coherence time of $T_2^{(3)} = 162(37)\,\mathrm{ms}$. In the second fit in red we assume a constant noise spectral density a plus a 50 Hz Gaussian noise peak with amplitude b. From the constant noise level a we estimate a corresponding coherence time of $T_2^{(3)} = 287\,\mathrm{ms}$. **b)** Long-term drift of the temperature and the magnetic field, where the B-field drifts for $\Delta B = 0.58\,\mathrm{mG}$ around $B = 4.77372(58)\,\mathrm{G}$ over a temperature range of $\Delta T = 0.16\,\mathrm{K}$ around $T = 24.16(16)\,^{\circ}\mathrm{C}$.

5 CHARACTERIZATION OF QUANTUM COMPUTERS

Hilbert space is a big place!

— Carlton M. Caves and Christopher A. Fuchs, 1996

A major roadblock for the development of useful quantum computers is to assess and overcome the inevitable errors that accumulate during the execution of a quantum algorithm. States and processes in a quantum device can be fully characterized by *tomography*. The implementation of Quantum State Tomography (QST) and Quantum Process Tomography (QPT) is explained in section 5.1.

There are also techniques which only partly yield information about dynamics in a quantum system, such as direct fidelity estimation [133–135] or randomized benchmarking [21–23], which is outlined in section 5.2.

Due to practical limitations of the aforementioned techniques, the group around Prof. Joseph Emerson and Prof. Joel J. Wallman, in a fruitful collaboration with our team, developed a new technique called *Cycle Benchmarking* (CB), which is able to efficiently characterize the performance of quantum operations [25]. The details of the CB protocol are outlined in section 5.3.

5.1 QUANTUM STATE AND PROCESS TOMOGRAPHY

A quantum state is fully determined by its density matrix ρ, as described in section 2.1. The goal of QST is to estimate all entries of this $2^N \times 2^N$ density matrix that defines an arbitrary N-qubit state. As an example, three 1-qubit density matrices are shown in fig. 5.1 which are defined as

$$\textbf{a)} \quad \rho = |0\rangle\langle 0| = 1/2(I + \sigma_z), \quad |\vec{r}| = 1 \tag{5.1}$$

$$\begin{aligned}\textbf{b)} \quad \rho &= 1/2(|0\rangle\langle 0| + i\,|0\rangle\langle 1| - i\,|1\rangle\langle 0| + |1\rangle\langle 1|) \\ &= 1/2(I - \sigma_y), \quad |\vec{r}| = 1,\end{aligned} \tag{5.2}$$

$$\textbf{c)} \quad \rho = 1/2I, \quad |\vec{r}| = 0. \tag{5.3}$$

As can be seen in eqs. (5.1) and (5.2), these states are eigenstates of the Pauli operators σ_z and σ_y. The state in eq. (5.3) is a completely mixed state with zero off-diagonal elements or quantum coherences.

Since the density matrix ρ can be expanded as in eq. (2.3), we can reconstruct the density matrix by measuring the expectation values of the three Pauli operators [9]

$$r_i = \langle\sigma_i\rangle = \mathrm{tr}(\rho\sigma_i) \quad \text{with} \quad i \in \{x, y, z\}. \tag{5.4}$$

If we can prepare n copies of the state and we employ projective measurements each time e.g. in z-basis, we get an estimate for the expectation value $\langle\sigma_z\rangle$, which is the average $\sum_i z_i/n$

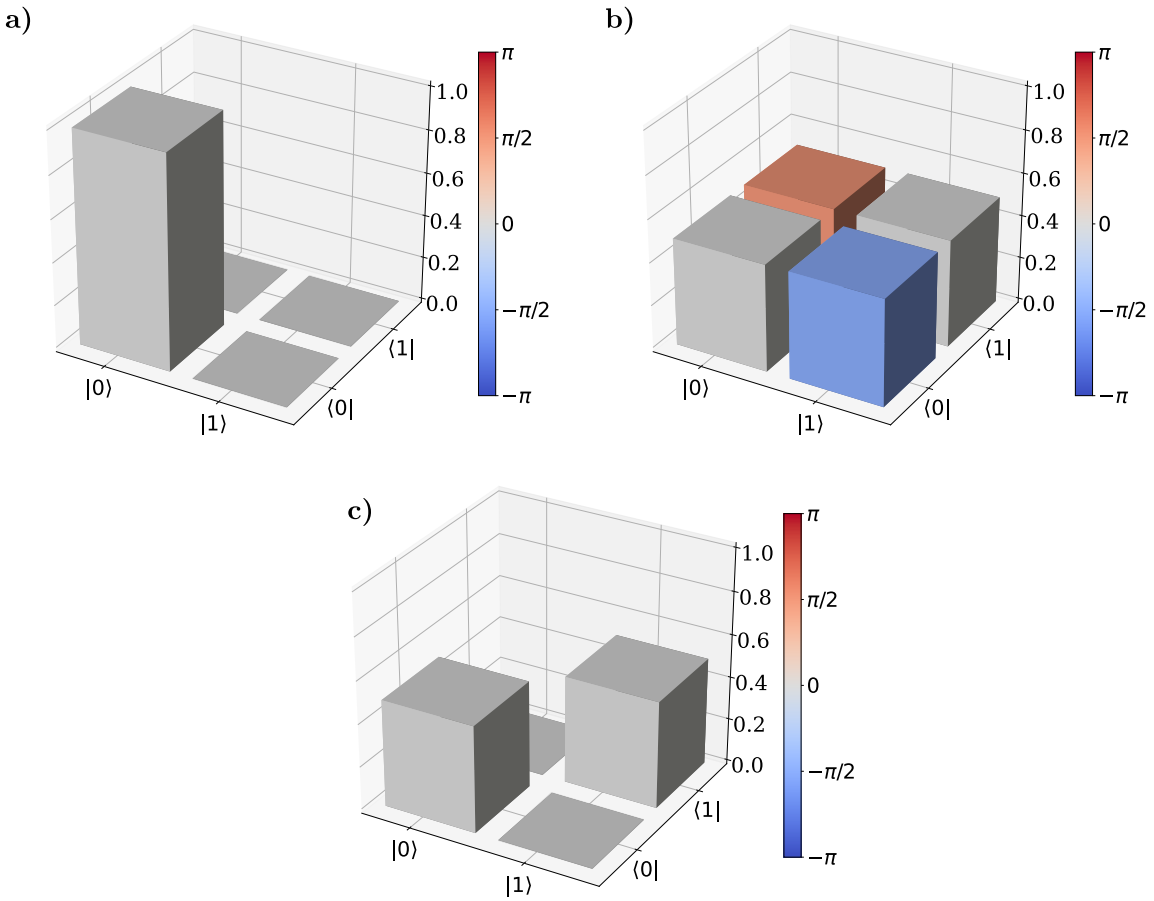

Figure 5.1: **1-qubit density matrices. a)** A pure state $|\psi\rangle = |0\rangle$, see eq. (5.1). **b)** A pure state $|\psi\rangle = 1/\sqrt{2}(|0\rangle - i\,|1\rangle)$, see eq. (5.2). **c)** A completely mixed state with $\rho = 1/2I$, see eq. (5.3).

of the measurement outcomes $z_i \in \{+1, -1\}$. Let $p(z_1)$ be the probability to measure the outcome $+1$, then the standard deviation of a single measurement (quantum projection noise) can be calculated as $\Delta\sigma_z = \sqrt{p(z_1)(1-p(z_1))}$ [106]. For large enough number of measurements n, when the results are approximately Gaussian distributed, the standard deviation of the expectation value is defined as $\Delta\langle\sigma_z\rangle = \Delta\sigma_z/\sqrt{n} = \sqrt{p(z_1)(1-p(z_1))/n}$.

In practice, measurement noise (e.g. quantum projection noise) can lead to unphysical results, like a density matrix with negative eigenvalues or a Bloch vector with $|\vec{r}| > 1$. Therefore we employ statistical methods in the post-processing, like e.g. maximum-likelihood estimation [136–139], to prevent unphysical results. Physical constraints on the $2^N \times 2^N$ Hermitian complex matrix ρ are that it has trace one, $\mathrm{tr}(\rho) = 1$, and that it is positive semi-definite, which means that $x^*\rho x \geq 0$ for all $x \in \mathbb{C}^{2^N}$. In the case of the maximum-likelihood reconstruction the idea is to find a density matrix that is as close as possible related to the measurement outcomes and that fulfills the physical constraints at the same time.

In general, an N-qubit system can be expanded similar to eq. (2.3) as [9]

$$\rho = \frac{1}{2^N}\sum_{\vec{v}} \mathrm{tr}(\sigma_{v_1} \otimes \sigma_{v_2} \otimes \cdots \otimes \sigma_{v_N}\rho)\sigma_{v_1} \otimes \sigma_{v_2} \otimes \cdots \otimes \sigma_{v_N}, \tag{5.5}$$

where we sum over the vectors $\vec{v} = (v_1, \ldots, v_N)$ and the components are chosen from the set $v_i \in \{I, X, Y, Z\}$. Taking into account the three different measurement bases $\{X, Y, Z\}$ per qubit, there are 3^N measurements necessary to reconstruct the full N-qubit density matrix.

The evolution of a quantum state can be described by the transformation of the initial density matrix ρ to the output density matrix ρ' as [9]

$$\rho' = \mathcal{E}(\rho), \tag{5.6}$$

where $\mathcal{E}$ is a completely positive (CP) and trace preserving (TP) map and describes the *quantum operation* or *quantum process*.

A map $\mathcal{E}$ is called positive if it maps positive elements to positive elements $\rho \geq 0 \rightarrow \mathcal{E}(\rho) \geq 0$, which is a necessary condition that the measurement probabilities stay positive. The map $\mathcal{E}$ is completely positive if $\mathcal{E} \otimes I^N$ is positive for all N. The reason why CP is a necessary physical condition can be made clear with the following example. If the input state is part of an entangled state $|\psi\rangle_{\mathrm{AB}}$ and $\mathcal{E}_{\mathrm{B}}$ acts only on the subspace B, the process $\mathcal{E}_{\mathrm{B}}$ must also preserve the positivity of the composite system ρ_{AB} [138].

To conserve the total probability, $\mathcal{E}$ must be trace preserving $\mathrm{tr}(\rho') = \mathrm{tr}(\rho)$ [138]. If we want to describe leakage out of the principle Hilbert space, the TP condition is relaxed to a non-increasing trace $\mathrm{tr}(\rho') \leq \mathrm{tr}(\rho)$.

Completely positive and trace preserving (CPTP) maps are a very powerful description of quantum processes, since we can utilize them to express unitary evolution, measurements and open quantum systems, which are systems that couple to the environment. If we want to describe an open or noisy quantum system, we can define the quantum process by a unitary transformation U of the product state between the principle system ρ and the environment ρ_{env} as $\mathcal{E}(\rho) = \mathrm{tr}_{\mathrm{env}}\left(U\rho \otimes \rho_{\mathrm{env}} U^\dagger\right)$. If we assume that the environment starts in the state $\rho_{\mathrm{env}} = |e_0\rangle\langle e_0|$ and that $\{|e\rangle_i\}$ is an orthonormal basis for the state space of the environment, we can express the quantum process as [9]

$$\mathcal{E}(\rho) = \sum_i E_i \rho E_i^\dagger, \tag{5.7}$$

where $E_i = \langle e_i|U|e_0\rangle$ is a so called Kraus operator on the state space of the principle system. Due to the summation over operators in eq. (5.7) this description is referred to as the *operator-sum representation* of $\mathcal{E}$. If we choose a fixed basis $\{\widetilde{E}_m\}$ such that $E_i = \sum_m e_{im}\widetilde{E}_m$, we can rewrite equation eq. (5.7) as [9]

$$\mathcal{E}(\rho) = \sum_{mn} \widetilde{E}_m \rho \widetilde{E}_n^\dagger \chi_{mn}, \tag{5.8}$$

where $\chi_{mn} = \sum_i e_{im} e_{in}^*$ are the elements of the *chi matrix* (χ_{mn}) describing the quantum process. Examples of three different 1-qubit χ matrices are depicted in fig. 5.2, where e.g. a depolarizing process can be expressed as

$$\mathcal{E}(\rho) = (1 - 3p/4) I\rho I + (p/4)(X\rho X + Y\rho Y + Z\rho Z), \tag{5.9}$$

with the depolarization probability p.

Since ρ has to stay Hermitian with trace one, the matrix χ contains in general $2^{4N} - 2^{2N}$ real parameters. Experimentally, we need 3^N measurements to determine the density matrices for 2^{2N} pure input states, resulting in 12^N measurements in total. In the case of a single qubit we would need to prepare 4 different pure input states, let the system evolve under the quantum process $\mathcal{E}$ and measure each evolved input state in 3 different bases to get an estimate of χ for a fixed set of operators $\{\widetilde{E}_m\}$.

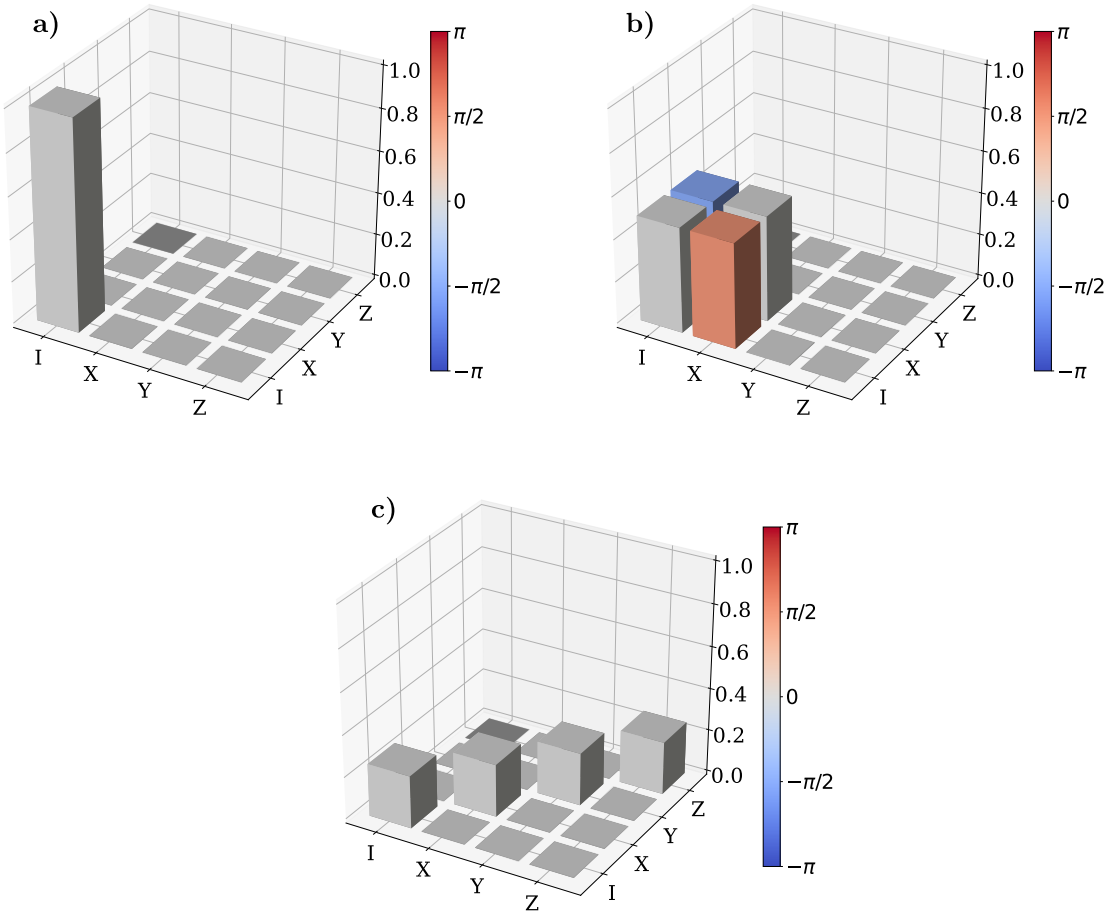

Figure 5.2: **1-qubit process matrices.** If the presented processes act on the pure input state $|0\rangle$, the output states can be described by the density matrices in fig. 5.1. **a)** The identity operation I. **b)** The unitary $X(\pi/2)$ operation. **c)** A completely depolarizing quantum process, see eq. (5.9) with $p = 1$.

As in the case of quantum state tomography, measurement noise can also lead to unphysical results in the estimation of the χ matrix. An elegant way to deal with this issue, is to use the Choi-Jamiolkowski isomorphism [140, 141] between the map $\mathcal{E}$ acting on the Hilbert space $\mathcal{H}$ and a positive semi-definite operator S acting on a larger Hilbert space $\mathcal{H} \otimes \mathcal{K}$. Using this equivalence the problem can be transformed into reconstructing the higher dimensional density matrix S, where the same techniques as for state tomography, like e.g. maximum-likelihood estimation, can be employed [138].

In practice it is of great importance to characterize quantum systems and to assess the noise affecting quantum operations. A severe limitation of state and process tomography is, that these techniques require an exponential number of measurements with increasing system size. In our system, with e.g. $N = 10$ qubits and a duration of 2 s per measurement, it would take ~ 1.4 days to do full state tomography and ~ 4000 years to implement process tomography, which is clearly not feasible in practice. Hence more efficient techniques are needed to assess the performance of quantum computers.

5.2 RANDOMIZED BENCHMARKING

As outlined in section 5.1, QPT is difficult in the presence of State Preparation and Measurement (SPAM) errors and is not feasible in practice for larger systems due to the exponential scaling of resources with the system size. RB [21–23] is a technique which was developed to overcome these difficulties. The idea behind RB is to implement a set of *randomly* chosen gates to extract only partial information about the quantum processes. In fact, RB estimates an average gate fidelity of the implemented set, rather than the fidelity of a specific gate. Also RB decouples SPAM errors from gate errors.

The gates used for RB are chosen from a finite group $\mathcal{C}_N$, the so-called Clifford group [142, 143]. The construction of the Clifford group is discussed in detail in appendix E. The usage of the Clifford group is motivated by the following aspects.

1. Any Clifford operation can be generated from a small set of single and two qubit operations (see appendix E).

2. Any quantum computation carried out with elements of the Clifford group can be simulated efficiently on classical hardware due to the Gottesman-Knill theorem [142].

3. The Clifford group plays an important role in the stabilizer formalism used for QEC, which is discussed in section 7.2.

Aspect 1. is very practical for experiments, because as can be seen in appendix E only three different gates must be calibrated in order to implement any Clifford gate.
Aspect 2. implies that we can calculate the expected outcome for any implementation of Clifford gate sequences. Hence, by keeping track of the implemented Clifford gates, we can calculate a final gate such that the implemented sequence composes to a desired unitary, such as e.g. the identity I or a bit flip X.
In the following paragraph the protocol for standard RB is presented after Ref. [23]:

1. Choose m gates uniformly at random from the Clifford group $\mathcal{C}_N$. Calculate the $(m+1)$th gate such that the complete sequence $S = C_1 \circ \cdots \circ C_{m+1} = I$ composes to the identity in the ideal case.

2. Measure the success probability $P(S) = \mathrm{tr}(E_\psi S(\rho_\psi))$, where ρ_ψ is the initial state taking into account preparation errors and E_ψ is the Positive Operator-Valued Measure (POVM) element taking into account measurement errors.

3. Average over n different random realizations to estimate an average sequence fidelity

$$F_{\mathrm{seq}}(m, \psi) = \frac{1}{n} \sum_{i=1}^{n} P(S_i). \tag{5.10}$$

4. If we assume that the errors are gate-independent we can estimate the average sequence fidelity for different sequence lengths m and fit the results with the model

$$F_{\mathrm{seq}}(m, \psi) = A p^m + B, \tag{5.11}$$

where the coefficient A absorbs state preparation errors and the coefficient B absorbs errors in the last gate and the measurement.

After fitting the results the average gate fidelity can be estimated from the decay parameter p and the Hilbert space dimension d as [23]

$$F_{\text{avg}} = p + (1-p)/d. \tag{5.12}$$

Note that the only assumption in this protocol is that the noise correlations are negligible for time scales longer than the time of an operation C_i, meaning that the noise of gate C_i does not depend on the previous implementations. The scheme of an RB sequence with length m is depicted in fig. 5.3. Experimentally, we have implemented single qubit RB

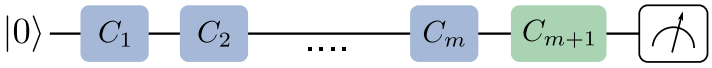

Figure 5.3: **1-qubit randomized benchmarking scheme.** The qubit is prepared in the state $|0\rangle$, then m Clifford gates C_i are chosen uniformly at random and applied to the qubit. Finally an inversion gate C_{m+1} is implemented before the qubit is measured.

in the same ion trap setup, but with different qubit lasers. The measurement results are depicted in fig. 5.4, where the estimated average gate infidelity for the old laser system[1] is $1-\mathcal{F}_{\text{avg,old}} = 4.4(4)\cdot 10^{-3}$ and for the new laser system[2] we estimate an infidelity of $1-\mathcal{F}_{\text{avg,new}} = 1.37(5)\cdot 10^{-4}$. The error rate with the new laser system is improved by a factor of more than 30, which is the result of smaller phase and intensity fluctuations of the new laser.

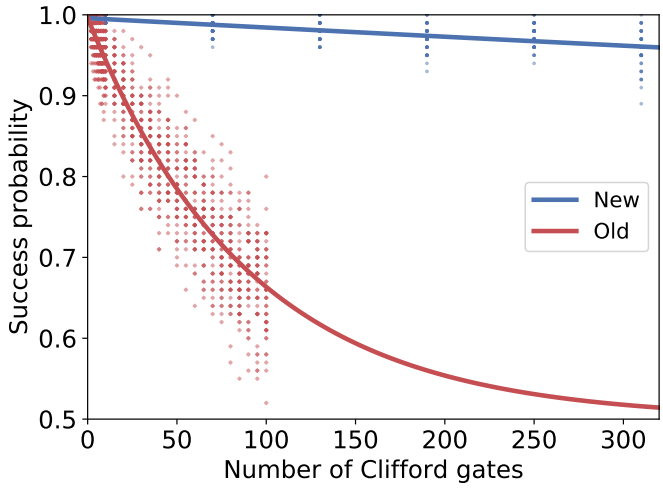

Figure 5.4: **1-qubit randomized benchmarking.** The success probability of the random sequences is plotted against the sequence length. Results for the old laser system are shown in red, whereas the results for the new laser system are depicted in blue. The estimated average gate infidelities are $1-\mathcal{F}_{\text{avg,old}} = 5.52(6)\cdot 10^{-3}$ and $1-\mathcal{F}_{\text{avg,new}} = 1.18(9)\cdot 10^{-4}$ per single qubit Clifford operation.

[1] Coherent 899 Ti:Sa
[2] M^2 SolSTis Ti:Sa

5.3 CYCLE BENCHMARKING

The content of this section is extracted from Ref. [25]

Cycle Benchmarking (CB) can be seen as a successor of standard RB, which overcomes some of the limitations of RB. As already mentioned in the introduction, the implementation of a Clifford gate used in RB requires $\mathcal{O}(N^2/\log N)$ primitive two-qubit operations, which is on the order of ~ 100 for a 10 qubit system. If we assume an error rate of $0.1-1\,\%$ per two-qubit operation this would lead to an error rate of $10-63\,\%$ per single Clifford gate. This substantially increases the number of measurements needed to perform the fitting to the exponential model outlined in section 5.2.

In current physical platforms the two-qubit operations are prone to a bigger error rate compared to the single qubit gates, which violates the assumption that the noise is gate independent. Thus the fidelity of an individual Clifford gate strongly depends on number of two-qubit gates required for the gate and the estimated average gate fidelity is less representative.

While RB can be performed on small subsets of the qubit register [144], such experiments do not explore the full Hilbert space and therefore will not detect important performance-limiting error mechanisms such as cross-talk. Moreover, errors in operations must be characterized in the context in which they are used because control sequences for a specific gate are often distorted by other gates performed in parallel.

One method to achieve this is to only perform gates in fixed modes of parallel operation. We refer to a parallel set of gates as a *cycle*, in analogy with a digital clock cycle. In typical architectures, there are two types of cycles, namely, cycles of single-qubit gates and cycles of multi-qubit gates. Undetected calibration and cross-talk errors will typically lead to coherent and spatially correlated errors that can lead to substantially larger algorithmic errors and can require higher overheads in fault-tolerant quantum error correction schemes [145]. Such errors can be converted to stochastic Pauli errors by randomizing the cycles of single-qubit gates in such a way that the overall ideal circuit remains unchanged, a technique known as randomized compiling [146]. The error rate due to the resulting stochastic Pauli errors can then be accurately quantified by the process fidelity.

In this chapter we introduce CB, a protocol for estimating the process fidelity of a global noise process affecting a quantum device that occur when a cycle of operations is applied to a quantum register. Under the assumption of Markovian noise such that the noise on each cycle of independent single-qubit gates is independent of the specific gates being implemented (see appendix F.1), we prove that CB is robust to SPAM errors and that the number of measurements required to estimate the process fidelity to a fixed precision is approximately independent of the number of qubits. We demonstrate the practicality of CB for many-qubit systems by using it to experimentally estimate the process fidelity of both non-entangling Pauli operations and the multi-qubit entangling MS-gate [83, 84] acting on up to ten qubits. We also confirm that the protocol and analysis methods, derived under theoretical assumptions, produce consistent results in our experimental system.

5.3.1 *Cycle benchmarking protocol*

We now outline how the CB protocol can quantify the effect of global and local error mechanisms affecting different primitive cycle operations of interest.

Mathematically, the ideal operation of interest is described by the corresponding unitary matrix G. Its action is expressed by a map $\mathcal{G} : \rho \to G\rho G^\dagger$ that acts on the state of the quantum register, described by the density matrix ρ. We denote the map of an ideal operation by capital calligraphic letters, such as $\mathcal{G}$, and their noisy experimental implementations will be indicated by an overset tilde, such as $\tilde{\mathcal{G}}$. We denote the composition of gates by the natural matrix operations for the map representation, so, e.g., $\mathcal{RG}$ means first apply $\mathcal{G}$ then apply $\mathcal{R}$, and $\mathcal{G}^m$ means apply $\mathcal{G}$ a total of m times. A particularly important class of processes are Pauli cycles $\mathcal{P}$, where the unitary matrix of the process is the N-qubit Pauli matrix P.

We evaluate the quality of a noisy process $\tilde{\mathcal{G}}$ by its process fidelity to the ideal target $\mathcal{G}$, which can be written as [133]

$$F(\tilde{\mathcal{G}}, \mathcal{G}) = \sum_{P \in \{I,X,Y,Z\}^{\otimes N}} 4^{-N} F_P(\tilde{\mathcal{G}}, \mathcal{G}), \tag{5.13}$$

where

$$F_P(\tilde{\mathcal{G}}, \mathcal{G}) = 2^{-N} \operatorname{tr}\left[\mathcal{G}(P)\tilde{\mathcal{G}}(P)\right]. \tag{5.14}$$

Each quantity $F_P(\tilde{\mathcal{G}}, \mathcal{G})$ can be experimentally estimated by preparing an eigenstate of P, applying the noisy gate $\tilde{\mathcal{G}}$, and then measuring the expectation value of the ideal outcome $\mathcal{G}(P)$. The process fidelity may be estimated by averaging $F_P(\tilde{\mathcal{G}}, \mathcal{G})$ over a set of Pauli matrices. However, a sampling protocol (as in direct fidelity estimation [133, 134]) for estimating these individual terms is not robust to SPAM errors. Robustness to SPAM is particularly important because SPAM errors can dominate the gate errors.

Inspired by randomized benchmarking [21], SPAM errors can be decoupled from the process fidelity by applying the noisy operation of interest $\tilde{\mathcal{G}}$ a total of m times and extracting the process fidelity from the decay of $F_P(\tilde{\mathcal{G}}^m, \mathcal{G}^m)$ as a function of the sequence length m. Extracting a meaningful error per application of the gate of interest is nontrivial for generic noise channels [147]. However, decay rates can be extracted straightforwardly for Pauli noise channels, that is, classical mixtures of Pauli operations that are applied to the register randomly with given probability. Mathematically, a Pauli noise channel is a map

$$\mathcal{E} : \rho \to \sum_{P \in \{I,X,Y,Z\}^{\otimes N}} \mu(P) P\rho P^\dagger \tag{5.15}$$

for some probability distribution μ. Such channels cannot exactly describe, for example, small over-rotation errors or amplitude damping channels.

Since the noise in our system is generic, we want to engineer the noise such that it can be described well by a Pauli noise channel. It has been shown that this can be accomplished by introducing a random Pauli cycle $\mathcal{R}$ at each time step between each application of the cycle of interest $\mathcal{G}$ [148](Wallman and Emerson, manuscript in preparation). This additional random Pauli cycle $\mathcal{R}$ comes with an additional overhead that will increase the number required gates to implement a given algorithm. Randomized Compiling (RC) has been developed to eliminate this overhead [146]. The resulting noise channel when using RC is then associated with the composition of $\mathcal{G}$ with a random Pauli cycle $\mathcal{R}$, called a dressed cycle $\mathcal{GR}$, which is an important characterization primitive for any algorithm implemented via randomized compiling [146]. Therefore CB estimates the average of the process fidelities of the dressed cycle $\tilde{\mathcal{G}}\tilde{\mathcal{R}}$

$$F_{\mathrm{RC}}(\tilde{\mathcal{G}}, \mathcal{G}) = \sum_{\mathcal{R} \in \{\mathcal{I},\mathcal{X},\mathcal{Y},\mathcal{Z}\}^{\otimes N}} 4^{-N} F(\tilde{\mathcal{G}}\tilde{\mathcal{R}}, \mathcal{GR}). \tag{5.16}$$

In addition to the dressed cycle fidelity, the process fidelity of the noisy gate $\tilde{\mathcal{G}}$ alone is of interest. The process fidelity of a specific gate $\tilde{\mathcal{G}}$ may be estimated by taking the ratio of the estimates obtained for $\tilde{\mathcal{G}}$ and the identity process $\tilde{\mathcal{I}}$, in analogy to interleaved benchmarking [149]. It should be noted that this method of estimating the fidelity of the noise on $\tilde{\mathcal{G}}$ alone is generally subject to a large systematic uncertainty [150], so the CB method is most precise in the important context of characterizing errors on dressed cycles [146].

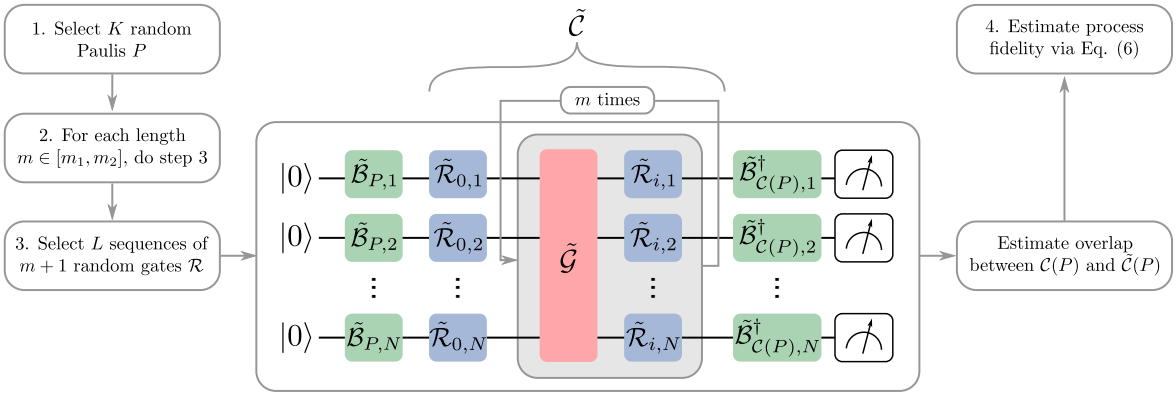

Figure 5.5: **Schematic circuit implementation of the experimental cycle benchmarking protocol.** The protocol can be subdivided into three parts, depicted by the different colors. The green gates $\tilde{\mathcal{B}}$ describe basis changing operations for the State Preparation and Measurement (SPAM) procedure. The red gates $\tilde{\mathcal{G}}$ are the noisy implementations of some gate of interest (in this work the global MS-gate acting on all qubits). The blue gates are random Pauli cycles that are introduced to create an effective Pauli channel per application of the gate of interest, where $\tilde{\mathcal{R}}_{i,j}$ denotes the j^{th} tensor factor of the i^{th} gate. Creating an effective Pauli channel per application enables errors to be systematically amplified under m-fold iterations for more precise and SPAM-free estimation of the errors in the interleaved red gates $\tilde{\mathcal{G}}$. The blue and the red gates together form the random circuit $\tilde{\mathcal{C}}$. The sequence of local operations before the first and last rounds of random Pauli cycles are identified as conceptually distinct but were compiled into the initial and final round of local gates in the experiment. The experimental parameters K, m, and L of this work and the exact definitions of $\tilde{\mathcal{B}}$ and $\tilde{\mathcal{R}}$ are given in section 6.1.

CB can be used to efficiently characterize non-Clifford gates by selecting random gates and correction operators using RC [146]. However, the general protocol for non-Clifford gates is more complex, so a simplified version for characterizing the errors occurring under a fixed cycle of Clifford gates $\mathcal{G}$ composed with a random Pauli cycle $\mathcal{R}$ is as follows (the protocol is illustrated in fig. 5.5, where we explain the motivation for each step further below):

1. Select a set of N-qubit Pauli matrices P with $K = |\mathsf{P}|$ elements.
2. Select two lengths m_1 and m_2 such that the multiple application of $\mathcal{G}$ composes to the identity $\mathcal{G}^{m_1} = \mathcal{G}^{m_2} = \mathcal{I}$.
3. Perform the following sequence for each Pauli matrix $P \in \mathsf{P}$, length $m \in (m_1, m_2)$, and $l \in (1, \ldots, L)$, where L describes the number of random sequences per Pauli.

3a. Select $m+1$ random N-qubit Pauli cycles $\mathcal{R}_0, \mathcal{R}_1, \ldots, \mathcal{R}_m$, and define the randomized circuit

$$\mathcal{C}(P) = \mathcal{R}_m \mathcal{G} \mathcal{R}_{m-1} \mathcal{G} \ldots \mathcal{R}_1 \mathcal{G} \mathcal{R}_0 \tag{5.17}$$

as illustrated in fig. 5.5.

3b. Calculate the expected outcome of the sequence $\mathcal{C}(P)$ assuming ideal gate implementations.

3c. [Main experiment] Implement $\mathcal{C}(P)$ and estimate the overlap

$$f_{P,m,l} = \mathrm{tr}[\mathcal{C}(P)\,\tilde{\mathcal{C}}(\rho)] \tag{5.18}$$

between the expected outcome and the noisy implementation $\tilde{\mathcal{C}}(\rho)$ for some initial state ρ that is a $+1$-eigenstate of P. State preparation and measurement are realized by applying the operations $\tilde{\mathcal{B}}_P$ and $\tilde{\mathcal{B}}^{\dagger}_{\mathcal{C}(P)}$ that are described in appendix F.2.

4. Estimate the composite process fidelity via

$$F_{\mathrm{RC}}(\tilde{\mathcal{G}}, \mathcal{G}) = \sum_{P \in \mathsf{P}} \frac{1}{|\mathsf{P}|} \left(\frac{\sum_{l=1}^{L} f_{P,m_2,l}}{\sum_{l=1}^{L} f_{P,m_1,l}} \right)^{\frac{1}{m_2 - m_1}} . \tag{5.19}$$

Step 1 ensures that the action of the N-qubit process is accurately estimated. In appendix F.5 we prove that the uncertainty of the fidelity estimate is independent of the number of qubits N, and the number of Pauli matrices K that need to be sampled depends only on the desired precision. This highlights the scalability of the protocol for large quantum processors.

Step 2 ensures that the measurement procedures for circuits in eq. (5.17) with two different values of m are the same. Having the same measurement procedures for the two values of m is crucial to decouple the SPAM errors from the decay in the process fidelity via the ratio in eq. (5.19). In our experiment, we always choose $m_1 = 4$ and m_2 to be an integer multiple of 4 as, for the considered gates, applying the operation four times subsequently yields the identity process $\mathcal{G}^4 = \mathcal{I}$.

In step 3a, we choose random Pauli cycles to engineer an effective Pauli noise process across the L randomizations. This enables us to extract a process fidelity from the decay of $\sum_{l=1}^{L} f_{P,m,l}/L$ with the sequence length m. Note that unlike typical randomized benchmarking protocols, the above protocol does not have an inversion gate. Formally, the final random Pauli can be regarded as a correction gate for the random Pauli gates in the rest of the circuit composed with another random Pauli that we use to isolate exponential decays as in character benchmarking [151].

In step 3b, for any Clifford cycle $\mathcal{G}$, Pauli matrix P, and Pauli cycles $\mathcal{R}_0, \ldots, \mathcal{R}_m$ the expected outcome of the ideal implementation $\mathcal{C}(P)$ is a Pauli matrix that can be efficiently calculated. Note that only the sign of $\mathcal{C}(P)$ depends on the random Pauli cycles. This sign is accounted for when estimating the expectation value with the procedure outlined in appendix F.3. Incorporating the sign engineers a measurement of the expectation value of $\mathcal{C}(P)$ that is robust to SPAM errors, as otherwise the expectation values result from a multi-exponential decay [147, 151].

In step 3c, we experimentally prepare an eigenstate of a Pauli matrix P, apply a circuit $\tilde{\mathcal{C}}$ with interleaved random Pauli cycles, and measure the expectation value of $\mathcal{C}(P)$. The explicit procedures we use for preparing the eigenstate and measuring the expectation value are described in appendix F.2. As discussed in appendix F.5, the number of measurements required to estimate the expectation value to a fixed additive precision is independent of the number of qubits.

As we prove in appendix F.4, the expected value of $F_{\mathrm{RC}}(\tilde{\mathcal{G}}, \mathcal{G})$ in eq. (5.19) for two values of m_1 and m_2 as in step 2 is equal to the composite process fidelity $F_{\mathrm{RC}}(\tilde{\mathcal{G}}, \mathcal{G})$ in eq. (5.16) up to $\mathcal{O}([1 - F_{\mathrm{RC}}(\tilde{\mathcal{G}}, \mathcal{G})]^2)$, and always provides a lower bound.

6

CHARACTERIZATION OF A SCALABLE ION TRAP QUANTUM COMPUTER USING CYCLE BENCHMARKING

The content of this chapter is extracted from Ref. [25]

The rigorous characterization of quantum operations offers the ability to compare different quantum computers and provides means for error analysis that can help to overcome limitations of current quantum computers. As motivated in chapter 5, Cycle Benchmarking (CB) is one of the most efficient ways to characterize quantum processes.

Here, we demonstrate the practicality of CB for multi-qubit systems by using it to experimentally estimate the process fidelity of cycles acting globally on quantum registers containing 2, 4, 6, 8, and 10 qubits. The specific cycles we consider consist of simultaneous local Pauli gates and multi-qubit entangling MS-gates combined with simultaneous local Pauli gates.

6.1 EXPERIMENTAL METHODS

The CB experiments are defined by a sequence of N-qubit Clifford gates according to the experimental protocol in fig. 5.5. We use two distinct types of Clifford gates, non-entangling and thus *local* Clifford gates (gates $\tilde{\mathcal{B}}$ in green and gates $\tilde{\mathcal{R}}$ in blue in fig. 5.5) and the fully entangling MS($\frac{\pi}{2}$)-gates (gates $\tilde{\mathcal{G}}$ in red in fig. 5.5), which act on all N-qubits in the register simultaneously. A local Clifford gate consists of a set $\mathcal{R} = \bigotimes_{j=1}^{N} R_j$ of individual single-qubit Clifford operations R_j acting on qubit j (see appendix E).

Following the protocol outlined in section 5.3.1, we need to implement various random sequences. These platform independent sequences are then compiled into the actual machine language [152]. In the presented experiments an elementary single qubit operation consist of addressed z-rotations sandwiched between two collective rotations around the x- or y-axis, e.g. $X(\pi/2)_1 = X(-\pi/4)_{12}Z(\pi)_1X(\pi/4)_{12}Z(\pi)_1$ for 2 qubits. The collective x- and y-rotations can be seen as simple basis changes on the entire register, and thus these basis changes can be shared by the individual qubit operations. By changing the temporal order of the collective x-, y-rotations and the individual z-rotations, the number of operations can be minimized. In fig. 6.1 we show the average number of operations per Clifford depending on the register size for the *direct* compilation of every single-qubit Clifford gate alone and for the *optimized* compilation, where the N single-qubit Clifford gates are compiled together. These results are obtained from the analysis of the implemented random sequences presented in table 6.1.

Since a local N-qubit Clifford operation contains N single-qubit Clifford operations, the average number of single-qubit rotations per local N-qubit Clifford operation scales linearly with N. To reduce the number of calibration measurements we only perform $\pi/2$ rotations. Thus e.g. a $Z(\pi)_j$ operation is implemented using two $Z(\pi/2)_j$ operations. On average we implement $1.27(2) \cdot N$ addressed $\pi/2$ rotations for a local N-qubit Clifford operation in the optimized case.

In table 6.1 we give an overview of the experimental parameters that were used to estimate the local CB and the dressed MS fidelities. The number of subspaces K describes

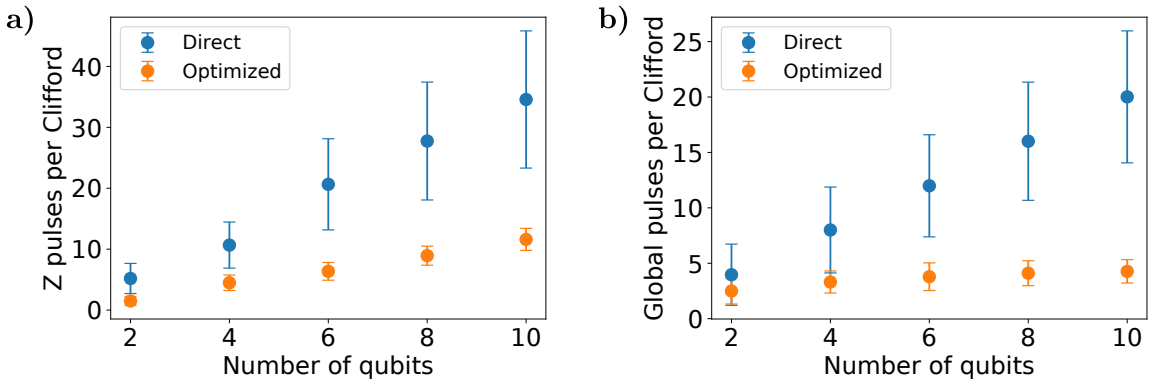

Figure 6.1: **Gate count versus register size.** Average number of **a)** $Z(\pi/2)_j$ and **b)** global operations needed to implement a local N-qubit Clifford gate. Here we compare the *direct* compilation of each single-qubit Clifford gate alone with pulse sequences that are *optimized* over the N-qubit register. The error bars represent the standard deviation of operation occurrences, as each Clifford gate contains a different number of $Z(\pi/2)_j$ and global operations.

the number of individual Pauli channels we explore. For each sequence length m we measure L different random sequences. We implement each sequence twice, once with and once without interleaved MS-gates, hence the total number of sequences is $T = 2 \cdot K \cdot n(m) \cdot L$, where $n(m)$ is the number of different lengths. We repeat every sequence $R = 100$ times to measure the outcome probabilities and to keep the projection noise below 5 %.

Table 6.1: **Parameters for the CB experiments.** Presented are the number of subspaces K, the sequence lengths m and the number of random sequences L for different register sizes. Since we implement each sequence twice, once with and once without interleaved MS-gates, the total number of sequences is $T = 2 \cdot K \cdot n(m) \cdot L$, where $n(m)$ is the number of different lengths and each individual sequence is repeated R times.

Qubits	K	m	L	T	R	Meas. time (h)
2	15	4, 40	10	600	100	2.6
4	255	4, 20	10	10200	100	15.7
6	43	4, 8, 12	10	2580	100	3.4
8	24	4, 8	10	960	100	2.0
10	21	4, 8	10	840	100	1.9

6.2 TESTING THE DEPENDENCE OF THE ESTIMATOR ON THE SEQUENCE LENGTH

If the noise in the system is memoryless or Markovian, we expect that the measured expectation values decay exponentially with the sequence length, as can also be seen for example in the single-qubit RB data in section 5.2. Hence, for Markovian noise, the estimated process fidelity is independent of the sequence lengths m_1 and m_2 to within $\mathcal{O}([1 - F_{\mathrm{RC}}(\tilde{\mathcal{G}}, \mathcal{G})]^2)$ (see theorem 3).

We test the dependence of the fidelity estimates on the sequence length by performing measurements at 3 different sequence lengths for 6 qubits, as described in table 6.1. We validate that the estimated process fidelity is independent of m_1 and m_2 by comparing the results of three different length pairs (4-8), (4-12) and (8-12). As can be seen in table 6.2, the estimated fidelities agree to within half a standard deviation, which supports the assumption that the noise in our experimental apparatus is Markovian.

Table 6.2: **6-qubit process fidelities (%) estimated via CB.** The fidelities are estimated using different pairs of sequence lengths $(m_1\text{-}m_2)$. The results illustrate that the estimated process fidelity is independent of the sequence lengths used, subject to the constraint in step 2 of the protocol.

$(m_1\text{-}m_2)$	Local gates	Dressed MS-gate
(4-8)	97.0(2)	91.3(5)
(4-12)	97.0(2)	91.2(4)
(8-12)	96.9(4)	91.3(8)

6.3 TESTING THE DEPENDENCE OF THE FIDELITY UNCERTAINTY ON THE REGISTER SIZE

For a benchmarking method to be scalable, it is important that the required resources do not increase exponentially with the system size. As we have shown in appendix F.5, the variance of the fidelity estimate is independent of the number of qubits N for constant resources. According to eq. (F.29), there exists an upper bound for the standard deviation of the estimated fidelity, that depends on the fidelity itself and the number of Pauli subspaces that have been investigated. Since the process fidelity is reduced for larger register sizes, also the variances themselves are expected to increase with N. We can eliminate the dependence on the fidelity by taking the ratio between the observed standard deviation σ and the theoretical upper bound thereof σ_{Pauli}. If the fidelity uncertainty is independent of N, then also the ratio $\sigma/\sigma_{\mathrm{Pauli}}$ must be independent of N.

In fig. 6.2 we plot the ratio between the standard deviation σ of the measured fidelity and the upper bound σ_{Pauli} against the number of qubits N in the register. In the data we cannot observe a clear trend or dependency of the observed variance relative to the worst-case bound, suggesting that the uncertainty of the fidelity estimate is indeed independent of the register size N. Moreover, since we experimentally benchmarked our quantum computer with similar resources for different qubit numbers N (see table 6.1), we can conclude that CB is scalable.

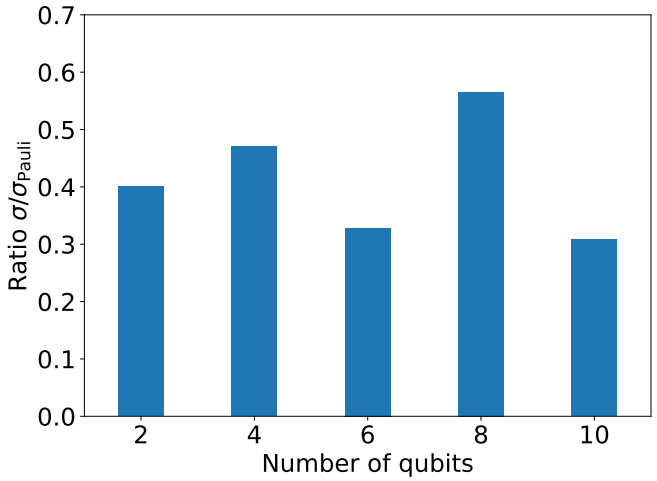

Figure 6.2: **Ratio of measured and theoretically bound fidelity uncertainties.** Ratio between the uncertainty on the fidelity estimate σ and it's theoretical upper bound from sampling Pauli channels σ_{Pauli} against the register size N.

6.4 ANALYZING THE FIDELITY LONG-TERM BEHAVIOR

Slow temperature fluctuations on the timescale of minutes to days cause changes in various components of our experimental apparatus, that can in turn influence the fidelity of the implemented quantum gates.

One of the major causes for a loss in fidelity is the change of the Rabi frequency over time. The Rabi frequency depends on the laser intensity at the position of the ion, as described in section 3.3.1. Temperature fluctuations can for example influence the efficiency of the AOMs or the alignment of the laser beam relative to the ion position. Since the single ion addressing laser beam is tightly focused to a spot size of $\sim 2\,\mu$m, a misalignment of $\sim 200\,$nm leads to a change in Rabi frequency of $\sim 10\,\%$.

We analyze the long-term behavior of the fidelity with 4-qubit CB as depicted in fig. 6.3. The $K = 4^N - 1 = 255$ subspaces were measured in 3 sessions, where the experimental system was recalibrated at the beginning of each session. We approximate the drift of the fidelity to be linear in first order and thus can describe the time dependent fidelity as $F(t) = F_0 - \epsilon t$. We obtain an average loss of fidelity of $\epsilon_{\text{L}} = 3.3(5) \cdot 10^{-3}\,\text{h}^{-1}$ for local gates and $\epsilon_{\text{I}} = 5.4(8) \cdot 10^{-3}\,\text{h}^{-1}$ for the dressed MS-gate, see table 6.3. This measurement suggests that we can expect a maximum loss of fidelity of 1 % when calibrating the apparatus every two hours.

Table 6.3: **4-qubit fidelity drift rates.** Here ϵ_{L} and ϵ_{D} describe the loss of fidelity per hour for local gates and the dressed MS-gate. The data corresponds to the estimated linear slopes of fig. 6.3

Session	ϵ_{L} (h^{-1})	ϵ_{D} (h^{-1})
1	$3.9(8) \cdot 10^{-3}$	$8.9(1.5) \cdot 10^{-3}$
2	$3.1(5) \cdot 10^{-3}$	$3.2(6) \cdot 10^{-3}$
3	$3.0(1.1) \cdot 10^{-3}$	$4.2(1.7) \cdot 10^{-3}$
Average	$3.3(5) \cdot 10^{-3}$	$5.4(8) \cdot 10^{-3}$

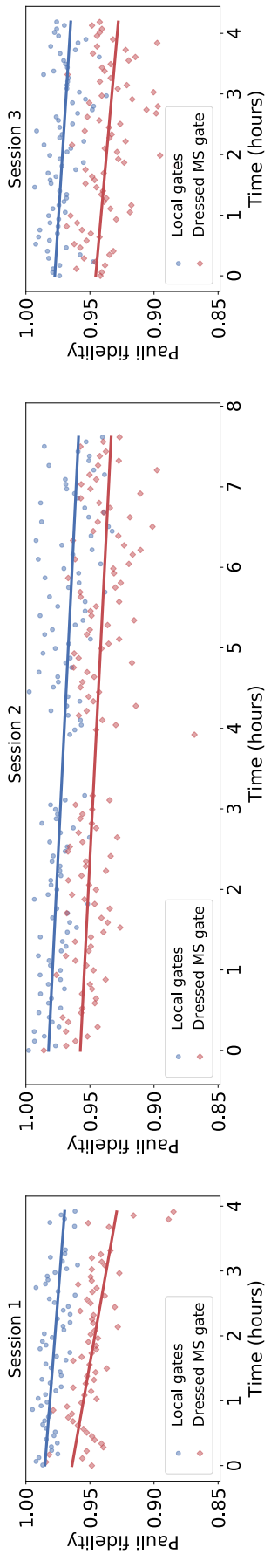

Figure 6.3: **Pauli fidelity estimation over time.** 4-qubit Pauli fidelities for local gates (blue) and the dressed MS-gate (red) plotted on the time in hours. We measured all 255 subspaces in three measurement sessions, where the experiment was recalibrated at the beginning of each session.

6.5 FINITE SAMPLING EFFECTS

The CB protocol is practical to implement on large processors because the fidelity can be accurately estimated using a number of Pauli matrices that is independent of the number of qubits N (see appendix F.5). To illustrate the rapid convergence under finite sample size, we performed CB of local Pauli operations on a 4 qubit register by exhaustively estimating all $4^4 - 1 = 255$ possible decay rates. We estimate the average fidelities via eq. (5.19) for multiple subsets P of the set of all Pauli matrices. For each $K = 1, \ldots, 100$, we evaluate the fidelity for 30 randomly chosen subsets P containing $|\mathsf{P}| = K$ Pauli matrices. The mean and standard deviation of the estimated fidelities as functions of the subset size are shown in fig. 6.4. In fig. 6.4 (b) we introduce two boundaries between which the observed standard deviation should lie if we are choosing appropriate sequence lengths and sample sufficiently many random circuits per sequence length. For the lower bound we assume quantum projection noise to be the only noise source. We evaluate the shot noise for the measured data and perform error propagation to calculate the lower bound $\sigma_{\text{lower}} = 0.00375(1)/\sqrt{K}$. This lower limit could be reached if the noise in the system is completely isotropic (e.g. global depolarizing). Biased noise or drift (see section 6.4) will lead to uncertainties bigger than those originating from quantum projection noise. We furthermore test that the fluctuations between different Pauli channels is bounded by an error model that assumes worst-case fluctuations between channels. This bound does not depend on the register size but only on the fidelity F and can be estimated via $\sigma_{\text{Pauli}} = (1 - F)/\sqrt{K} = 0.0275(8)/\sqrt{K}$ (see appendix F.5).

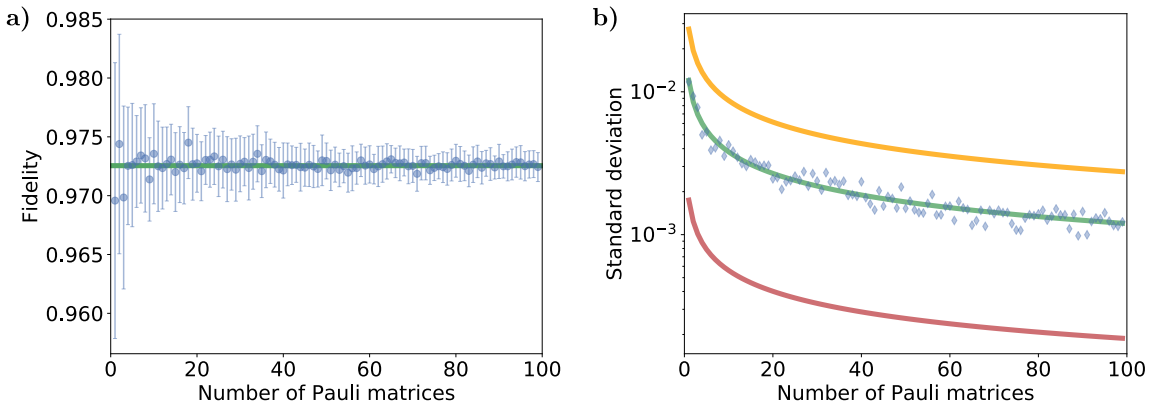

Figure 6.4: **Experimental evidence demonstrating rapid convergence under finite sample size with favorable constant factors. a)** Mean fidelity estimates from 30 randomly sampled subsets of Pauli matrices as a function of the size K of the subset. The error bars illustrate the standard deviation of the 30 samples, that is, the standard error of the mean. The green line describes the mean fidelity $F = 97.25(8)\,\%$ calculated from the complete data set. **b)** The standard deviation of the fidelity from plot **a)** against K including a bound due to finite sampling of Pauli channels $\sigma_{\text{Pauli}} = 0.0275(8)/\sqrt{K}$ in orange, a fit of the standard deviation $\sigma = 0.0127(2)/\sqrt{K}$ in green and a fit of the expected projection noise $\sigma_{\text{lower}} = 0.00375(1)\sqrt{K}$ in red (see appendix F.5).

The observed standard error of the mean $\sigma = 0.0127(2)/\sqrt{K}$ is larger than the lower bound given by quantum projection noise, but smaller than the worst-case bound from sampling finite Pauli channels. The data demonstrate that we can estimate the process

fidelity F to an uncertainty smaller than $(1-F)/\sqrt{K}$ independent of the register size with other experimental parameters held fixed (the parameters are listed in table 6.1).

6.6 CYCLE BENCHMARKING RESULTS

We performed CB on local operations and with an interleaved MS-gate on registers containing 2, 4, 6, 8, and 10 qubits. The process fidelity as a function of the number of qubits in the register is shown in fig. 6.5 and table 6.4. While it is expected that the fidelity over the full register decreases with increasing register size, an important question is whether the effective error rate per qubit increases, or significant cross-talk effects appear, with increasing numbers of qubits.

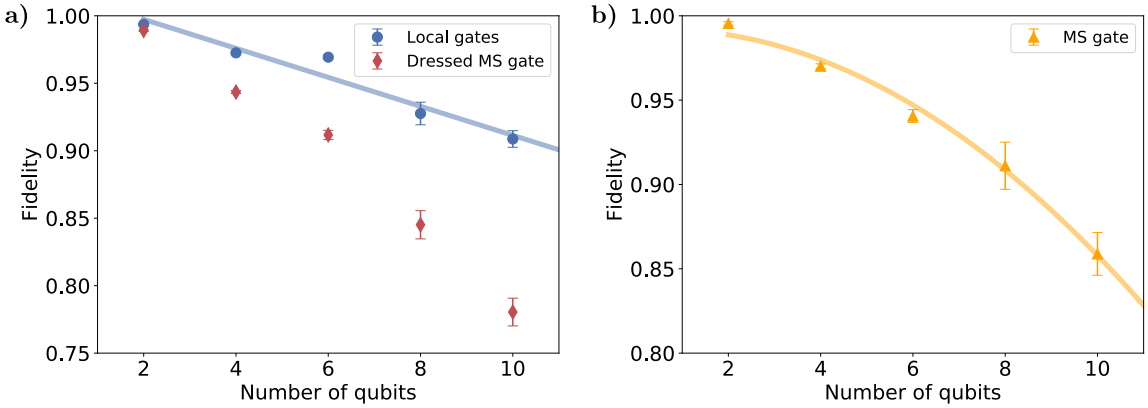

Figure 6.5: **Experimental estimates of how rapidly error rates increase as the processor size increases. a)** Process fidelities obtained under cycle benchmarking for local gates (blue circles) and for sequences containing dressed Mølmer-Sørensen (MS) gates (red diamonds), that is, MS-gates composed with a random Pauli cycle, plotted against the number of qubits in the register. The local operations are consistent with independent errors fitted according to eq. (6.1). **b)** Estimate of the process fidelity of an MS-gate obtained by taking the ratio of dressed MS and local process fidelities. The data is fitted to eq. (6.2) and is consistent with a constant error per two-qubit coupling.

We observe that the fidelity for local CB (blue circles in fig. 6.5 (a)) decays linearly with register size N, as

$$F = 1 - \epsilon_P N, \tag{6.1}$$

with $\epsilon_P = 0.011(2)$. The linear decay of the fidelity indicates that our single-qubit Pauli operations do not show increasing error rates per qubit or a significant onset of cross-talk errors as the register size increases. Each single-qubit Pauli operation requires n_S native gates, where on average $\langle n_S \rangle = 1.27$, independent of the system size. Therefore the effective process fidelity of a native single-qubit gate is $1 - \epsilon_P / \langle n_S \rangle = 0.992(1)$.

The CB measurements with interleaved MS-gates give the process fidelity of the MS-gate composed with a round of local randomizing gates as in eq. (5.16) (a dressed MS-gate, see red diamonds in fig. 6.5 (a)). This determines the error rate when a circuit is implemented by randomized compiling [146]. The process fidelity of the interleaved gate can be estimated by the ratio of the dressed MS and local fidelities as in interleaved randomized benchmarking [149]. The resulting estimates are plotted in fig. 6.5 (b). We note

that these estimates may have a large systematic error that is on the same order as the overall error rate [150]. This systematic uncertainty primarily arises due to coherent over- and under-rotations with similar rotation axes. The MS-gate performs rotations around the non-local axes $\sigma_x^{(i)} \otimes \sigma_x^{(j)}$, which are substantially different from the single-qubit rotation axes. Therefore it is unlikely that any coherent errors on the MS-gate accumulate with the errors on the single-qubit rotations, and so we neglect this systematic error. We conjecture that the process fidelity of the MS-gate should decay quadratically due to an error in each of the $\binom{N}{2}$ couplings between pairs of qubits introduced by the MS-gate. If we assume an average error rate ϵ_2 per two-qubit coupling, we can describe the MS-gate fidelity as

$$F_{\mathrm{MS}} = 1 - \epsilon_2 \frac{N^2 - N}{2} . \tag{6.2}$$

Fitting this model to the results in fig. 6.5 (b) gives an estimated error per two-qubit coupling of $\epsilon_2 = 0.0030(2)$. However, we cannot harness these two-qubit couplings individually in the experiment and thus they cannot be compared to individually available gates. The deviations of the fidelity estimates from the model defined in eq. (6.2) are within the expected statistical uncertainty and we believe that these deviations arise mainly from day-to-day fluctuations in the experiment.

Table 6.4: **Process fidelities (%) estimated via CB.** Measured fidelities for local gates, dressed MS-gates and the inferred MS-gate fidelity as depicted in fig. 6.5.

Qubits	Local gates	Dressed MS-gate	MS-gate
2	99.37(7)	98.92(8)	99.6(1)
4	97.25(8)	94.3(1)	97.0(2)
6	96.9(2)	91.2(3)	94.1(4)
8	92.8(8)	85(1)	91(2)
10	90.9(6)	78(1)	86(2)

7

QUANTUM ERROR CORRECTION PROTOCOLS

We have learned that it is possible
to fight entanglement with entanglement.

— John Preskill [9]

The content of this chapter is partly extracted from Ref. [153]

The improvement of quantum computing architectures from early designs and current Noisy Intermediate-Scale Quantum (NISQ) devices [26] to full-fledged quantum computers hinges on achieving fault-tolerance using QEC [9, 26, 154–156]. The basis of QEC is storing and manipulating quantum information distributed over blocks of physical qubits that form logical qubits. A number of experiments have demonstrated significant technological progress towards Quantum Error Correction (QEC) [157–162], including the creation of non-trivial QEC codes [163, 164], error detection [165–167], correction of errors [168–171] and qubit loss [172], and operations on single [173–178] and on two logical qubits in non-topological codes [179, 180].

The principles of QEC and the resulting scaling of error rates are explained in section 7.1. As introduced in section 2.4, one of the most promising road towards QEC is offered by topological codes, which require only short-range interactions in 2D architectures [40, 181, 182]. In section 7.2 the stabilizer formalism, a versatile tool used in many QEC codes, is presented. One prominent example of topological codes is the surface code [44, 183, 184], which is outlined in section 7.3.

7.1 PRINCIPLES OF QUANTUM ERROR CORRECTION

Similar to the concept of classical error correction, the basic idea of QEC is to utilize redundancy to reduce the effective error rate [9]. In contrast to classical error correction, due to the non-cloning theorem [9] the information in a quantum computer cannot simply be copied from one qubit to another. It also not possible to just measure a qubit, to check whether an error has occured, because the measurement would project any superpostition into the measurement basis and hence destroy the quantum state.

Furtunately, these difficulties are not a fundamental problem that prevent QEC to work, as will be explained in the following. An arbitrary single qubit error can be decomposed into Pauli X and Pauli Z errors, similar to the state of a single qubit described in section 2.1. For simplicity, we assume first that a single qubit is only affected by an X-type or bit-flip error with probability p that maps the quantum state ρ as $\mathcal{E}(\rho) = (1-p)\rho + pX\rho X$ e.g. $\mathcal{E}(|0\rangle\langle 0|) = (1-p)|0\rangle\langle 0| + p|1\rangle\langle 1|$. The simplest code to protect a qubit against a bit-flip error is the three qubit repetition code [9, 185]. Note that this code is not able to correct Z-type (phase-flip) errors.

In the three qubit repetition code we encode a single logical qubit into three *phyiscal* or *data* qubits as $|0_L\rangle = |000\rangle$ and $|1_L\rangle = |111\rangle$. Thus, an arbitrary logical state is defined as $|\psi_L\rangle = \alpha\,|000\rangle + \beta\,|111\rangle = \alpha\,|0_L\rangle + \beta\,|1_L\rangle$. We assume that single qubit X errors occur uncorrelated on any of the three data qubits with probability p. After a single qubit error has

occured, the logical qubit is in one of four possible states, that can be detected by measuring the following projectors [9]

$$P_0 = |000\rangle\langle 000| + |111\rangle\langle 111| \quad \text{No error,} \tag{7.1}$$
$$P_1 = |100\rangle\langle 100| + |011\rangle\langle 011| \quad \text{Error on qubit 1,} \tag{7.2}$$
$$P_2 = |010\rangle\langle 010| + |101\rangle\langle 101| \quad \text{Error on qubit 2,} \tag{7.3}$$
$$P_3 = |001\rangle\langle 001| + |110\rangle\langle 110| \quad \text{Error on qubit 3,} \tag{7.4}$$

where we deduce whether an error has occured on a data qubit via majority voting. The outcomes of the projective measurements are called *error syndromes*. If the logical qubit is e.g. in the corrupted state $|\psi_L\rangle = \alpha\,|100\rangle + \beta\,|011\rangle$, the measurement $\langle\psi_L|P_1|\psi_L\rangle = 1$ reveals that a bit flip has happened on the first qubit. Note that this measurement does not destroy the qubit state, since the state $|\psi_L\rangle = P_1\,|\psi_L\rangle$ is the same before and after the measurement. Knowing what error has occured on which qubit, we can apply a correcting X operation on qubit 1 to recover the logical qubit state $|\psi_L\rangle = \alpha\,|000\rangle + \beta\,|111\rangle$. Since qubits can only be measured individually in the experiment, the measurement projectors in eqs. (7.1) to (7.4) cannot be implemented directly on the data qubits. Therefore, the error syndroms are mapped onto *auxiliary* or *syndrome* qubits, which can be individually measured in-sequence without disturbing the state of the data qubits, as explained in section 7.2.1. As can be seen in eqs. (7.1) to (7.4), in the case of the three qubit repetition code there exist four error syndroms, which require two auxiliary qubits that can store these two bits of information.

If no or at most one single qubit error occurs, the error correction works perfectly, otherwise it fails. Since the probability for a single qubit error is p, the combined probability that any other error (two or more qubit X errors) occurs and the error correction fails is $p_e = 3p^2(1-p) + p^3$ [9]. If the error rate is low enough $p < 0.5$, a single qubit error is more likely than any other error $p > p_e$ and the error correction procedure works on average. Consequently, the repeated implementation of the three qubit repetition code reduces the error probability from p to $p_e \propto \mathcal{O}(p^2)$ on average provided that $p < 0.5$.

In section 7.3 a more complex code, the surface code is introduced, that is able to correct arbitrary single qubit errors.

In general, QEC codes are classified by the number triplet $[N, k, d]$, where N is the number of physical qubits, k describes the number of encoded qubits and d is the code distance. The distance d of the code is the minimal Hamming distance between codewords, i.e., the required minimum number of single-qubit Pauli operators mapping any one codeword to another. Since the correction procedure is based on majority voting, a code with distance d can generally correct up to $(d-1)/2$ errors and detect up to $d-1$ errors.

7.2 STABILIZER CODES

In this section we outline a framework to describe QEC codes in a very compact fashion [9].

If every element of a group $\mathcal{G}$ can be written as a product of elements from the subgroup $\{g_1, ..., g_n\}$, we write $\mathcal{G} = \langle g_1, ..., g_n\rangle$ and we call the elements $g_1, ..., g_n$ the *generators* of the group $\mathcal{G}$. Consider the set of single qubit Pauli operators $P = \{I, X, Y, Z\}$, then the Pauli group for a single qubit is defined as the Pauli operators up to multiplication with $\{\pm 1, \pm i\}$ as [9]

$$\mathcal{P}_1 = \Big\{\pm I, \pm iI, \pm X, \pm iX, \pm Y, \pm iY, \pm Z, \pm iZ\Big\} = \langle iI, X, Z\rangle, \tag{7.5}$$

where the matrices iI, X, Z are the generators of the group. For an N-qubit system the Pauli group consists of the N-fold tensor products of Pauli matrices as

$$\mathcal{P}_N = \Big\{ s \cdot \sigma_1 \otimes \cdots \otimes \sigma_N \quad | \quad s \in \{\pm 1, \pm i\};\ \sigma_i \in P \Big\}. \tag{7.6}$$

Suppose a state $|\psi\rangle$ is a $+1$ eigenstate of an operator S such that $S|\psi\rangle = +1|\psi\rangle$, then we say that the state $|\psi\rangle$ is *stabilized* by the operator S. If a set of states $C = \{|\psi_i\rangle\}$ is stabilized under the action of elements of the group $\mathcal{S} = \{S_i\}$, $\mathcal{S}$ is called a *stabilizer* [9]. Specifically, the stabilizer $\mathcal{S}$ is a subgroup of the Pauli group $\mathcal{P}_N$ acting on the vector space C such that

$$\mathcal{S} = \Big\{ S_i \in \mathcal{P}_N \quad | \quad S_i|\psi_j\rangle = +1|\psi_j\rangle \ \forall\ |\psi_j\rangle \in C \Big\}. \tag{7.7}$$

We can now use stabilizers to define QEC codes. Suppose we encode k logical qubits into N physical qubits, then the $[N, k, d]$ stabilizer code is defined as the code space C stabilized by the subgroup $\mathcal{S}$ of $\mathcal{P}_N$ such that $-I \notin \mathcal{S}$ and $\mathcal{S}$ has $N-k$ independent and commuting generators $\mathcal{S} = \langle g_i, ..., g_{N-k} \rangle$ [9]. We denote the code as $C(\mathcal{S})$. Finally, for each of the k encoded qubits we choose the set of logical Pauli operators $\{X_L, Z_L\}$ which obey the same commutation relation as the single qubit Pauli matrices. In principle, we can choose any 2^k orthonormal vectors in $C(\mathcal{S})$ to act as logical operators, but typically we use a systematic way to define the logical operators as described in Ref. [9].

As an example we come back to the three qubit repetition code introduced in the previous section with the codewords $|0_L\rangle = |000\rangle$ and $|1_L\rangle = |111\rangle$. The code stabilizers are mutually commuting operators S_i in the three-qubit Pauli group $\mathcal{P}_3$ that map the code subspace to itself while acting as identity on the encoded information, i.e., $S_i|0_L\rangle = |0_L\rangle$, $S_i|1_L\rangle = |1_L\rangle$ and $[S_i, S_j] = 0$. Since our code consists of three physical qubits while encoding a single logical qubit, we can expect to find two independent, commuting Pauli operators with this property. Indeed, we find $S_1 = Z_1Z_2$ and $S_2 = Z_2Z_3$ which can be used to generate a group $\mathcal{S}$ under multiplication, i.e., $\mathcal{S} = \langle S_1, S_2 \rangle = \{\mathbb{I}, S_1, S_2, S_1S_2\}$. Since the code subspace is an eigenspace of these operators we can simultaneously measure all stabilizers without disturbing the logical information. Without errors, measuring stabilizers will always result in the same outcome, namely $+1$. However, were an error X_1 to occur, the measurement outcome of stabilizer S_1, its so-called *syndrome* s_1, would change sign since $\{S_1, X_1\} = 0$. The only other combination of X-errors that could possibly lead to the syndromes $s_1 = -1$ and $s_2 = +1$ is a two-qubit error X_2X_3, that is not correctable. In practice, we collect these syndromes by measuring auxiliary qubits, so-called *syndrome qubits*, which encode the eigenvalues of associated stabilizers. That is, a projective stabilizer measurement can be performed by entangling data qubits with a syndrome qubit and measuring the latter. As a result, we end up with the same majority vote as before but without measuring the logical state of the encoded qubit.

In this formalism, the group of operators that leaves the stabilizer group invariant, called the *normalizer* $N(\mathcal{S}) \subset \mathcal{P}_3$, defines the logical operations. We are only considering Pauli operators and hence, the group of operators that commutes with all stabilizers, called the *centralizer* $C(\mathcal{S})$ of $\mathcal{S}$ is also the normalizer. Since this definition includes stabilizers themselves, we define the group of logical operators as a quotient group $\mathcal{L} = N(\mathcal{S})/\mathcal{S}$ such that logical operators form equivalence classes under multiplication with stabilizers. In the three qubit case, the equivalence classes are $[\mathbb{I}]_\mathcal{S}, [Z_1]_\mathcal{S}, [X_1X_2X_3]_\mathcal{S}$, i.e., one for each logical operation.

QEC is done to protect our encoded information from nontrivial logical errors in $\mathcal{L}$. Since we are only considering products of Pauli operators, elements of $\mathcal{L}$ are also just products

of Pauli operators. This allows us to infer the minimum number of single-qubit errors composing a logical error, i.e., its *distance d*. To see this, consider the nontrivial operator $Z_L \in \mathcal{L}$ and its weight $w(Z_L)$ which is the number of nontrivial terms in the product of Pauli operators. In our example, $Z_L = Z_1$, i.e., its weight is 1 and a single-qubit Z-error can cause a logical Z-error. In other words, the above code can tolerate no Z-errors and its distance is therefore $d = 1$. However, w.r.t. logical X-operators $[X_1X_2X_3]_{\mathcal{S}}$, the minimum weight of any logical X-operator is $d = 3$ such that the code can correct 1 and detect 2 X-errors.

In summary, stabilizer codes require us to measure stabilizers and extract syndromes throughout a quantum computation. The syndromes are then analyzed by a majority vote to infer the errors that have occurred. Logical operators are operators that commute with all stabilizers but are not stabilizers themselves.

7.2.1 *Stabilizer readout*

In QEC we need to be able to measure the error syndrome during the computation without affecting the logical quantum state. This is achieved by mapping the eigenvalue of the stabilizer onto an auxiliary qubit A. As in the previous section, we use as an example the three qubit repetition code and encode one logical qubit on three data qubits with the codewords $|0_L\rangle = |000\rangle$ and $|1_L\rangle = |111\rangle$. In the correction procedure it is necessary to measure the expectation value of the stabilizer Z_2Z_3, since it is one of the code stabilizers. A standard circuit diagram and a circuit diagram for ion trap experiments of the Z_2Z_3 stabilizer readout are depicted in fig. 7.1 **a)** and **b)**. As can be seen in fig. 7.1 **a)**, the circuit consists only of two CNOT operations between the data and the auxiliary qubits. During computation the logical qubit is in some unknown state $|\psi_L\rangle = \alpha\,|0_L\rangle + \beta\,|1_L\rangle$. Since $Z_2Z_3\,|\psi_L\rangle = (-1)^m\,|\psi_L\rangle$, the measurement outcome $m \in \{0, 1\}$ of the auxiliary qubit reveals the eigenvalue of the Z_2Z_3 stabilizer without disturbing the logical state. Note, that although we use entangling gates to map the eigenvalue of the stabilizer onto an auxiliary qubit A, ideally this syndrome qubit does not get entangled with the data qubits.

To measure an X-type stabilizer we introduce basis changing operations on the data qubits, as illustrated in fig. 7.1 **c)** and **d)**. More details on stabilizer readout for ion-trap architectures can be found in Ref. [186].

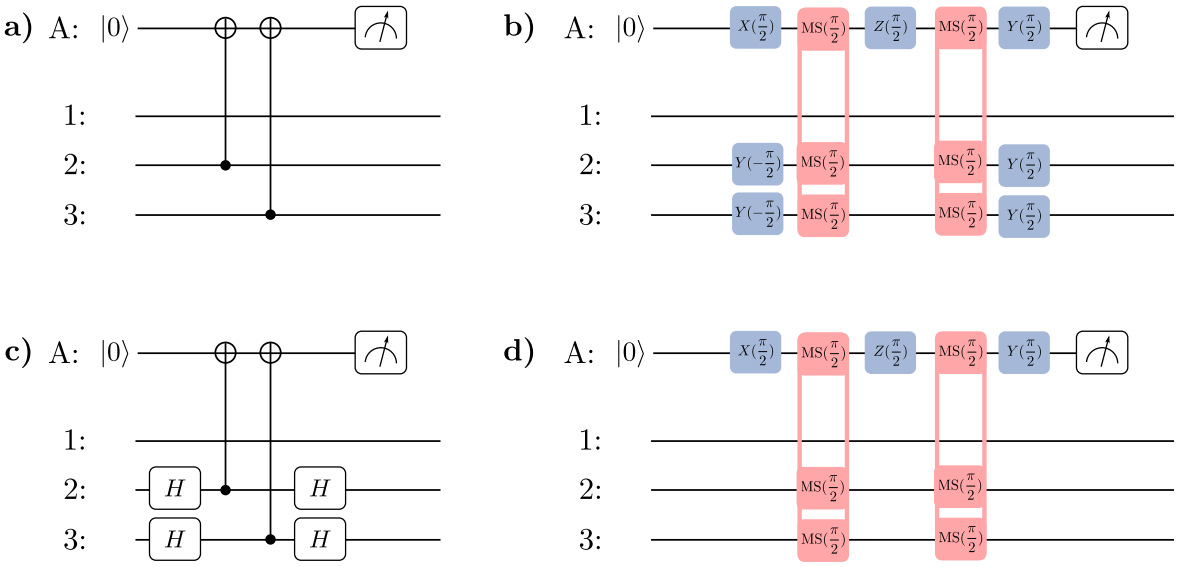

Figure 7.1: **Stabilizer readout.** Standard circuit model representation of stabilizer readouts are presented in **a)** and **c)** and the respective implementation thereof in our ion-trap quantum computer is depicted in **b)** and **d)**. As an example the Z_2Z_3 stabilizer readout is shown in **a)** and **b)** and the X_2X_3 stabilizer measurement is illustrated in **c)** and **d)**.

7.3 SURFACE CODE

Here, we consider a general construction of surface codes in the stabilizer formalism. Consider N qubits laid out on the vertices V of a bicolored square lattice as displayed in Fig. 7.2. We associate a stabilizer with each colored plaquette $p_{x,z} \in P_{x,z}$ as follows,

$$S^X_{p_x} = \prod_{v \in \mathcal{N}(p_x)} X_v \tag{7.8}$$

$$S^Z_{p_z} = \prod_{v \in \mathcal{N}(p_z)} Z_v \tag{7.9}$$

where $\mathcal{N}(p_{x,z}) \subset V$ is the set of vertices neighboring a plaquette $p_{x,z}$ and P_x is the set of orange faces and P_z is the set of every other aquamarine plaquettes. Hence, X-Stabilizers S^X are placed on orange plaquettes while Z-Stabilizers S^Z are placed on aquamarine plaquettes. Since neighboring plaquettes always share two vertices, stabilizers commute for all $p \in P = P_x \cup P_z$. For the lattice under consideration, there are $s = N - 1$ independent, commuting

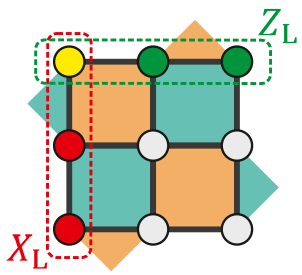

Figure 7.2: **Standard surface code of distance 3.** The standard surface code is defined on a square lattice with (data) qubits located on vertices. Stabilizers are associated with faces and boundaries. Aquamarine faces and boundaries indicate Z-type stabilizers as in eq. (7.9). Orange faces and boundaries indicate X-type stabilizers as in eq. (7.8). The dashed line in red describes a logical Pauli-X operator and the dashed green line defines a logical Pauli-Z operator. The two operators anti-commute at the crossing drawn in yellow.

stabilizers. Therefore, the Hilbert space, which is the simultaneous $+1$ eigenspace of all stabilizers, has $N - s = 1$ degree of freedom. This degree of freedom is a qubit since we can define logical X_L and Z_L Pauli-operators. In the case of the surface code, logical operators are products of Pauli-operators connecting opposite boundaries of the lattice. To see this, consider a line drawn on the lattice connecting top and bottom boundaries as indicated by dashed frames in Fig. 7.2. Placing X-operators on vertices crossed by this line, we obtain an operator commuting with all stabilizers but which is not a stabilizer itself. Therefore, this operator corresponds to a logical operator X_L. At the same time, we can analogously draw a line for the dual lattice connecting left and right boundary. Placing Z-operators along this line, we obtain an operator commuting with all stabilizers but anti-commuting with X_L. Therefore, this product of Pauli-Z operators defines the logical Z-operator Z_L. Note that the shortest line connecting opposite boundaries crosses 3 vertices. Therefore, the code can correct up to one single-qubit error and has distance $d = 3$.

In order to perform QEC, we continuously measure the code stabilizers. Whenever a stabilizer measurement result, i.e., its *syndrome*, changes sign from $+1$ to -1, we have detected an error. Assuming that less than $(d-1)/2$ errors have occurred, we can associate with each syndrome a correction procedure which recovers the state of all $+1$ stabilizers from the erroneous state without causing a logical error.

8

LATTICE SURGERY

The content of this chapter is extracted from Ref. [153]

As motivated in section 2.4, Lattice Surgery (LS) [41, 59, 60] is one of the most resource efficient ways to implement logical operations, where groups of physical qubits, arranged on lattices, can be merged and split. In LS, the QEC code itself is altered by merging and splitting initially separate encodings, rather than operating on all physical qubits. We outline the procedure at the specific expample of LS on two surface code qubits in section 8.1.

Such code modifications can be used to efficiently manipulate logical qubits, or to adapt the robustness of a specific code to different noise processes [187]. LS further enables entanglement generation between logical qubits and can be complemented with measurement-based protocols [57, 188, 189] for logical state teleportation and manipulation [59], as outlined in section 8.1.

8.1 LATTICE SURGERY WITH SURFACE CODE QUBITS

Here, we consider Lattice Surgery (LS) in general as a method to project seperated logical qubits onto a joint eigenstate of their respective logical Pauli operators. In this section we outline only the basic operations of the LS procedure and we give a more detailed description of the experimental implementation thereof in section 8.2.

We illustrate the concept of LS using two 2×2 stabilizer QEC codes $\mathcal{S}^A, \mathcal{S}^B$ with logical Pauli operators $P_{\mathrm{L}}^A \in \{X_{\mathrm{L}}^{\mathrm{A}}, Z_{\mathrm{L}}^{\mathrm{A}}\}, \tilde{P}_{\mathrm{L}}^B \in \{X_{\mathrm{L}}^{\mathrm{B}}, Z_{\mathrm{L}}^{\mathrm{B}}\}$, as depicted in fig. 8.1 **A**. Note that this codes have a distance of $d = 2$, such that they can detect up to 1 single qubit error. The minimum instance of the surface code that is able to correct one single qubit error, is a 3×3 code with distance $d = 3$.

LS proceeds in two steps: *Merging* and *splitting*.

First we *merge* the two separated codes $\mathcal{S}^A, \mathcal{S}^B$ into a new stabilizer code $\mathcal{S}^M$ by projecting onto a joint eigenstate $P_{\mathrm{L}}^A \otimes \tilde{P}_{\mathrm{L}}^B$. In order for this to be fault-tolerant, we measure a number of so-called *merging* stabilizers $\{S_i^M\}_i$ across the boundary such that $\prod_i S_i^M = P_{\mathrm{L}}^A \otimes \tilde{P}_{\mathrm{L}}^B$, as depicted in fig. 8.1 **B**.

Note that surface code LS usually distinguishes Z-type and X-type LS in association with the respective boundaries along which LS is performed. Note that, Z-type and X-type LS therefore refers to a projection onto an $X_L^A X_{\mathrm{L}}^B$ or $Z_L^A Z_{\mathrm{L}}^B$ eigenstate. Let us further point out that one may encounter a different terminology in terms of *rough* and *smooth* LS in the literature [41, 155]. That notation is due to a different surface code representation and may be associated with what we call Z- and X-type LS, respectively.

After the projection, the merged code is just a new surface code $\mathcal{S}^M$ on an asymmetric lattice, as e.g. a 2×4 surface code depicted in fig. 8.1 **B, a** or a 4×2 surface code illustrated in fig. 8.1 **B, b**. The merging stabilizers are just surface code stabilizers at the interface between the two codes. Stabilizers at the boundary that do not commute with the merging stabilizers $\{S_i^M\}_i$ are discarded from the stabilizer group $\mathcal{S}^M$ and only the product of boundary operators remain since they commute. Notably, the merged code encodes only a single logical qubit and $P_{\mathrm{L}}^A \otimes \tilde{P}_{\mathrm{L}}^B$ is contained as a stabilizer. That is, this procedure projects

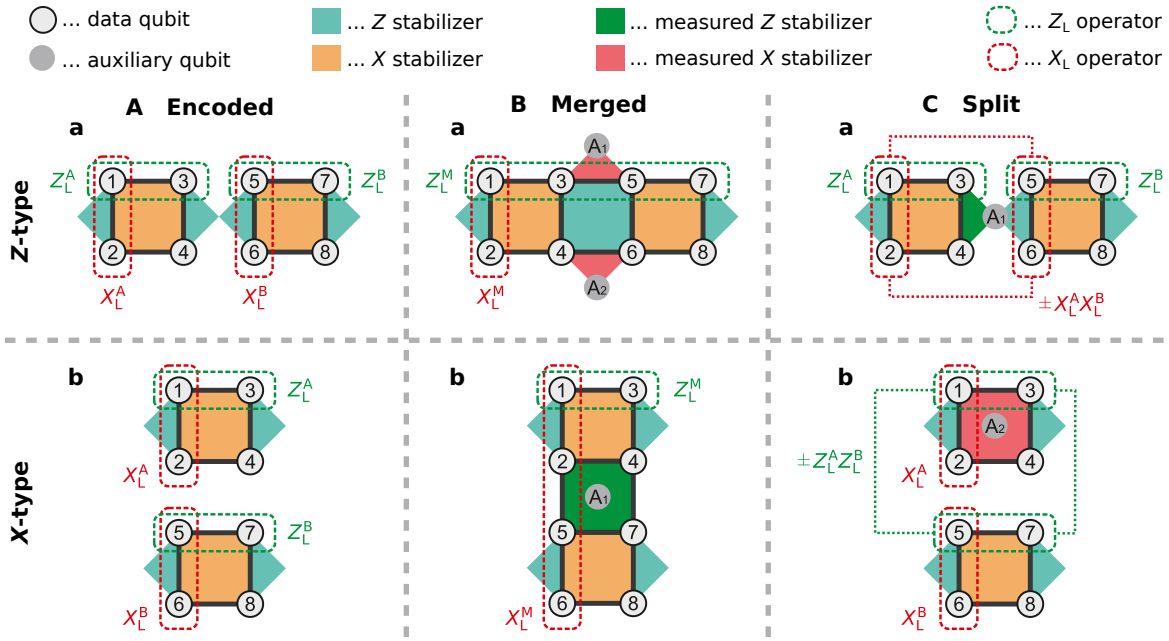

Figure 8.1: **Surface code lattice surgery in theory.** Surface code LS between Z-type and X-type boundaries implementing logical joint measurements $M_{P\tilde{P}}^{\pm} = (\mathbb{I} \pm P_L^A P_L^B)/2$ with $P_L = X_L$ (top) and $P_L = Z_L$ (bottom), respectively. **Encoded:** The two initial surface codes are defined on 2×2 lattices where X-stabilizers are associated with orange faces and Z-stabilizer with aquamarine faces. Logical operators are products of Pauli operators connecting opposite boundaries. **Merged:** Treating the two codes as a single (asymmetric) surface code, (merging) stabilizers along the boundaries are measured (indicated in red/green) such that their product is $P_L^A P_L^B$. **Split:** In order to split the merged code while preserving the eigenstate of $P_L^A P_L^B$, the boundary stabilizers of the original code are measured (indicated in green/red).

onto an eigenstate of $\pm P_L^A \otimes \tilde{P}_L^B$. The eigenvalue ± 1 is determined by the measurement outcome of the product of merging stabilizers.

Now, we want to recover the two initial logical qubits while remaining in an eigenstate of $P_L^A \otimes \tilde{P}_L^B$. To this end, we *split* the merged code by measuring stabilizers of the separated codes $\mathcal{S}^A, \mathcal{S}^B$ along the aligned boundaries as illustrated in fig. 8.1 **C**. Since these stabilizers anti-commute with merging stabilizers, the set $\{S_i^M\}_i$ is discarded from the stabilizer groups and we recover the original two codes. However, since all stabilizers always commute with the logical operators, the resulting state remains an eigenstate of $P_L^A \otimes \tilde{P}_L^B$.

In conclusion, LS acts as a joint measurement $M_{P\tilde{P}}^{\pm} = (\mathbb{I} \pm P_L^A \otimes \tilde{P}_L^B)/\sqrt{2}$ which can be implemented fault-tolerantly.

We can utilize the operation $(\mathbb{I} \pm X_L^A X_L^B)/\sqrt{2}$ (Z-type) and $(\mathbb{I} \pm Z_L^A Z_L^B)/\sqrt{2}$ (X-type) to generate entangled logic states. In our experiment we implement $(\mathbb{I} + X_L^A X_L^B)/\sqrt{2}$ (Z-type) and $(\mathbb{I} + Z_L^A Z_L^B)/\sqrt{2}$ (X-type) and hence we are able to generate three out of four logical Bell states depending on the initial encodings,

$$
\begin{aligned}
|\phi_L^+\rangle &= \tfrac{1}{\sqrt{2}} \left(|0_L^A 0_L^B\rangle + |1_L^A 1_L^B\rangle \right), \\
|\phi_L^-\rangle &= \tfrac{1}{\sqrt{2}} \left(|0_L^A 0_L^B\rangle - |1_L^A 1_L^B\rangle \right), \\
|\psi_L^+\rangle &= \tfrac{1}{\sqrt{2}} \left(|0_L^A 1_L^B\rangle + |1_L^A 0_L^B\rangle \right).
\end{aligned}
\tag{8.1}
$$

The fidelity of the generated state with respect to the logical Bell states can be estimated by measuring the expectation values of the three common stabilizers $\langle Z_L^A Z_L^B, X_L^A X_L^B, Y_L^A Y_L^B \rangle$ and evaluating the results as follows [190]

$$\begin{aligned}
\mathcal{F}\left(|\phi_L^+\rangle\right) &= \tfrac{1}{4}\left(1 + \langle Z_L^A Z_L^B\rangle + \langle X_L^A X_L^B\rangle - \langle Y_L^A Y_L^B\rangle\right), \\
\mathcal{F}\left(|\phi_L^-\rangle\right) &= \tfrac{1}{4}\left(1 + \langle Z_L^A Z_L^B\rangle - \langle X_L^A X_L^B\rangle + \langle Y_L^A Y_L^B\rangle\right), \\
\mathcal{F}\left(|\psi_L^+\rangle\right) &= \tfrac{1}{4}\left(1 - \langle Z_L^A Z_L^B\rangle - \langle X_L^A X_L^B\rangle - \langle Y_L^A Y_L^B\rangle\right).
\end{aligned} \tag{8.2}$$

In addition, the joint Pauli measurements $M_{P\tilde{P}}^{\pm} = (\mathbb{I} \pm P_L^A \otimes \tilde{P}_L^B)/\sqrt{2}$ can be used to implement a logical CNOT gate and a logical Hadamard H gate as well as to implement state teleportation through a measurement-based scheme, as illustrated in fig. 8.2.

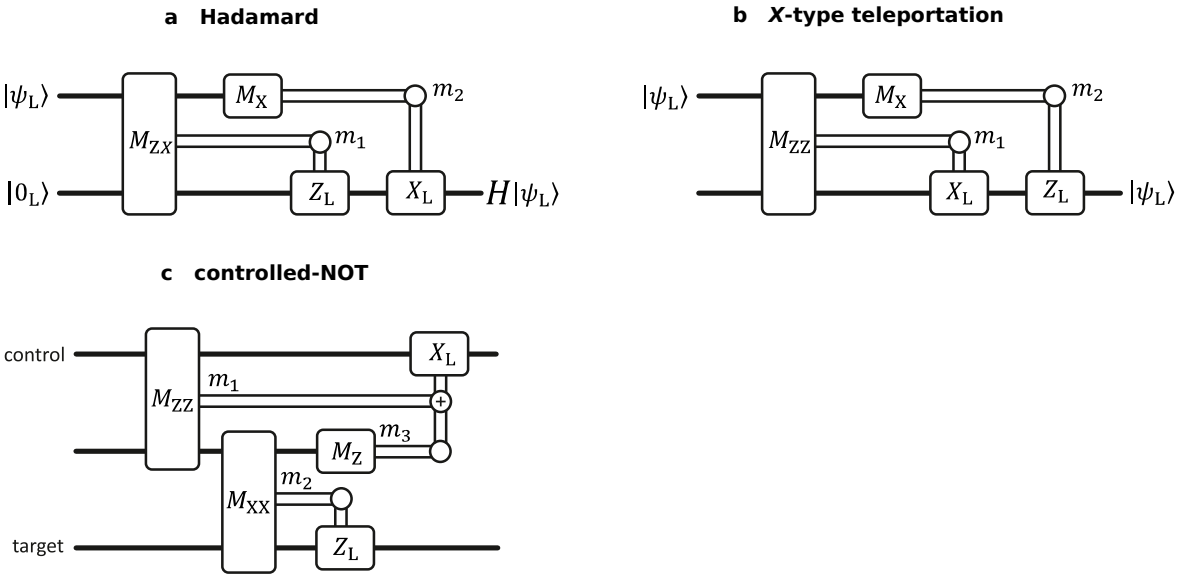

Figure 8.2: **Fault-tolerant logic gates with lattice surgery.** LS enables measurement-based implementations of logic gates and logical state teleportation. LS operations are logical joint measurements of the form $M_{P\tilde{P}} = (\mathbb{I} \pm P\tilde{P})/\sqrt{2}$. Thick lines indicate logical qubits in the circuit model and double lines represent classical bits indicating measurement outcomes $m_i = 0, 1$. Pauli-corrections need to be applied which are conditioned on the measurement outcomes as $P_L^{m_i}$. $\oplus$ represents an XOR-gate between classical bits. **a**, Measurement-based implementation of a logical Hadamard gate H based on the teleportation protocol. **b**, Measurement-based teleportation protocol for state teleportation between two logical qubits using X-type LS. **c**, Measurement-based implementation of a logical CNOT-gate between arbitrary control and target qubits requiring an auxiliary qubit in the $|+_L\rangle$-state.

8.2 ENTANGLEMENT OF LOGICAL QUBITS

We consider the minimal instance of a surface code — a 4-qubit code encoding a single logical qubit —as the central component of our experimental implementation, as introduced in section 8.1. We define the stabilizer codes $\mathcal{S}^A$ and $\mathcal{S}^B$ for two initially separate logical qubits labelled A and B as

$$\begin{aligned}
\mathcal{S}^A &= \langle S_1^A, S_2^A, S_3^A\rangle = \langle -Z_1Z_2, -Z_3Z_4, +X_1X_2X_3X_4\rangle, \\
\mathcal{S}^B &= \langle S_1^B, S_2^B, S_3^B\rangle = \langle -Z_5Z_6, -Z_7Z_8, +X_5X_6X_7X_8\rangle.
\end{aligned} \tag{8.3}$$

The logical states $|\psi_L^{A/B}\rangle$ spanning the respective code spaces for A and B are defined as the simultaneous +1 eigenstates of all stabilizers, i.e., $S_i^{A/B}|\psi_L^{A/B}\rangle = |\psi_L^{A/B}\rangle$, $\forall i \in \{1,2,3\}$. Therefore, we find that each surface encodes a single logical qubit in the two *codewords*

$$|0_L\rangle = \frac{1}{\sqrt{2}}(|0101\rangle + |1010\rangle), \tag{8.4}$$

$$|1_L\rangle = \frac{1}{\sqrt{2}}(|1001\rangle + |0110\rangle). \tag{8.5}$$

Note that we choose a negative sign for the Z stabilizers in eq. (8.3), because this encodes the logical qubits in a Decoherence-Free-Subspace (DFS) which is advantageous for the experiemental implementation.

As outlined in section 7.3, logical operators are Pauli operations acting on data qubits connecting opposite boundaries. Therefore, the logical operators are defined up to multiplication with other logical operators, stabilizers and the imaginary unit i as

$$\begin{aligned} \mathcal{L}^A &= \langle i, Z_L^A, X_L^A\rangle / \mathcal{S}^A = \langle i, Z_1Z_3, X_1X_2\rangle / \mathcal{S}^A, \\ \mathcal{L}^B &= \langle i, Z_L^B, X_L^B\rangle / \mathcal{S}^B = \langle i, Z_5Z_7, X_5X_6\rangle / \mathcal{S}^B, \end{aligned} \tag{8.6}$$

where $\langle P_L\rangle / \mathcal{S}$ indicates that logical Pauli operators P_L form equivalence classes defined up to multiplication with stabilizers. The logical Y-operator is determined as $Y_L := iZ_LX_L$ and we find $Y_L^A = Y_1X_2Z_3$ and $Y_L^B = Y_5X_6Z_7$. The action of logical operators is to map codewords to codewords. For instance, a logical bit-flip operator $X_L^A = X_1X_2$ maps $|0\rangle_L^A$ to $|1\rangle_L^A$.

As explained in chapter 3, our available gate set includes local single-qubit Z rotations, multi-qubit X and Y rotations and a multi-qubit entangling MS-gate. The local operations can also be employed on various different Zeeman-transitions in order to spectroscopically decouple and recouple specific qubits from the computational subspace. As an example we present the corresponding circuit diagram for the LS procedure along the Z-type boundary in fig. 8.3, which is used for the implementations presented fig. 8.4, and in fig. 8.7 (Z-type). Each local operation (depicted in green and blue in fig. 8.3) consists of a series of multi-qubit X or Y rotations and single-qubit Z rotations. When performing an MS-gate, only a subset of qubits is present in the computational subspace (depicted in red in fig. 8.3).

We start with the encoding procdure by preparing each logical qubit in the state $|0_L\rangle = \frac{1}{\sqrt{2}}(|0101\rangle + |1010\rangle)$ utilizing one 4-qubit MS-gate plus a number of local gates. For the stabilizer measurements in the merging and splitting steps we employ 6 3-qubit MS-gates plus a number of local gates. In between the aforementioned operations we also implement gates that couple the qubits in or out of the computational subspace.

As a first example, we present experimental results for case where the logical qubits are prepared in the state $|0_L^A 0_L^B\rangle$. We can create encoded states with average stabilizer expectation values of $\langle|S_i|\rangle = 0.868(4)$, see fig. 8.4 **A, b**. We make use of the obtained stabilizer information and post-select our data on states with valid code stabilizers as explained in the following.

Since the utilized surface code comprising 4 data qubits is an error detection code with distance $d = 2$, the code can detect arbitrary single qubit errors in theory. To detect all single qubit errors, one needs to measure all three code stabilizers of one logical qubit. This requires additional stabilizer measurements and auxiliary qubits. Since the focus of this work is to show the processing capabilities of LS rather than the error detection capability of the surface code, we leave this for future investigations. Nevertheless, we can already

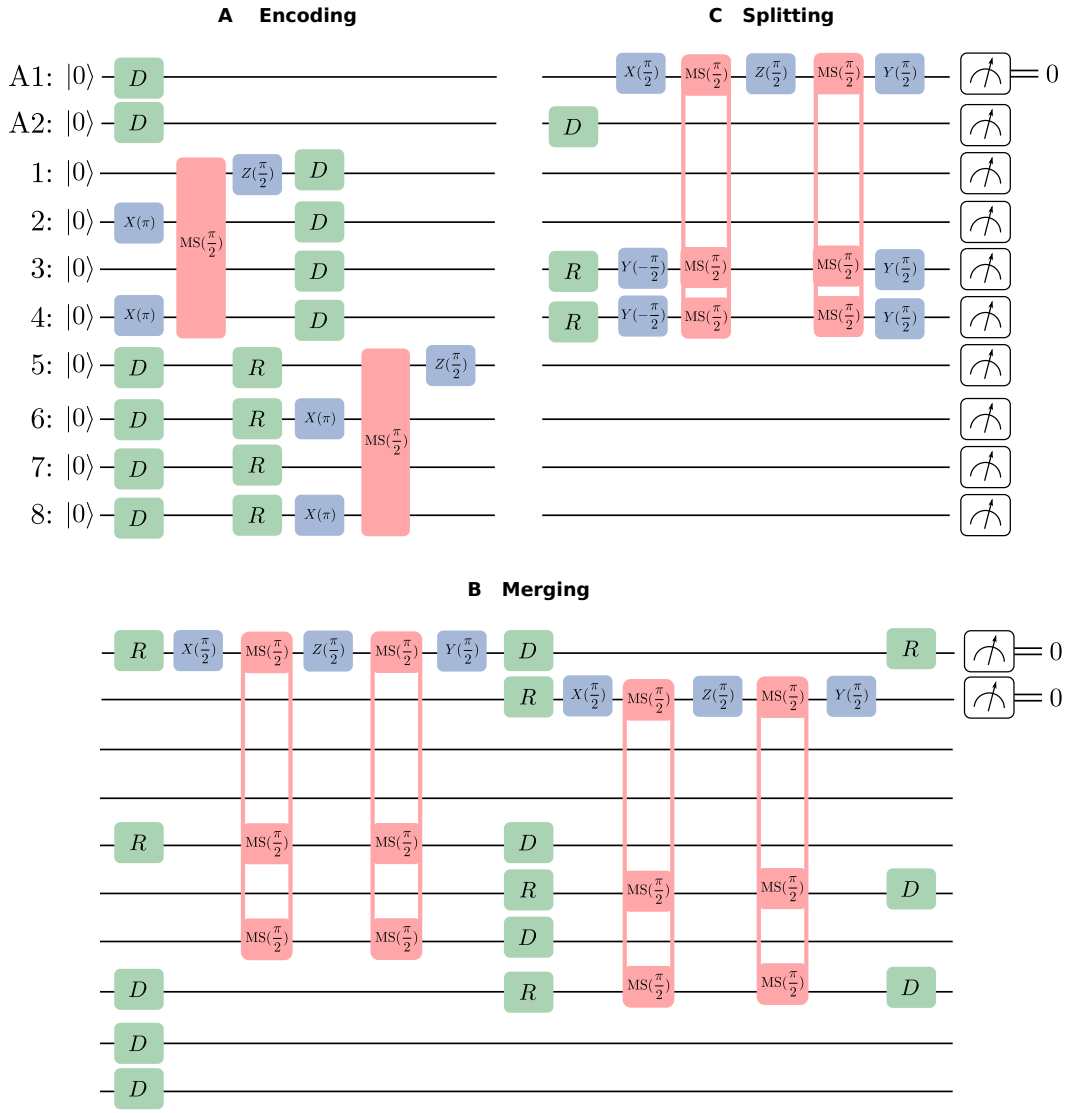

Figure 8.3: **Example circuit used for lattice surgery.** Gate sequence for **A** encoding the state $|0_{\mathrm{L}}^{\mathrm{A}} 0_{\mathrm{L}}^{\mathrm{B}}\rangle$ and performing **B** the merging and **C** the splitting along the Z-type boundary. We employ decoupling (D in green) and recoupling (R in green) operations to move qubits in or out of the computational subspace. The local operations are depicted in blue. The multi-qubit entangling MS-gates are pictured in red. We implement one in-sequence measurement on the auxiliary qubits right after merging the two logical qubits and one measurement of all qubits at the end of the sequence.

make use of the measurements we perform to detect whether or not stabilizers have been correct. For example, if we measure logical qubit A in the Z-basis, we also check stabilizers $S_1 = Z_1Z_2$ and $S_2 = Z_3Z_4$ and therefore, detect any single-qubit X-error on any of the 4 data qubits. Analogously, measuring in the X-basis allows us to detect single-qubit Z-errors by checking the stabilizer $S_3 = X_1X_2X_3X_4$. If we measure in the Y-basis we check the stabilizer $S_2 = Z_3Z_4$ and detect any single-qubit X-error on data qubits 3 and 4, but ignore errors on qubit 1 and 2. In general, we are not able to detect any 2-qubit or multi-qubit errors. Discarding the measurements with erroneous stabilizer values introduces a reduced survival probability, but increases the fidelities significantly compared to the raw fidelities

without post selection, as can be observed in all logical stabilizers plots throughout this chapter.

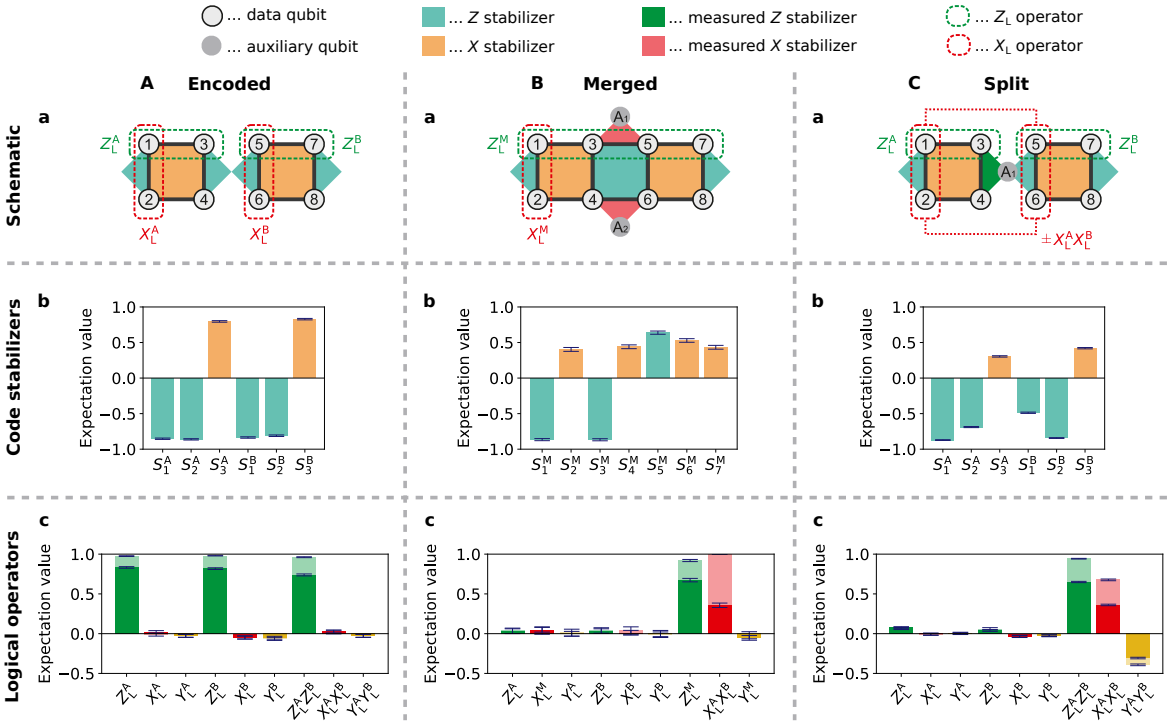

Figure 8.4: **Experimental Z-type surface code lattice surgery.** Experimental results and schematics for LS between Z-type boundaries. Error detected and post-selected measurements are presented in light colored bars. **A Encoded. a,** Two surface codes defined on 2×2 lattices with **b,** average code stabilizer values of $\langle |S_i| \rangle = 0.868(4)$. **c,** We observe (raw|post selected) state fidelities $\mathcal{F}(|0_L^A\rangle) = 93.8(4)|99.3(2)\,\%$ and $\mathcal{F}(|0_L^B\rangle) = 93.4(5)|99.4(2)\,\%$ for the encodings $|0_L^A\rangle$, $|0_L^B\rangle$, respectively. **B Merged. a,** The stabilizers S_6^M, S_7^M along the boundaries are measured (dark red) using auxiliary qubits A_1,A_2. **b,** We observe average stabilizer values and **c,** logical state fidelities of $\langle |S_i| \rangle = 0.669(8)$ and $\mathcal{F}(|0_L^M\rangle) = 86.4(1.0)|97.9(5)\,\%$, respectively. **C Split. a,** One boundary stabilizer S_2^A of the original code is measured (green) reusing auxiliary qubit A_1 and the associated syndrome is observed. In this way, we recover the original codes with **b,** average stabilizer values of $\langle |S_i| \rangle = 0.603(3)$ which are now in a logical Bell state $|\phi_L^+\rangle$ with **c,** fidelity $\mathcal{F}(|\phi_L^+\rangle) = 58.0(1.6)|75.3(1.6)\,\%$.

For the encoded states $|0_L^A\rangle$ and $|0_L^B\rangle$ we infer fidelities of $\mathcal{F}(|0_L^A\rangle) = 93.8(4)|99.3(2)\,\%$ and $\mathcal{F}(|0_L^B\rangle) = 93.4(5)|99.4(2)\,\%$, where the first value describes the raw fidelity, while the second represents the observed fidelity after post-selection and we use this format throughout this chapter to present fidelities of both uncorrected and post-selected data.

We now outline the Z-type LS procedure in detail and show how to utilize the protocol to perform a logical joint measurement $M_{XX}^{\pm} = (\mathbb{I} \pm X_L^A X_L^B)/\sqrt{2}$. The procedure is illustrated again in fig. 8.4 **B, a** and **C, a** for the two introduced 2×2 surface codes $\mathcal{S}^A$ and $\mathcal{S}^B$. We first *merge* the two separate codes $\mathcal{S}^A, \mathcal{S}^B$ into a new stabilizer code $\mathcal{S}^M$ by measuring *merging* stabilizers $S_6^M = X_3X_5$ and $S_7^M = X_4X_6$ between the boundaries. These stabilizers commute with all stabilizers of the original codes except S_2^A and S_1^B, and are chosen such that their joint measurement corresponds to the joint logical measurement M_{XX}, i.e., $S_6^M S_7^M = X_L^A X_L^B$.

As a result, we obtain the new code by discarding all stabilizers that anti-commute with the merging stabilizers, depicted in fig. 8.4 **B, a**,

$$\begin{aligned}\mathcal{S}^{\mathrm{M}} &= \langle S_1^{\mathrm{M}}, S_2^{\mathrm{M}}, S_3^{\mathrm{M}}, S_4^{\mathrm{M}}, S_5^{\mathrm{M}}, S_6^{\mathrm{M}}, S_7^{\mathrm{M}}\rangle \\ &= \langle S_1^{\mathrm{A}}, S_3^{\mathrm{A}}, S_2^{\mathrm{B}}, S_3^{\mathrm{B}}, S_2^{\mathrm{A}} S_1^{\mathrm{B}}, +X_3X_5, +X_4X_6\rangle. \end{aligned} \tag{8.7}$$

Note that this code already encodes the desired joint logical eigenstate since $X_{\mathrm{L}}^{\mathrm{A}} X_{\mathrm{L}}^{\mathrm{B}}$ is included as a stabilizer in the merged code $\mathcal{S}^{\mathrm{M}}$. In fact, the measurement outcomes $m, m' \in \{0,1\}$ of $S_6^{\mathrm{M}}, S_7^{\mathrm{M}}$, respectively, are random such that $m_1 = m + m'$ specifies the eigenvalue associated with $X_{\mathrm{L}}^{\mathrm{A}} X_{\mathrm{L}}^{\mathrm{B}}$ as $(-1)^{m_1}$. The merged code is an asymmetric 2×4 surface code encoding a single logical qubit, where the logical operators are defined as

$$\mathcal{L}^{\mathrm{M}} = \langle i, Z_{\mathrm{L}}^{\mathrm{M}}, X_{\mathrm{L}}^{\mathrm{M}}\rangle / \mathcal{S}^{\mathrm{M}} = \langle i, Z_{\mathrm{L}}^{\mathrm{A}} Z_{\mathrm{L}}^{\mathrm{B}}, X_{\mathrm{L}}^{\mathrm{A}}\rangle / \mathcal{S}^{\mathrm{M}}, \tag{8.8}$$

and $Y_{\mathrm{L}}^{\mathrm{M}} = Y_{\mathrm{L}}^{\mathrm{A}} Z_{\mathrm{L}}^{\mathrm{B}}$.

With the Z-type merge we effectively merged the logical Z-operators and performed the desired logical joint measurement $M_{\mathrm{XX}}^{\pm}$. Its expectation value ± 1 is given by the product of expectation values of merging stabilizers $S_6^{\mathrm{M}}, S_7^{\mathrm{M}}$.

Performing the measurement of the $S_6^{\mathrm{M}} = X_3X_5$ and $S_7^{\mathrm{M}} = X_4X_6$ stabilizers requires Quantum-Non-Demolition (QND) measurements implemented by series of local and entangling gates, as described in section 7.2.1. Considering two merging stabilizers mapped onto auxiliary qubits $A1$ and $A2$, we have the possibility to detect one of four possible outcomes $(m, m') = (0,0), (0,1), (1,0), (1,1)$. In the Supplementary Information, we present data for all possible outcomes for the chosen input state. For experimental simplicity the following results are for the case $(m, m') = (0,0)$. The merged surface code, as defined in eq. (8.7), is illustrated in fig. 8.4 **B, b**. The data confirms the merged stabilizers with an average stabilizer expectation value of $\langle |S_i| \rangle = 0.669(8)$. Starting from the state $|0_{\mathrm{L}}^{\mathrm{A}} 0_{\mathrm{L}}^{\mathrm{B}}\rangle$, the merged logical state is a $+1$ eigenstate of the logical $Z_{\mathrm{L}}^{\mathrm{M}} = Z_{\mathrm{L}}^{\mathrm{A}} Z_{\mathrm{L}}^{\mathrm{B}}$ operator, as can be seen in fig. 8.4 **B, c**. The data reveals a state fidelity of $\mathcal{F}(|0_{\mathrm{L}}^{\mathrm{M}}\rangle) = 86.4(1.0)|97.9(5)\,\%$ after merging.

Now, we must recover the two initial logical qubits while keeping the previously obtained expectation value of $X_{\mathrm{L}}^{\mathrm{A}} X_{\mathrm{L}}^{\mathrm{B}}$. To this end, we *split* the merged code by measuring Z-stabilizers S_2^{A} or S_1^{B} along the merged boundaries as depicted in fig. 8.4 **C, a**. These operators commute with all stabilizers in $\mathcal{S}^{\mathrm{M}}$ that define the separated logical qubits $\mathcal{S}^{\mathrm{A}}, \mathcal{S}^{\mathrm{B}}$. In particular, the measured stabilizers all commute with $X_{\mathrm{L}}^{\mathrm{A}}, X_{\mathrm{L}}^{\mathrm{B}}$, i.e., the code remains in an eigenstate of $X_{\mathrm{L}}^{\mathrm{A}} X_{\mathrm{L}}^{\mathrm{B}}$. The stabilizer measurement has random outcomes $m'' \in \{0,1\}$, where a corretion operation in case of $m'' = 1$ needs to be implemented.

We perform the spliting by mapping S_2^{A} onto auxiliary qubit A1 for the case $m'' = 0$. Thereby we restore the initial code space with an average stabilizer expectation value of $\langle |S_i| \rangle = 0.603(3)$, shown in fig. 8.4 **C, b**. The resulting projective measurement $(\mathbb{I} + X_{\mathrm{L}}^{\mathrm{A}} X_{\mathrm{L}}^{\mathrm{B}})/\sqrt{2}$ maps the initial product state $|0_{\mathrm{L}}^{\mathrm{A}} 0_{\mathrm{L}}^{\mathrm{B}}\rangle$ onto a maximally entangled, logical Bell state $|\phi_{\mathrm{L}}^{+}\rangle = \frac{1}{\sqrt{2}}\left(|0_{\mathrm{L}}^{\mathrm{A}} 0_{\mathrm{L}}^{\mathrm{B}}\rangle + |1_{\mathrm{L}}^{\mathrm{A}} 1_{\mathrm{L}}^{\mathrm{B}}\rangle\right)$. In order to deduce the fidelity of the generated state with respect to the logical Bell state, we measure the common logical stabilizers $\langle Z_{\mathrm{L}}^{\mathrm{A}} Z_{\mathrm{L}}^{\mathrm{B}}, X_{\mathrm{L}}^{\mathrm{A}} X_{\mathrm{L}}^{\mathrm{B}}, -Y_{\mathrm{L}}^{\mathrm{A}} Y_{\mathrm{L}}^{\mathrm{B}}\rangle$ obtaining the fidelity accrding to eq. (8.2). In fig. 8.4 **C, c**, we present the results for the Bell state generation. From the common stabilizer measurements, we infer a logical Bell state fidelity of $\mathcal{F}(|\phi_{\mathrm{L}}^{+}\rangle) = 58.0(1.6)|75.3(1.6)\,\%$, where the raw fidelity exceeds the separability limit of 50 % [191] by 5 sigma.

X-type LS implements the joint measurement $M_{\mathrm{ZZ}}^{+} \propto \mathbb{I} + Z_{\mathrm{L}}^{\mathrm{A}} Z_{\mathrm{L}}^{\mathrm{B}}$ and differs from Z-type LS only in so far that both codes are considered to be rotated by 90 degrees before LS.

Equivalently, one can understand X-type lattices surgery as merging and splitting along the upper/lower instead of the left/right boundaries, as illustrated in fig. 8.5 **a**. In the case of two 2×2 surface codes, measuring the merging stabilizer $S_7^{\mathrm{M}} = Z_2 Z_4 Z_5 Z_7$, we obtain a 4×2 asymmetric surface code

$$\begin{aligned} \bar{\mathcal{S}}^{\mathrm{M}} &= \langle \bar{S}_1^{\mathrm{M}}, \bar{S}_2^{\mathrm{M}}, \bar{S}_3^{\mathrm{M}}, \bar{S}_4^{\mathrm{M}}, \bar{S}_5^{\mathrm{M}}, \bar{S}_6^{\mathrm{M}}, \bar{S}_7^{\mathrm{M}} \rangle \\ &= \mathcal{S}^{\mathrm{A}} \times \mathcal{S}^{\mathrm{B}} \times \langle +Z_2 Z_4 Z_5 Z_7 \rangle . \end{aligned} \tag{8.9}$$

which can be split by discarding the merging stabilizer. It is worth noting that the merging operation already concludes the LS since the merging stabilizer is in fact $Z_{\mathrm{L}}^{\mathrm{A}} \otimes Z_{\mathrm{L}}^{\mathrm{B}}$. This is an artifact of reducing the general LS procedure for a larger surface code to a distance $d = 2$ surface code. Nevertheless, the general procedure requires the measurement of X-stabilizers along the boundary which is why we still include here. The results for the X-type LS are presented in fig. 8.5 and we report a Bell state fidelity of $\mathcal{F}(|\phi_{\mathrm{L}}^{+}\rangle) = 63.9(2.8)|78.0(2.7)\,\%$.

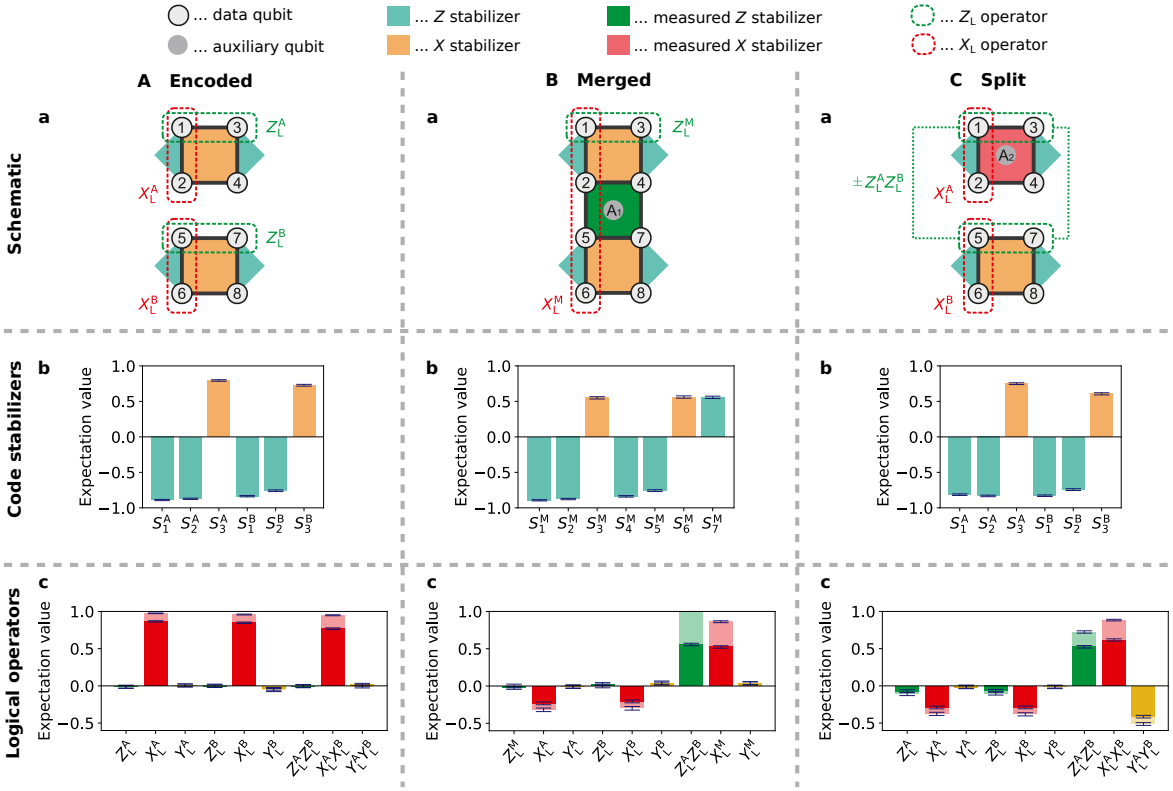

Figure 8.5: **Experimental X-type surface code lattice surgery.** Experimental results and schematics for LS between X-type boundaries. Error detected and post-selected measurements are presented in light colored bars. **A Encoded. a,** Two surface codes defined on 2×2 lattices with **b,** average code stabilizer values of $\langle |S_i| \rangle = 0.813(4)$. **c,** We observe (raw|post selected) state fidelities $\mathcal{F}(|+_{\mathrm{L}}^{\mathrm{A}}\rangle) = 93.3(5)|98.7(2)\,\%$ for logical qubit A and $\mathcal{F}(|+_{\mathrm{L}}^{\mathrm{B}}\rangle) = 92.4(5)|97.9(3)\,\%$ for logical qubit B. **B Merged. a,** The stabilizer S_7^{M} along the boundaries are measured (green) using auxiliary qubit A_1. **b,** We observe average stabilizer values and **c,** logical state fidelities of $\langle |S_i| \rangle = 0.719(5)$ and $\mathcal{F}(|+_{\mathrm{L}}^{\mathrm{M}}\rangle) = 76.2(8)|93.1(6)\,\%$, respectively. **C Split. a,** We measure the stabilizer $\bar{S}_6^{\mathrm{M}}$ by using auxiliary qubit A_2 as syndrome qubit to perform the splitting and obtain **b,** average stabilizer values of $\langle |S_i| \rangle = 0.763(5)$. **c,** The fidelity of the generated state to the logical Bell state is $\mathcal{F}(|\psi_{\mathrm{L}}^{+}\rangle) = 63.9(2.8)|78.0(2.7)\,\%$.

8.3 QUANTUM STATE TELEPORATION BETWEEN LOGICAL QUBITS

We demonstrate quantum state teleportation for the input states $|0_L^A 0_L^B\rangle$, $|1_L^A 0_L^B\rangle$, and $|+_L^A 0_L^B\rangle$. After performing Z-type LS (i.e., encoding, merging, splitting), we measure logical qubit A in the Z-basis and apply a logical X_L gate on qubit B if qubit A was found in $|1_L^A\rangle$ (see fig. 8.6). Succeeding the teleportation protocol, we measure logical state fidelities for qubit B of $\mathcal{F}\left(|0_L^B\rangle\right) = 87(2)|97(1)\,\%$, $\mathcal{F}\left(|1_L^B\rangle\right) = 81(2)|93(2)\,\%$ and $\mathcal{F}\left(|+_L^B\rangle\right) = 71(1)|85(2)\,\%$, given the input states $|0_L^A 0_L^B\rangle$, $|1_L^A 0_L^B\rangle$, and $|+_L^A 0_L^B\rangle$, respectively.

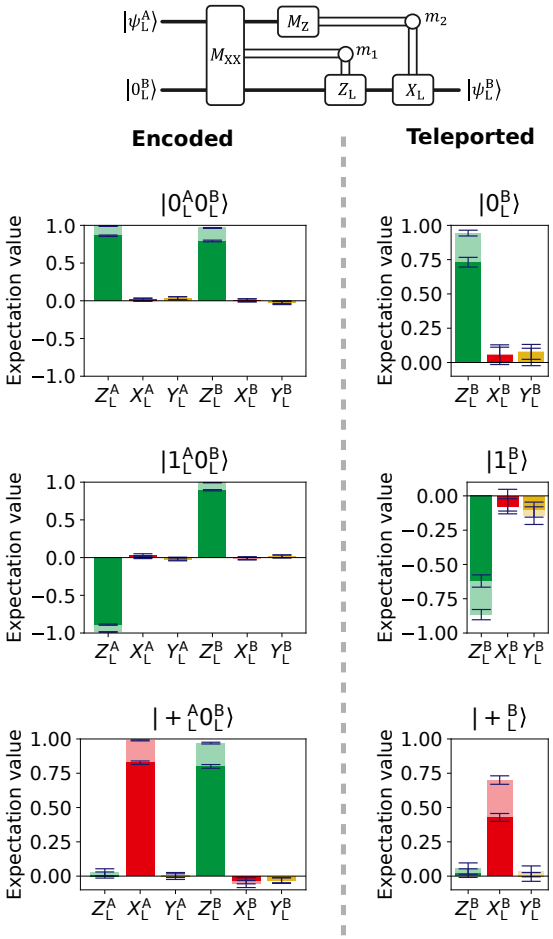

Figure 8.6: **Teleportation of quantum information via LS.** We prepare the logical qubits A, B in the states $|0_L^A 0_L^B\rangle$, $|1_L^A 0_L^B\rangle$, and $|+_L^A 0_L^B\rangle$, and use LS to teleport the state from logical qubit A to logical qubit B. We measure fidelities of the teleported quantum states of $\mathcal{F}\left(|0_L^B\rangle\right) = 87(2)|97(1)\,\%$ $\mathcal{F}\left(|1_L^B\rangle\right) = 81(2)|93(2)\,\%$, and $\mathcal{F}\left(|+_L^B\rangle\right) = 71(1)|85(2)\,\%$.

8.4 ADDITIONAL BELL STATE EXPERIMENTS

As explained in section 8.2, the LS procedure consists of two main parts: first, merging two logical qubits into a single logical qubit, and second, splitting the logical qubit again into two logical qubits. In total, this procedure corresponds to the operation $(\mathbb{I} \pm X_L^A X_L^B)/\sqrt{2}$ (Z-type) or $(\mathbb{I} \pm Z_L^A Z_L^B)/\sqrt{2}$ (X-type).

In addition to the experiments presented in section 8.2, we also performed LS along the Z-type boundary for input states $|0_L^A 0_L^B\rangle$, $|0_L^A 1_L^B\rangle$, $|1_L^A 0_L^B\rangle$, and $|1_L^A 1_L^B\rangle$ and along the X-type

boundary for input states $|+^{\mathrm{A}}_{\mathrm{L}}+^{\mathrm{B}}_{\mathrm{L}}\rangle$, $|+^{\mathrm{A}}_{\mathrm{L}}-^{\mathrm{B}}_{\mathrm{L}}\rangle$, $|-^{\mathrm{A}}_{\mathrm{L}}+^{\mathrm{B}}_{\mathrm{L}}\rangle$ and $|-^{\mathrm{A}}_{\mathrm{L}}-^{\mathrm{B}}_{\mathrm{L}}\rangle$. The results are presented in fig. 8.7 and in table 8.1. We observe that the resulting state fidelity $\mathcal{F}^{\mathrm{Bell}}$ for the initial state $|-^{\mathrm{A}}_{\mathrm{L}}+^{\mathrm{B}}_{\mathrm{L}}\rangle$ is significantly lower than for the other input states. We suspect that imperfect calibration is responsible for the decreased fidelity.

In general the individual code stabilizers S_i have different absolute values because some stabilizers include two physical qubits, whereas others comprise four physical qubits. Moreover, some physical qubits are involved more frequently in error prone physical gates than others. Hence we do not expect the stabilizer values to be uniformly distributed and we use error propagation to calculate the error of the mean stabilizer values $\langle|S_i|\rangle$.

If we use the error-detecting capabilities of the 2×2 surface code, we can discard measurements where we find a single qubit error. This introduces a survival probabilities (SP) for each LS procedure, that would be 100 % if there would be no single qubit errors. We present the measured survival probabilities (SP) also in table 8.1. Since we use multi-qubit MS-gates to implement LS, we expect to have multi-qubit errors which cannot be detected and hence reduce the efficiency of the error detection.

As mentioned in section 8.2, we can detect single qubit errors on any qubit in X- and Z-basis, but only on two qubits in the Y-basis. As can be seen in the data, we indeed detect less single qubit errors in the Y-basis and thus we get a higher survival probability SP_Y compared to SP_X and SP_Z.

Note, that we expect the multi-qubit MS-gates to introduce multi-qubit errors, which cannot be detected. This can be seen in section 8.2, where the SP_X values are higher for X-type LS compared to Z-type LS, because the merging procedure for the X-type LS requires two 5-qubit MS gates, whereas the merging for Z-type LS needs four 3-qubit MS gates.

In summary, using the error detection capabilities of the implemented surface code increases the fidelities by $28(3)$ % with Survival Probabilitys (SPs) of $64(4)$ % on average.

Table 8.1: **Bell state generation data.** Summary of the Bell state generation experiments for various different input states, along the Z-type and the X-type boundary. Presented are the individual code stabilizers S_i^{A} and $\S_i^{\mathrm{B}}$ for qubits A and B as well as the mean of all absolute stabilizer values $\langle|S_i|\rangle$. The Bell state fidelities $\mathcal{F}^{\mathrm{Bell}}$ and the post selected fidelities $\mathcal{F}^{\mathrm{Bell,PS}}$ are given in percent (%). The survival probabilities (SP) after post selection are also displayed in percent (%). The last column shows the number of taken single shot measurements per basis.

Bound.	Input	S_1^A	S_2^A	S_3^A	S_1^B	S_2^B	S_3^B	$\langle\|S_i\|\rangle$	$\mathcal{F}^{\mathrm{Bell}}$	$\mathcal{F}^{\mathrm{Bell,PS}}$	SP_Z	SP_X	SP_Y	SP	Shots
Z-type	$\|0_{\mathrm{L}}^{\mathrm{A}}0_{\mathrm{L}}^{\mathrm{B}}\rangle$	-0.87(1)	-0.69(1)	0.30(1)	-0.49(1)	-0.84(1)	0.42(1)	0.603(3)	57.9(1.6)	75.3(1.6)	62	49	77	63(12)	90000[a]
Z-type	$\|0_{\mathrm{L}}^{\mathrm{A}}0_{\mathrm{L}}^{\mathrm{B}}\rangle$	-0.90(1)	-0.55(3)	0.33(3)	-0.48(3)	-0.91(1)	0.45(3)	0.60(1)	55.7(5.0)	69.7(5.4)	62	52	74	63(9)	9000[b]
Z-type	$\|0_{\mathrm{L}}^{\mathrm{A}}1_{\mathrm{L}}^{\mathrm{B}}\rangle$	-0.90(1)	-0.54(3)	0.43(3)	-0.42(3)	-0.88(2)	0.38(3)	0.59(1)	56.6(4.9)	72.7(5.2)	59	51	74	61(9)	9000
Z-type	$\|1_{\mathrm{L}}^{\mathrm{A}}0_{\mathrm{L}}^{\mathrm{B}}\rangle$	-0.90(1)	-0.51(3)	0.32(3)	-0.43(3)	-0.87(2)	0.39(3)	0.57(1)	54.2(5.0)	67.3(5.7)	59	50	68	59(7)	9000
Z-type	$\|1_{\mathrm{L}}^{\mathrm{A}}1_{\mathrm{L}}^{\mathrm{B}}\rangle$	-0.89(1)	-0.51(3)	0.46(3)	-0.42(3)	-0.86(2)	0.41(3)	0.59(1)	55.9(5.1)	74.3(5.1)	58	51	76	62(11)	9000
X-type	$\|+_{\mathrm{L}}^{\mathrm{A}}+_{\mathrm{L}}^{\mathrm{B}}\rangle$	-0.81(1)	-0.83(1)	0.75(1)	-0.83(1)	-0.74(1)	0.61(2)	0.76(1)	63.9(2.8)	78.0(2.7)	70	72	80	74(4)	9000
X-type	$\|+_{\mathrm{L}}^{\mathrm{A}}-_{\mathrm{L}}^{\mathrm{B}}\rangle$	-0.79(1)	-0.80(1)	0.72(1)	-0.79(1)	-0.64(2)	0.52(2)	0.71(1)	59.3(3.2)	73.1(3.3)	63	66	73	68(4)	9000
X-type	$\|-_{\mathrm{L}}^{\mathrm{A}}+_{\mathrm{L}}^{\mathrm{B}}\rangle$	-0.58(2)	-0.65(2)	0.63(2)	-0.75(1)	-0.62(2)	0.49(2)	0.62(1)	49.3(3.3)	63.6(3.8)	54	62	66	61(5)	9000
X-type	$\|-_{\mathrm{L}}^{\mathrm{A}}-_{\mathrm{L}}^{\mathrm{B}}\rangle$	-0.77(1)	-0.80(1)	0.76(1)	-0.83(1)	-0.77(1)	0.59(2)	0.75(1)	62.4(2.9)	76.8(2.7)	69	71	79	73(4)	9000

[a] Data for plots presented in fig. 8.4. The data was taken on a different day with a larger sample size compared to the rest of the data in this table.
[b] Data for plots presented in fig. 8.7.

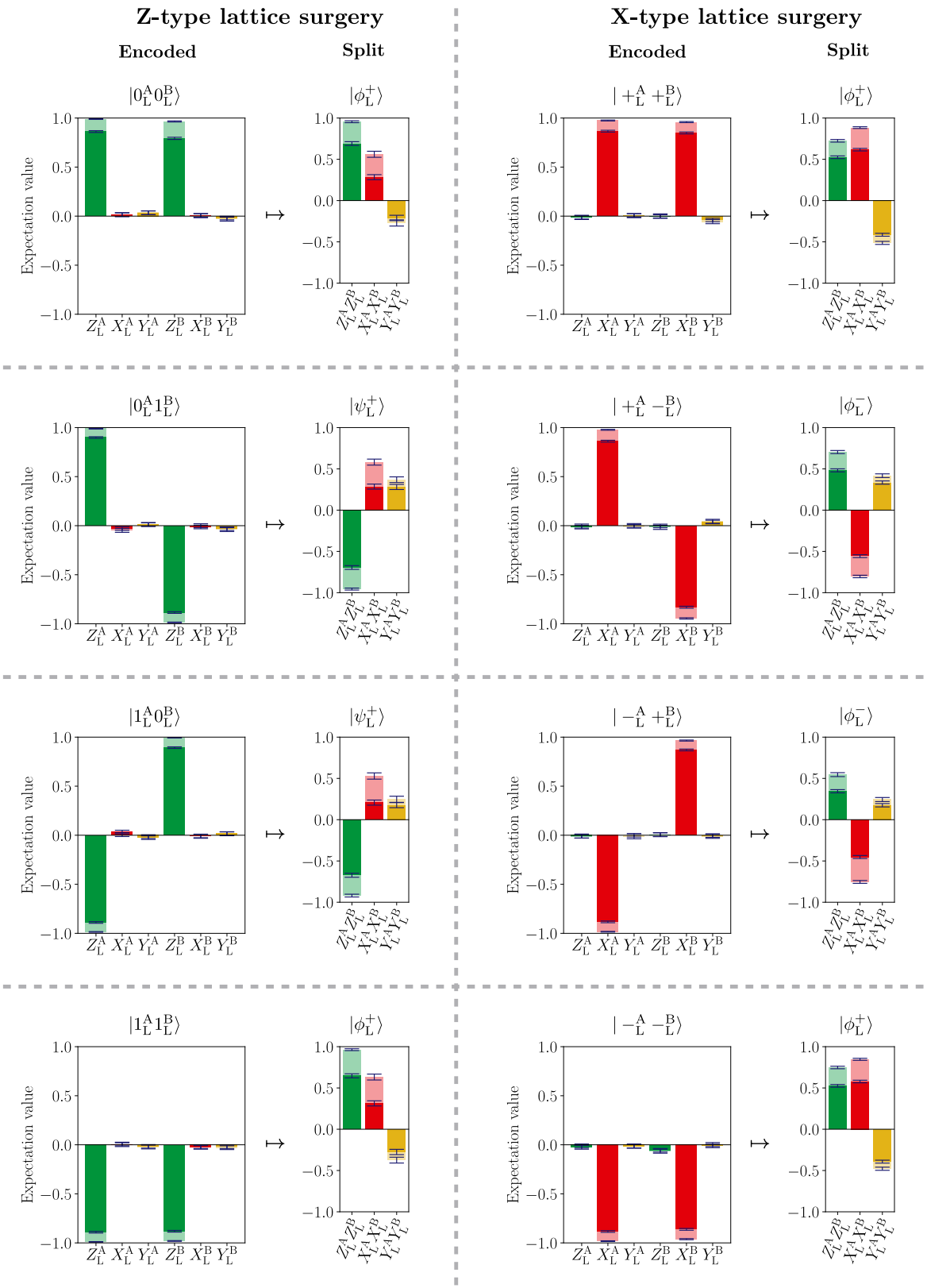

Figure 8.7: **Generation of logical Bell states.** Bell state generation with various input states along the Z-type (left) and the X-type (right) boundary associated with projections $(\mathbb{I} + X_L^A X_L^B)/\sqrt{2}$ and $(\mathbb{I} + Z_L^A Z_L^B)/\sqrt{2}$, respectively. Detailed information about code stabilizers, fidelities and survival probabilities is given in table 8.1. These results should be understood in the same way as fig. 8.4 and fig. 8.5 before and after LS.

8.5 EXPERIMENTAL METHODS

The experimental circuit to implement the LS procdure is outlined in section 8.2. We recall that we employ one 4-qubit MS-gate plus a number of local gates to prepare the state $|0_L\rangle$. To prepare the state $|1_L\rangle$ we implement the same number of gates as for the state $|0_L\rangle$ but on different qubits. The state $|+_L\rangle$ is implemented using two 2-qubit MS-gates plus a number of local gates. Again, to prepare the state $|-_L\rangle$ we use the same number of gates as for the state $|+_L\rangle$ but on different qubits. The total number of gates required to implement the different experiments is presented in table 8.2.

To get an estimated of the expected fidelities we neglect small multi-qubit gate errors, assume a single-qubit gate fidelity of 99.7 % and use the known MS-gate fidelities [25]. By simple multiplication of the fidelities of the individual gates we infer expected Bell state fidelities of ~ 63 % (Z-type) and ~ 57 % (X-type). The measured state fidelities of this work of $58(2)$ % (Z-type) and $64(3)$ % (X-type) reflect the expected fidelities very well. We suspect that the main reason for the deviation between expected and measured fidelities is the DFS in which the individual encodings reside, which was not taken into account for the above considerations.

Table 8.2: **Implemented gates for lattice surgery.** Number of gates used for the complete LS circuit (encoding, merging and splitting). We present the number of local 1-qubit gates, local N-qubit gates and N-qubit MS-gates. Note that the input states $|0_L\rangle, |1_L\rangle$ as well as $|+_L\rangle, |-_L\rangle$ require the same amount of physical gates.

Boundary	Input	1-qubit	N-qubit	2-MS	3-MS	4-MS	5-MS
Z-type	$\|0_L^A 0_L^B\rangle$	101	52	0	6	2	0
Z-type	$\|+_L^A 0_L^B\rangle$	116	60	2	6	1	0
X-type	$\|+_L^A +_L^B\rangle$	121	60	4	0	0	4

Another experimental detail concerns the in-sequence measurment of the auxiliary qubits. As mentioned in section 8.2, the presented results only account for the cases where the auxiliary qubits A1 and A2 reveal a measurement outcome of $m, m' = 0$. We limited the experiments to those outcomes for the following reasons.

When merging the two logical qubits, we map the merging stabilizer information onto the auxiliary qubits A1 and A2. Subsequently, we decouple all the data qubits from the computational subspace and perform a projective measurement only on the auxiliary qubits. The measurement is realized by illuminating the ion string with the 397 nm laser and collecting the fluorescence light of the ions. Since this is an in-sequence measurement, which means that we will continue with coherent operations after the measurement, the measurement procedure should be as short as possible that the qubits are not exposed to decoherence processes for too long. The fastet way to detect 397 nm light in our experiement is to use the fast photo-multiplier-tube.

Due to this experimental procedure, the in-sequence measurements come with two difficulties. First, this measurement reveals information about how many ions are bright, but not which ones. Second, the ion chain heats up and the qubits partially leave the computational subspace if the ions scatter 397 nm light. Without an in-sequence cooling and state preparation technique we cannot do any high-fidelity gate operations after the detection. Hence, we can only proceed with the algorithm in the case where both auxiliary qubits are found in the dark state $|1\rangle$, where no 397 nm photons are scattered. Therefore, we actually

only use data where both auxiliary qubits were measured to be $m = m' = 1$. If necessary, we invert the state of the individual auxiliary qubits right before the measurement to investigate all possible syndrome measurement outcomes $(m, m') = (0,0), (0,1), (1,0), (1,1)$. In fig. 8.8 we verify the change in the code stabilizers and logical operators for the different outcome combinations of m and m'. In our data we observe the expected behaviour, that the stabilizers $\mathcal{S}_6^{\mathrm{M}}$ and $\mathcal{S}_7^{\mathrm{M}}$ change sign depending on the measurement outcomes. By splitting the merged qubit again we implement the operation $(\mathbb{I} + (-1)^{m+m'} X_{\mathrm{L}}^{\mathrm{A}} X_{\mathrm{L}}^{\mathrm{B}})/2$ (see fig. 8.8) such that the Bell state $|\phi^+\rangle$ or $|\phi^-\rangle$ is generated, depending on the outcomes m, m'.

Since we cannot measure all possible syndrome outcomes, the experimental implementations have a Survival Probability (SP) of lower than 100 %. When merging the logical qubits along the Z-type boundary we measure two auxiliary qubits, where we only use one of four possible outcomes. In theory this leaves us with a SP of 25 %. If we merge the qubits along the X-type boundary we only use one auxiliary qubit and we are left with 50 % of the data in theory. In practice, we expect this numbers to be lower due to imperfections in the spectroscopic decoupling of the data qubits from the measurement. While this lowers the SP, this also increases the fidelity because we detect and discard the measurement if a data qubit is not in the decoupled subspace. When splitting the logical qubit, we map stabilizer information onto one auxiliary qubit, which again results in a SP of 50 %. In practice, the reduction of the SPs can be eliminated by introducing re-cooling and state preparation techniques into the experimental apparatus.

We measure each sequence in the three logical Pauli bases $\{X, Y, Z\}$ to get an estimate for all individual stabilizers and logical operators. All measured SPs are summarized in table 8.3. In addition, the SP is further reduced if we make use of the error-detection capability of the implemented surface code, as already described in section 8.2.

Table 8.3: **Survival probabilities of stabilizer measurements.** We present Survival Probabilities (SP) for various input states after merging $\mathrm{SP}_\sigma^{\mathrm{M}}$ and after splitting $\mathrm{SP}_\sigma^{\mathrm{S}}$, where $\sigma \in \{X, Y, Z\}$ denotes the respective logical Pauli measurement basis and $\langle \mathrm{SP} \rangle$ describes the average value. For each measurement basis and input state we perform 9000 measurements in total. The values are given in (%).

Input	$\mathrm{SP}_Z^{\mathrm{M}}$	$\mathrm{SP}_X^{\mathrm{M}}$	$\mathrm{SP}_Y^{\mathrm{M}}$	$\langle \mathrm{SP}^{\mathrm{M}} \rangle$	$\mathrm{SP}_Z^{\mathrm{S}}$	$\mathrm{SP}_X^{\mathrm{S}}$	$\mathrm{SP}_Y^{\mathrm{S}}$	$\langle \mathrm{SP}^{\mathrm{S}} \rangle$
$\lvert 0_{\mathrm{L}}^{\mathrm{A}} 0_{\mathrm{L}}^{\mathrm{B}} \rangle$	22.5	22.7	21.9	22.4(3)	49.5	47.6	45.7	47.6(19)
$\lvert 0_{\mathrm{L}}^{\mathrm{A}} 1_{\mathrm{L}}^{\mathrm{B}} \rangle$	23.5	22.3	22.8	22.8(5)	47.4	49.1	47.9	48.2(9)
$\lvert 1_{\mathrm{L}}^{\mathrm{A}} 0_{\mathrm{L}}^{\mathrm{B}} \rangle$	22	22.7	21.6	22.1(4)	47	48.8	47.7	47.9(9)
$\lvert 1_{\mathrm{L}}^{\mathrm{A}} 1_{\mathrm{L}}^{\mathrm{B}} \rangle$	21.6	22.2	21	21.6(5)	49.1	46.5	47.6	47.7(13)

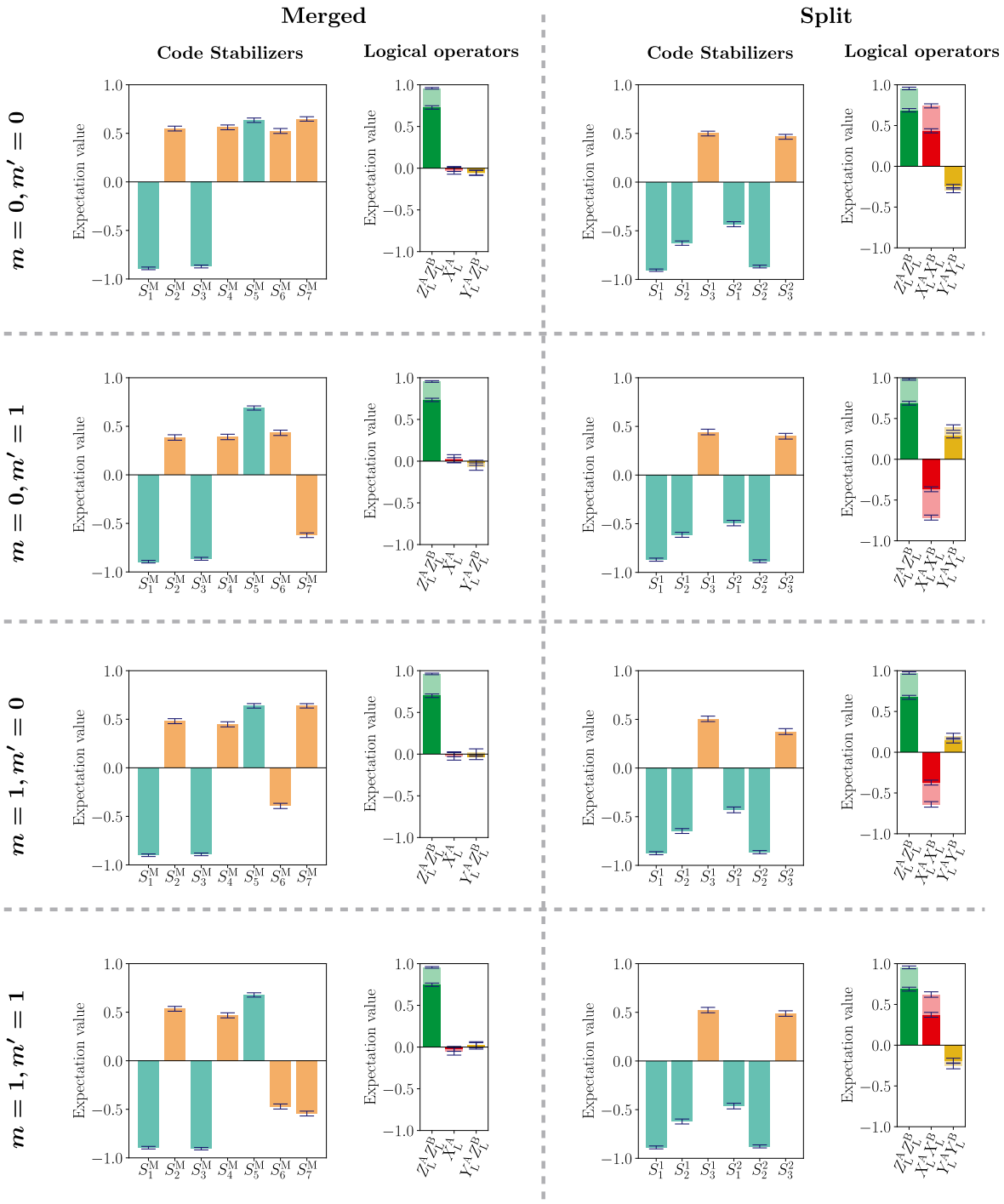

Figure 8.8: **Auxiliary qubit outcomes.** Measurements for different outcomes m, m' of the auxiliary qubits A1, A2 during Z-type merging. Starting in the state $|0_L^A 0_L^B\rangle$, different measurement outcomes are selected by inverting the state of the auxiliary qubits right before measurement of the merging stabilizers. The data verifies the expected change of stabilizers $\mathcal{S}_6^M$ and $\mathcal{S}_7^M$ in the merged state and the different resulting Bell states depending on implemented interaction $(\mathbb{I} + (-1)^{m+m'} X_L^A X_L^B)/\sqrt{2}$.

9 SUMMARY AND OUTLOOK

Alea iacta est. (The die has been cast.)

— Gaius Iulius Caesar

In this thesis, two major milestones towards scalable quantum computation are presented. The first milestone is the experimental implementation of the rigorous characterization of a large-scale quantum computer via Cycle Benchmarking (CB), outlined in chapters 5 and 6. The second milestone focuses on the first demonstration of entangling logical qubits with Lattice Surgery (LS), presented in chapters 7 and 8.

The CB protocol is a robust and efficient technique to estimate the fidelity of multi-qubit quantum processes. The fidelity corresponds to the effective error rate under Randomized Compiling (RC). The protocol is robust in the sense, that it gives faithful results in presence of SPAM and coherent errors. It should be noted that the performance of the same operation in a circuit without RC can differ significantly from the estimated fidelity of its constituents due to the addition or cancellation of coherent errors [192]. This is a general issue with performance metrics for quantum operations [193] and we want to emphasize that RC has been designed to eliminate these coherent errors. The protocol is efficient, because the total experimental time and post-processing resources required for our implementation were approximately independent of the number of qubits, after accounting for the additional tests performed on specific numbers of qubits. This is achieved because the uncertainty of the fidelity estimate is independent of the number of qubits N, and the number of Pauli matrices K that need to be sampled depends only on the desired precision. CB also provides insight into how noise scales within a fixed architecture. In our ion trap, the fidelity of local gates across the whole register decreased linearly with N, demonstrating that our native single-qubit gates have an average fidelity of $99.2(1)\,\%$ and do not deteriorate with the register size. Thus we have demonstrated a scalable method to validate a major requirement for fault-tolerant quantum computation. In addition, we performed interleaved CB protocols to estimate the performance of the multi-qubit entangling MS gate. From the ratio between the dressed MS and the local CB fidelities we infer entangling gate fidelities ranging from $99.6(1)\,\%$ to $86(2)\,\%$ for 2 to 10 qubits. The data from CB also gives estimates of the diagonal of the Pauli-Liouville representation of the effective noise. A natural open question is how to use this procedure to reconstruct the underlying noise model, which we leave for future work.

LS enables entanglement generation between logical qubits and can be complemented with measurement-based protocols for logical state teleportation and manipulation. In this thesis, we have demonstrated entanglement generation and teleportation via LS between two logical qubits, each encoded in a 4-qubit surface code, on a 10-qubit ion trap quantum information processor. We have implemented both the Z- and X-type variants of LS [44, 59], a technique that is considered [60, 194] to be key for operating future fault-tolerant quantum computers. For current NISQ-era devices, certification of logical entanglement [195] generated via LS can provide means for benchmarking. Besides increasing the numbers of physical and logical qubits, future challenges lie in the implementation of LS between arbitrary topological codes [59] to exploit different features such as transversal gate imple-

mentation or high noise tolerance of the respective codes. In this way, LS can function as a fault-tolerant interface between quantum memories and quantum processors.

For the future, there are still many open and interesting challenges in building a scalable quantum computer. Essentially, it will come down to increasing the fidelity of the quantum processes and connecting more and more qubits. Along the way, we need to find the most suitable atomic species to combine with the best available toolbox. A good combination must provide the fastest and most error-free state preparation, state detection, and qubit manipulation techniques. To increase the number of qubits, new trap architectures are needed that enable advanced ion arrangements and techniques such as ion shuttling or ion position reconfiguration. Features integrated into the trap, such as optics, microwave antennas, and photodetection electronics, would enrich the available toolbox. Another interesting possibility would be to use a larger Hilbert space by using more than two quantum states. Together with improvements in quantum error correction protocols and algorithmic advances, future quantum computers could outperform classical computers in the evaluation of complex problems.

A

THE ZEEMAN EFFECT

The magnetic moment $\vec{\mu}_j = \vec{\mu}_l + \vec{\mu}_s$ of an electron in an atom is the sum of the orbital angular momentum $\vec{\mu}_l$ and the spin angular momentum $\vec{\mu}_s$ of the electron. The *anomalous Zeeman effect* [97] describes the coupling of the total angular momentum $\vec{\mu}_j$ to a weak bias magnetic field $\vec{B}$. The perturbed part of the Hamiltonian can be described as $H_M = -\vec{\mu}_j \cdot \vec{B}$, which means that the interaction changes the electronic energy depending on the projection of the magnetic moment onto the direction of the magnetic field. If we assume that the magnetic field is aligned in the z direction with strength $|\vec{B}| = B$, then the time average of the magnetic moment projection along z is $\langle \mu_j \rangle_z = -m_j g_j \mu_\mathrm{B}$ and the frequency shift of an electronic state is defined as [97]

$$\Delta\nu = m_j g_j \frac{\mu_\mathrm{B}}{h} B, \tag{A.1}$$

where m_j is the z-projection of the total angular momentum, g_j describes the Landé factor, μ_B is the Bohr magneton and h is the Planck constant. Note the value of $\mu_\mathrm{B}/h \approx 1.3996\,\mathrm{MHz/G}$. In eq. (A.1) we can see that the degeneracy of the fine structure levels is lifted when a bias magnetic field is applied.

The frequency shift of a given transition can be calculated by the difference of the shifts of the involved states $|\psi\rangle$ and $|\psi'\rangle$ as

$$\Delta\nu(|\psi\rangle \leftrightarrow |\psi'\rangle) = \frac{\mu_\mathrm{B}}{h} B \left(m_J g_J - m'_J g'_J\right) = \frac{\mu}{h} B, \tag{A.2}$$

where μ describes the sensitivity of the respective transition. Values for transitions typically used in the experiment are given in table B.4. Using eq. (A.2) and measuring two transition frequencies $\nu^{(1)} = \nu_0 + \Delta\nu^{(1)}$ and $\nu^{(2)} = \nu_0 + \Delta\nu^{(2)}$ we can estimate the magnitude of the magnetic field as

$$B = \frac{h(\nu^{(1)} - \nu^{(2)})}{\mu^{(1)} - \mu^{(2)}} = \frac{h(\Delta\nu^{(1)} - \Delta\nu^{(2)})}{\mu^{(1)} - \mu^{(2)}}. \tag{A.3}$$

B

PROPERTIES OF CALCIUM II

In table B.1 some important transition properties for ion trapping experiments with $^{40}Ca^{+}$ are presented. Properties of the lowest energy state are shown in table B.2 and in table B.3. In table B.4 the Zeeman shift of various transitions in $^{40}Ca^{+}$ are listed.

Table B.1: **Optical transitions in $^{40}Ca^{+}$ and ^{40}Ca.** Presented are observed wavelengths in air and transition branching ratios. AOM frequency shift describes the difference frequency between the light measured at the wavelength meter and the light sent to the ion.

	Transition	Wavelength (nm)	Branching ratio (%)	Shift (MHz)
$^{40}Ca^{+}$	$4^2S_{1/2} \leftrightarrow 4^2P_{3/2}$	393.366 [196]	93.47(3) [197]	...
	$4^2S_{1/2} \leftrightarrow 4^2P_{1/2}$	396.847 [196]	93.565(7) [198]	$0/+200$
	$4^2S_{1/2} \leftrightarrow 3^2D_{5/2}$	729.147[1] [196]		+620
	$4^2S_{1/2} \leftrightarrow 3^2D_{3/2}$	732.389 [196]		
	$3^2D_{3/2} \leftrightarrow 4^2P_{3/2}$	849.802 [196]	0.661(4) [197]	
	$3^2D_{5/2} \leftrightarrow 4^2P_{3/2}$	854.209 [196]	5.87(2) [197]	+400
	$3^2D_{3/2} \leftrightarrow 4^2P_{1/2}$	866.214 [196]	6.435(7) [198]	+400
^{40}Ca	$4s^1S_0 \leftrightarrow 4p^1P_1$	422.673 [200]		
	$4p^1P_1 \leftrightarrow cont.$	~ 375		

Table B.2: **Lifetimes in $^{40}Ca^{+}$.** Lifetimes and resulting linewidths of the five lowest lying quantum states in $^{40}Ca^{+}$.

State	Lifetime (s)	Linewidth (Hz)
$4^2P_{3/2}$	$6.92(2) \cdot 10^{-9}$ [201]	$23 \cdot 10^6$
$4^2P_{1/2}$	$7.10(2) \cdot 10^{-9}$ [201]	$22.4 \cdot 10^6$
$3^2D_{3/2}$	1.20(1) [202]	0.133
$3^2D_{5/2}$	1.168(7) [202]	0.136
$4^2S_{1/2}$	−	−

[1] A precisely measured value of the $4^2S_{1/2} \leftrightarrow 3^2D_{5/2}$ transition frequency in $^{40}Ca^{+}$ is $\nu = 411\,042\,129\,776\,393.2(1.0)$ Hz [199]

Table B.3: **g-factors in $^{40}Ca^{+}$.** g_j-factors and the result Zeeman shift of the five lowest lying quantum states in $^{40}Ca^{+}$.

State	g_j-factor	$\Delta\nu_{\text{Zeeman}}$ (MHz/G)
$4^2P_{3/2}$	$\sim 4/3$	~ 1.87
$4^2P_{1/2}$	$\sim 2/3$	~ 0.93
$3^2D_{3/2}$	$\sim 4/5$	~ 1.12
$3^2D_{5/2}$	1.2003340(2) [199]	~ 1.68
$4^2S_{1/2}$	2.00225664(9) [203]	~ 2.80

Table B.4: **Magnetic field shifts in $^{40}Ca^{+}$.** First order Zeeman shift of the $|S_{1/2}, m_j\rangle \mathrel{\hat{=}} |m_S\rangle$ to $|D_{5/2}, m_j\rangle \mathrel{\hat{=}} |m_D\rangle$ transitions.

Transition	Zeeman shift (MHz/G)
$\lvert m_S = -1/2\rangle \leftrightarrow \lvert m_D = -5/2\rangle$	-2.80
$\lvert m_S = -1/2\rangle \leftrightarrow \lvert m_D = -3/2\rangle$	-1.12
$\lvert m_S = -1/2\rangle \leftrightarrow \lvert m_D = -1/2\rangle$	$+0.56$
$\lvert m_S = -1/2\rangle \leftrightarrow \lvert m_D = +1/2\rangle$	$+2.24$
$\lvert m_S = -1/2\rangle \leftrightarrow \lvert m_D = +3/2\rangle$	$+3.92$
$\lvert m_S = +1/2\rangle \leftrightarrow \lvert m_D = -3/2\rangle$	-3.92
$\lvert m_S = +1/2\rangle \leftrightarrow \lvert m_D = -1/2\rangle$	-2.24
$\lvert m_S = +1/2\rangle \leftrightarrow \lvert m_D = +1/2\rangle$	-0.56
$\lvert m_S = +1/2\rangle \leftrightarrow \lvert m_D = +3/2\rangle$	$+1.12$
$\lvert m_S = +1/2\rangle \leftrightarrow \lvert m_D = +5/2\rangle$	$+2.80$
$\lvert m_S = -1/2\rangle \leftrightarrow \lvert m_S = +1/2\rangle$	$+2.80$
$\lvert m_D = -1/2\rangle \leftrightarrow \lvert m_D = +1/2\rangle$	$+1.68$
$\lvert m_D = -5/2\rangle \leftrightarrow \lvert m_D = +5/2\rangle$	$+8.40$

C

LASER NOISE INDUCED BY THE WATER COOLER

Mechanical vibrations affecting the Ti:Sa laser can induce frequency fluctuations. As discussed in section 4.2.2, the water cooling system used to temperature stabilize the Ti:Sa crystal induces vibrations. To suppress this acoustic noise we replace the former water cooler[1] with a new water cooling system[2]. Since the PDH error signal reflects the noise that the servo loop has to compensate, we can use the error signal to measure the frequency noise induced by the water cooling system. In fig. C.1 we analyze the frequency spectrum of the PDH error signal for different water cooling settings. In fig. C.1 **a)** a comparison between the former (ThermoTek) and the current (SMC) cooling system is illustrated. As can be seen the error signal with the current cooling system is considerably lower in the frequency range up to 10 kHz. In fig. C.1 **b)** measurements of the error signal with different water flows in the current cooling system (SMC) are presented. With the reduced water flow of 0.43 l/min compared to a flow of 1.5 l/min almost all noise induced by the water cooling system can be removed.

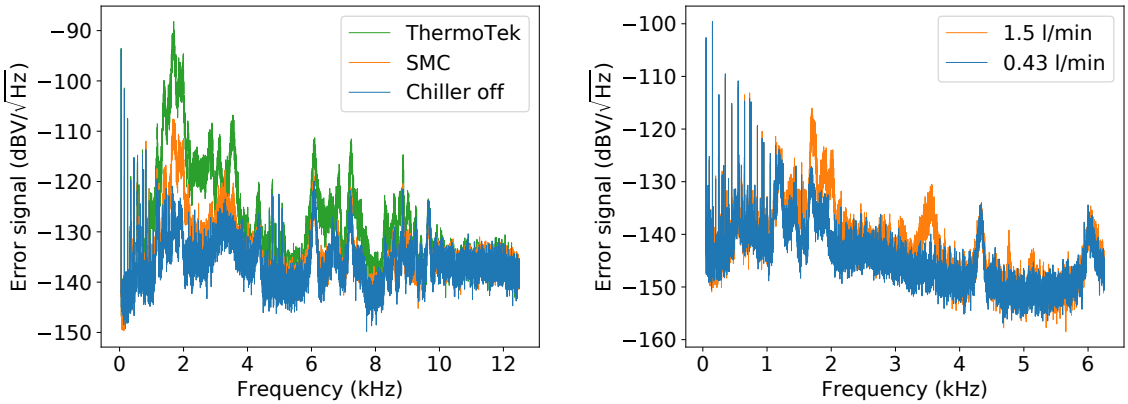

Figure C.1: **729 nm laser error signal spectrum.** Frequency spectrum of PDH error signal of the 729 nm laser stabilized to the HFC cavity. **a)** Comparison between the former (ThermoTek), the current (SMC) and the cooling system being switched off (Chiller off). **b)** Comparison between two water flows of 1.5 l/min and 0.43 l/min in the current (SMC) cooling system.

[1] ThermoTek T255P-3CR
[2] SMC HECR002-A5

D

HIGH FINESSE CAVITY DETAILS

As discussed in section 4.2.2 the 729 nm laser is stabilized to a high finesse cavity (HFC). Since the distance of the cavity mirrors defines the frequency reference for the laser, it is important that the optical length of the cavity changes as little as possible. Therefore the spacer between the cavity mirrors is made from ultra low expansion (ULE[1]) material, which has a zero coefficient of thermal expansion (CTE) to first order at a certain temperature [123]. We characterize the temperature dependence of the HFC by changing the cavity temperature and observing the frequency difference between the ion and the laser locked to the HFC, as depicted in fig. D.1. The temperature is measured from a NTC 10 kΩ thermistor[2] inside the heat shield and stabilized with a SRS PTC10 controller driving peltier elements inside the vacuum chamber. We assume a quadratic temperature dependence of the cavity length and estimate the zero expansion temperature $T_0 = 8.38(3)\,^\circ\mathrm{C}$.

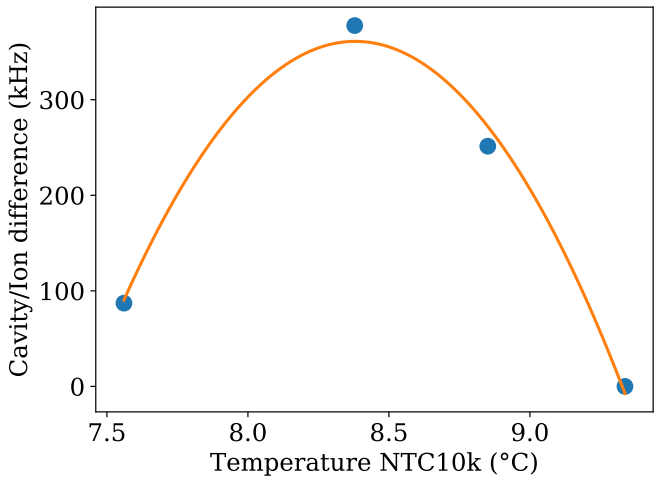

Figure D.1: **HFC temperature dependence.** The frequency difference between the laser locked to cavity and the ion was measured via Ramsey spectroscopy over the course of about one month relative to the cavity temperature. From a quadratic fit $f = A + B(T - T_0)^2$ we estimate the zero expansion temperature $T_0 = 8.38(3)\,^\circ\mathrm{C}$. Since the thermalization time of the ULE spacer inside the vacuum chamber is several days, and the frequency measurements were done at different waiting periods after changing the temperature, the error bars are omitted.

[1] Corning, ULE, titania silicate glass

[2] Steinhart-Hart coefficients: A=2.108508173e-3, B=0.7979204727e-4, C=6.535076315e-7 calculated at https://www.thinksrs.com/downloads/programs/therm%20calc/ntccalibrator/ntccalculator.html

Since the mirrors and the ULE spacer relax and age inside the vacuum chamber, the cavity length changes over time [123]. This drift is extremely slow and we can assume it to be linear, as can be seen in fig. D.2. Over the course of about half year we measure a linear drift of 19.426 mHz/s, which corresponds to an increase in the cavity length of $3.66 \cdot 10^{-18}$ m/s or about one classical proton diameter per second. We compensate this drift by setting a phase continuous sweep on the frequency generator[3] driving the two double pass AOMs before the HFC (see fig. 4.2).

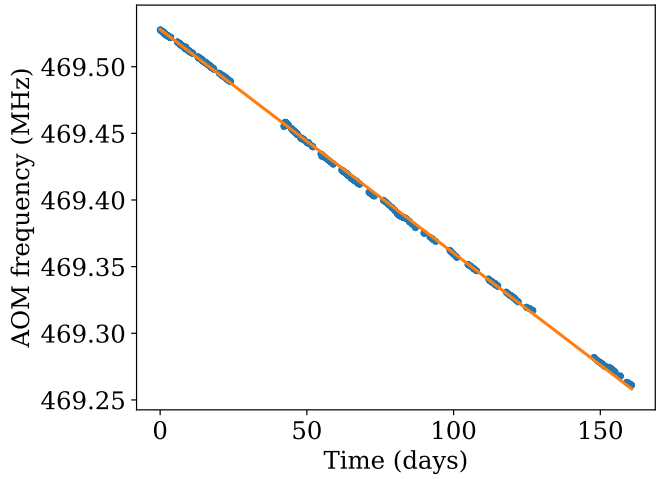

Figure D.2: **HFC drift over time.** The center frequency of the pulsed double pass AOM relative to the $|S_{1/2}\rangle \leftrightarrow |D_{5/2}\rangle$ transition at $\vec{B} = 0$ G. Data was taken from the 04.01.2020 to the 16.06.2020 and we estimate a linear drift of -19.426 mHz/s.

[3] Rohde & Schwarz SMB100B increases frequency with 0.1 Hz step size every 2.0512 s.

E

THE CLIFFORD GROUP

In the literature one finds various slightly different notations for the Clifford group, in the this work we will follow the derivation from Ref. [143]. To construct the Clifford group we use the N-qubit Pauli matrices which are defined with the single-qubit Pauli operators $P = \{I, X, Y, Z\}$ as [143]

$$P_N = \{\sigma_1 \otimes \cdots \otimes \sigma_N \quad | \quad \sigma_i \in P\}. \tag{E.1}$$

In simple terms, an element C of the Clifford group is a unitary operation that maps non-identity Pauli matrices $P_N^* = P_N \backslash \{I^{\otimes N}\}$ onto non-identity Pauli matrices via conjugation as [143]

$$\mathcal{C}_N = \{C \in U(2^N) \quad | \quad \sigma \in \pm P_N^* \Rightarrow C\sigma C^\dagger \in \pm P_N^*\}/U(1), \tag{E.2}$$

up to a multiplication with a global complex phase $U(1)$. Note, that Pauli matrices are also Clifford matrices since $PQP^\dagger = \pm QPP^\dagger = \pm Q$ for all Pauli matrices P, Q.

In the single-qubit case ($N = 1$) we have $\pm P_1^* = \{\pm X, \pm Y, \pm Z\}$. Because of the conjugation rule, the fact that $XZ = iY$ and also that $CXC^\dagger$ and $CZC^\dagger$ anti-commute, the Clifford elements are completely determined by the images of X and Z. If we consider that X can be mapped to any element in $\pm P_1^*$, then Z can be mapped to the elements $\pm P_1^* \backslash \{\pm CXC^\dagger\}$ and we have $|\mathcal{C}_1| = 6 \cdot 4$ distinct Clifford gates $C \in \mathcal{C}_1$. All the 24 single-qubit Clifford operations are listed in table E.1.

For the N-qubit case it can be shown, that the number of Clifford gates grows exponentially as [143]

$$|\mathcal{C}_N| = 2^{N^2+2N} \prod_{J=1}^{N} (4^j - 1). \tag{E.3}$$

Another important point is that the Clifford group can be constructed from a very small gate set [143]

$$\mathcal{C}_N = \langle H_i, P_i, CNOT_{ij} \rangle / U(1), \tag{E.4}$$

where the Hadamard H_i and the Phase gate P_i act on qubit i, and the $CNOT_{ij}$ acts on qubits i, j. Thus, experimentally it is only necessary to calibrate three different gates to implement any Clifford operation.

Table E.1: **Single-qubit Clifford operations.** The 24 single-qubit Clifford unitaries that map a specific Pauli operation onto another Pauli operation and their decomposition into elementary rotations as defined in section 3.3.1 [204].

X	Y	Z	Decomposition
$+X$	$+Y$	$+Z$	I
$+X$	$-Y$	$-Z$	$X(\pi)$
$-X$	$+Y$	$-Z$	$Y(\pi)$
$-X$	$-Y$	$+Z$	$Z(\pi)$
$+X$	$-Z$	$+Y$	$X(\frac{\pi}{2})$
$+X$	$+Z$	$-Y$	$X(-\frac{\pi}{2})$
$-X$	$-Z$	$-Y$	$Z(\pi)X(\frac{\pi}{2})$
$-X$	$+Z$	$+Y$	$Z(\pi)X(-\frac{\pi}{2})$
$+Z$	$+Y$	$-X$	$Y(\frac{\pi}{2})$
$-Z$	$+Y$	$+X$	$Y(-\frac{\pi}{2})$
$+Z$	$-Y$	$+X$	$Z(\pi)Y(\frac{\pi}{2})$
$-Z$	$-Y$	$-X$	$Z(\pi)Y(-\frac{\pi}{2})$
$-Y$	$+X$	$+Z$	$Z(\frac{\pi}{2})$
$+Y$	$-X$	$+Z$	$Z(-\frac{\pi}{2})$
$+Y$	$+X$	$-Z$	$X(\pi)Z(\frac{\pi}{2})$
$-Y$	$-X$	$-Z$	$X(\pi)Z(-\frac{\pi}{2})$
$-Y$	$-Z$	$+X$	$Z(\frac{\pi}{2})X(\frac{\pi}{2})$
$+Y$	$-Z$	$-X$	$Z(\frac{\pi}{2})X(-\frac{\pi}{2})$
$-Y$	$+Z$	$-X$	$Z(-\frac{\pi}{2})X(\frac{\pi}{2})$
$+Y$	$+Z$	$+X$	$Z(-\frac{\pi}{2})X(-\frac{\pi}{2})$
$+Z$	$+X$	$+Y$	$Z(\frac{\pi}{2})Y(\frac{\pi}{2})$
$-Z$	$+X$	$-Y$	$Z(\frac{\pi}{2})Y(-\frac{\pi}{2})$
$+Z$	$-X$	$-Y$	$Z(-\frac{\pi}{2})Y(\frac{\pi}{2})$
$-Z$	$-X$	$+Y$	$Z(-\frac{\pi}{2})Y(-\frac{\pi}{2})$

F

CYCLE BENCHMARKING SUPPLEMENT

The content of this chapter is extracted from the supplemental material of Ref. [25]

F.1 MATHEMATICAL ASSUMPTIONS

In this section, we specify the state preparation and measurement (SPAM) procedures, obtain expressions for the expected values of steps in the protocol over the set of all Pauli matrices $\mathsf{P}^N = \{I, X, Y, Z\}^{\otimes N}$, and analyze the uncertainties in experimental estimates of those expected values. We conclude by giving a simple expression for the ideal MS gate that facilitates the calculation of $\mathcal{C}(P)$.

For this appendix only, we abuse notation slightly by implicitly defining the channel $\mathcal{P}(A) = PAP^\dagger$ for any Pauli matrix P, so that we can use expressions such as $\sum_P \mathcal{P}$.

We begin by specifying the mathematical assumptions we use in our analysis. We assume that initializing N ions into the ground state corresponds to preparing a mixed state ρ that is independent of any subsequent control operations to be applied. We assume that measuring the ions in the computational basis corresponds to performing a fixed positive-operator-valued measurement (POVM) that depends only upon the number of ions in the trap and not on any prior control operations. We assume that the noise in our implementations of a cycle is Markovian on the timescale of the cycle and is independent and identically distributed each time a cycle is applied. These three assumptions are standard in benchmarking and tomography literature.

Finally, we also assume that the noise in a cycle of independent single-qubit gates is independent of the specific single-qubit gates being implemented. Specifically, we assume that the noisy Markovian implementation $\tilde{\mathcal{C}}$ of a cycle $\mathcal{C}$ of single-qubit gates can be written as $\tilde{\mathcal{C}} = \mathcal{A}\mathcal{C}$ for some fixed completely positive and trace-preserving map $\mathcal{A}$. The assumption of gate-independent noise on the random Pauli gates is weaker than the corresponding assumption in randomized benchmarking, namely, that the noisy implementation of *any* N-qubit Clifford gate $\mathcal{C}_N$ can be written as $\tilde{\mathcal{C}}_N = \mathcal{A}\mathcal{C}_N$, independent of the number of entangling gates required to implement $\mathcal{C}_N$. We expect that this assumption can be further relaxed using the analysis of Ref. [146] at the cost of more cumbersome notation. This will be subject of future research.

F.2 STATE PREPARATION AND MEASUREMENT PROCEDURES

In our experiment, we can only directly perform noisy preparations and measurements in the N-qubit computational basis $\{|z\rangle : z \in \mathbb{Z}_2^N\}$. We now specify the basis changes and coarse graining we use to perform other preparations and measurements. For an N-qubit matrix Q (e.g., P, $\mathcal{C}(P)$ from the main text), let $\mathcal{B}_Q$ rotate the computational basis to an eigenbasis of Q such that

$$\sum_{z \in \mathbb{Z}_2^N} \mathrm{tr}\left[\mathcal{B}_Q(|z\rangle\langle z|)Q\right] \mathcal{B}_Q(|z\rangle\langle z|) = Q. \tag{F.1}$$

For the processes we investigated, $\mathcal{C}(P)$ is always an N-qubit Pauli matrix. Therefore, we only need to prepare eigenstates of Pauli matrices P and measure the expectation value of Pauli matrices $\mathcal{C}(P)$. Consequently, our SPAM procedures are fully specified by defining $\mathcal{B}_Q$ for arbitrary Pauli matrices Q. We choose to construct the $\mathcal{B}_Q$ out of local Clifford operators to maximize the SPAM coefficients (which results in a smaller statistical uncertainty). Specifically, let $P|_j$ denote the jth tensor factor of a matrix, $\mathcal{A}_I = \mathcal{A}_Z = \mathcal{I}$ and

$$\mathcal{A}_X(Z) = X, \quad \mathcal{A}_X(X) = Y$$
$$\mathcal{A}_Y(Z) = Y, \quad \mathcal{A}_Y(Y) = X.$$

Then we choose the basis-changing gate for an N-qubit Pauli matrix Q to be

$$\mathcal{B}_Q = \bigotimes_{j=1}^{N} \mathcal{A}_{Q|_j}. \tag{F.2}$$

Note that the basis changing procedure is independent of the sign of Q.

We now specify the coarse-graining procedure we use to measure the expectation value of observables. Suppose a system is in a state ρ and let $\Pr(z|Q)$ be the probability of observing the computational basis outcome z after applying the process $\mathcal{B}_Q^\dagger$. One measures the expectation value of Q [e.g., $Q = \mathcal{C}(P)$] by applying $\mathcal{B}_Q^\dagger$, measuring in the computational basis, and averaging the probabilities of the outcomes weighted by the coefficients $\operatorname{tr}[\mathcal{B}_Q(|z\rangle\langle z|)Q]$, where the weights are computed from the ideal quantities. From eq. (F.1) and by the linearity of the trace,

$$\operatorname{tr}[Q\rho] = \sum_{z\in\mathbb{Z}_2^N} \operatorname{tr}[\mathcal{B}_Q(|z\rangle\langle z|)Q] \Pr(z|Q). \tag{F.3}$$

Note that as we average the relative frequencies over all outcomes and $\operatorname{tr}[\mathcal{B}_Q(|z\rangle\langle z|)Q]$ is in the unit disc, the number of measurements required to estimate the expectation value of Q to a fixed additive precision is independent of the number of qubits N by a standard application of, e.g., Hoeffding's inequality [205].

The above estimation procedure will include several sources of SPAM error per qubit, including errors in qubit initialization, measuring qubits in the computational basis, and in the local processes used to change the basis. Consequently, a protocol has to be robust to SPAM errors to provide a practical characterization of a multi-qubit gate.

F.3 MODELLING THE DECAY AS A FUNCTION OF THE SEQUENCE LENGTH

We now determine the expected value of $\sum_{l=1}^{L} f_{P,m,l}/L$ for fixed values of P and m under the assumptions specified in appendix F.1.

Theorem 1. *Let $\mathcal{G}$ be a Clifford cycle and $\tilde{\mathcal{G}}$ be an implementation of $\mathcal{G}$ with Markovian noise. Suppose there exists a process $\mathcal{A}$ such that $\tilde{\mathcal{R}} = \mathcal{A}\mathcal{R}$ for any Pauli process $\mathcal{R}$. Then for a fixed Pauli matrix P and positive integer m, the expected value of $f_{P,m,l}$ from step 3c of the protocol over all random Pauli processes $\mathcal{R}_0, \ldots, \mathcal{R}_m$ is*

$$\langle f_{P,m,l}\rangle = \beta \prod_{j=0}^{m-1} F_{\mathcal{G}^j(P)}(\mathcal{E}, \mathcal{I}),$$

where $\mathcal{E} = \mathcal{G}^\dagger\tilde{\mathcal{G}}\mathcal{A}$ and β is a scalar that depends only on P and $\mathcal{G}^m(P)$. Moreover, $\beta = 1$ in the absence of SPAM errors.

Proof. Substituting $\tilde{\mathcal{R}}_i = \mathcal{A}\mathcal{R}_i$ into the noisy version of eq. (5.17) (i.e., overset each operator with a $\sim$), the average superoperator applied over all sequences for a fixed choice of random sequences is

$$\tilde{\mathcal{C}} = \mathcal{A}\mathcal{R}_m\tilde{\mathcal{G}}\ldots\mathcal{A}\mathcal{R}_1\tilde{\mathcal{G}}\mathcal{A}\mathcal{R}_0. \tag{F.4}$$

Inserting $\mathcal{G}\mathcal{G}^\dagger$ between the ideal Pauli processes $\mathcal{R}_i$ and the adjacent $\tilde{\mathcal{G}}$ gives

$$\tilde{\mathcal{C}} = \mathcal{A}\mathcal{R}_m\mathcal{G}\mathcal{E}\ldots\mathcal{R}_1\mathcal{G}\mathcal{E}\mathcal{R}_0 \tag{F.5}$$

where $\mathcal{E} = \mathcal{G}^\dagger\tilde{\mathcal{G}}\mathcal{A}$. We can now do a standard relabelling of the randomizing gates to obtain a twirl by setting $\mathcal{T}_0 = \mathcal{R}_0$ and recursively defining

$$\mathcal{R}_i = \mathcal{T}_i\mathcal{G}\mathcal{T}_{i-1}^\dagger\mathcal{G}^\dagger \tag{F.6}$$

for $i > 0$. With this relabelling,

$$\tilde{\mathcal{C}} = \mathcal{A}\mathcal{T}_m\mathcal{G}\mathcal{T}_{m-1}^\dagger\mathcal{E}\mathcal{T}_{m-1}\ldots\mathcal{T}_1^\dagger\mathcal{E}\mathcal{T}_1\mathcal{G}\mathcal{T}_0^\dagger\mathcal{E}\mathcal{T}_0. \tag{F.7}$$

The $\mathcal{T}_i$ are all Pauli processes because $\mathcal{G}\mathcal{P}\mathcal{G}^\dagger$ is a Pauli process for any Pauli process $\mathcal{P}$ and any Clifford process $\mathcal{G}$. Moreover, the $\mathcal{T}_i$ are uniformly random because the Pauli processes are sampled uniformly at random and form a group. Therefore averaging independently over all $\mathcal{T}_0, \ldots, \mathcal{T}_{m-1}$ for a fixed choice of $\mathcal{T}_m$ results in the effective superoperator

$$\mathcal{A}\mathcal{T}_m(\mathcal{G}\tilde{\mathcal{E}})^m, \tag{F.8}$$

where

$$\tilde{\mathcal{E}} = 4^{-N}\sum_{P\in\mathsf{P}^N}\mathcal{P}^\dagger\mathcal{E}\mathcal{P}. \tag{F.9}$$

Now note that $\tilde{\mathcal{E}}$ is invariant under conjugation by Pauli operators and so $\tilde{\mathcal{E}}(Q) \propto Q$ for all $Q \in \mathsf{P}^N$ [206]. As the Pauli matrices form a trace-orthogonal basis for the set of matrices,

$$\begin{aligned}
\tilde{\mathcal{E}}(Q) &= 2^{-N}\operatorname{tr}\left[Q^\dagger\tilde{\mathcal{E}}(Q)\right]Q \\
&= 4^{-N}\sum_{P\in\mathsf{P}^N}2^{-N}\operatorname{tr}\left[Q\mathcal{P}^\dagger\mathcal{E}\mathcal{P}(Q)\right]Q \\
&= 4^{-N}\sum_{P\in\mathsf{P}^N}2^{-N}\operatorname{tr}\left[\mathcal{P}(Q)\mathcal{E}\mathcal{P}(Q)\right]Q \\
&= 4^{-N}\sum_{P\in\mathsf{P}^N}2^{-N}\operatorname{tr}\left[Q\mathcal{E}(Q)\right]Q \\
&= F_Q(\mathcal{E},\mathcal{I})Q,
\end{aligned} \tag{F.10}$$

for any $Q \in \mathsf{P}^N$, where we have used the fact that $\mathcal{P}(Q) = PQP^\dagger = \pm Q$ for any Pauli matrices P, Q and eq. (5.14) .

For any two Pauli matrices $P, Q \in \mathsf{P}^N$, let

$$\eta(Q,P) = \begin{cases} 1 & \text{if } QP = PQ \\ -1 & \text{otherwise.} \end{cases} \tag{F.11}$$

Then, from eq. (F.8) with $P' = \mathcal{G}^m(P)$ for convenience, the expected outcome of the ideal circuit is $\mathcal{C} = \eta(T_m, P)P'$. Now note that under measurement errors and noisy changes of basis [i.e., errors in the $\Pr(z|Q)$] and folding the residual $\mathcal{A}$ into the measurement, eq. (F.3) gives the expectation value of some operator $\tilde{P}'$ (which is not uniquely defined). Since only the weights in eq. (F.3) depend on the sign of P' and are calculated from the ideal expressions, the noisy measurement for $-P'$ gives the expectation value of $-\tilde{P}'$ by linearity.

Let ρ be the prepared state after applying a noisy change of basis. Then the expectation value of $f_{P,m,l}$ in step 3c over all sequences is

$$\begin{aligned}\langle f_{P,m,l}\rangle &= 4^{-N} \sum_{T_m \in \mathsf{P}^N} \eta(T_m, P') \operatorname{tr}\left[\mathcal{T}_m^\dagger(\tilde{P}')(\mathcal{G}\tilde{\mathcal{E}})^m(\rho)\right] \\ &= \alpha_P \operatorname{tr}\left[P'(\mathcal{G}\tilde{\mathcal{E}})^m(\rho)\right] \end{aligned} \tag{F.12}$$

by Lemma 2 below, where $\alpha_P = 2^{-N}\operatorname{tr}[P\tilde{P}']$ is 1 in the absence of errors.

Expanding $\rho = \sum_{Q\in\mathsf{P}^N} \rho_Q Q$ and noting that $\mathcal{G}$ is a Clifford cycle, eq. (F.12) reduces to

$$\langle f_{P,m,l}\rangle = \sum_{Q\in\mathsf{P}^N} \alpha_P \rho_Q \operatorname{tr}\left[P'\mathcal{G}^m(Q)\right] \prod_{j=0}^{m-1} F_{\mathcal{G}^j(Q)}(\mathcal{E}, \mathcal{I}). \tag{F.13}$$

As the Pauli matrices are trace-orthogonal and $P' = \mathcal{G}^m(P)$, $\operatorname{tr}\left[\mathcal{G}^m(Q)P'\right] = 2^N\delta_{Q,P}$. Therefore

$$\langle f_{P,m,l}\rangle = 2^N \alpha_P \rho_P \prod_{j=0}^{m-1} F_{\mathcal{G}^j(P)}(\mathcal{E}, \mathcal{I}), \tag{F.14}$$

where $\rho_P = 2^{-N}$ in the absence of SPAM errors, so that $\beta = 2^N\alpha_P\rho_P = 1$ in the absence of SPAM errors. □

In the above proof, we make use of the following lemma proven and applied to randomized benchmarking in Ref. [207].

Lemma 2. *For any matrix M and any Pauli matrix P,*

$$4^{-N} \sum_{Q\in\mathsf{P}^N} \eta(Q, P)\mathcal{Q}(M) = 2^{-N} \operatorname{tr}\left[PM\right] P.$$

Proof. As the Pauli matrices form an orthogonal basis for the space of matrices, we can write

$$M = \sum_{R\in\mathsf{P}^{\otimes N}} m_R R, \tag{F.15}$$

where $m_R = 2^{-N}\operatorname{tr}(RM)$. As $\mathcal{Q}(R) = \eta(Q, R)R$ for any Pauli matrix R,

$$4^{-N} \sum_{Q\in\mathsf{P}^N} \eta(Q, P)\mathcal{Q}(M) = \sum_{R\in\mathsf{P}^{\otimes N}} m_R(\eta_P \cdot \eta_R)R \tag{F.16}$$

by linearity, where

$$\eta_P \cdot \eta_R = 4^{-N} \sum_{Q\in\mathsf{P}^N} \eta(Q, R)\eta(P, R). \tag{F.17}$$

As $\eta(Q, P)$ is a real 1-dimensional representation of the Pauli group for any fixed Pauli matrix P and $\eta(Q, P)$ and $\eta(Q, R)$ are inequivalent as representations for $P \neq R$,

$$4^{-N} \sum_{Q} \eta(P^{(m)}, Q)\eta(P, Q) = \delta(P, R) \tag{F.18}$$

by Schur's orthogonality relations. □

F.4 ESTIMATING THE PROCESS FIDELITY

We now prove that the expectation value of eq. (5.19) provides an accurate, yet conservative, estimate of the process fidelity in eq. (5.16) under the same assumptions as in eq. (5.14) .

Theorem 3. *Let*

$$\hat{F} = 4^{-N} \sum_{P \in \mathsf{P}^N} \left(\frac{\langle f_{P,m_2,l} \rangle}{\langle f_{P,m_1,l} \rangle} \right)^{\frac{1}{m_2 - m_1}}$$

be the expected outcome of the cycle benchmarking protocol over all randomizations. Let $\mathcal{G}$ be a Clifford cycle and $\tilde{\mathcal{G}}$ be an implementation of $\mathcal{G}$ with Markovian noise. Suppose there exists a process $\mathcal{A}$ such that $\tilde{\mathcal{R}} = \mathcal{A}\mathcal{R}$ for any Pauli process $\mathcal{R}$. Then $\hat{F} \leq F_{\mathrm{RC}}(\tilde{\mathcal{G}}, \mathcal{G})$ and

$$\hat{F} - F_{\mathrm{RC}}(\tilde{\mathcal{G}}, \mathcal{G}) = \mathcal{O}\left([1 - F_{\mathrm{RC}}(\tilde{\mathcal{G}}, \mathcal{G})]^2 \right).$$

Proof. First, recall that the process fidelity is linear and for any unitary process $\mathcal{U}$,

$$F(\tilde{\mathcal{G}}, \mathcal{U}) = F(\mathcal{U}^\dagger \tilde{\mathcal{G}}, \mathcal{I}).$$

Therefore from eq. (5.16) ,

$$\begin{aligned} F_{\mathrm{RC}}(\tilde{\mathcal{G}}, \mathcal{G}) &= 4^{-N} \sum_{R \in \mathsf{P}^N} F(\tilde{\mathcal{G}}\tilde{\mathcal{R}}, \mathcal{G}\mathcal{R}) \\ &= 4^{-N} \sum_{R \in \mathsf{P}^N} F(\mathcal{R}\mathcal{G}^\dagger \tilde{\mathcal{G}} \mathcal{A}\mathcal{R}, \mathcal{I}) \\ &= F(\tilde{\mathcal{E}}, \mathcal{I}). \end{aligned}$$

Moreover, $F(\mathcal{E}, \mathcal{I}) = F(\tilde{\mathcal{E}}, \mathcal{I})$ by eq. (5.13) and eq. (F.10), and so we will prove statements for $F(\mathcal{E}, \mathcal{I})$.

Now fix a Pauli matrix P and note that if m_1 and $m_2 = m_1 + \delta m$ are chosen so that $P' = \mathcal{G}^{m_2}(P) = \mathcal{G}^{m_1}(P)$ (guaranteed by step 2 of the protocol), then

$$\left(\frac{\langle f_{P,m_2,l} \rangle}{\langle f_{P,m_1,l} \rangle} \right)^{1/\delta m} = \prod_{j=0}^{\delta m - 1} F_{\mathcal{G}^j(P')}(\mathcal{E}, \mathcal{I})^{1/\delta m} \tag{F.19}$$

by Theorem 1, as the scalar is the same for m_1 and m_2. That is, the terms being averaged over in eq. (5.19) are themselves geometric means of $F_Q(\tilde{\mathcal{E}}, \tilde{\mathcal{I}})$ for different Pauli matrices Q obtained by applying $\mathcal{G}$ to the sampled P. Formally, let $w(Q|P', \delta m)$ be the relative frequency of Q in the list $(\mathcal{G}^j(P') : j = 0, \ldots, \delta m - 1)$. Then

$$\left(\frac{\langle f_{P,m_2,l} \rangle}{\langle f_{P,m_1,l} \rangle} \right)^{1/\delta m} = \prod_{Q \in \mathsf{P}^N} F_Q(\mathcal{E}, \mathcal{I})^{\omega(Q|\mathcal{G}^{m_1}(P), \delta m)} \tag{F.20}$$

By the inequality of the weighted arithmetic and geometric means,

$$\left(\frac{\langle f_{P,m_2,l} \rangle}{\langle f_{P,m_1,l} \rangle} \right)^{1/\delta m} \leq \sum_{Q \in \mathsf{P}^N} w(Q|P, \delta m) F_Q(\mathcal{E}, \mathcal{I}). \tag{F.21}$$

As $\mathcal{G}$ is a Clifford matrix, $\sum_{P\in\mathsf{P}^N}\omega(Q|P,\delta m)=1$ for all Pauli matrices Q. Therefore summing eq. (F.21) over all input Pauli matrices P gives $\hat{F}\leq F(\mathcal{E},\mathcal{I})$. To prove the approximate statement, let $r_Q=1-F_Q(\mathcal{E},\mathcal{I})$. Expanding eq. (F.20) to second order in the r_Q gives

$$\left(\frac{\langle f_{P,m_2,l}\rangle}{\langle f_{P,m_1,l}\rangle}\right)^{1/\delta m}=1-\sum_{Q\in\mathsf{P}^N}\omega(Q|P,\delta m)r_Q+\mathcal{O}(r_Q^2).$$

The approximate claim then holds as $\mathcal{O}(r_Q^2)=\mathcal{O}([1-F(\mathcal{E},\mathcal{I})]^2)$ by Lemma 4 below. □

Lemma 4. *For any completely positive and trace-preserving map $\mathcal{E}$ and any Pauli matrix P,*

$$0\leq 1-F_P(\mathcal{E},\mathcal{I})\leq 2-2F(\mathcal{E},\mathcal{I}).$$

Proof. Note that eq. (F.10) holds for any completely positive and trace preserving map $\mathcal{E}$ with $\tilde{\mathcal{E}}$ as defined in eq. (F.9). In particular, $F_P(\tilde{\mathcal{E}},\mathcal{I})=F_P(\mathcal{E},\mathcal{I})$ for all $P\in\mathsf{P}^N$ and so $F(\tilde{\mathcal{E}},\mathcal{I})=F(\mathcal{E},\mathcal{I})$ by eq. (5.13) . As $\tilde{\mathcal{E}}$ is covariant under Pauli channels, there exists a probability distribution $p(Q)$ over the set of Pauli matrices such that [206].

$$\tilde{\mathcal{E}}(A)=\sum_Q p(Q)QAQ^\dagger. \tag{F.22}$$

For any Kraus operator decomposition, the process fidelity can be written as [20]

$$F(\tilde{\mathcal{E}},\mathcal{I})=\sum_Q p(Q)|\operatorname{tr}Q|^2/4^N=p(I). \tag{F.23}$$

Substituting eq. (F.22) into eq. (5.14) and using $[P,I]=0$, $p(Q)\geq 0$, and eq. (F.23) gives

$$\begin{aligned}F_P(\tilde{\mathcal{E}},\mathcal{I})&=\sum_{Q:[Q,P]=0}2p(Q)-1\\&\geq 2p(I)-1=2F(\tilde{\mathcal{E}},\mathcal{I})-1.\end{aligned} \tag{F.24}$$

The lower bound follows as the $F_P(\tilde{\mathcal{E}},\mathcal{I})$ are eigenvalues of $\tilde{\mathcal{E}}$ and hence are in the unit disc [208]. □

F.5 FINITE SAMPLING EFFECTS

We now consider the effect of finite samples. Specifically, we will show that with appropriate choices of sequence lengths, the uncertainty in the estimate $\hat{F}$ obtained via eq. (5.13) will scale as $O([1-F]/\sqrt{K})$ where the implicit constants are independent of the number of qubits. We will also show that if the experimental parameters are chosen appropriately, the implicit constant should be at most 1, that is, $\sigma\leq(1-F)/\sqrt{K}$. All the "approximately normal" statements in this section can be replaced by rigorous statements using the results of [209], Hoeffding's inequality [205] and the union bound, at the expense of additional notation and less favorable (but pessimistic) constants.

First, note that estimating the expectation value of the sequence labelled by l with a finite number of measurements R will produce an estimate of each expectation value $\langle f_{P,m,l}\rangle$ with an error $\epsilon_{P,m,l}$ that is approximately normally distributed with the standard deviation $\sigma_{P,m,l}\propto 1/\sqrt{R}$ independent of the number of qubits by the central limit theorem. Averaging the estimated expectation values $\langle f_{P,m,l}\rangle$ over a finite number L of random sequences will give an estimate of $\langle f_{P,m,l}\rangle$ with an error $\epsilon_{P,m}$ that is approximately normally distributed

with standard deviation $\sigma_{P,m} \propto 1/\sqrt{L}$ that is independent of the number of qubits, again by the central limit theorem. Formally, the error in $\langle f_{P,m,l} \rangle$ can be divided into the average of a number of normally distributed random variables (the errors on the individual estimates), which contributes $O(1/\sqrt{LR})$ to $\sigma_{P,m}$, and the error from sampling a finite number of random sequences, which contributes $O(1/\sqrt{L})$ to $\sigma_{P,m}$. Hence, the error will be dominated by the finite number of random sequences. Using a series expansion of the ratio

$$\hat{F}_P := \left(\frac{\langle f_{P,m_2,l} \rangle + \epsilon_{P,m_2}}{\langle f_{P,m_1,l} \rangle + \epsilon_{P,m_1}} \right)^{1/\delta m},$$

the estimated process fidelity obtained by averaging $\hat{F}_P$ over K Pauli matrices will satisfy

$$\begin{aligned} \hat{F} &= \frac{1}{K} \sum_P \hat{F}_P \\ &\approx \sum_P \frac{F_P}{K} + \sum_P \frac{\delta\epsilon_P}{K\delta m}, \end{aligned} \tag{F.25}$$

where we define $\delta\epsilon_P = \epsilon_{P,m_2} - \epsilon_{P,m_1}$. Note that $\delta\epsilon_P$ is a difference between two approximately normal random variables with standard deviation $O(1/\sqrt{L})$ (neglecting the subleading term $O[1/\sqrt{LR}]$) and so $\mathbb{V}(\delta\epsilon_P) = O(1/L)$. Assuming that the $\delta\epsilon_P$ and F_P are independent, the expected variance of the estimate $\hat{F}$ over K Pauli matrices sampled uniformly with replacement is

$$\begin{aligned} \mathbb{V}^2(\hat{F}) &\approx K\,\mathbb{V}_P^2\left(\frac{F_P}{K}\right) + K\,\mathbb{V}^2\left(\frac{\delta\epsilon_P}{K\delta m}\right) \\ &\approx \frac{\mathbb{V}_P^2(F_P)}{K} + \frac{\mathbb{V}^2\left(\delta\epsilon_P\right)}{K\delta m^2}. \end{aligned} \tag{F.26}$$

We now show that both terms in eq. (F.26) can be made to scale as $(1-F)^2/K$ by choosing parameters appropriately. The first term satisfies

$$\mathbb{V}^2(\hat{F}_P) \leq [1 - F(\mathcal{E}, \mathcal{I})]^2 \tag{F.27}$$

since for any Pauli matrix P,

$$\begin{aligned} |F(\mathcal{E},\mathcal{I}) - F_P(\mathcal{E},\mathcal{I})| &\leq \max_{Q \in \mathsf{P}^N} |F(\mathcal{E},\mathcal{I}) - F_P(\mathcal{E},\mathcal{I})| \\ &\leq 1 - F(\mathcal{E},\mathcal{I}) \end{aligned} \tag{F.28}$$

by Lemma 4. Furthermore, if the δm are chosen to be proportional to $1/(1-F)$, then the variance of $\hat{F}$ is proportional to $(1-F)^2$, so that we can efficiently estimate $1-F$ to multiplicative precision. The values of m in table 6.1 approximately satisfy this condition. With such choices of δm, we then have $\mathbb{V}^2(\hat{F}) = O[(1-F)^2/K]$. Furthermore, if L and R are sufficiently large so that $\mathbb{V}^2(\delta\epsilon_P)$ is negligible, than the variance of the estimator will satisfy

$$\mathbb{V}^2(\hat{F}) \leq (1-F)^2/K =: \sigma^2_{\text{Pauli}}. \tag{F.29}$$

It can be seen in fig. 6.4 that the standard deviation decreases with the square-root of the sampled subspaces K, with a least squares fit giving $\sigma = 0.0127(2)/\sqrt{K}$. This is consistent with the above analysis, which was based on the assumption that the $\delta\epsilon_P$ and F_P are independent. If we assume quantum projection noise ($\sqrt{p(1-p)/R}$) to be the only error

source in the experiments, where p is the probability of measuring a certain outcome and R is the number of times a sequence is repeated, we can calculate a lower bound σ_{lower} for the measured data. This lower bound could be reached if the noise in the noise in the system is completely isotropic (e.g. global depolarizing). Biased noise or drift (see fig. 6.3) will lead to uncertainties bigger than those originating from quantum projection noise.

The observed standard deviation σ is larger than the lower bound given by quantum projection noise $\sigma_{\text{lower}} = 0.00375(1)/\sqrt{K}$ but smaller than the upper bound $\sigma_{\text{Pauli}} = 0.0275(8)/\sqrt{K}$ on the contribution from sampling a finite number of Pauli matrices. This suggests that the other source of statistical uncertainty, namely, a finite number of randomizations L and measurements per sequence R, is sufficiently small to allow us to accurately estimate the process fidelity.

F.6 CORRECTION OPERATORS FOR THE MS GATE

We performed cycle benchmarking for the identity and MS gates. The MS gate satisfies $\text{MS}^4 = I$, so that we can restrict m to be an integral multiple of 4. Indeed, $\text{MS}^2 \propto X^{\otimes N}$ so that we could restrict m to be even numbers by keeping track of the sign (which would depend on the Pauli matrix P). To compute the expectation value of $\mathcal{C}(P)$, we need to know how an arbitrary Pauli operator Q propagates through the MS gate. Using $\text{MS} \propto (I - iX^{\otimes N})/\sqrt{2}$ for even N gives

$$\begin{aligned}\mathcal{MS}(Q) &= \text{MS}Q\text{MS}^\dagger \\ &= \begin{cases} Q & \text{if } QX^{\otimes N} = X^{\otimes N}Q \\ iQX^{\otimes N}\text{MS} & \text{otherwise.} \end{cases}\end{aligned} \tag{F.30}$$

G

LIST OF PUBLICATIONS

The experimental results presented in this thesis lead to the following journal publications:

1. [25] A. Erhard, J. J. Wallman *et.al.* Characterizing large-scale quantum computers via cycle benchmarking. *Nature Comm.* **10**, 5347 (2019)

2. [153] A. Erhard, H. Poulsen-Nautrup *et.al.* Entangling logical qubits with lattice surgery. *Nature* **589**, 220–224 (2021)

During my work as a PhD student I contributed to the following publications:

3. [210] E. A. Martinez *et al.* Real-time dynamics of lattice gauge theories with a few-qubit quantum computer. *Nature* **534**, 516–519 (2016).

4. [211] L. Postler *et al.* Experimental quantification of spatial correlations in quantum dynamics. *Quantum* **2**, 90 (2018).

5. [212] C. Greganti *et.al.*Cross-verification of independent quantum devices. arXiv:1905.09790 (2019)

6. [172] R. Stricker *et.al.* Experimental deterministic correction of qubit loss. *Nature* **585**, 207–210 (2020)

7. [111] A. K. Pal *et.al.* Relaxation times do not capture logical qubit dynamics. arXiv:2012.07911 (2020)

BIBLIOGRAPHY

[1] Alan Mathison Turing, *"On computable numbers, with an application to the entscheidungsproblem,"* J. of Math **58**, 5 (1936).

[2] David Elieser Deutsch, Adriano Barenco, and Artur Ekert, *"Universality in quantum computation,"* Proceedings of the Royal Society of London. Series A: Mathematical and Physical Sciences **449**, 669 (1995).

[3] Peter W Shor, *"Algorithms for quantum computation: discrete logarithms and factoring,"* in *Proceedings 35th annual symposium on foundations of computer science* (1994).

[4] Richard P Feynman, *"Simulating physics with computers,"* Int. J. Theor. Phys **21** (1982).

[5] Stephen Wiesner, *"Conjugate coding,"* ACM Sigact News **15**, 78 (1983).

[6] Artur K Ekert, *"Quantum cryptography based on bell's theorem,"* Phys. Rev. Lett. **67**, 661 (1991).

[7] Charles H Bennett, *"Quantum cryptography using any two nonorthogonal states,"* Phys. Rev. Lett. **68**, 3121 (1992).

[8] Rolf Landauer *et al.*, *"Information is physical,"* Physics Today **44**, 23 (1991).

[9] Michael A. Nielsen and Isaac L. Chuang, *Quantum Computation and Quantum Information: 10th Anniversary Edition* (Cambridge University Press, 2010).

[10] Adriano Barenco, Charles H Bennett, Richard Cleve, David P DiVincenzo, Norman Margolus, Peter Shor, Tycho Sleator, John A Smolin, and Harald Weinfurter, *"Elementary gates for quantum computation,"* Phys. Rev. A **52**, 3457 (1995).

[11] Isaac L. Chuang and Michael A. Nielsen, *"Prescription for experimental determination of the dynamics of a quantum black box,"* J. Mod. Opt. **44**, 2455 (1997).

[12] Seth T. Merkel, Jay M. Gambetta, John A. Smolin, Stefano Poletto, Antonio D. Córcoles, Blake R. Johnson, Colm A. Ryan, and Matthias Steffen, *"Self-consistent quantum process tomography,"* Phys. Rev. A **87**, 062119 (2013).

[13] Robin Blume-Kohout, John King Gamble, Erik Nielsen, Jonathan Mizrahi, Jonathan D Sterk, and Peter Maunz, *"Robust, self-consistent, closed-form tomography of quantum logic gates on a trapped ion qubit,"* arXiv:1310.4492 (2013).

[14] Robin Blume-Kohout, John King Gamble, Erik Nielsen, Kenneth Rudinger, Jonathan Mizrahi, Kevin Fortier, and Peter Maunz, *"Demonstration of qubit operations below a rigorous fault tolerance threshold with gate set tomography,"* Nat. Commun. **8**, 14485 (2017).

[15] Steven T. Flammia, David Gross, Yi-Kai Liu, and Jens Eisert, *"Quantum tomography via compressed sensing: error bounds, sample complexity and efficient estimators,"* New J. Phys. **14**, 095022 (2012).

[16] Andrey V. Rodionov, Andrzej Veitia, R. Barends, J. Kelly, Daniel Sank, J. Wenner, John M. Martinis, Robert L. Kosut, and Alexander N. Korotkov, *"Compressed sensing quantum process tomography for superconducting quantum gates,"* Phys. Rev. B **90**, 144504 (2014), 1407.0761.

[17] Yaakov S Weinstein, Timothy F. Havel, Joseph Emerson, Nicolas Boulant, Marcos Saraceno, Seth Lloyd, and David G. Cory, *"Quantum process tomography of the quantum Fourier transform,"* J. Chem. Phys. **121**, 6117 (2004).

[18] T. Monz, K. Kim, W. Hänsel, M. Riebe, A. S. Villar, P. Schindler, M. Chwalla, M. Hennrich, and R. Blatt, *"Realization of the quantum toffoli gate with trapped ions,"* Phys. Rev. Lett. **102**, 040501 (2009).

[19] Michał Horodecki, Paweł Horodecki, and Ryszard Horodecki, *"General teleportation channel, singlet fraction, and quasidistillation,"* Phys. Rev. A **60**, 1888 (1999).

[20] Michael A. Nielsen, *"A simple formula for the average gate fidelity of a quantum dynamical operation,"* Phys. Lett. A **303**, 249 (2002).

[21] Joseph Emerson, Robert Alicki, and Karol Życzkowski, *"Scalable noise estimation with random unitary operators,"* J. Optics B **7**, S347 (2005).

[22] Christoph Dankert, Richard Cleve, Joseph Emerson, and Etera Livine, *"Exact and approximate unitary 2-designs and their application to fidelity estimation,"* Phys. Rev. A **80**, 012304 (2009).

[23] Easwar Magesan, Jay M. Gambetta, and Joseph Emerson, *"Scalable and Robust Randomized Benchmarking of Quantum Processes,"* Phys. Rev. Lett. **106**, 180504 (2011).

[24] Scott Aaronson and Daniel Gottesman, *"Improved simulation of stabilizer circuits,"* Phys. Rev. A **70**, 052328 (2004).

[25] Alexander Erhard, Joel J Wallman, Lukas Postler, Michael Meth, Roman Stricker, Esteban A Martinez, Philipp Schindler, Thomas Monz, Joseph Emerson, and Rainer Blatt, *"Characterizing large-scale quantum computers via cycle benchmarking,"* Nat. Commun. **10**, 5347 (2019).

[26] John Preskill, *"Fault-tolerant quantum computation,"* in *Introduction to Quantum Computation* (World-Scientific, 1997) Chap. 8, pp. 213–269.

[27] Daniel Gottesmann, *Stabilizer Codes and Quantum Error Correction*, Ph.D. thesis, Caltech (1997).

[28] Daniel Gottesman, *"Theory of fault-tolerant quantum computation,"* Phys. Rev. A **57**, 127 (1998).

[29] Wojciech Hubert Zurek and Raymond Laflamme, *"Quantum logical operations on encoded qubits,"* Phys. Rev. Lett. **77**, 4683 (1996).

[30] Emanuel Knill, Raymond Laflamme, and Wojciech Zurek, *"Threshold accuracy for quantum computation,"* arXiv:quant-ph/9610011 (1996).

[31] John Preskill, *"Reliable quantum computers,"* Proceedings of the Royal Society of London. Series A: Mathematical, Physical and Engineering Sciences **454**, 385 (1998).

[32] David A. Herrera-Martí, Austin G. Fowler, David Jennings, and Terry Rudolph, *"Photonic implementation for the topological cluster-state quantum computer,"* Phys. Rev. A **82**, 032332 (2010).

[33] N. Cody Jones, Rodney Van Meter, Austin G. Fowler, Peter L. McMahon, Jungsang Kim, Thaddeus D. Ladd, and Yoshihisa Yamamoto, *"Layered architecture for quantum computing,"* Phys. Rev. X **2**, 031007 (2012).

[34] David P DiVincenzo, *"Fault-tolerant architectures for superconducting qubits,"* Physica Scripta **T137**, 014020 (2009).

[35] Peter Groszkowski, Austin G. Fowler, Felix Motzoi, and Frank K. Wilhelm, *"Tunable coupling between three qubits as a building block for a superconducting quantum computer,"* Phys. Rev. B **84**, 144516 (2011).

[36] J. Kruse, C. Gierl, M. Schlosser, and G. Birkl, *"Reconfigurable site-selective manipulation of atomic quantum systems in two-dimensional arrays of dipole traps,"* Phys. Rev. A **81**, 060308 (2010).

[37] Norman Y Yao, Liang Jiang, Alexey V Gorshkov, Peter C Maurer, Geza Giedke, J Ignacio Cirac, and Mikhail D Lukin, *"Scalable architecture for a room temperature solid-state quantum information processor,"* Nat. Commun. **3**, 1 (2012).

[38] Muir Kumph, Michael Brownnutt, and Rainer Blatt, *"Two-dimensional arrays of radio-frequency ion traps with addressable interactions,"* New J. Phys. **13**, 073043 (2011).

[39] David Kielpinski, Chris Monroe, and David J Wineland, *"Architecture for a large-scale ion-trap quantum computer,"* Nature **417**, 709 (2002).

[40] Bjoern Lekitsch, Sebastian Weidt, Austin G Fowler, Klaus Mølmer, Simon J Devitt, Christof Wunderlich, and Winfried K Hensinger, *"Blueprint for a microwave trapped ion quantum computer,"* Science Advances **3**, e1601540 (2017).

[41] Clare Horsman, Austin G. Fowler, Simon Devitt, and Rodney Van Meter, *"Surface code quantum computing by lattice surgery,"* New J. Phys. **14**, 123011 (2012).

[42] Peter W. Shor, *"Scheme for reducing decoherence in quantum computer memory,"* Phys. Rev. A **52**, R2493 (1995).

[43] Andrew Steane, *"Multiple-particle interference and quantum error correction,"* Proceedings of the Royal Society of London. Series A: Mathematical, Physical and Engineering Sciences **452**, 2551 (1996).

[44] Austin G. Fowler, Matteo Mariantoni, John M. Martinis, and Andrew N. Cleland, *"Surface codes: Towards practical large-scale quantum computation,"* Phys. Rev. A **86**, 032324 (2012).

[45] Raymond Laflamme, Cesar Miquel, Juan Pablo Paz, and Wojciech Hubert Zurek, *"Perfect quantum error correcting code,"* Phys. Rev. Lett. **77**, 198 (1996).

[46] A Yu Kitaev, *"Fault-tolerant quantum computation by anyons,"* Annals of Physics **303**, 2 (2003).

[47] Héctor Bombín, *"An introduction to topological quantum codes,"* arXiv:1311.0277 (2013).

[48] Sergey B Bravyi and A Yu Kitaev, *"Quantum codes on a lattice with boundary,"* arXiv:quant-ph/9811052 (1998).

[49] Michael H Freedman and David A Meyer, *"Projective plane and planar quantum codes,"* Foundations of Computational Mathematics **1**, 325 (2001).

[50] David S. Wang, Austin G. Fowler, and Lloyd C. L. Hollenberg, *"Surface code quantum computing with error rates over 1 %,"* Phys. Rev. A **83**, 020302 (2011).

[51] Yu Tomita and Krysta M. Svore, *"Low-distance surface codes under realistic quantum noise,"* Phys. Rev. A **90**, 062320 (2014).

[52] Christopher Chamberland, Aleksander Kubica, Theodore J Yoder, and Guanyu Zhu, *"Triangular color codes on trivalent graphs with flag qubits,"* New J. Phys. **22**, 023019 (2020).

[53] H. Bombin and M. A. Martin-Delgado, *"Topological quantum distillation,"* Phys. Rev. Lett. **97**, 180501 (2006).

[54] H. Bombin and M. A. Martin-Delgado, *"Topological computation without braiding,"* Phys. Rev. Lett. **98**, 160502 (2007).

[55] Bryan Eastin and Emanuel Knill, *"Restrictions on transversal encoded quantum gate sets,"* Phys. Rev. Lett. **102**, 110502 (2009).

[56] Sergey Bravyi and Alexei Kitaev, *"Universal quantum computation with ideal Clifford gates and noisy ancillas,"* Phys. Rev. A **71**, 022316 (2005).

[57] Robert Raussendorf and Jim Harrington, *"Fault-Tolerant Quantum Computation with High Threshold in Two Dimensions,"* Phys. Rev. Lett. **98**, 190504 (2007).

[58] Austin G. Fowler, Ashley M. Stephens, and Peter Groszkowski, *"High-threshold universal quantum computation on the surface code,"* Phys. Rev. A **80**, 052312 (2009).

[59] Hendrik Poulsen Nautrup, Nicolai Friis, and Hans J. Briegel, *"Fault-tolerant interface between quantum memories and quantum processors,"* Nat. Commun. **8**, 1321 (2017).

[60] M. Gutiérrez, M. Müller, and A. Bermúdez, *"Transversality and lattice surgery: Exploring realistic routes toward coupled logical qubits with trapped-ion quantum processors,"* Phys. Rev. A **99**, 022330 (2019).

[61] Erwin Schrödinger, *"Are there quantum jumps? Part II,"* The British Journal for the Philosophy of science **3**, 233 (1952).

[62] Thomas Ruster, Christian T Schmiegelow, Henning Kaufmann, Claudia Warschburger, Ferdinand Schmidt-Kaler, and Ulrich G Poschinger, *"A long-lived Zeeman trapped-ion qubit,"* Applied Physics B **122**, 254 (2016).

[63] Ye Wang, Mark Um, Junhua Zhang, Shuoming An, Ming Lyu, Jing-Ning Zhang, L-M Duan, Dahyun Yum, and Kihwan Kim, *"Single-qubit quantum memory exceeding ten-minute coherence time,"* Nat. Phot. **11**, 646 (2017).

[64] David P DiVincenzo, *"The physical implementation of quantum computation,"* Progress of Physics **48**, 771 (2000).

[65] Wolfgang Paul and Helmut Steinwedel, *"Ein neues Massenspektrometer ohne Magnetfeld,"* Zeitschrift für Naturforschung A **8**, 448 (1953).

[66] MG Raizen, JM Gilligan, James C Bergquist, Wayne M Itano, and David J Wineland, *"Ionic crystals in a linear Paul trap,"* Phys. Rev. A **45**, 6493 (1992).

[67] Fouad G Major, Viorica N Gheorghe, and Günther Werth, *Charged particle traps: physics and techniques of charged particle field confinement* (Springer Science & Business Media, 2005).

[68] Stefan Timo Gulde, *Experimental Realization of Quantum Gates and the Deutsch-Jozsa Alogrithm with Trapped Calcium Ions*, Ph.D. thesis, University of Innsbruck (2003).

[69] Daniel FV James, *"Quantum dynamics of cold trapped ions with application to quantum computation,"* Appl. Phys. B **66**, 181 (1998).

[70] Dietrich Leibfried, Rainer Blatt, Christopher Monroe, and David Wineland, *"Quantum dynamics of single trapped ions,"* Reviews of Modern Physics **75**, 281 (2003).

[71] Giovanna Morigi, Jürgen Eschner, and Christoph H Keitel, *"Ground state laser cooling using electromagnetically induced transparency,"* Phys. Rev. Lett. **85**, 4458 (2000).

[72] CF Roos, D Leibfried, A Mundt, F Schmidt-Kaler, J Eschner, and R Blatt, *"Experimental demonstration of ground state laser cooling with electromagnetically induced transparency,"* Phys. Rev. Lett. **85**, 5547 (2000).

[73] Regina Lechner, Christine Maier, Cornelius Hempel, Petar Jurcevic, Ben P Lanyon, Thomas Monz, Michael Brownnutt, Rainer Blatt, and Christian F Roos, *"Electromagnetically-induced-transparency ground-state cooling of long ion strings,"* Phys. Rev. A **93**, 053401 (2016).

[74] Simon Webster, *Raman sideband cooling and coherent manipulation of trapped ions*, Ph.D. thesis, University of Oxford (2005).

[75] Christian Roos, *Controlling the quantum state of trapped ions*, Ph.D. thesis, University of Innsbruck (2000).

[76] Michael Chwalla, *Precision spectroscopy with $^{40}Ca^{+}$ ions in a Paul trap*, Ph.D. thesis, University of Innsbruck (2009).

[77] Philipp Schindler, *Quantum computation and simulation with trapped ions using dissipation*, Ph.D. thesis, University of Innsbruck (2013).

[78] David J Wineland and Wayne M Itano, *"Laser cooling of atoms,"* Phys. Rev. A **20**, 1521 (1979).

[79] C. A Blockley, D. F Walls, and H Risken, *"Quantum collapses and revivals in a quantized trap,"* Europhysics Letters (EPL) **17**, 509 (1992).

[80] David J Wineland, C Monroe, Wayne M Itano, Dietrich Leibfried, Brian E King, and Dawn M Meekhof, *"Experimental issues in coherent quantum-state manipulation of trapped atomic ions,"* Journal of Research of the National Institute of Standards and Technology **103**, 259 (1998).

[81] Rudolf Grimm, Matthias Weidemüller, and Yurii B Ovchinnikov, "*Optical dipole traps for neutral atoms,*" in *Advances in atomic, molecular, and optical physics*, Vol. 42 (Elsevier, 2000) pp. 95–170.

[82] H. Häffner, S. Gulde, M. Riebe, G. Lancaster, C. Becher, J. Eschner, F. Schmidt-Kaler, and R. Blatt, "*Precision measurement and compensation of optical stark shifts for an ion-trap quantum processor,*" Phys. Rev. Lett. **90**, 143602 (2003).

[83] Anders Sørensen and Klaus Mølmer, "*Quantum computation with ions in thermal motion,*" Phys. Rev. A **82**, 1971 (1999).

[84] Anders Sørensen and Klaus Mølmer, "*Entanglement and quantum computation with ions in thermal motion,*" Phys. Rev. A **62**, 022311 (2000).

[85] Norman F Ramsey, "*A molecular beam resonance method with separated oscillating fields,*" Phys. Rev. **78**, 695 (1950).

[86] Philipp Schindler, Daniel Nigg, Thomas Monz, Julio T Barreiro, Esteban Martinez, Shannon X Wang, Stephan Quint, Matthias F Brandl, Volckmar Nebendahl, Christian F Roos, *et al.*, "*A quantum information processor with trapped ions,*" New J. Phys. **15**, 123012 (2013).

[87] Roman Stricker, *Gatteroperationen hoher Güte in einem optischen Quantenbit*, Master's thesis, University of Innsbruck (2017).

[88] Erwin L Hahn, "*Spin echoes,*" Phys. Rev. **80**, 580 (1950).

[89] Daniel Nigg, *Towards fault tolerant quantum computation*, Ph.D. thesis, University of Innsbruck (2017).

[90] W Neuhauser, M Hohenstatt, P Toschek, and H Dehmelt, "*Optical-sideband cooling of visible atom cloud confined in parabolic well,*" Phys. Rev. Lett. **41**, 233 (1978).

[91] David J Wineland, Robert E Drullinger, and Fred L Walls, "*Radiation-pressure cooling of bound resonant absorbers,*" Phys. Rev. Lett. **40**, 1639 (1978).

[92] Jürgen Eschner, Giovanna Morigi, Ferdinand Schmidt-Kaler, and Rainer Blatt, "*Laser cooling of trapped ions,*" JOSA B **20**, 1003 (2003).

[93] F Diedrich, E Peik, JM Chen, W Quint, and H Walther, "*Observation of a phase transition of stored laser-cooled ions,*" Phys. Rev. Lett. **59**, 2931 (1987).

[94] David J Wineland, JC Bergquist, Wayne M Itano, JJ Bollinger, and CH Manney, "*Atomic-ion Coulomb clusters in an ion trap,*" Phys. Rev. Lett. **59**, 2935 (1987).

[95] R Blümel, JM Chen, E Peik, W Quint, W Schleich, YR Shen, and H Walther, "*Phase transitions of stored laser-cooled ions,*" Nature **334**, 309 (1988).

[96] Giovanna Morigi and Shmuel Fishman, "*One-dimensional coulomb crystals at low temperatures,*" Journal of Physics B: Atomic, Molecular and Optical Physics **39**, S221 (2006).

[97] Wolfgang Demtröder, *Experimentalphysik 3: Atome, Moleküle und Festkörper* (Springer-Verlag, 2010).

[98] RH Dicke, *"The effect of collisions upon the doppler width of spectral lines,"* Phys. Rev. **89**, 472 (1953).

[99] JI Cirac, LJ Garay, R Blatt, AS Parkins, and P Zoller, *"Laser cooling of trapped ions: The influence of micromotion,"* Phys. Rev. A **49**, 421 (1994).

[100] Lei-Lei Yan, Shi-Lei Su, and Mang Feng, *"Determining temperature and Rabi frequency regarding trapped ions in Doppler cooling: An analytic investigation,"* arXiv:1902.00302 (2019).

[101] JH Wesenberg, RJ Epstein, D Leibfried, RB Blakestad, J Britton, JP Home, Wayne M Itano, John D Jost, E Knill, C Langer, *et al.*, *"Fluorescence during doppler cooling of a single trapped atom,"* Phys. Rev. A **76**, 053416 (2007).

[102] J. I. Cirac, R. Blatt, A. S. Parkins, and P. Zoller, *"Laser cooling of trapped ions with polarization gradients,"* Phys. Rev. A **48**, 1434 (1993).

[103] S. Ejtemaee and P. C. Haljan, *"3D Sisyphus cooling of trapped ions,"* Phys. Rev. Lett. **119**, 043001 (2017).

[104] M K Joshi, A Fabre, C Maier, T Brydges, D Kiesenhofer, H Hainzer, R Blatt, and C F Roos, *"Polarization-gradient cooling of 1D and 2D ion Coulomb crystals,"* New J. Phys. **22**, 103013 (2020).

[105] I. Marzoli, J. I. Cirac, R. Blatt, and P. Zoller, *"Laser cooling of trapped three-level ions: Designing two-level systems for sideband cooling,"* Phys. Rev. A **49**, 2771 (1994).

[106] W. M. Itano, J. C. Bergquist, J. J. Bollinger, J. M. Gilligan, D. J. Heinzen, F. L. Moore, M. G. Raizen, and D. J. Wineland, *"Quantum projection noise: Population fluctuations in two-level systems,"* Phys. Rev. A **47**, 3554 (1993).

[107] Q. A. Turchette, Kielpinski, B. E. King, D. Leibfried, D. M. Meekhof, C. J. Myatt, M. A. Rowe, C. A. Sackett, C. S. Wood, W. M. Itano, C. Monroe, and D. J. Wineland, *"Heating of trapped ions from the quantum ground state,"* Phys. Rev. A **61**, 063418 (2000).

[108] M. Brownnutt, M. Kumph, P. Rabl, and R. Blatt, *"Ion-trap measurements of electric-field noise near surfaces,"* Rev. Mod. Phys. **87**, 1419 (2015).

[109] K. Lakhmanskiy, P. C. Holz, D. Schärtl, B. Ames, R. Assouly, T. Monz, Y. Colombe, and R. Blatt, *"Observation of superconductivity and surface noise using a single trapped ion as a field probe,"* Phys. Rev. A **99**, 023405 (2019).

[110] Mu Qiao, Ye Wang, Zhengyang Cai, Botao Du, Pengfei Wang, Chunyang Luan, Wentao Chen, Heung-Ryoul Noh, and Kihwan Kim, *"Double-electromagnetically-induced-transparency ground-state cooling of stationary two-dimensional ion crystals,"* Phys. Rev. Lett. **126**, 023604 (2021).

[111] Amit Kumar Pal, Philipp Schindler, Alexander Erhard, Ángel Rivas, Miguel-Angel Martin-Delgado, Rainer Blatt, Thomas Monz, and Markus Müller, *"Relaxation times do not capture logical qubit dynamics,"* (2020), arXiv:2012.07911 [quant-ph].

[112] Hartmut Häffner, Christian F Roos, and Rainer Blatt, *"Quantum computing with trapped ions,"* Physics reports **469**, 155 (2008).

[113] Thomas Monz, *Quantum information processing beyond ten ion-qubits*, Ph.D. thesis, University of Innsbruck (2011).

[114] Esteban Martinez, *Quantum Computation and Quantum Simulation with a trapped-ion Quantum Computer*, Ph.D. thesis, University of Innsbruck (2017).

[115] Michael Meth, *Dynamische Kontrolle von Laserimpulsenzur Quanteninformationsverarbeitung*, Master's thesis, University of Innsbruck (2017).

[116] F Schmidt-Kaler, H Häffner, S Gulde, M Riebe, GPT Lancaster, T Deuschle, C Becher, W Hänsel, J Eschner, CF Roos, *et al.*, *"How to realize a universal quantum gate with trapped ions,"* Applied Physics B **77**, 789 (2003).

[117] RWP Drever, John L Hall, FV Kowalski, J_ Hough, GM Ford, AJ Munley, and H Ward, *"Laser phase and frequency stabilization using an optical resonator,"* Applied Physics B **31**, 97 (1983).

[118] Eric D Black, *"An introduction to Pound–Drever–Hall laser frequency stabilization,"* American journal of physics **69**, 79 (2001).

[119] Jan Benhelm, *Precision spectroscopy and quantum information processing with trapped Calcium ions*, Ph.D. thesis, University of Innsbruck (2008).

[120] Long-Sheng Ma, Peter Jungner, Jun Ye, and John L Hall, *"Delivering the same optical frequency at two places: accurate cancellation of phase noise introduced by an optical fiber or other time-varying path,"* Optics letters **19**, 1777 (1994).

[121] W Zhang, MJ Martin, C Benko, JL Hall, J Ye, C Hagemann, T Legero, U Sterr, F Riehle, GD Cole, *et al.*, *"Reduction of residual amplitude modulation to 1× 10-6 for frequency modulation and laser stabilization,"* Optics letters **39**, 1980 (2014).

[122] Gerhard Kirchmair, *Quantum non-demolition measurements and quantum simulation*, Ph.D. thesis, University of Innsbruck (2010).

[123] Janis Alnis, Arthur Matveev, Nikolai Kolachevsky, Th Udem, and TW Hänsch, *"Subhertz linewidth diode lasers by stabilization to vibrationally and thermally compensated ultralow-expansion glass fabry-pérot cavities,"* Physical Review A **77**, 053809 (2008).

[124] Thomas Kessler, Christian Hagemann, C Grebing, T Legero, Uwe Sterr, Fritz Riehle, MJ Martin, L Chen, and J Ye, *"A sub-40-mhz-linewidth laser based on a silicon single-crystal optical cavity,"* Nat. Phot. **6**, 687 (2012).

[125] M. Bishof, X. Zhang, M. J. Martin, and Jun Ye, *"Optical spectrum analyzer with quantum-limited noise floor,"* Phys. Rev. Lett. **111**, 093604 (2013).

[126] Sebastian Häfner, Stephan Falke, Christian Grebing, Stefan Vogt, Thomas Legero, Mikko Merimaa, Christian Lisdat, and Uwe Sterr, *"*8×10^{-17} *fractional laser frequency instability with a long room-temperature cavity,"* Opt. Lett. **40**, 2112 (2015).

[127] D G Matei, T Legero, Ch Grebing, S Häfner, Ch Lisdat, R Weyrich, W Zhang, L Sonderhouse, J M Robinson, F Riehle, J Ye, and U Sterr, *"A second generation of low thermal noise cryogenic silicon resonators,"* Journal of Physics: Conference Series **723**, 012031 (2016).

[128] Abraham Savitzky and Marcel JE Golay, *"Smoothing and differentiation of data by simplified least squares procedures."* Analytical chemistry **36**, 1627 (1964).

[129] Ernst Schloemann, *"Fluctuations of the magnetic field generated by permanent magnets,"* Journal of Applied Physics **55**, 2470 (1984).

[130] Wolfgang Nolting, *Grundkurs Theoretische Physik 3* (Springer, 2007).

[131] Wayne M Itano, *"External-field shifts of the $^{199}Hg^{+}$ optical frequency standard,"* J. Res. Natl. Inst. Stand. Technol. **105**, 829 (2000).

[132] Christian F Roos, *"Precision frequency measurements with entangled states,"* arXiv:quant-ph/0508148 (2005).

[133] Steven T. Flammia and Yi-Kai Liu, *"Direct Fidelity Estimation from Few Pauli Measurements,"* Phys. Rev. Lett. **106**, 230501 (2011).

[134] Marcus P. da Silva, Olivier Landon-Cardinal, and David Poulin, *"Practical Characterization of Quantum Devices without Tomography,"* Phys. Rev. Lett. **107**, 210404 (2011).

[135] Osama Moussa, Marcus P. da Silva, Colm A Ryan, and Raymond Laflamme, *"Practical Experimental Certification of Computational Quantum Gates Using a Twirling Procedure,"* Phys. Rev. Lett. **109**, 070504 (2012).

[136] Zdenek Hradil, *"Quantum-state estimation,"* Phys. Rev. A **55**, R1561 (1997).

[137] Daniel FV James, Paul G Kwiat, William J Munro, and Andrew G White, *"On the measurement of qubits,"* in *Asymptotic Theory of Quantum Statistical Inference: Selected Papers* (World Scientific, 2005) pp. 509–538.

[138] Zdeněk Hradil, Jaroslav Řeháček, Jaromír Fiurášek, and Miroslav Ježek, *"3 maximum-likelihood methods in quantum mechanics,"* in *Quantum state estimation* (Springer, 2004) pp. 59–112.

[139] Hartmut Häffner, Wolfgang Hänsel, CF Roos, Jan Benhelm, Michael Chwalla, Timo Körber, UD Rapol, Mark Riebe, PO Schmidt, Christoph Becher, *et al.*, *"Scalable multiparticle entanglement of trapped ions,"* Nature **438**, 643 (2005).

[140] Andrzej Jamiołkowski, *"Linear transformations which preserve trace and positive semidefiniteness of operators,"* Reports on Mathematical Physics **3**, 275 (1972).

[141] Man-Duen Choi, *"Completely positive linear maps on complex matrices,"* Linear algebra and its applications **10**, 285 (1975).

[142] Daniel Gottesman, *"The Heisenberg representation of quantum computers,"* arXiv:quant-ph/9807006 (1998).

[143] Maris Ozols, *"Clifford group,"* (Online resource, 2008).

[144] Jay M. Gambetta, Antonio D. Córcoles, Seth T. Merkel, Blake R. Johnson, John A. Smolin, Jerry M. Chow, Colm A. Ryan, Chad Rigetti, Stefano Poletto, Thomas A. Ohki, Mark B. Ketchen, and Matthias Steffen, *"Characterization of addressability by simultaneous randomized benchmarking,"* Phys. Rev. Lett. **109**, 240504 (2012).

[145] John Preskill, *"Sufficient condition on noise correlations for scalable quantum computing,"* Quantum Info. Comput. **13**, 181–194 (2013).

[146] Joel J. Wallman and Joseph Emerson, *"Noise tailoring for scalable quantum computation via randomized compiling,"* Phys. Rev. A **94**, 052325 (2016).

[147] Arnaud Carignan-Dugas, Joel J. Wallman, and Joseph Emerson, *"Characterizing universal gate sets via dihedral benchmarking,"* Phys. Rev. A **92**, 060302 (2015).

[148] Emanuel Knill, *"Quantum computing with realistically noisy devices,"* Nature **434**, 39 (2005), arXiv:0410199 [quant-ph].

[149] Easwar Magesan, Jay M. Gambetta, Blake R. Johnson, Colm A. Ryan, Jerry M. Chow, Seth T. Merkel, Marcus P. da Silva, George A. Keefe, Mary B. Rothwell, Thomas A. Ohki, Mark B. Ketchen, and M. Steffen, *"Efficient Measurement of Quantum Gate Error by Interleaved Randomized Benchmarking,"* Phys. Rev. Lett. **109**, 080505 (2012).

[150] Arnaud Carignan-Dugas, Joel J Wallman, and Joseph Emerson, *"Bounding the average gate fidelity of composite channels using the unitarity,"* New J. Phys. **21**, 053016 (2019).

[151] Jonas Helsen, Xiao Xue, Lieven MK Vandersypen, and Stephanie Wehner, *"A new class of efficient randomized benchmarking protocols,"* npj Quantum Information **5**, 1 (2019).

[152] Esteban A Martinez, Thomas Monz, Daniel Nigg, Philipp Schindler, and Rainer Blatt, *"Compiling quantum algorithms for architectures with multi-qubit gates,"* New J. Phys. **18**, 063029 (2016).

[153] Alexander Erhard, Hendrik Poulsen Nautrup, Michael Meth, Lukas Postler, Roman Stricker, Martin Stadler, Vlad Negnevitsky, Martin Ringbauer, Philipp Schindler, Hans J Briegel, Rainer Blatt, Nicolai Friis, and Thomas Monz, *"Entangling logical qubits with lattice surgery,"* Nature **589**, 220 (2021).

[154] Simon J. Devitt, William J. Munro, and Kae Nemoto, *"Quantum error correction for beginners,"* Rep. Prog. Phys. **76**, 076001 (2013).

[155] Barbara M. Terhal, *"Quantum error correction for quantum memories,"* Rev. Mod. Phys. **87**, 307 (2015).

[156] Earl T. Campbell, Barbara M. Terhal, and Christophe Vuillot, *"Roads towards fault-tolerant universal quantum computation,"* Nature **549**, 172 (2017).

[157] D. G. Cory, M. D. Price, W. Maas, E. Knill, R. Laflamme, W. H. Zurek, T. F. Havel, and S. S. Somaroo, *"Experimental Quantum Error Correction,"* Phys. Rev. Lett. **81**, 2152 (1998).

[158] E. Knill, R. Laflamme, R. Martinez, and C. Negrevergne, *"Benchmarking Quantum Computers: The Five-Qubit Error Correcting Code,"* Phys. Rev. Lett. **86**, 5811 (2001).

[159] J. Chiaverini, D. Leibfried, T. Schaetz, M. D. Barrett, R. B. Blakestad, J. Britton, J. D. Itano, W. M. Jost, E. Knill, C. Langer, R. Ozeri, and D. J. Wineland, *"Realization of quantum error correction,"* Nature **432**, 602 (2004).

[160] Nicolas Boulant, Lorenza Viola, Evan M. Fortunato, and David G. Cory, *"Experimental Implementation of a Concatenated Quantum Error-Correcting Code,"* Phys. Rev. Lett. **94**, 130501 (2005).

[161] Jingfu Zhang, Dorian Gangloff, Osama Moussa, and Raymond Laflamme, *"Experimental quantum error correction with high fidelity,"* Phys. Rev. A **84**, 034303 (2011).

[162] James R. Wootton and Daniel Loss, *"Repetition code of 15 qubits,"* Phys. Rev. A **97**, 052313 (2018).

[163] B. A. Bell, D. A. Herrera-Martí, M. S. Tame, D. Markham, W. J. Wadsworth, and J. G. Rarity, *"Experimental demonstration of a graph state quantum error-correction code,"* Nat. Commun. **5**, 3658 (2014).

[164] Maika Takita, Andrew W. Cross, A. D. Córcoles, Jerry M. Chow, and Jay M. Gambetta, *"Experimental Demonstration of Fault-Tolerant State Preparation with Superconducting Qubits,"* Phys. Rev. Lett. **119**, 180501 (2017).

[165] J. Kelly, R. Barends, A. G. Fowler, A. Megrant, E. Jeffrey, T. C. White, D. Sank, J. Y. Mutus, B. Campbell, Yu Chen, Z. Chen, B. Chiaro, A. Dunsworth, I.-C. Hoi, C. Neill, P. J. J. O'Malley, C. Quintana, P. Roushan, A. Vainsencher, J. Wenner, A. N. Cleland, and John M. Martinis, *"State preservation by repetitive error detection in a superconducting quantum circuit,"* Nature **519**, 66 (2015).

[166] Norbert M. Linke, Mauricio Gutierrez, Kevin A. Landsman, Caroline Figgatt, Shantanu Debnath, Kenneth R. Brown, and Christopher Monroe, *"Fault-tolerant quantum error detection,"* Sci. Adv. **3**, e1701074 (2017).

[167] Christian Kraglund Andersen, Ants Remm, Stefania Lazar, Sebastian Krinner, Nathan Lacroix, Graham J. Norris, Mihai Gabureac, Christopher Eichler, and Andreas Wallraff, *"Repeated quantum error detection in a surface code,"* Nat. Phys. **16**, 875 (2020).

[168] Takao Aoki, Go Takahashi, Tadashi Kajiya, Jun-ichi Yoshikawa, Samuel L. Braunstein, Peter van Loock, and Akira Furusawa, *"Quantum error correction beyond qubits,"* Nat. Phys. **5**, 541 (2009).

[169] M. D. Reed, L. DiCarlo, L. Nigg, S. E.and Sun, L. Frunzio, S. M. Girvin, and R. J. Schoelkopf, *"Realization of three-qubit quantum error correction with superconducting circuits,"* Nature **482**, 382 (2012).

[170] G. Waldherr, Y. Wang, S. Zaiser, M. Jamali, T. Schulte-Herbrüggen, H. Abe, T. Ohshima, J. Isoya, J. F. Du, P. Neumann, and J. Wrachtrup, *"Quantum error correction in a solid-state hybrid spin register,"* Nature **506**, 204 (2014).

[171] Nissim Ofek, Andrei Petrenko, Reinier Heeres, Philip Reinhold, Zaki Leghtas, Brian Vlastakis, Yehan Liu, Luigi Frunzio, S. M. Girvin, L. Jiang, Mazyar Mirrahimi, M. H. Devoret, and R. J. Schoelkopf, *"Extending the lifetime of a quantum bit with error correction in superconducting circuits,"* Nature **536**, 441 (2016).

[172] Roman Stricker, Davide Vodola, Alexander Erhard, Lukas Postler, Michael Meth, Martin Ringbauer, Philipp Schindler, Thomas Monz, Markus Müller, and Rainer Blatt, *"Experimental deterministic correction of qubit loss,"* Nature **585**, 207 (2020).

[173] Jingfu Zhang, Raymond Laflamme, and Dieter Suter, *"Experimental Implementation of Encoded Logical Qubit Operations in a Perfect Quantum Error Correcting Code,"* Phys. Rev. Lett. **109**, 100503 (2012).

[174] Daniel Nigg, Markus Müller, Esteban A. Martinez, Philipp Schindler, Markus Hennrich, Thomas Monz, Miguel A. Martin-Delgado, and Rainer Blatt, *"Quantum computations on a topologically encoded qubit,"* Science **345**, 302 (2014).

[175] Rami Barends, Julian Kelly, Anthony Megrant, Andrzej Veitia, Daniel Sank, Evan Jeffrey, Ted C. White, Josh Y. Mutus, Austin G. Fowler, B. Campbell, Yu Chen, Zijun Chen, Ben Chiaro, Andrew Dunsworth, Charles Neill, Peter O'Malley, Pedram Roushan, Amit Vainsencher, Jim Wenner, Alexander N. Korotkov, Andrew N. Cleland, and John M. Martinis, *"Superconducting quantum circuits at the surface code threshold for fault tolerance,"* Nature **508**, 500 (2014).

[176] Reinier W. Heeres, Philip Reinhold, Nissim Ofek, Luigi Frunzio, Liang Jiang, Michel H. Devoret, and Robert J. Schoelkopf, *"Implementing a universal gate set on a logical qubit encoded in an oscillator,"* Nat. Commun. **8**, 94 (2017).

[177] Ming Gong, Xiao Yuan, Shiyu Wang, Yulin Wu, Youwei Zhao, Chen Zha, Shaowei Li, Zhen Zhang, Qi Zhao, Yunchao Liu, Futian Liang, Jin Lin, Yu Xu, Hui Deng, Hao Rong, He Lu, Simon C. Benjamin, Cheng-Zhi Peng, Xiongfeng Ma, Yu-Ao Chen, Xiaobo Zhu, and Jian-Wei Pan, *"Experimental verification of five-qubit quantum error correction with superconducting qubits,"* arXiv:1907.04507 (2019).

[178] L. Hu, Y. Ma, W. Cai, X. Mu, Y. Xu, W. Wang, Y. Wu, H. Wang, Y. P. Song, C.-L. Zou, S. M. Girvin, L-M. Duan, and L. Sun, *"Quantum error correction and universal gate set operation on a binomial bosonic logical qubit,"* Nat. Phys. **15**, 503 (2019).

[179] Kevin S. Chou, Jacob Z. Blumoff, Christopher S. Wang, Philip C. Reinhold, Christopher J. Axline, Yvonne Y. Gao, L. Frunzio, M. H. Devoret, Liang Jiang, and R. J. Schoelkopf, *"Deterministic teleportation of a quantum gate between two logical qubits,"* Nature **561**, 368 (2018).

[180] Robin Harper and Steven T. Flammia, *"Fault-Tolerant Logical Gates in the IBM Quantum Experience,"* Phys. Rev. Lett. **122**, 080504 (2019).

[181] Rami Barends, Julian Kelly, Anthony Megrant, Andrzej Veitia, Daniel Sank, Evan Jeffrey, Ted C White, Josh Mutus, Austin G Fowler, Brooks Campbell, *et al.*, *"Superconducting quantum circuits at the surface code threshold for fault tolerance,"* Nature **508**, 500 (2014).

[182] N Cody Jones, Rodney Van Meter, Austin G Fowler, Peter L McMahon, Jungsang Kim, Thaddeus D Ladd, and Yoshihisa Yamamoto, *"Layered architecture for quantum computing,"* Phys. Rev. X **2**, 031007 (2012).

[183] Alexei Kitaev, *"Fault-tolerant quantum computation by anyons,"* Ann. Phys. **303**, 2 (2003).

[184] Eric Dennis, Alexei Kitaev, Andrew Landahl, and John Preskill, *"Topological quantum memory,"* J. Math. Phys. **43**, 4452 (2002).

[185] Philipp Schindler, Julio T Barreiro, Thomas Monz, Volckmar Nebendahl, Daniel Nigg, Michael Chwalla, Markus Hennrich, and Rainer Blatt, *"Experimental repetitive quantum error correction,"* Science **332**, 1059 (2011).

[186] Alejandro Bermudez, Xiaosi Xu, Ramil Nigmatullin, Joe O'Gorman, Vlad Negnevitsky, Philipp Schindler, Thomas Monz, UG Poschinger, Cornelius Hempel, J Home, *et al.*, *"Assessing the progress of trapped-ion processors towards fault-tolerant quantum computation,"* Phys. Rev. X **7**, 041061 (2017).

[187] Hendrik Poulsen Nautrup, Nicolas Delfosse, Vedran Dunjko, Hans J. Briegel, and Nicolai Friis, *"Optimizing quantum error correction codes with reinforcement learning,"* Quantum **3**, 215 (2019).

[188] Robert Raussendorf and Hans J. Briegel, *"A One-Way Quantum Computer,"* Phys. Rev. Lett. **86**, 5188 (2001).

[189] B. P. Lanyon, P. Jurcevic, M. Zwerger, C. Hempel, E. A. Martinez, W. Dür, H. J. Briegel, R. Blatt, and C. F. Roos, *"Measurement-Based Quantum Computation with Trapped Ions,"* Phys. Rev. Lett. **111**, 210501 (2013).

[190] Nicolai Friis, Oliver Marty, Christine Maier, Cornelius Hempel, Milan Holzäpfel, Petar Jurcevic, Martin B. Plenio, Marcus Huber, Christian Roos, Rainer Blatt, and Ben Lanyon, *"Observation of Entangled States of a Fully Controlled 20-Qubit System,"* Phys. Rev. X **8**, 021012 (2018).

[191] Michał Horodecki and Paweł Horodecki, *"Reduction criterion of separability and limits for a class of distillation protocols,"* Phys. Rev. A **59**, 4206 (1999).

[192] Joel J. Wallman, *"Error rates in quantum circuits,"* arXiv:1511.00727 (2015).

[193] Alexei Gilchrist, Nathan K. Langford, and Michael A. Nielsen, *"Distance measures to compare real and ideal quantum processes,"* Phys. Rev. A **71**, 062310 (2005).

[194] Daniel Litinski, *"A Game of Surface Codes: Large-Scale Quantum Computing with Lattice Surgery,"* Quantum **3**, 128 (2019).

[195] Nicolai Friis, Giuseppe Vitagliano, Mehul Malik, and Marcus Huber, *"Entanglement Certification From Theory to Experiment,"* Nat. Rev. Phys. **1**, 72 (2019).

[196] B. Edlén and P. Risberg, *"The Spectrum of Singly-Ionized Calcium, Ca II,"* Ark. Fys. (Stockholm) **10** (1956).

[197] R Gerritsma, G Kirchmair, F Zähringer, J Benhelm, R Blatt, and CF Roos, *"Precision measurement of the branching fractions of the $4p^2P_{3/2}$ decay of Ca II,"* The European Physical Journal D **50**, 13 (2008).

[198] Michael Ramm, Thaned Pruttivarasin, Mark Kokish, Ishan Talukdar, and Hartmut Häffner, *"Precision measurement method for branching fractions of excited $P_{1/2}$ states applied to $^{40}Ca^+$,"* Phys. Rev. Lett. **111**, 023004 (2013).

[199] M Chwalla, J Benhelm, K Kim, G Kirchmair, T Monz, M Riebe, P Schindler, AS Villar, W Hänsel, CF Roos, *et al.*, *"Absolute Frequency Measurement of the $^{40}Ca^+$ $4s^2S_{1/2} - 3d^2D_{5/2}$ Clock Transition,"* Phys. Rev. Lett. **102**, 023002 (2009).

[200] G. Risberg, *"The Spectrum of Atomic Calcium, Ca I, and Extensions to the Analysis of Ca II,"* Ark. Fys. (Stockholm) **37** (1968).

[201] Jian Jin and DA Church, *"Precision lifetimes for the* Ca^+ $4p^2P$ *levels: Experiment challenges theory at the 1% level,"* Phys. Rev. Lett. **70**, 3213 (1993).

[202] PA Barton, CJS Donald, DM Lucas, DA Stevens, AM Steane, and DN Stacey, *"Measurement of the lifetime of the* $3d^2d_{5/2}$ *state in* $^{40}Ca^+$*,"* Phys. Rev. A **62**, 032503 (2000).

[203] G Tommaseo, T Pfeil, G Revalde, G Werth, P Indelicato, and JP Desclaux, *"The* g_J*-factor in the ground state of* Ca^+*,"* The European Physical Journal D-Atomic, Molecular, Optical and Plasma Physics **25**, 113 (2003).

[204] Marc Hein, Wolfgang Dür, Jens Eisert, Robert Raussendorf, M Nest, and H-J Briegel, *"Entanglement in graph states and its applications,"* arXiv:0602096 (2006).

[205] Wassily Hoeffding, *"Probability Inequalities for Sums of Bounded Random Variables,"* Journal of the American Statistical Association **58**, 13 (1963).

[206] AS Holevo, *"Additivity conjecture and covariant channels,"* International Journal of Quantum Information **3**, 41 (2005).

[207] Jonas Helsen, Xiao Xue, Lieven MK Vandersypen, and Stephanie Wehner, *"A new class of efficient randomized benchmarking protocols,"* npj Quantum Information **5**, 1 (2019).

[208] David E Evans and R. Hoegh-Krohn, *"Spectral Properties of Positive Maps on* C^**-Algebras,"* Journal of the London Mathematical Society **17**, 345 (1978).

[209] Robin Harper, Ian Hincks, Chris Ferrie, Steven T. Flammia, and Joel J. Wallman, *"Statistical analysis of randomized benchmarking,"* Phys. Rev. A **99**, 052350 (2019).

[210] Esteban A Martinez, Christine A Muschik, Philipp Schindler, Daniel Nigg, Alexander Erhard, Markus Heyl, Philipp Hauke, Marcello Dalmonte, Thomas Monz, Peter Zoller, *et al.*, *"Real-time dynamics of lattice gauge theories with a few-qubit quantum computer,"* Nature **534**, 516 (2016).

[211] Lukas Postler, Ángel Rivas, Philipp Schindler, Alexander Erhard, Roman Stricker, Daniel Nigg, Thomas Monz, Rainer Blatt, and Markus Müller, *"Experimental quantification of spatial correlations in quantum dynamics,"* Quantum **2**, 90 (2018).

[212] C Greganti, TF Demarie, M Ringbauer, JA Jones, V Saggio, IA Calafell, LA Rozema, A Erhard, M Meth, L Postler, *et al.*, *"Cross-verification of independent quantum devices,"* arXiv:1905.09790 (2019).

COLOPHON

This document was typeset using the typographical look-and-feel `classicthesis` developed by André Miede and Ivo Pletikosić. The style was inspired by Robert Bringhurst's seminal book on typography "*The Elements of Typographic Style*". `classicthesis` is available for both LaTeX and LyX:

`https://bitbucket.org/amiede/classicthesis/`

Final Version as of May 18, 2021 (classicthesis v4.6).